



TECHNISCHE UNIVERSITÄT MÜNCHEN

Wissenschaftszentrum Weihenstephan für Ernährung, Landnutzung und Umwelt

Lehrstuhl für Analytische Lebensmittelchemie

**Molecular-level analysis of non-volatile Maillard
reaction products and their chemical interplay in
model reactions**

Daniel Hemmler

Vollständiger Abdruck der von der Fakultät Wissenschaftszentrum Weihenstephan für Ernährung, Landnutzung und Umwelt der Technischen Universität München zur Erlangung des akademischen Grades eines

Doktors der Naturwissenschaften

genehmigten Dissertation.

Vorsitzender: Prof. Dr. Erwin Grill

Prüfer der Dissertation:

1. apl. Prof. Dr. Philippe Schmitt-Kopplin
2. Prof. Dr. Karl-Heinz Engel
3. Prof. Dr. Varoujan Yaylayan (McGill University, Kanada)

Die Dissertation wurde am 09.04.2019 bei der Technischen Universität München eingereicht und durch die Fakultät Wissenschaftszentrum Weihenstephan für Ernährung, Landnutzung und Umwelt am 22.08.2019 angenommen.

This page intentionally left blank

Acknowledgements

Nearly four years of research have been summarized in this thesis. Regardless, the curiosity to discover something new every day has remained. Not everything that we have discovered in the recent years was in the direct focus of this work. Therefore, I am all the more pleased to continue working on these exciting projects in the future. The past years have been a very enriching time both personally and professionally, which I do not want to miss. All this would not have been possible without the support and help of so many wonderful people.

First of all, I would like to specially thank my supervisor Prof. Dr. Philippe Schmitt-Kopplin, who gave me the opportunity to do this work in his exceptional research group. You always had a sympathetic ear (and an open door) for my affairs. I also thank you for the freedom you gave me in this research and for your help and support not only in tricky situations. The many delighted discussions and your creative ideas have continually inspired me in my work.

I am very grateful to Prof. Dr. Michael Rychlik, Prof. Dr. Andrew Taylor and Dr. James Marshall for the countless fruitful discussions on the topic, helping me in publishing this work and the ongoing mentoring. Thanks to James, Andy and all of Waltham's team for your incredible hospitality at the annual meetings in the UK and the terrific organization. I thank Dr. Chloé Roullier-Gall for the training and support, especially in the beginning of my work. Your didactic skills have made it very easy for me to find my way around quickly and to familiarize with the topic and the analytical techniques. I want to thank Prof. Dr. Michael Gonsior for giving me the opportunity to carry out a part of my experiments in his lab at the Chesapeake Biological Laboratory and for his hospitality during my stay in Maryland.

A very big thank you to all my colleagues. You all have the gift of being outstanding colleagues and friends at the same time. Thanks for this unforgettable time. Many thanks to Jenny Uhl, Astrid Bösl and Anja Brinckmann for their support in all administrative matters. I could always rely on your help and your tireless efforts have greatly eased my work. I thank Dr. Alexander Ruf and Dr. Franco Moritz for the many inspiring scientific and non-scientific discussions – often continued in the beer garden. Thanks Dr. Constanze Müller for the many great discussions, your advice and that you have endured me daily on just 10.30 m², which was certainly not always easy. I also thank Dr. Michael Witting for his help and the fruitful discussions, especially on R programming and LC-MS. I thank Dr. Basem Kanawati for his support and advice in FT-ICR-MS troubleshooting. I thank Dr. Marianna Lucio for helping me in statistical

questions. Further, I would like to thank Dr. Norbert Hertkorn and Dr. Silke Heinzmann for NMR discussions. I also thank Brigitte Lock for technical assistance in the laboratory and all other colleagues for the many delightful discussions, their help and the amazing working atmosphere in the group.

Finally, I would like to thank my family and all my friends who have had to endure some scientific discussions but have always managed to free my mind. Susi, especially in busy times, you often had to put my interests over yours. Nevertheless, you always stood by my side and gave me your full support, love and eventually provided the necessary balance. Thank you for everything! I would like to express my deepest gratitude to my parents for their unconditional support and love. Without you I would not be where I am today. You supported me in all my decisions and always gave me the right advice, even in difficult times.

This page intentionally left blank

Abstract

Non-enzymatic reactions between amino compounds (*e.g.* amino acids, peptides, or proteins) and reducing sugars, also known as Maillard reaction (MR), lead to a very complex and interconnected reaction network and eventually form a heterogeneous mixture of hundreds of Maillard reaction products (MRPs). The MR is of great importance in heated and stored foods, where it is crucial for the formation of taste, aromas, and color, but also for the formation of food-born toxins, such as acrylamide. In addition, under physiological conditions, such glycation reactions can lead to irreversible protein damage (*e.g.* by protein-crosslinking) and cellular dysfunctions, especially in diabetic and aged tissues. Controlling the MR towards the formation of desired products while, at the same time, the formation of unwanted reaction products is avoided, requires a comprehensive and molecular understanding of the overall reaction processes and the interplay of MRPs in the reaction network. While this is usually not possible in real samples, model systems provide an ideal environment to fundamentally study downstream reaction products and their formation pathways.

In this thesis, non-targeted (ultra)high-resolution mass spectrometry methods and data analysis strategies were developed and used to holistically monitor initial and intermediate MRPs and to study their formation pathways on a molecular level. Different sugar-amino acid model systems were probed under thermal and photochemical conditions. Even in very simple model systems (*i.e.* mixtures of two precursors) hundreds of MRPs could be resolved on the level of accurate molecular formulae. In general, amino acid precursors were mainly responsible for the chemical diversity while the sugar precursors more drove the reaction rates but led to very similar chemical compositions. Studying model systems at different reaction times allowed to comprehensively and gradually follow the formation of reaction products. Mass difference analysis, modified Kendrick mass defect analysis, and van Krevelen diagrams were used to study the model systems in a reactivity-related context. It turned out that most of the MRPs followed simple and repetitive reaction patterns, including dehydration, carbonyl cleavage and redox reactions. Moreover, when comparing different model systems, the same reaction patterns were found. This led to the identification of some general Maillard reaction pathways that involved more than 70 reaction intermediates that can be formed independently of the amino acid precursor and only differ in the composition of the amino acids' side chain. These pathways can be integrated into known pathways and provide an ordered scope on

novel and systematic downstream reactions in an environment of rather chaotic reactions.

Irradiation of thermally formed MRPs with simulated sunlight led to a fast and selective decomposition. Nitrogen containing heterocycles were major targets for photochemical degradation reactions. Oxidative cleavage reactions involving the incorporation of reactive oxygen species, such as singlet oxygen, into the molecular structures of MRPs led to a great pool of yet unknown photoproducts. While the chemical reactions among different sugar-amino acid model systems under thermal conditions are very similar, photochemical reactions showed a very high amino acid specificity and differed fundamentally from traditional Maillard reactions.

Zusammenfassung

Nichtenzymatische Reaktionen zwischen Aminoverbindungen (z. B. Aminosäuren, Peptide oder Proteine) und reduzierenden Zuckern, auch Maillard-Reaktion (MR) genannt, führen zu einem sehr komplexen und miteinander verbundenen Reaktionsnetzwerk und bilden schließlich eine heterogene Mischung aus Hunderten von Maillard-Reaktionsprodukten (MRPs). Die MR ist in erhitzten und gelagerten Lebensmitteln von großer Bedeutung, wo sie für die Bildung von Geschmack, Aromen und Farbe, aber auch für die Bildung von lebensmittelspezifischen Toxinen wie Acrylamid entscheidend ist. Unter physiologischen Bedingungen können solche Glykierungsreaktionen außerdem zu irreversiblen Proteinschäden (z. B. durch Proteinvernetzung) und zellulären Funktionsstörungen, insbesondere in diabetischen und gealterten Geweben, führen. Die Steuerung der MR hinsichtlich der Bildung von gewünschten Reaktionsprodukten, während gleichzeitig die Bildung unerwünschter Reaktionsprodukte vermieden wird, erfordert ein umfassendes und molekulares Verständnis der gesamten Reaktionsprozesse und des Zusammenspiels der MRPs im Reaktionsnetzwerk. Während dies in realen Proben normalerweise nicht möglich ist, bieten Modellsysteme eine ideale Umgebung, um nachfolgende Reaktionsprodukte und ihre Bildungswege grundlegend zu untersuchen.

In dieser Arbeit wurden nicht-zielgerichtete (ultra)hochauflösende massenspektrometrische Methoden und Datenanalysestrategien entwickelt, um anfängliche und intermediäre MRPs holistisch zu überwachen und ihre Bildungswege auf molekularer Ebene zu untersuchen. Verschiedene Zucker-Aminosäure-Modellsysteme wurden unter thermischen und photochemischen Bedingungen untersucht. Selbst in sehr einfachen Modellsystemen (d. H. Gemische aus zwei Reaktanten) konnten Hunderte von MRPs auf der Ebene exakter Summenformeln aufgelöst werden. Im Allgemeinen waren Aminosäure-Reaktanten hauptsächlich für die chemische Diversität verantwortlich, während Zucker vielmehr die Reaktionsraten bestimmten, jedoch zu sehr ähnlichen chemischen Zusammensetzungen führten. Durch die Untersuchung von Modellsystemen zu unterschiedlichen Zeitpunkten konnte die Bildung der Reaktionsprodukte vollumfänglich und schrittweise verfolgt werden. Massendifferenzanalyse, modifizierte Kendrick-Massendefektanalyse und van Krevelen-Diagramme wurden verwendet, um die Modellsysteme in einem reaktivitätsbezogenen Kontext zu untersuchen. Es stellte sich heraus, dass die meisten MRPs einfachen und sich wiederholenden Reaktionsmustern, einschließlich Dehydratisierung,

Carbonylsplaltung und Redoxreaktionen, folgten. Beim Vergleich verschiedener Modellsysteme wurden zudem die gleichen Reaktionsmuster gefunden. Dies führte zur Identifizierung einiger allgemeiner Maillard-Reaktionswege, an denen mehr als 70 Reaktionsintermediate beteiligt waren, die unabhängig von Aminosäure-Reaktanten gebildet werden können und sich nur in der Zusammensetzung der Aminosäureseitenketten unterscheiden. Diese Reaktionswege können in bereits bekannte integriert werden und bilden einen geordneten Rahmen von neuartigen und systematischen Reaktionen in einer Umgebung ansonst eher chaotischer Reaktionsabläufe.

Die Bestrahlung thermisch gebildeter MRPs mit simuliertem Sonnenlicht führte zu einem schnellen und selektiven Abbau. Vor allem stickstoffhaltige Heterozyklen waren anfällig für photochemische Abbaureaktionen. Oxidative Spaltungsreaktionen, unter Einbau reaktiver Sauerstoffspezies (wie z. B. Singulett-Sauerstoff) in die molekularen Strukturen der MRPs, führten zu einem großen Pool aus bislang unbekanntem photochemischen Reaktionsprodukten. Während die chemischen Reaktionen zwischen verschiedenen Zucker-Aminosäure-Modellsystemen unter thermischen Bedingungen sehr ähnlich sind, zeigten photochemische Reaktionen eine sehr hohe Aminosäurespezifität und unterschieden sich grundlegend von üblichen Maillard-Reaktionen.

Table of Contents

Scientific Communications	V
Abbreviations	IX
Chapter 1 General Introduction and Methods	1
1.1 Chemistry of the Maillard reaction	2
1.1.1 Comprehensive description of pathways leading to color formation	2
1.1.2 Dicarbonyls – reactive intermediates responsible for the chemical diversity in the advanced Maillard reaction?	5
1.1.3 The final phase: formation of stable end products or restart of the reaction cascade?	9
1.2 Challenges and strategies to decipher the Maillard reaction puzzle	12
1.2.1 Short overview of analytical methods used to detect MRPs and AGEs	14
1.2.2 Non-targeted metabolomics - a promising toolbox in the holistic characterization of early and intermediate MRPs	18
1.3 Model systems	20
1.4 Analytical methods for high- and ultrahigh-resolution measurements	24
1.4.1 Chemical Space	24
1.4.2 Direct-infusion Fourier transform ion cyclotron resonance mass spectrometry	25
1.4.3 Tandem HILIC-RP LC-MS/MS	28
1.5 Motivation and aim of the thesis	28
Chapter 2 Evolution of Complex Maillard Chemical Reactions, Resolved in Time	31
2.1 Introduction	32
2.2 Experimental procedures	33
2.2.1 Maillard model systems	33
2.2.2 Direct-infusion FT-ICR mass spectrometry	33
2.2.3 Processing of FT-ICR-MS data	33
2.2.4 Classification into reaction pools	34
2.2.5 Average carbon oxidation state	34
2.3 Results and discussion	35
2.3.1 Compositional characterization of ribose-glycine MRPs	35
2.3.2 Time-resolved interplay between MRPs	38

2.4 Conclusions	40
Chapter 3 Insights into the Chemistry of Non-Enzymatic Browning Reactions in Different Ribose-Amino Acid Model Systems	41
3.1 Introduction.....	42
3.2 Experimental procedures	43
3.2.1 Chemicals.....	43
3.2.2 Model systems.....	43
3.2.3 Direct-infusion FT-ICR mass spectrometry	44
3.2.4 UV-absorbance.....	44
3.2.5 Data analysis	45
3.3 Results and discussion	45
3.3.1 Reaction monitoring by direct-infusion FT-ICR mass spectrometry	45
3.3.2 Formation of reaction products monitored over time.....	46
3.3.3 Compositional characteristics of MRPs	49
3.3.4 General Maillard reaction scheme	52
3.4 Conclusions	59
Chapter 4 Sunlight Selectively Modifies Maillard Reaction Products in a Wide Array of Chemical Reactions	61
4.1 Introduction.....	62
4.2 Experimental procedures	63
4.2.1 Chemicals and reagents.....	63
4.2.2 Maillard model systems	63
4.2.3 Irradiation experiments	64
4.2.4 Excitation emission matrix fluorescence.....	64
4.2.5 FT-ICR-MS analysis.....	65
4.2.6 Tandem HILIC-RP LC-MS/MS.....	65
4.2.7 Data analysis	66
4.3 Results and discussion	66
4.3.1 Effect of simulated solar irradiation on absorption and fluorescent properties of MRPs.....	66
4.3.2 Holistic characterization of photosensitive MRPs	70
4.4 Conclusions	80
Chapter 5 Concluding Discussion and Outlook	83
A Appendix Chapter 1: Tandem HILIC-RP Liquid Chromatography for Increased Polarity Coverage in Food Analysis.....	89
A.1 Introduction	90

A.2	Experimental procedures	91
A.2.1	Reagents	91
A.2.2	Reference standards.....	91
A.2.3	Sample preparation.....	92
A.2.4	Instrumental setup.....	92
A.2.5	Chromatographic conditions	93
A.2.6	Data processing.....	93
A.3	Results and discussion	94
A.3.1	Principle setup	94
A.3.2	Analysis of food-relevant reference standards.....	95
A.3.3	Online pre-fractionation of sample components (loading step).....	98
A.3.4	Non-targeted analysis of red wines.....	98
A.3.5	Application to other food samples.....	101
A.4	Conclusions	104
B	Appendix Chapter 2.....	105
B.1	Processing of FT-ICR-MS data.....	105
B.2	Classification into reaction pools.....	107
B.3	Assigned molecular formulae	108
B.4	Average carbon oxidation state.....	114
C	Appendix Chapter 3.....	117
C.1	Direct-infusion FT-ICR mass spectra.....	117
C.2	Classification of reaction products.....	118
C.3	Consideration of different sugar precursors	119
C.4	Formation of enamins and amino ketones.....	120
C.5	Compositional characterization of MRPs.....	120
C.6	General formation and degradation pathways of MRPs.....	121
D	Appendix Chapter 4.....	133
D.1	Changes in pH during irradiation experiments	133
D.2	Holistic characterization of photosensitive MRPs.....	134
D.3	Photooxidation of MRPs by singlet oxygen	137
D.4	The role of imidazole groups in photochemical reactions.....	138
D.5	Chemical diversity of thermally formed MRPs	139
D.6	Compositional description of antioxidants	140
D.7	LC-MS/MS analysis of AGE markers	141
D.8	Compositional descriptors.....	143

Table of Contents

Bibliography	145
List of Tables.....	161
List of Figures	163
List of Schemes.....	171
Curriculum Vitae.....	173
Eidesstattliche Erklärung.....	177

Scientific Communications

Publications

Publications directly addressed in this thesis:

Chapter 2: Hemmler, D., Roullier-Gall, C., Marshall, J. W., Rychlik, M., Taylor, A. J. & Schmitt-Kopplin, P. Evolution of Complex Maillard Chemical Reactions, Resolved in Time. *Scientific Reports* **7**, 3227 (2017).

Chapter 3: Hemmler, D., Roullier-Gall, C., Marshall, J. W., Rychlik, M., Taylor, A. J. & Schmitt-Kopplin, P. Insights into the Chemistry of Non-Enzymatic Browning Reactions in Different Ribose-Amino Acid Model Systems. *Scientific Reports* **8**, 16879 (2018).

Chapter 4: Hemmler, D., Gonsior, M., Powers, L. C., Marshall, J. W., Rychlik, M., Taylor, A. J. & Schmitt-Kopplin, P. Simulated Sunlight Selectively Modifies Maillard Reaction Products in a Wide Array of Chemical Reactions. *Chemistry – A European Journal* **25**, 13208–13217 (2019).

Appendix Chapter 1: Hemmler, D., Heinzmann, S. S., Wöhr, K., Schmitt-Kopplin, P. & Witting, M. Tandem HILIC-RP liquid chromatography for increased polarity coverage in food analysis. *Electrophoresis* **39**, 1645–1653 (2018).

Further publications within the framework of the doctoral studies:

Sillner, N., Walker, A., Hemmler, D., Bazanella, M., Heinzmann, S. S., Haller, D., & Schmitt-Kopplin, P. Milk-Derived Amadori Products in Feces of Formula-Fed Infants. *Journal of Agricultural and Food Chemistry* **67**, 8061–8069 (2019).

Haslauer, K. E., Hemmler, D., Schmitt-Kopplin, P. & Heinzmann, S. S. Guidelines for the Use of Deuterium Oxide (D₂O) in ¹H NMR Metabolomics. *Analytical Chemistry* **91**, 11063–11069 (2019).

Roullier-Gall, C., Kanawati, B., Hemmler, D., Druschel, G. K., Gougeon, R. D. & Schmitt-Kopplin, P. Electrochemical triggering of the Chardonnay wine metabolome. *Food Chemistry* **286**, 64-70 (2019).

Moritz, F., Hemmler, D., Kanawati, B., Schnitzler, J.-P. & Schmitt-Kopplin, P. in *Fundamentals and Applications of Fourier Transform Mass Spectrometry*, edited by B. Kanawati & P. Schmitt-Kopplin (Elsevier, Amsterdam, 2019), pp. 357-405.

Rychlik, M., Kanawati, B., Roullier-Gall, C., Hemmler, D., Liu, Y., Hervé, A., Gougeon, R. D., Gmelch, L., Gotthardt, M. & Schmitt-Kopplin, P. in *Fundamentals and Applications of Fourier Transform Mass Spectrometry* edited by B. Kanawati & P. Schmitt-Kopplin (Elsevier, Amsterdam, 2019), pp. 651-677.

Roullier-Gall, C., Signoret, J., Hemmler, D., Witting, M. A., Kanawati, B., Schäfer, B., Gougeon, R. D. & Schmitt-Kopplin, P. Usage of FT-ICR-MS Metabolomics for Characterizing the Chemical Signatures of Barrel-Aged Whisky. *Frontiers in Chemistry* **6**, 29 (2018).

Roullier-Gall, C., Hemmler, D., Gonsior, M., Li, Y., Nikolantonaki, M., Aron, A., Coelho, C., Gougeon, R. D. & Schmitt-Kopplin, P. Sulfites and the wine metabolome. *Food Chemistry* **237**, 106–113 (2017).

Oral presentations

Lunch seminar at the Waltham Centre for Pet Nutrition, Mars Petcare UK, 2019, Waltham-on-the-Wolds, United Kingdom. Title: *Deep molecular-level analysis of the interplay between non-volatile Maillard reaction products in model chemical reactions.*

Invited talk at the 13th International Symposium on the Maillard reaction, 2018, Montreal, Canada. Title: *Diversity of the Maillard reaction - Searching for regular patterns in a complex reaction cascade.*

Invited talk at the analytica conference, 2018, Munich, Germany. Title: *The Maillard Reaction Revisited: A Time-Resolved Chemical Story.*

28. Doktorandenseminar Hohenroda, 2018, Hohenroda, Germany. Title: *Tandem-LC zur Umfassenden Charakterisierung von Maillard-Reaktionsprodukten in Non-Target-Analysen.*

Poster presentations

12th Wartburg Symposium on Flavor Chemistry & Biology, 2019, Eisenach, Germany. Title: *Fingerprinting the Maillard Reaction - Studying Complex Reaction Cascades using Metabolomics Inspired Approaches.*

Faraday Discussion: Challenges in analysis of complex natural mixtures, 2019, Edinburgh, United Kingdom. Title: *Molecular-level monitoring of Maillard reaction networks*.

13th European Fourier Transform Mass Spectrometry Workshop, 2018, Freising, Germany. Title: *Time-Resolved Evolution of Non-Enzymatic Browning Reactions*.

Max Rubner Conference on Food Metabolomics, 2016, Karlsruhe, Germany. Title: *Metabolomics-based discovery of early Maillard reactions*.

252nd American Chemical Society National Meeting & Exposition, 2016, Philadelphia, United States. Title: *An Explorative Study to Understand the Chemical Diversity in Maillard Reactions*.

45. Deutscher Lebensmittelchemikertag, 2016, Freising, Germany. Title: *Umfassende Analyse früher Produkte der Maillardreaktion durch Ultrahochauflösende Massenspektrometrie (UHRMS)*.

11th Wartburg Symposium on Flavor Chemistry & Biology, 2016, Eisenach, Germany. Title: *Comprehensive analysis of early Maillard reaction products by ultrahigh-resolution mass spectrometry*.

Abbreviations

<i>2D-LC</i>	Two-dimensional liquid chromatography
<i>ACN</i>	Acetonitrile
<i>AGE</i>	Advanced glycation end product
<i>ARP</i>	Amadori rearrangement product
<i>BSA</i>	Bovine serum albumin
<i>CAMOLA</i>	Carbon module labeling
<i>CE</i>	Capillary electrophoresis
<i>CEL</i>	<i>N</i> ^ε -(Carboxyethyl)lysine
<i>CML</i>	<i>N</i> ^ε -(Carboxymethyl)lysine
<i>DBE</i>	Double bond equivalents
<i>DBE/C</i>	Double bond equivalents per carbon atom
<i>DI</i>	Direct-infusion
<i>DNA</i>	Deoxyribonucleic acid
<i>EC50</i>	Half maximal effective concentration
<i>EEM</i>	Excitation emission matrix
<i>ELISA</i>	Enzyme-linked immunosorbent assay
<i>ESI</i>	Electrospray ionization
<i>FAB</i>	Fast atom bombardment
<i>FAST</i>	Fluorescence of advanced Maillard products and soluble tryptophan
<i>FT-ICR-MS</i>	Fourier transform ion cyclotron resonance mass spectrometry
<i>GC</i>	Gas chromatography
<i>GOLD</i>	Glyoxal-lysine dimer
<i>H/C</i>	Hydrogen-to-carbon ratio
<i>HILIC</i>	Hydrophilic interaction chromatography
<i>HMDB</i>	Human Metabolome Database
<i>HMF</i>	Hydroxymethylfurfural

<i>ICR</i>	Ion cyclotron resonance
<i>IEC</i>	Ion exchange chromatography
<i>IUPAC</i>	International Union of Pure and Applied Chemistry
<i>KMD</i>	Kendrick mass defect
<i>LC</i>	Liquid chromatography
<i>LM-1</i>	Pentodilysine
<i>log₂FC</i>	Log ₂ fold change
<i>m/z</i>	Mass-to-charge ratio
<i>MALDI</i>	Matrix-assisted laser desorption/ionization
<i>MD</i>	Mass difference
<i>MG-H1</i>	Methylglyoxal-derived hydroimidazolone 1
<i>MGO</i>	Methylglyoxal
<i>MOLD</i>	Methylglyoxal-lysine dimer
<i>MR</i>	Maillard reaction
<i>MRP</i>	Maillard reaction product
<i>MS</i>	Mass spectrometry
<i>MS/MS</i>	Tandem mass spectrometry
<i>NADH</i>	Nicotinamide adenine dinucleotide
<i>NMR</i>	Nuclear magnetic resonance
<i>O/C</i>	Oxygen-to-carbon ratio
<i>OS_c</i>	Average carbon oxidation state
<i>PARAFAC</i>	Parallel factor analysis
<i>PCA</i>	Principal component analysis
<i>ppb</i>	Parts per billion
<i>ppm</i>	Parts per million
<i>RNase</i>	Ribonuclease
<i>ROS</i>	Reactive oxygen species
<i>RP</i>	Reversed-phase
<i>RPLC</i>	Reversed-phase liquid chromatography
<i>RSD</i>	Relative standard deviation
<i>S/N</i>	Signal-to-noise ratio

<i>SEC</i>	Size exclusion chromatography
<i>t-Boc</i>	<i>tert</i> -Butyloxycarbonyl protecting group
<i>TOF-MS</i>	Time of flight mass spectrometry
<i>UPLC</i>	Ultra-performance liquid chromatography
<i>UV</i>	Ultraviolet
<i>Vis</i>	Visible

Chapter 1 |

General Introduction and Methods

In 1912, Louis C. Maillard noticed that aqueous mixtures of glucose and amino acids produce brown-colored solutions after heating.^[1] Nowadays, the immense significance of the Maillard reaction (MR) in food and health science is well accepted. While in food products, the MR is the main contributor to aroma and color formation, under physiological conditions, the same type of reactions can lead to irreversible protein damage, the so called advanced glycation end products (AGEs), which are associated with a wide range of diseases.^[2-4] Many Maillard reaction products (MRPs) and AGEs serve as important indicators for the nutritional quality or thermal damage of food products or the progress of protein damage *in vivo*.^[5-7] After an initial condensation reaction between carbonyl and amino moieties, subsequent downstream reactions produce a multitude of chemical compounds. Although the term MR suggests a single type of reaction, in fact the MR is a superimposition of simple and parallel chemical transformations leading to thousands of intermediates and reaction products. Most of the current knowledge in MRPs and reaction pathways has been deduced from studies on model systems. Even after more than 100 years studying the MR and over 50 000 scientific publications on the topic,^[2] the entire chemical complexity and reactions still have not been fully resolved. In order to control the MR towards the formation of desired reaction products, it is of great importance to understand the entire chemical collective. The MR is more than single compound changes and the importance of interactions should not be overlooked. Especially in biological research areas, the rapid progress in holistic analytical methods (“-omics” technologies) and data evaluation strategies allows an ever better and more comprehensive characterization of a sample’s molecular composition. It would be a logical consequence to apply non-targeted approaches to study also the MR, to deliver a comprehensive understanding of the multitude of intermediates and reaction products formed as well as their interconnectivity in the reaction network.

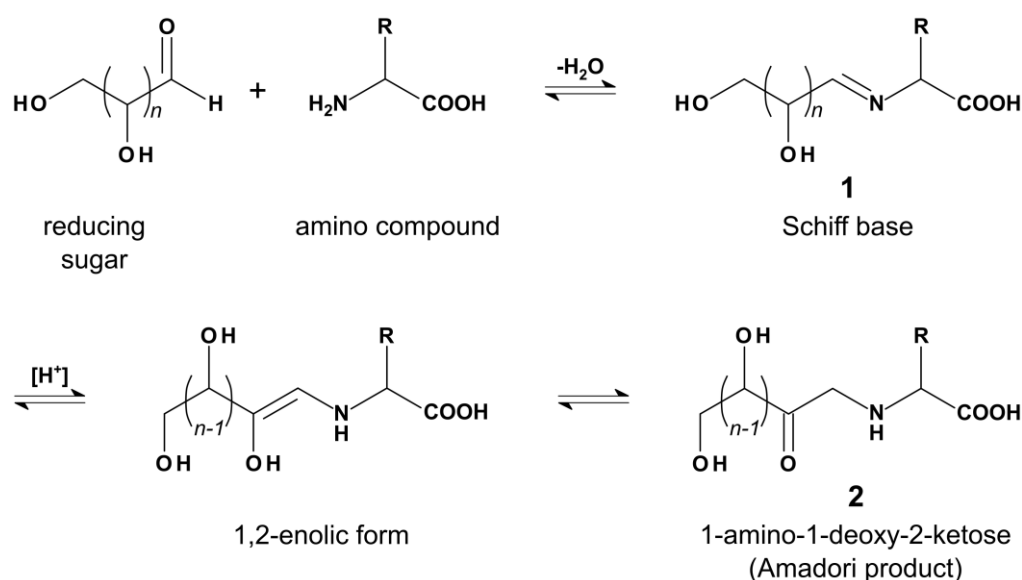
1.1 Chemistry of the Maillard reaction

From a chemical point of view, the MR describes a reaction between carbonyl and amino compounds. Although the term “Maillard reaction” usually is exclusively used for reactions between reducing sugars and amino compounds (such as amino acids, peptides or proteins), a wide range of other carbonyl and amino compounds react in identical or Maillard-analogous reactions. As shown in Scheme 1.1, in an initial step, spontaneous condensation between the carbonyl and amino group forms an *N*-glycosylamine (1), which is prone to undergo enolization and may rearrange into a 1-amino-1-deoxy-2-ketose structure (Amadori rearrangement product, ARP, 2). In a similar way to aldoses, ketoses rearrange to the corresponding 2-amino-2-deoxyaldoses (Heyns products).^[8] The subsequent breakdown of the ARP initiates a multitude of chemical reactions, which continuously produce new intermediates and reaction products (intermediate or advanced phase). Many of the reactions in the advanced phase are found in a similar way in caramelization reactions (sugar decomposition without the action of an amino compound). However, the MR requires less energy for the degradation of sugar moieties than the same reaction pathways would need in caramelization type reactions. In the final phase, reactive intermediates turn into more stable compounds including aromatic and heterocyclic compounds. Although the initial step of the reaction cascade is reversible (Scheme 1.1),^[9,10] subsequent irreversible breakdown reactions can shift the initial carbonyl-amine condensation towards completion. The detailed chemistry in non-enzymatic browning reactions has been the topic of numerous excellent reviews^[4,11–13] and books.^[3,14,15] Hence, in this chapter, only a brief summary of general reaction mechanisms is given, which are mainly responsible for the wide chemical diversity found in the MR.

1.1.1 Comprehensive description of pathways leading to color formation

In 1953, John E. Hodge provided a first comprehensive description of reaction mechanisms participating in the MR and finally leading to the formation of brown polymers (melanoidins).^[16] Over the past decades, the Hodge scheme (see also Figure 2.3c) has only been slightly extended,^[17,18] but still remains fundamentally correct in its original form. According to Hodge, the ARP is the central intermediate found in the early MR, which is responsible for all further downstream reactions. Hodge divided the MR into seven general types of reactions:

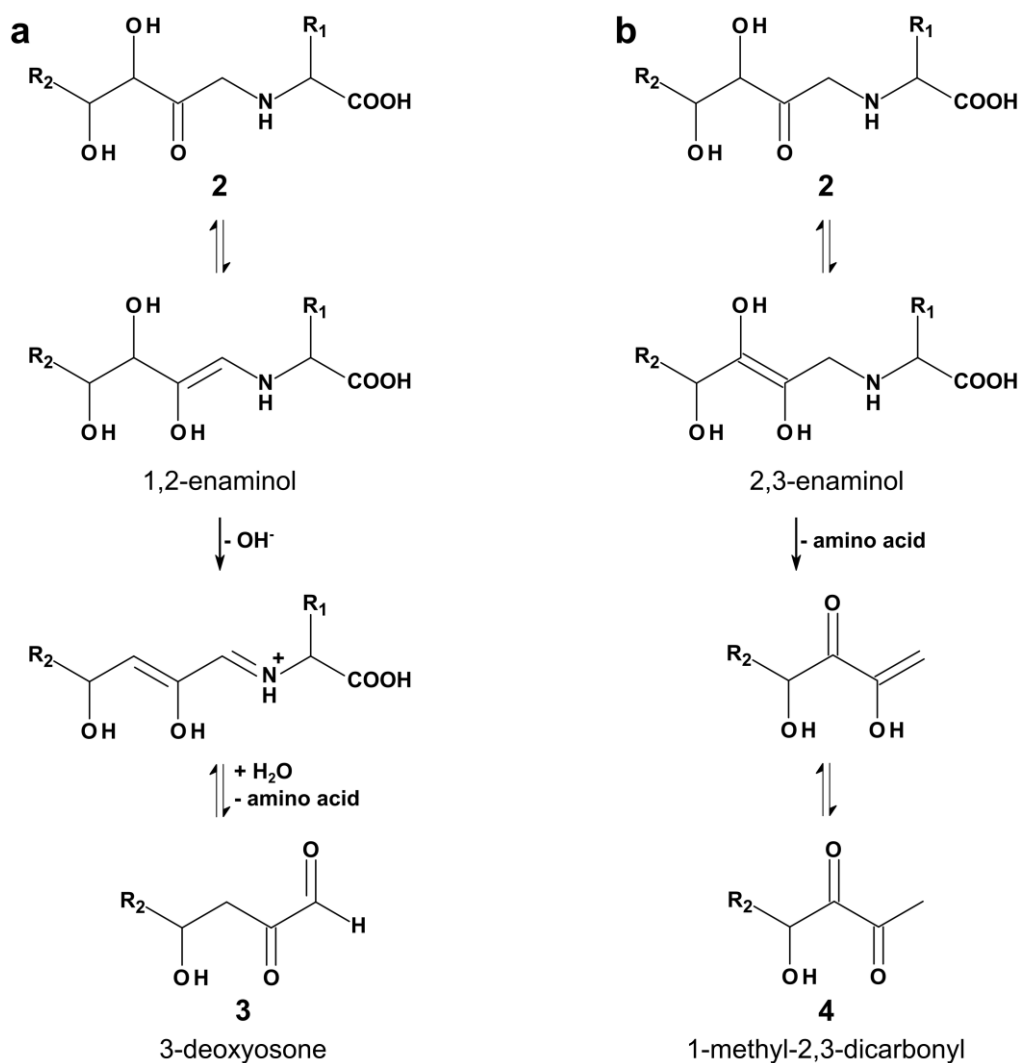
- i. Initial or early stage:
 - (a) Sugar-amine condensation (\rightarrow *N*-substituted glycosylamine)
 - (b) Amadori rearrangement (\rightarrow ARP)
- ii. Intermediate or advanced stage:
 - (c) Sugar dehydration (\rightarrow furfurals and reductones)
 - (d) Sugar fragmentation (\rightarrow fission products)
 - (e) Strecker degradation (\rightarrow Strecker aldehydes and enaminals)
- iii. Final stage:
 - (f) Aldol condensation (\rightarrow aldols and nitrogen-free polymers)
 - (g) Aldehyde-amine condensation (\rightarrow *N*-containing heterocycles and polymers)



Scheme 1.1 | Generalized scheme showing the initial stage of the Maillard reaction for aldose sugars with different carbon chain lengths (n). The two reaction precursors undergo a spontaneous condensation reaction (the intermediate formed by addition of the amino compound to the carbonyl moiety is not shown). The formed Schiff base then rearranges into the Amadori product. In a similar way, ketoses form 2-amino-2-deoxyaldoses (Heyns product) after rearrangement.

Decomposition of the ARP and the MR in general, strongly depends on the pH. Decomposition rates of the ARP increase with increasing pH. Davidek *et al.* studied the decomposition of *N*-(1-deoxy-D-fructos-1-yl)-glycine at different pH values.^[9] After heating an aqueous solution containing the purified ARP for seven hours at 90 °C, about 70% of the original ARP remained unreacted at pH 5. By comparison, when the pH was 8, the ARP was almost completely degraded. Low pH values favor 1,2-enolization (Scheme 1.2a), which may form 3-deoxy- α -dicarbonyls (3). By

comparison, 1-deoxy- α -dicarbonyls (**4**) are formed through the 2,3-enolization pathway (Scheme 1.2b), which predominates at increased pH values.^[4] Dicarbonyls are unstable intermediates, which can easily undergo decomposition, isomerization and cyclization.^[19] For example, α -oxoaldehydes are up to 20 000 fold more reactive than their parent sugar.^[20] The many possible routes and intermediates of sugar decomposition in the MR has not yet been completely elucidated.



Scheme 1.2 | Formation of dicarbonyls by decomposition of the ARP in the intermediate phase, adapted from Nursten (2005).^[14] (a) Low pH values favor the formation of 3-deoxyosones and ultimately furfural via the 1,2-enolization pathway. (b) At high pH values 2,3-enolization rates are thought to be increased leading to 1-deoxy-dicarbonyls.

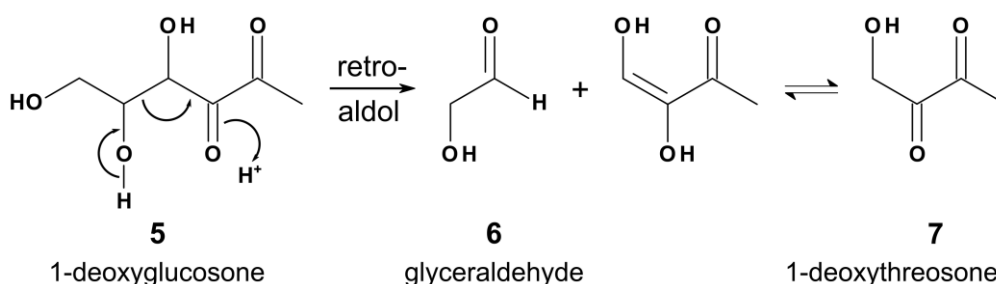
1.1.2 Dicarbonyls – reactive intermediates responsible for the chemical diversity in the advanced Maillard reaction?

Major attention has been drawn to dicarbonyls, especially α -dicarbonyls, because of their significant role as precursors in the formation of color, flavor and aroma compounds and their *in vivo* participation in advanced glycation reactions.^[4,21] Carbonyls and dicarbonyls formed in the intermediate phase are excellent targets for the Strecker degradation of amino acids and new amine condensation reactions leading to new Amadori or Amadori-like intermediates followed by a restart of the reaction cascade. Dicarbonyls are mainly formed by dehydration of the sugar moieties, decomposition of the ARP (Scheme 1.2), and different types of fragmentation reactions on the carbohydrate backbone into smaller fragments.^[4,21] For example, hexoses may lead to C₅/C₁, C₄/C₂, and C₃/C₃ fragments. Many of these fragmentation products have a considerably high reactivity, easily reacting with each other or with other fission, carbonyl, or amine compounds.^[18,22,23] Additionally, carbonyl shifts within the ARP and subsequent dehydration products produce a multitude of isomers.^[24] Three major dicarbonyl fragmentation mechanisms are currently discussed in the literature:^[22,25] (i) retro-aldol reaction, (ii) α -dicarbonyl cleavage, and (iii) β -dicarbonyl cleavage. Pathways (ii) and (iii) can be subclassified into hydrolytic α -dicarbonyl cleavage, oxidative α -dicarbonyl cleavage, hydrolytic β -dicarbonyl cleavage, and amine-induced β -dicarbonyl cleavage.^[21]

Retro-aldol reactions. Historically, retro-aldol fission of carbohydrate structures was the first considered mechanism and already proposed by Hodge.^[16] Retro-aldol reactions (Scheme 1.3) can occur on β -hydroxycarbonyls (**5**), which are cleaved into short-chain hydroxycarbonyls (**6**) and (di)carbonyls (**7**). Such reactions have been shown to occur with free sugars,^[4] ARPs,^[26] and Heyns products.^[27] Methylglyoxal (MGO) and glyceraldehyde are perhaps the most prominent intermediates, which can be explained by retro-aldol reactions.^[28] While browning in a sugar-amine MR is observed only after an induction period, MGO and glyceraldehyde readily react to form brown chromophores and were shown to have much faster reaction rates than the parent sugar.^[18,29] This suggests a dominating role of these short-chain carbonyls in browning reactions.

α -Dicarbonyl cleavage. α -Dicarbonyls can break at the carbon-carbon bond between the two carbonyl moieties either by disproportionation (hydrolytic cleavage)^[30] or by oxidative cleavage as discovered by Davidek and co-workers.^[31] The hydrolytic fission mechanism (Scheme 1.4a) cleaves α -dicarbonyls into a carboxylic acid (**8**) and a corresponding aldehyde (**9a**). This pathway has been frequently used in literature to explain the formation of short-chain carboxylic acids in the degradation of carbohydrates^[30,32,33] or sugar moieties on MRPs,^[32,34,35]

respectively. However, lack of completeness in the reported studies has until now not allowed a definitive proof of the mechanism.^[19,21] Stimulated by this fact, Davidek *et al.* reinvestigated the formation of short-chain carboxylic acids by incubation of 2,3-pentanedione and 2,4-pentanedione with glycine at 120 °C (pH 6-10), respectively.^[19] 2,4-Pentanedione turned out to be the much better acetic acid precursor. Additionally, acetic acid and acetone were detected in similar concentrations, confirming β -dicarbonyl cleavage as the major pathway of acetic acid formation (see below). By comparison, decomposition of 2,3-pentanedione by hydrolytic α -dicarbonyl cleavage should yield acetic acid and propanal or propionic acid and acetaldehyde, respectively. Neither propanal nor acetaldehyde could be detected. In contrast to the expectations, Davidek and co-workers could detect propionic acid and acetic acid in minor, but similar concentration levels, which gave rise to an oxidative cleavage pathway.

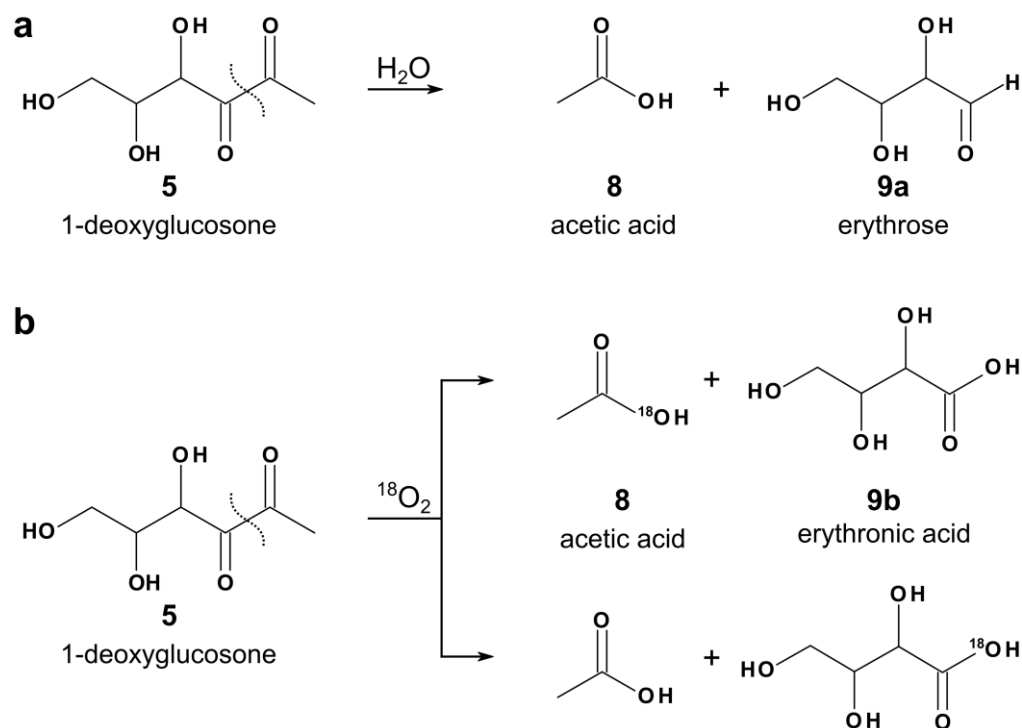


Scheme 1.3 | Retro-aldolization of β -hydroxycarbonyls, adapted from Smuda and Glomb (2013).^[21]

In a subsequent work, Davidek and co-workers investigated the mechanism of oxidative α -dicarbonyl cleavage by using $^{18}\text{O}_2$ and ^{18}O -enriched water. The formation of carboxylic acids from α -dicarbonyls via oxidative cleavage (Scheme 1.4b) first requires incorporation of activated molecular oxygen species (*e.g.* singlet oxygen or hydroperoxides) at a carbonyl-carbon. The so formed alkoxyradical rearranges in a Baeyer-Villiger-type reaction to an acid anhydride. Subsequent hydrolysis yields two carboxylic acids (**8** and **9b**).^[31]

β -Dicarbonyl cleavage. In a β -dicarbonyl cleavage (Scheme 1.5), 1,3-dicarbonyls are cleaved in a retro-Claisen-type reaction into “carboxylated nucleophiles” (**10**, *e.g.* carboxylic acids or carboxylic acid amides) and corresponding α -hydroxycarbonyls (**11**).^[19,21,36] Cleavage of β -dicarbonyls has been shown to be the major carboxylic acid formation pathway in hexose and pentose MR systems under neutral and alkaline conditions.^[19,37,38] Hydroxides and amines have been reported as possible nucleophilic agents. However, there is no reason why other nucleophiles

present in a MR pool (e.g. cysteine residues) should not participate in a β -dicarbonyl cleavage.



Scheme 1.4 | Two possible α -dicarbonyl cleavage reactions. (a) Hydrolytic α -dicarbonyl cleavage adapted from Ginz *et al.* (2000),^[33] and (b) oxidative α -dicarbonyl cleavage as reported by Davidek and co-workers (2006).^[31]

Strecker degradation. The term Strecker degradation nowadays refers to all types of oxidative deamination reactions on α -amino acids.^[39] In the MR, particularly α -dicarbonyl structures act as oxidizing agents to provoke decarboxylation. According to Scheme 1.6, the reaction between a dicarbonyl and an amino acid forms an α -iminocarbonyl (**12**), which readily undergoes decarboxylation. This step is usually followed by hydrolysis of the intermediate (**13**) to produce an α -amino carbonyl (**14**) and a free aldehyde (**15**, Strecker aldehyde), which carries the amino acid side chain.^[39,40] In recent years, some further pathways relevant under MR conditions, have been discovered, such as the direct degradation of amino acids at elevated temperatures^[41] or the formation of Strecker aldehydes directly from the ARP.^[42,43]

1.1.3 The final phase: formation of stable end products or restart of the reaction cascade?

As discussed before, major pathways of the intermediate phase lead to the formation of a wide range of new carbonyl species, many of which have considerably higher reactivity than the initial parent sugar. According to Hodge, the compounds formed in the intermediate phase are then transferred into larger products mainly by aldol condensation and carbonyl-amine condensation reactions (final phase).^[16] While the intermediate phase is characterized by decomposition reactions, such as dehydration and dicarbonyl fission reactions, the final phase leads to an increase of the chain length resulting in higher molecular weight compounds.

Historically, reactions in the final phase were attributed to the formation of high molecular weight and colored compounds (melanoidins), which represent stable end products. However, more recent research also indicates that aldol condensations in the final phase can lead to the formation of volatile and uncolored compounds of lower molecular weights.^[46-48] Final phase reactions cannot exclusively be considered to produce stable end products. For example, aldehyde-amine condensations between reactive carbonyl intermediates from the advanced phase may react with any amine source in the reaction pool to form new ARP-like structures, which then can pass through the entire reaction cycle (Figure 1.1). Hence, a significant number of compounds formed in the final phase can be considered as prospective secondary precursors in the MR. In a similar way, aldol condensations lead to the formation of β -hydroxycarbonyls, which can either directly react with amines, undergo amine reactions after enolization or directly undergo typical breakdown reactions of the intermediate phase (dehydration and fission). Consequently, the chemical diversity of formed molecules in the MR can be expected to follow an exponential increase. Nevertheless, among many extrinsic factors, in simple two-reactant MR systems, the overall reaction rate is largely determined by the availability of unprotonated amino groups and free carbonyl moieties of the parent sugar precursor.

Formation of heterocyclic compounds. Heterocyclic compounds can be considered as major building blocks of many types of late MRPs, including stable end products. They build the key structures in melanoidins, flavor active compounds, antioxidants, and protein crosslinks. Crucial heterocyclic MRPs, identified in Maillard model systems, include derivatives of furan, oxazole, imidazole, pyrrole, pyrazine, pyridine, thiazole, and thiophene compounds.^[49-51]

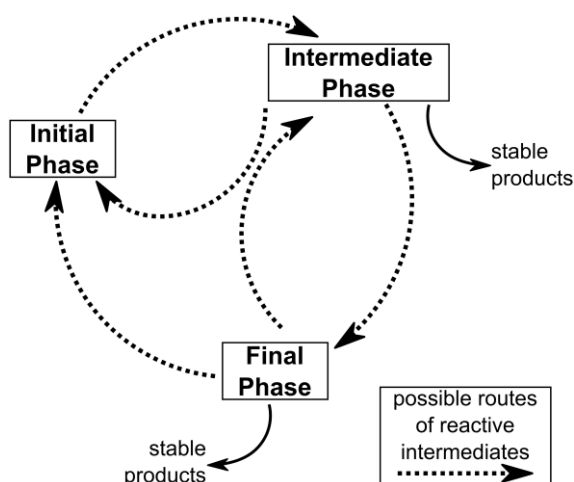


Figure 1.1 | Scheme of possible routes of reactive intermediates produced in the initial, intermediate, and final phase of the Maillard reaction, respectively. Some reactive intermediates formed throughout the Maillard reaction might act as secondary precursors leading to a restart of the reaction cascade. Stable reaction products, including short-chain carboxylic acids, heterocyclic compounds and melanoidins, are mainly formed in the intermediate and final phase.

Simple furan derivatives can be built by consecutive dehydration of sugars. By comparison, more complex nitrogen or sulfur containing heterocycles usually require two reactive species of the intermediate phase. A seemingly endless number of possible combinations of reactive candidates formed in the intermediate phase can therefore lead to very diverse heterocyclic products. A good overview on the formation of simple heterocycles from intermediate MRPs is given by Yaylayan and Haffenden.^[45] Key intermediates of the advanced phase are α -aminocarbonyls, α -hydroxycarbonyls and dicarbonyls, which can readily undergo condensation reactions followed by dimerization or cyclization. The α -aminocarbonyls formed in the Strecker degradation of amino acids can form pyrazine derivatives through dimerization.^[52] Pyrroles can be built by condensation reactions between dicarbonyls and α -aminocarbonyls,^[47] ARPs,^[53] or free amino acids.^[54] Along with pyrazines, imidazoles and oxazoles are major heterocyclic MRPs, which can be formed from various intermediates.^[45,55] Many of the lysine-lysine crosslinking AGEs contain imidazole structures. For example, glyoxal and methylglyoxal react with lysine residues on proteins to form the imidazolium derivatives GOLD and MOLD, respectively.^[56]

Formation of colored compounds. Melanoidins are colored and often nitrogen-containing compounds of high molecular weight, which are formed in the final phase of the MR.^[57] Such melanoidins were found in various types of food products, including coffee,^[58] bakery products,^[59] chocolate,^[60] and beer.^[61] For example, a typical coffee brew dry matter consists of up to 25% melanoidins.^[62]

Fogliano and Morales estimated the daily melanoidin intake to be 10 g in a typical Western diet, where coffee and bread are the major sources.^[63] Because of the emerging beneficial and health promoting effects (*e.g.* antioxidant, anti-inflammatory, antimicrobial and prebiotic activities), melanoidins have recently been suggested as potential functional food ingredients.^[57]

Despite the high relevance in foods, current knowledge about the chemical structures of colored MRPs is relatively contentious. In the past, it mainly was assumed that color originates from high molecular weight polymers formed in the final phase of the MR. These polymers were assumed to have molecular weights of up to several thousand Daltons and to be stable end products. The most frequently discussed hypothesis states that melanoidins are formed by polymerization of low-molecular weight and reactive Maillard intermediates leading to compounds with a wide molecular weight distribution.^[64] This assumption is in line with the typical shape of UV/Vis absorption spectra observed in MR systems (Figure 1.2). Absorption curves usually do not show discrete absorption maxima but rather show a continuous asymptotic shape, which was interpreted as an overlay of several discrete chromophores, such as found in a polymer distribution.^[65] Tressl and co-workers indeed could detect linear oligomerization products with up to six monomeric units by MALDI-TOF-MS, which were formed from *N*-methyl-2-(hydroxymethyl)-pyrrole in a model reaction between 2-deoxy-ribose and methylamine.^[66] However, it has yet not been possible to unambiguously assign a melanoidin-structure with a molecular weight in the range of several thousand Daltons.

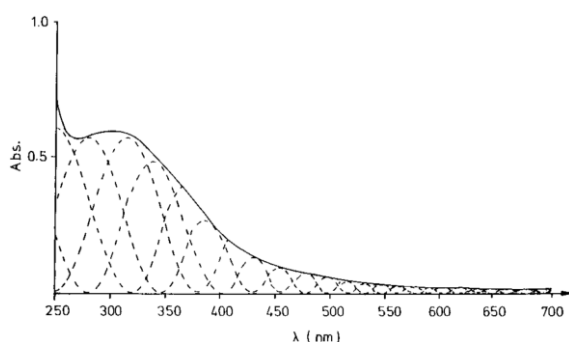


Figure 1.2 | UV/Vis-spectrum of a typical melanoidin (solid curve) interpreted as the sum of many individual chromophores (dashed curves).

Reprinted with permission from Hofmann, T. *Journal of Agricultural and Food Chemistry* 1998, 46, 3891–3895. Copyright 1998 American Chemical Society.

After fractionation of a glucose-glycine model system (4 h at 95 °C in phosphate buffered solutions, pH 7) by ultracentrifugation, Hofmann found that the majority of MRPs have a molecular weight below 1 kDa.^[67] This low molecular weight

fraction also made the major contribution to the overall color observed. Almost identical results were obtained for a glucose-alanine model system.^[67] Therefore, it is now proposed that melanoidins in food products consist of low-molecular weight chromophores, which are covalently attached to uncolored macromolecules, such as polysaccharides or proteins.^[63,68] This assumption is supported by a series of publications from Hofmann, who, for example, showed that four molecules of furfural formed a red-colored chromophore cross-linked with a lysine residue of casein.^[69,70] Hofmann also incubated β -casein (about 24 kDa) together with glucose at 95 °C at pH 7 for four hours. He found highest color yields for reaction products larger than 100 kDa. This could be explained by small chromophores, which were attached to β -casein oligomers formed via carbohydrate-induced oligomerization.^[67]

1.2 Challenges and strategies to decipher the Maillard reaction puzzle

As outlined in Chapter 1.1, pathways leading to MRPs are not just linear downstream reactions. In fact, the MR must be considered as a highly branched network of interacting precursors and intermediates, where many MRPs can be produced from multiple interconnected pathways. Especially in controlling the MR towards the formation of desired reaction products and kinetic modelling approaches, understanding of the entire chemical interplay is needed. For example, the formation of acrylamide, a probable carcinogen that caused worldwide attention in the early 2000s, is mainly formed by the reaction between asparagine and dicarbonyl compounds.^[71] Therefore, reduction of acrylamide precursors (e.g. reduction of asparagine or trapping of dicarbonyls) would be a promising chemical mitigation strategy to lower acrylamide levels.^[72] However, nowadays, multiple alternative acrylamide formation pathways have been identified.^[73] For example, the formation of acrylamide from aspartic acid, β -alanine or β -alanine containing peptides (e.g. carnosine) does not necessarily require interaction with dicarbonyls.^[74] The same is true for studies, which consider the degradation of isolated and purified intermediates. In such a case, degradation studies provide only information on linear downstream reactions while the role of these intermediates in the overall reaction cascade remains overlooked. Altogether, holistic approaches, which allow the monitoring of the formation of hundreds of MRPs in parallel, are needed.

Although over the last decades huge progress has been achieved in elucidating some specific MRPs, including their formation and degradation pathways, to date, it

has not been possible to fully resolve the entire set of chemicals and reaction routes involved in the MR network. Several intrinsic and extrinsic factors must be considered, which make a simultaneous analysis challenging.

Molecular diversity. The chemical structures, molecular weights, and eventually physicochemical properties of MRPs are strongly defined by the reaction precursors as well as the many chemical transformations and this diversity has a major impact on the choice of analytical methods to investigate the MR. This diversity ranges from highly polar molecules formed mainly in the early and intermediate phase to nonpolar MRPs in the later stages. The molecular weights of compounds range from small by-products (*e.g.* CO₂, glyoxal, H₂S) to high molecular weight compounds in the kDa range.^[75,76] Additionally, the type of reaction precursors has a strong effect on the molecular diversity found in the downstream reactions. For example, most expected MRPs in an amino acid-sugar reaction lead to intermediates and reaction products not larger than a few hundred Daltons. By comparison, when considering proteins as amino source, MRPs must be expected to be found additionally in the molecular weight range of the investigated protein. In reaction systems with multiple amino and carbonyl precursors, such as real food samples, the almost limitless combining possibilities of precursors further increase the molecular diversity in reaction products.

Isomeric diversity. Especially imines and sugar derivatives are susceptible to undergo several isomerization reactions.^[24,77] Each isomer may lead to specific downstream reaction products, finally contributing to the diversity of MRPs.^[77] Because of the high similarity in physicochemical properties and the fact that mass spectrometry (MS) alone cannot differentiate between isomers, analysis of the isomeric forms in the MR is still a major challenge.

Dynamic concentration range. As a consequence of the multiple reaction pathways, the concentration yields decrease from the initial condensation products, through the intermediate MRPs to the final products.^[78] Although the ARP concentrations strongly depend on the type of precursors, they are usually found in the percent molar range.^[79,80] Sugar fragmentation products of the intermediate stage were found to contribute in the ‰ to lower % range to the total flux of MRPs^[81] while volatile end products are usually detected in trace amounts only.^[78] In general, there is no direct correlation between the induced response threshold of a substance (*e.g.* odor detection, color activity, EC₅₀) and its concentration. Consequently, at first, all MRPs need to be considered of equal relevance, independently of their concentrations.

Chemical and physical factors. Several chemical factors (*e.g.* type and concentration of precursor molecules, pH, buffer substances, water activity, metal ions) and physical factors (*e.g.* temperature, pressure, reaction time) have a major

impact on the outcome of the MR.^[28,82-84] The type of carbonyl and amino precursor as well as the pH are the major factors that influence the chemistry of the reaction products formed. By comparison, temperature, reaction time, and water activity have been shown to primarily influence the reaction rates while chemical structures remain mainly unchanged.^[85]

All these intrinsic and extrinsic factors influence the physicochemical properties of MRPs, their diversity and the overall complexity (number of formed MRPs). Until now, there exists no analytical technique, which can detect all MRPs simultaneously. Nevertheless, because of its high resolution and sensitivity, in recent years, MS has emerged as the key tool to study MRPs.

1.2.1 Short overview of analytical methods used to detect MRPs and AGEs

The high separation efficiency and good reproducibility as well as relatively easy interpretability of electron impact spectra has made online coupling of gas chromatography to mass spectrometry (GC-MS) the workhorse in routine analysis of volatile and semi-volatile MRPs.^[47,86-88] Comprehensive MS/MS databases, in combination with retention time indices are available and often allow standard-free compound identification in non-targeted screenings.^[89,90] However, analysis of MRPs by GC is limited to volatile compounds and hence focuses mainly on MRPs of the later stages, such as aroma compounds and small heterocycles or by-products. Nevertheless, derivatization of non-volatile and hydrophilic MRPs or pyrolysis of the sample can provide non-volatile MRPs access to GC-MS methods.^[91,92] It must also be stressed that derivatization reagents themselves, as well as time and temperature effects, induced by the derivatization or pyrolysis step, may significantly influence sensitive systems, such as the MR.

By comparison, there exists no gold standard analytical method for the detection of non-volatile MRPs and AGEs.^[93] Analysis of these type of compounds would ideally require analytical tools that provide high resolution, sensitivity, specificity and that allow characterization of molecules on a structural level. In recent years, MS has certainly prevailed as the key method to study non-volatile MRPs in both, model systems and real samples.^[94] Structural information can be achieved by fragmentation experiments (MS/MS) and comparison to results from nuclear magnetic resonance (NMR) spectroscopy experiments. The use of isotopically enriched precursors is an elegant but expensive way to trace atoms in reaction products back to their position in the initial precursor.^[26,95,96] The high mass accuracy of high-

resolution mass analyzers readily allows the elemental composition of formed MRPs to be determined.

Because the analytical tools used to study MRPs and AGEs strongly depend on the physicochemical properties of the target compounds and the type of samples and ultimately cover the entire repertoire of analytical chemistry, only the most frequently applied methodologies are briefly outlined here. These methods can be roughly divided into: (i) direct detection by spectroscopic methods, (ii) direct detection by mass spectrometry, (iii) hyphenated analytical methods, and (iv) immunochemical methods.

Direct detection by spectroscopic methods. UV/Vis absorption and fluorescence measurements are still frequently used as rapid and low-cost methods to assess the reaction progress of the MR. However, their limited resolving power does not usually provide molecular-resolution but rather reflects the sum of responses from the chromophores of the molecules in the sample mixture. Because of their non-destructive mode of detection, spectroscopic methods are ideal detectors to monitor the formation of reaction products online.

Absorption measurements in the UV/Vis range are widely used to determine intermediate (usually at 294 nm) or final chromophores (usually around 420 nm).^[97] However, in real samples often other chromophores disturb the selective detection of MRPs, but UV/Vis spectroscopy provides a fast possibility to evaluate the progress of browning in model systems.

Many MRPs formed in the intermediate and final stage of the MR, including imidazole and pyrrole derivatives, are fluorescent.^[98] Fluorescence spectroscopy has good selectivity and provides the highest sensitivity among the spectroscopic techniques. However, many factors, such as pH, temperature, scattering and inner filter effects, or the presence of quenching substances, affect the wavelength and response of fluorescence phenomena.^[98,99] Besides MRPs, main contributors to fluorescence in food products are riboflavin, vitamin A, aromatic amino acids, NADH, porphyrins, chlorophylls, and lipid oxidation products.^[98] The FAST index (fluorescence of advanced Maillard products and soluble tryptophan) has been developed for rapid and routine evaluation of the heat treatment of dairy products.^[100] It is based on the simultaneous quantification of protein denaturation estimated by the tryptophan fluorescence (F_{Trp} : ex. 290 nm, em. 340 nm) and enrichment of fluorescent MRPs (F_{AMP} : ex. 330 nm, em. 420 nm) in the milk fraction soluble at pH 4.6. The ratio between F_{Trp} and F_{AMP} is the FAST index.^[100] Skin autofluorescence has been shown to correlate with tissue levels of AGEs, such as pentosidine, carboxymethyllysine (CML) and collagen-linked fluorescence.^[101] Therefore, non-

invasive and *in vivo* fluorescence measurements can be used to predict the accumulation of AGEs and chronic complications in diabetes type 1 and 2.^[102]

Direct mass spectrometry measurements. Continuous progression in the development of high-resolution mass analyzers, such as time-of-flight (TOF), Orbitrap, or Fourier transform ion cyclotron resonance (FT-ICR) instruments, nowadays, allows the direct analysis of MRPs. Although MS alone is not able to resolve isomers, high-resolution MS allows the separation of thousands of features in a single analysis.^[103] High-field FT-ICR mass analyzers allow the measurement of molecular mass with an accuracy in the ppb range and thereby provide direct access to the molecular formulae of the recorded ions (see also Chapter 1.4.2). Nowadays, electrospray ionization (ESI) and matrix-assisted laser desorption/ionization (MALDI) are the most frequently used ion sources in direct MS measurements for the detection of non-volatile and high-molecular weight MRPs, respectively. In the 1990s, fast atom bombardment (FAB) was used as a derivatization-free method to detect early MRPs in model systems.^[104,105] However, because of its low sensitivity and ionization efficiency as well as complicated coupling to liquid chromatography (LC), in recent years, FAB has almost completely been replaced by ESI and MALDI.

In one of the first studies using MALDI-MS, Lapolla and co-workers incubated bovine serum albumin (BSA) with different levels of glucose at 37 °C.^[106] After 28 days of incubation with 0.2 M glucose, they noticed an increase in the molecular mass of the BSA ion signal by 2 120 Da, which was explained by the non-enzymatic condensation of 13 glucose units onto the protein.^[106] It must be stressed that the increase in molecular mass was exclusively assigned to glucose condensation. Possible downstream reactions of the formed ARPs or condensation reactions of glucose decomposition products (*e.g.* deoxyglucosones or glyoxal) were not considered. In another study, Lapolla and co-workers compared the glycation level of IgG in three groups, namely healthy subjects, well-controlled and badly-controlled diabetic patients.^[107] Analysis by MALDI-MS revealed different glycation levels. The average increase in molecular mass of IgG was 581 ± 347 Da, $1\,128 \pm 339$ Da, and $2\,556 \pm 1\,120$ Da for the healthy subjects, well-controlled, and badly-controlled patients, respectively. After employing MALDI-MS to papain digested IgG it was found that most glycation sites were located on the Fab fragment.^[108] The authors suggested that the immune deficiency of diabetic patients might be explained by higher glycation levels on the Fab fragment and hence reduced antibody-antigen recognition.

Hyphenated methods. To further increase the separation efficiency and to reduce ion suppression and adduct formation, separation techniques, such as liquid chromatography (LC) or capillary electrophoresis (CE), can be directly coupled to MS.

In a similar way, simple optical detectors (such as Photo Diode Arrays) can be used in combination with LC or CE. Especially in the quantification of target compounds in complex samples, such as food or tissue extracts, LC-MS, GC-MS, and CE-MS have become the methods of choice.

Carbohydrate precursors and derivatives formed in the course of the MR can be analyzed by ion-exchange chromatography (IEC) or hydrophilic interaction chromatography (HILIC).^[109,110] However, best separation efficiency and superior detection limits in the fmol range are currently only reached in GC-MS after silylation of the hydroxyl groups.^[111] Blank and co-workers developed an IEC method with pulsed amperometry detection to separate and quantify several ARPs in the presence of high sugar levels.^[79] Conversion of ϵ -lactulose-lysine into furosine by acid hydrolysis followed by ion-pair reversed phase LC (RPLC) and detection at 280 nm is the reference method to indirectly determine the amount of ARPs in heat-treated milk.^[112] The most common method to analyze α -dicarbonyls involves their derivatization with *o*-phenylenediamine. The so formed quinoxaline derivatives can then be analyzed by RPLC coupled to UV and/or MS detection.^[113] LC-MS/MS and GC-MS (after derivatization with bromine) are the main setups used to determine acrylamide in thermally processed foods.^[114] Scheijen *et al.* used ultra-performance LC-MS/MS to quantify CML, carboxyethyllysine (CEL), and a methylglyoxal-derived hydroimidazolone (MG-H1) in 190 food items frequently consumed in the Netherlands.^[115]

In recent years, many attempts have been made to implement CE-based methods as alternatives to routinely used LC applications.^[116,117] Several CE modes have been used to separate and quantify furosine,^[118,119] acrylamide,^[120,121] or anionic melanoidins.^[116,122] Capillary zone electrophoresis provides higher separation efficiency and covers a broader molecular weight range compared to GC- and LC-based methods. However, the low sample amounts applied in CE are usually not enough for a complete characterization of MRPs and low detection levels limit the use of this technique. Nonetheless, CE-MS seems to be a promising tool in the characterization of intact glycosylated proteins compared to LC-MS or size exclusion chromatography (SEC).^[123–125] Determination of glycation sites by LC-MS/MS requires enzymatic digestion or hydrolysis of the proteins into smaller fragments prior to chromatographic separation. Although SEC is an ideal separation technique for high-molecular weight compounds, it has only moderate separation power and, more important, hyphenation to MS dramatically restricts the composition of the mobile phase.^[126]

Immunological methods. Detection of MRPs and AGEs based on immunoassays provides a fast method with theoretically very high specificity towards

the target compound. Monoclonal and polyclonal antibodies have been produced, which specifically bind to protein-bound AGEs, such as pyrroline,^[127,128] fructose-derived AGEs,^[129] or CML.^[130] These antibodies can be used in enzyme-linked immunosorbent assays (ELISA) to detect and quantify AGEs *in vivo* and *in vitro*. However, for some ELISA tests, only poor specificity and lower reproducibility as compared to LC-MS has been reported.^[131,132]

1.2.2 Non-targeted metabolomics - a promising toolbox in the holistic characterization of early and intermediate MRPs

Comprehensive analysis of amino acid-sugar model systems faces similar analytical prerequisites and challenges as found in metabolomic analysis. As compared to other “-omics” disciplines, such as genomics or proteomics, metabolites have a greater variation in composition compared to genes or proteins. The relatively simple chemical building blocks of genes (sequence of four bases) and proteins (sequence of 20 amino acids) allow straightforward sequence analysis benefiting from well-established techniques.^[133] By comparison, analytical studies of the metabolome usually require several different analytical methods, including separation techniques hyphenated to MS (*i.e.* LC-MS, CE-MS, or GC-MS) and direct methods (*e.g.* direct-infusion ultrahigh-resolution MS, or NMR).

Metabolome and foodome. The term metabolome was introduced by Oliver *et al.* in 1998 and describes the full set of small-molecular weight compounds (metabolites) in a biological sample.^[134] Since then, thousands of studies have been published aiming at a comprehensive analysis of metabolites in biological samples and foods. With regard to existing “-omics” definitions, foodomics has recently been introduced.^[135] Following the definition of the metabolome, the foodome comprises all compounds in a food sample under study and/or in a biological system that interacts with the investigated food at a given time.^[136] Studying the entire foodome usually requires the integration of several “-omics” disciplines (*e.g.* metabolomics, proteomics, transcriptomics).^[135,137]

Although amino acids and sugars are abundant and omnipresent compounds in both biological and food samples, the number of identified MRPs or pathways of the MR in metabolomics or foodomics studies is surprisingly low. One factor that hinders the study of MRPs by metabolomic approaches is the lack of comprehensive compound databases, which would allow rapid and standard-free structure assignments in high-throughput screenings. Moreover, classical metabolome and foodome analysis do not distinguish between enzymatic and non-enzymatic reactions. It can be assumed that a considerable number of (putatively) identified compounds in

metabolomics studies were falsely assigned to a biochemical pathway, even when these metabolites were produced through non-enzymatic processes (e.g. MR or lipid peroxidation). For example, Beleggia and co-workers could identify about 70 metabolites in dried pasta products.^[138] Although none of those metabolites were assigned to a MRP, indirect evidence for the formation of MRPs was suggested by good correlation of responses between reducing sugars and amino acids during pasta making. Jeandet *et al.* used NMR and ultrahigh-resolution MS to investigate the metabolite composition of a 170-year-old champagne revealing increased levels of 5-hydroxymethylfurfural (HMF), which the authors could attribute to originate from thermal treated grape juice (syrup), which most likely was added during manufacturing in the 19th century to increase the sugar content.^[139] However, whether HMF was formed by the MR or via caramelization remained unclear.

Application of non-targeted metabolomics to study the MR. Metabolites are a class of chemicals, similar to early and intermediate MRPs formed in reactions between sugars and amino acids, with a high diversity in physicochemical properties and molecular weights usually not exceeding 1 000 Da.^[140] According to Fiehn,^[133] metabolites can be studied in different ways: (i) targeted analysis, (ii) metabolite profiling, (iii) metabolite fingerprinting, and (iv) metabolomics. By far the most frequently used approaches to study the MR are targeted approaches. Here, one or a few *a priori* selected compounds are identified and quantified. Sample preparation and analytical methods are optimized in terms of extraction, identification, and quantitation of the compounds to be studied. Metabolite profiling is a semi-targeted approach where a subset of the metabolome (e.g. one metabolic pathway) is comprehensively studied. For instance, investigating all dicarbonyls in a Maillard system after derivatization and selective enrichment could be considered as a semi-targeted profiling approach. The latter two definitions (metabolite fingerprinting and metabolomics) describe rigorous non-targeted approaches. Non-target is a hypothesis-free but discovery-based and data-driven strategy to break down (in theory) the whole chemical composition of a sample into ultimately meaningful components or to describe the interplay of all compounds in an explorative and holistic way on the molecular level.^[141–143] Hence, comprehensive detection of all metabolites (or MRPs) in a sample under study is the basic prerequisite of non-targeted studies. However, unlike genomics or proteomics, in metabolomics the detectable compound range is strongly shaped by physical restrictions of the analytical instrumentation used. For example, in ESI-MS it is the mostly polar to semi-polar compounds that are recorded. Further restrictions (e.g. molecular mass range) are possible. The term metabolomics was suggested to be reserved for comprehensive analysis of all metabolites in a sample, including their quantities and unambiguous identities.^[133] This definition sets high demands on analytical methods, which in most cases, cannot be fulfilled.

Metabolite fingerprinting aims at rapid classification of samples.^[133] It uses the advantage of sophisticated analytical technologies, which leads to large, complex and multivariate data structures. Advanced data visualization and multivariate approaches allow reduction of data dimensionality and interpretation of the acquired data. If the resolving power of an analytical method is high enough to obtain valid information of a sample's composition, this type of analysis provides unique and often information-rich signatures, even though quantities and exact identities of all compounds are not known. Nevertheless, in non-targeted approaches unknowns are not excluded and considered of equal importance compared to known compounds. Depending on the analytical tools used, these signatures can contain several dimensions of information (e.g. compositions, structures, quantities) and build the basis to discover the unknown and the unexpected.

The non-targeted strategy is a promising tool to discover new MRPs, formation pathways and to improve understanding of the entire reaction network. The performance of targeted methods in gaining quantitative measures cannot be replaced by non-targeted methods. Using a combination of both together provides a complementary approach. In targeted experiments, we can eventually only detect and quantify what we are looking for.^[144] A few markers alone are not often able to give an efficient description of the induced changes in the whole reaction system. The development in non-targeted methods and data analysis strategies in the field of “-omics” disciplines has made huge progress in recent years. Especially metabolomics seems to be a promising field, which provides many useful tools to study the MR in sugar-amino acid model systems.

1.3 Model systems

The limitations of analytical techniques to analyze the MR have been discussed in the previous section and it is clear that the complexity of the MR is a major challenge. When considering studying the MR in food products, the many other reactions (e.g. vitamin degradation, lipid peroxidation), which may interact with the MR network or lead to the same reaction products, make it even more difficult to unambiguously trace back identified reaction products to their precursors or *vice versa*. In contrast to real samples, model systems provide a simple and low-cost environment to control the sample composition (e.g. type of precursors) and/or reaction conditions so as to simplify the analytical process and allow better elucidation of the precursors, intermediates, downstream products and their formation mechanisms.

Table 1.1 shows some indicators used as chemical Maillard or AGE markers and the way in which they were historically identified. Model systems played a central role in the elucidation of chemical structures and formation pathways of all the markers shown. A typical approach in elucidation of chemical or biological markers is to first identify unknowns in real samples, such as foods or diseased tissues. This is then followed by using model systems to investigate the exact route of formation. Interestingly, many of the markers shown in Table 1.1 were first identified in model systems and only later, the relevance of these markers was confirmed in real samples.

Table 1.1 | First observation and characterization of selected compounds identified as markers for the Maillard reaction and advanced glycation.

Marker	First identification
Furosine (1966)	First observed in heated dried skim milk. Glucose and lysine were then found as precursors in model experiments. ^[145,146]
Pyrraline (1980)	Isolated and identified from a glucose-lysine model system. ^[147]
N ^ε -CML (1986)	Identified after incubation of N ^α -formyl-N ^ε -fructoselysine and identified in glucose-poly-L-lysine and glucose-RNase model systems, respectively. ^[148]
Pentosidine (1989)	Isolated and identified from human extracellular matrix. Structure confirmation and elucidation of the formation pathway by <i>in vitro</i> experiments using lysine-arginine-pentose model systems. ^[149,150]
Argpyrimidine (1997)	Purified and identified from model systems containing methylglyoxal and N ^α - <i>t</i> -Boc-arginine. ^[151]
Pronyl-lysine (2002)	Antioxidant activity was recognized in bread crust. Pronyl-lysine could then be structurally characterized after isolation from a model mixture containing acetylformoin and N ^α -acetyl-L-lysine. ^[152]
Formyllysine (2010)	Purification and characterization from pentose-lysine model systems. ^[153]

Preparation of model systems in practice. To minimize the influence of extrinsic factors, such as air, contaminant introduction or solvent evaporation, all model systems studied in Chapters 2-4 were prepared in sealed glass vials according to Figure 1.3. Model systems were prepared by mixing equal amounts of aqueous sugar and

amino acid stock solutions, respectively. After sealing the vials, the model systems were heated at 100 °C. Many of the studies, reported in literature, used buffered model systems. For example, phosphate buffer is a popular buffer to maintain neutral pH, *i.e.* to mimic physiological conditions.^[154-156] However, it is well-known that many molecular anions, such as phosphate, accelerate the MR by catalytic action.^[9,154,157] Additionally, inorganic buffer ions are prone to form undesired adducts and clusters in MS.^[158] To avoid any impact of buffering agents on the response of MRPs or decrease in spectral quality, here, no extra buffer substances were added to the model systems. In unbuffered model systems, the initial pH mainly depends on the type of amino acid precursor. With increasing reaction time, the pH decreases because of formation of acidic reaction products.^[35] For instance, degradation reactions on the sugar backbone, as shown in Chapter 1.1.2, can form carboxylic acids, which contribute to the decrease of the pH value. In sample preparation for comprehensive non-targeted studies, it is crucial to avoid any step, which would lead to selective enrichment or loss of analytes, respectively. Hence, maximum compound recovery was achieved by applying no additional sample preparation steps other than dilution or sample concentration under vacuum.

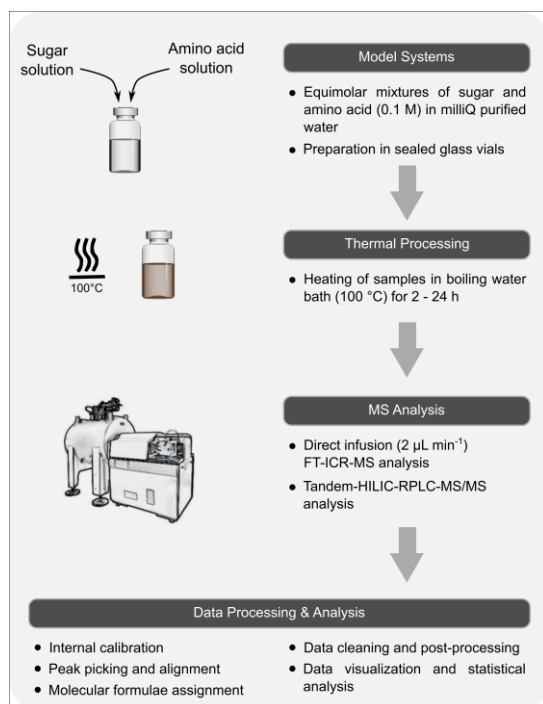


Figure 1.3 | Analytical workflow to study Maillard reaction products by non-targeted mass spectrometry.

Classification into reaction pools. In 1997, Yaylayan described the MR by the formation and interaction of so called “chemical pools” (Figure 1.4).^[159] The downstream decomposition of well-known precursors (sugar, amino acid, and ARP) ends in a collection of precursor reaction products (primary fragmentation pools). Reaction products of the primary fragmentation pools can then lead to further products by reactions within the same fragmentation pool (“self-interaction”) or with another fragmentation pool (“secondary interaction”). Compared to the Hodge scheme, which does not reflect the origin of different intermediates other than Amadori or Heyns degradation products, Yaylayan’s approach takes into account that amino acids and sugars can undergo independent degradation reactions, respectively.^[159] Accordingly, three types of primary reactions can occur in model systems: (i) Maillard reaction as the result between the interaction of carbonyls with amino compounds, (ii) caramelization reactions (sugar degradation without the interaction with an amino compound), and (iii) independent amino acid degradation reactions. The contribution of reactions (ii) and (iii) to the overall reaction products might lead to an overestimation of the MR.^[160] It is therefore of great value to study also “control samples” containing only the sugar and amino acid precursor, respectively. A more detailed view on the preparation of the sugar-amino acid model systems and “control samples” is given in the method sections of Chapters 2-4, respectively.

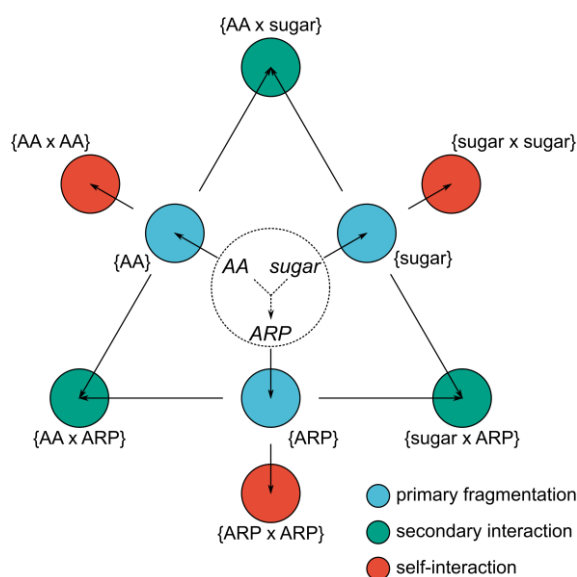


Figure 1.4 | Holistic description of the Maillard reaction using the concept of “chemical pools”.

Adapted with permission from Yaylayan, V.A. *Trends in Food Science & Technology* 1997, 8, 13–18. Copyright 1997 Elsevier.

1.4 Analytical methods for high- and ultrahigh-resolution measurements

1.4.1 Chemical Space

The contemporary analysis of complex systems at the molecular level requires the integrated use of holistic analytical methods providing high-resolution in different analytical dimensions. Known (*e.g.* precursors) or at least expected compounds (*e.g.* from literature) and a much larger set of unknown compounds build the chemical space of analytes, which must be covered by non-targeted methods. The number of relevant elemental compositions (compositional dimension) and the number of underlying structures (isomeric dimension) sets the total number of analytes to study (Figure 1.5a).^[161] Exact numbers of both dimensions are not known. However, for the simplest sugar-amino acid model systems it is enough to consider MRPs formed by the combination of C, H, N, and/or O atoms. If cysteine and/or methionine are studied the chemical space logically will expand by sulfur.

The maximum number of possible elemental compositions (molecular formulae) is eventually limited by the number of all possible combinations for a set of elements in a given molecular weight range. For instance, considering the elements C, H, O, and N only, as many as $1.5 \cdot 10^7$ element combinations not exceeding 1 000 Da can be computed. It seems logical that not every combination of elements represents a presumed stable molecule. Hence, several deterministic and heuristic rules have been developed to constrain the set of combinatorial formula solutions to chemically more meaningful ones.^[162,163] Comprehensive chemical databases usually contain a lot less formula entries. For example, about 6 500 and 5 500 unique molecular formulae ($C_{\geq 1}H_{\geq 1}N_{\geq 0}O_{\geq 0}$) not exceeding 1 000 Da are currently listed in the Human Metabolome Database (HMDB v4.0, www.hmdb.ca) and in the Food Database (FooDB v1.0, www.foodb.ca), respectively. The number of underlying chemical structures is about ten and three times higher in these databases (Figure 1.5b), respectively. Notwithstanding this, only 0.1% (HMDB) and 0.6% (FooDB) of all listed compounds have been reported as possible or known MRPs or AGEs (Figure 1.5c).

High-resolution MS is the key technique to accurately determine the molecular formulae of hundreds to several thousands of detected features. According to Marshall and Hendrickson,^[164] separation of isobaric species (*i.e.* ions with different elemental compositions but the same nominal mass) can only be sufficiently resolved when the resolving power is greater than 100 000, which is the prerequisite for an unambiguous formulae assignment. Currently, in routine analysis, such high resolution can only be provided by Orbitrap and FT-ICR mass analyzers.^[165,166] The

number of potential underlying isomers strongly depends on the type and number of atoms connected in a molecule. Because MS alone cannot resolve molecules with the same exact mass, integration of high-performance separation techniques is essential to resolve the isomeric dimension. Coupling of high-performance separation techniques, such as LC, to MS dramatically increases the total resolution and hence overall peak capacity (Figure 1.6).

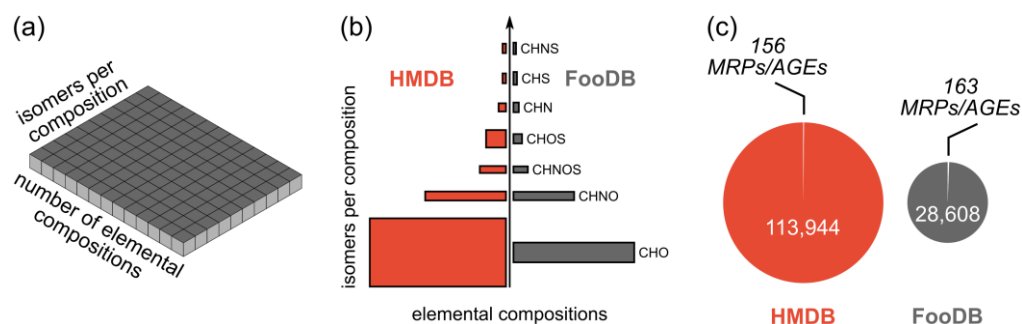


Figure 1.5 | Definition of chemical space and its coverage by comprehensive databases. (a) The number of elemental compositions and the number of underlying chemical structures per composition build the chemical space, which must be covered by analytical methods in non-targeted approaches. (b) Chemical subspaces, which are relevant for simple sugar-amino acid model systems and their coverage by HMDB v4.0 and FooDB v1.0 databases, respectively. Widths of the boxes represent the relative number of elemental compositions and heights represent the average number of isomers per composition, respectively. Therefore, the area illustrates the coverage of the chemical subspaces. (c) Number of all compounds and compounds listed as possible MRPs or AGEs in the HMDB v4.0 and FooDB v1.0 database, respectively.

1.4.2 Direct-infusion Fourier transform ion cyclotron resonance mass spectrometry

Among all types of mass analyzers, FT-ICR-MS offers highest resolution and mass accuracy (Figure 1.6).^[167] In FT-ICR-MS, the orbital frequencies of ions in a strong and homogenous magnetic field (usually 7 – 15 Tesla) are measured, which depend on the magnetic field strength and the ions' mass-to-charge (m/z) ratio.^[168] Highly precise frequency measurements result in very narrow peak shapes and ultimately in superb mass resolving power reaching several hundred thousand to more than a million with mass accuracy in the ppb range. Because of the ultrahigh resolving power, FT-ICR-MS offers the most coherent experimental evidence for the chemical diversity in complex systems.^[169] It is assumed that comprehensive databases contain less than 10% of the compounds disclosed in FT-ICR spectra.^[170] The vast majority of detected features remains unknown (“chemical dark matter”).^[171] Because the resolution increases with

increasing ion flight path, FT-ICR-MS has a relatively long acquisition time per scan. Duty cycles of typically one to several seconds are needed to achieve ultrahigh resolution. Consequently, online-coupling to fast and efficient chromatography significantly reduces the realizable mass resolving power.^[172,173] Notwithstanding this, when operated in direct-infusion (DI) mode, maximum performance can be achieved in routine measurements. In this case, FT-ICR-MS allows the molecular formulae of thousands of compounds to be collected in a single experiment.^[103,162,174,175] Electrospray ionization is the most frequently used MS interface because of its good ionization efficiency for a wide range of compound classes and its minor ability to form in-source fragments. Normally, up to several hundreds of single spectra are accumulated in DI experiments. On summing many single spectra, the initial signal-to-noise ratios increase by up to $n^{1/2}$ (where n is the number of acquired scans),^[176] which ultimately can lead to very low detection limits. A critical issue in DI-MS is ion suppression, which may lead to an underestimation of the true complexity and inaccurate reflection of ion abundances. However, it must be stressed that ion suppression generally increases with increasing concentration. Because model systems are usually not restricted in sample volume, highly diluted samples can be subjected to analysis and several hundreds of scans can be accumulated to achieve the required detection limits. Detailed experimental conditions used in this thesis are given in the methods sections of Chapters 2-4, respectively.

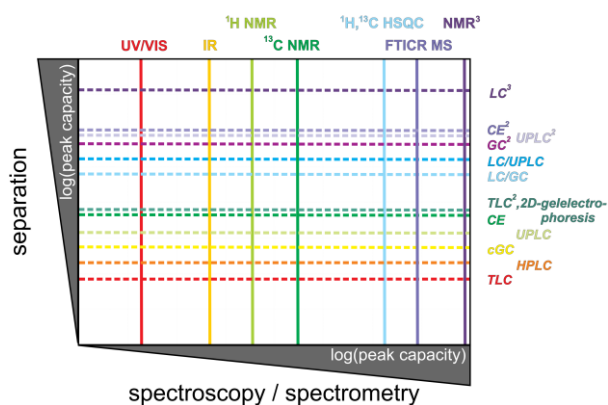


Figure 1.6 | Theoretical peak capacities of common separation techniques and spectroscopic / spectrometric detectors. The maximum overall peak capacity in hyphenated setups results from the product of the two peak capacities from the separation and detection techniques.

Adapted with permission from Hertkorn, N.; Ruecker, C.; Meringer, M.; Gugisch, R.; Frommberger, M.; Perdue, E.M.; Witt, M.; Schmitt-Kopplin, P. *Analytical and Bioanalytical Chemistry* 2007, 389, 1311–1327. Copyright 2007 Springer.

The complex data structure of broadband measurements requires advanced data post-processing, filtering, and formulae assignment strategies.^[175,177,178] Subsequent visualization tools and data analysis helps to extract meaningful

information. Van Krevelen diagrams (Figure 1.7) and Kendrick mass defect plots are powerful tools in the visualization and interpretation of complex broadband spectra. They allow qualitative analysis of major compound classes, the identification of possible chemical transformations (*e.g.* dehydration, oxidation and methylation) and can be helpful in eliminating false formula assignments.^[179–181] Molecular descriptors, such as the number of double-bond-equivalents (DBE, sum of rings and double bonds in a molecule), average carbon oxidation state (OS_C), aromaticity index or its equivalent, which can be computed from the obtained molecular formulae, further support data interpretation.^[182–184]

The more complete the analysis of a (Maillard) reaction system is, the more precursor-product signal pairs can be assumed to be present in the spectral data. The mass difference between such two peaks represents the net mass change and can be translated into a net chemical transformation if the mass precision and accuracy is high enough. Hence, mass difference statistics and constructed graphs thereof can be used to study a sample in a reactivity-related context. Although computation is often challenging, several approaches have been developed to study mass differences on a large scale in non-targeted FT-ICR-MS datasets.^[140] Mass differences between known and unknown MRPs further can help to decipher the “chemical dark matter”.^[142,185]

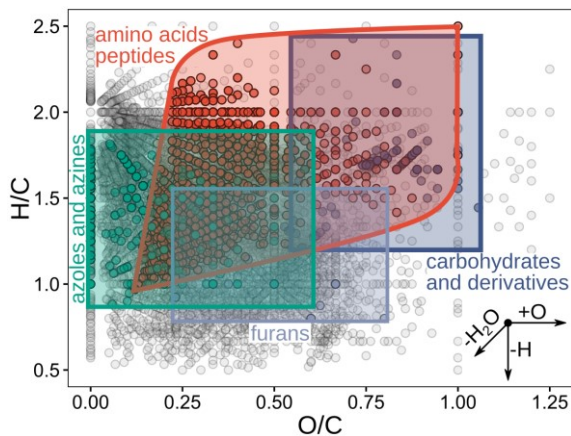


Figure 1.7 | Van Krevelen diagram illustrating the position of different compound classes relevant to the Maillard reaction. H/C versus O/C atomic ratios of around 7 500 CHNOS compounds taken from HMDB v4.0. Common positions of compound classes formed during the MR are highlighted: carbohydrates and derivatives (dark blue), amino acids and peptides (red), furans (light blue), and azoles and azines (green).

1.4.3 Tandem HILIC-RP LC-MS/MS

Reaction products formed during the MR span a polarity gradient ranging from highly polar sugar precursors to very nonpolar MRPs mainly formed in the advanced and final stages (see also Chapter 1.1). To comprehensively analyze MRPs by chromatography, at least two independent chromatographic runs using stationary phases with different selectivity are required. Reversed-phase LC has proved itself as a robust standard method for the analysis of a wide range of rather nonpolar analytes.^[186] By comparison, HILIC usually achieves better retention and separation of hydrophilic and ionic analytes.^[187,188] However, two independent chromatographic runs are time-consuming and require stable samples that do not change in their composition between the two measurements. Additionally, alignment of unknown compounds, which show retention on both stationary phases, is challenging in non-targeted screenings. Combination of two stationary phases in a single chromatographic setup is possible, either in two-dimensional (2D-LC) or one-dimensional chromatography. The second dimension in comprehensive 2D-LC requires very fast separation, which is usually achieved by short columns and fast elution gradients. Consequently, the maximum separation efficiency usually can only be fully exploited for the column in the first dimension. By comparison, the combination of two columns in a one-dimensional system at best would double the peak capacity compared to single-column chromatography while retaining the full separation efficiency of both columns, respectively. To maximize compound coverage in food matrices, we developed a tandem HILIC-RP LC system, which combines HILIC and RP chromatography in a single chromatographic run.^[189] **The full record of the related publication can be found in Appendix A (Hemmler et al. *Electrophoresis* 2018, 39, 1645–1653).** The presented method has been successfully applied to study MRPs as shown in Chapter 4.

1.5 Motivation and aim of the thesis

Reducing sugars and amino acids are essential molecular components for life. They are omnipresent molecules and occur spatially close to one another (*e.g.* in living cells). Therefore, it is obvious that the MR might play a role in virtually every biological system or any system originally derived from biological material. Nowadays, the important role of the MR in food products and under physiological conditions is well accepted. A very recent discussion even considers the MR and Maillard-type reactions to play a role in the formation of prebiotic molecules from simple carbonyl and amino

sources.^[190] However, it is generally supposed that the MR leads to an extraordinary high chemical diversity and complexity, ultimately leading to thousands of different molecular structures. Even after more than 100 years studying the MR, the entire chemical network has not been fully resolved. Currently, compounds in the early phase of the MR, the ARPs or Heyns products, and stable end products (*e.g.* aroma-active molecules) can be properly characterized. However, in the intermediate phase, comprehensive knowledge of chemical networks and interactions between the chemical compounds is missing, knowledge that would allow a better understanding of the whole reaction network. A deeper understanding of the pathways that lead to the formation of MRPs with key properties (*e.g.* antioxidants, toxic or aroma-active compounds) could lead to manipulation of the MR to deliver the desired compounds and eventually improve food quality or disease control.

Although there is a lack of comprehensive databases that can be used to study the MR in holistic non-targeted approaches, in recent years, promising strategies have been developed, which allow the study of yet unknown molecules. It is of high importance to improve the understanding of the interplay of different intermediates and reaction products. Here, it is often not decisive to know every exact chemical structure at the beginning but, instead, studying the interconnectivity of features in the reaction cascade will eventually lead to a reduced but meaningful set of compounds, which can then be studied in more detail using targeted approaches. Especially the field of metabolomics seems to be a promising toolbox providing analytical strategies to comprehensively unravel MRPs on a molecular level.

The outline of this thesis is summarized in Figure 1.8. In **Chapter 2 (Hemmler et al. *Scientific Reports* 2017, 7, 3227)**, we describe the gradual and thermal formation of MRPs in simple ribose-glycine model systems. Direct-infusion FT-ICR-MS fingerprinting was used to demonstrate the remarkable complexity and diversity of reaction products as well as the interconnectivity of chemical transformations in the overall reaction cascade. We then extended this initial study to multiple amino acid and sugar precursors (**Chapter 3; Hemmler et al. *Scientific Reports* 2018, 8, 16879**) in order to explore common and precursor-specific MRPs and reaction pathways. While the formation of MRPs upon thermal processing or long-term storage has been known for a long time, the effect of different energy regimes on MRPs or AGEs is largely unknown. Encouraged by this, we studied the chemical changes of MRPs upon exposure to solar radiation (**Chapter 4; Hemmler et al. *Chemistry – A European Journal* 2019, 25, 13208–13217**), which is of special relevance in the shelf-life of foods and phototoxicity mechanisms sensitized by AGEs.

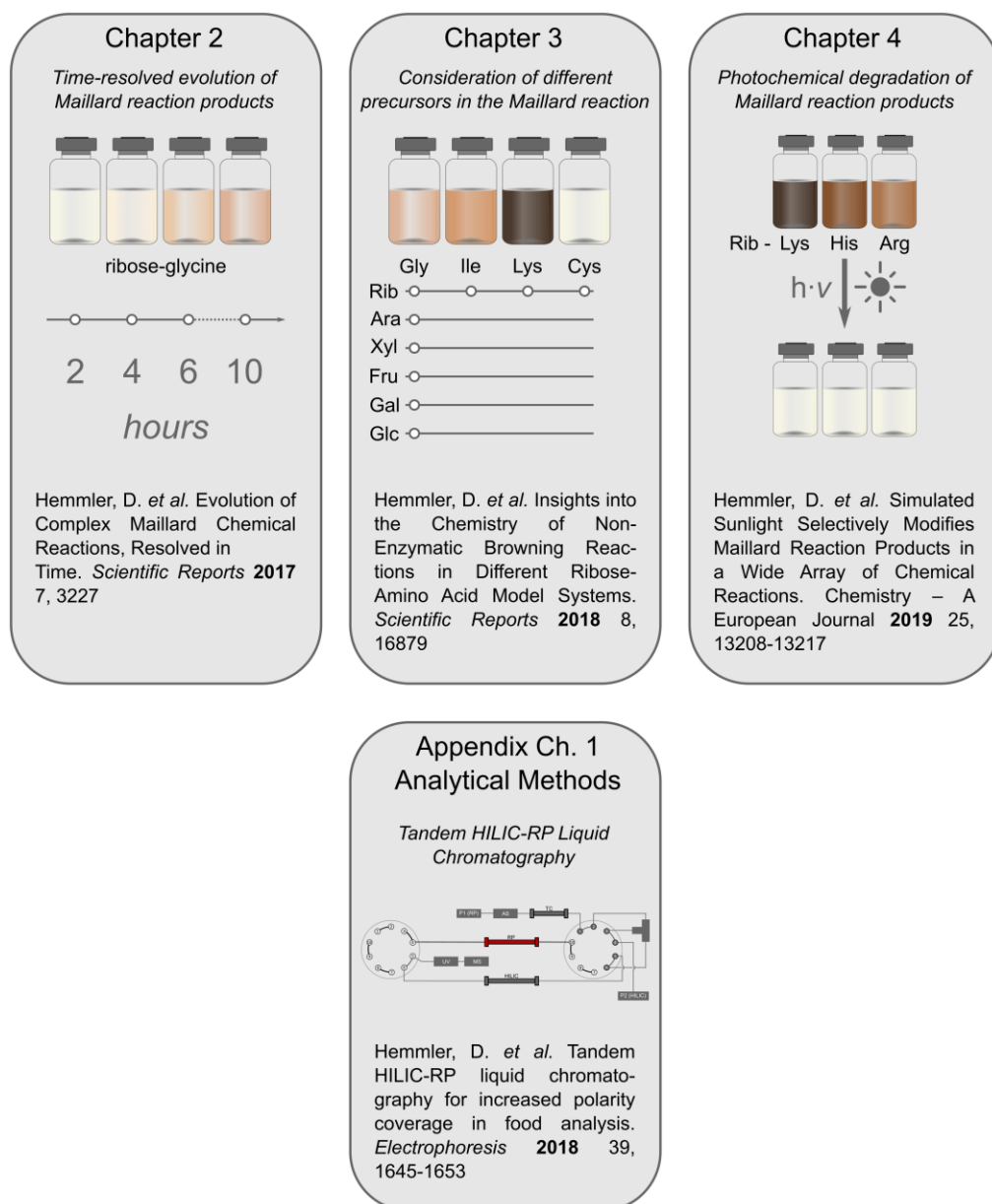


Figure 1.8 | Outline of the thesis.

Chapter 2 |

Evolution of Complex Maillard Chemical Reactions, Resolved in Time

In this study, we monitored the thermal formation of early ribose-glycine Maillard reaction products over time by ion cyclotron resonance mass spectrometry. Here, we considered sugar decomposition (caramelization) apart from compounds that could only be produced in the presence of the amino acid. More than 300 intermediates as a result of the two initial reactants were found after ten hours (100 °C) to participate in the interplay of the Maillard reaction cascade. Despite the large numerical variety, the majority of intermediates follow simple and repetitive reaction patterns. Dehydration, carbonyl cleavage, and redox reactions turned out to have a large impact on the diversity the Maillard reaction causes. Although the Amadori breakdown is considered as the main Maillard reaction pathway, other reactive intermediates, often of higher molecular weight than the Amadori rearrangement product, contribute to a large extent to the multitude of intermediates we observed.

This chapter has been published as [Hemmler, D.](#), Roullier-Gall, C., Marshall, J. W., Rychlik, M., Taylor, A. J. & Schmitt-Kopplin, P. Evolution of Complex Maillard Chemical Reactions, Resolved in Time. *Scientific Reports* 7, 3227 (2017).

Reprint permitted under the Creative Commons Attribution 4.0 International License (<http://creativecommons.org/licenses/by/4.0/>).

Candidate's contributions: D.H. designed the research. D.H. performed the experiments and analyzed the data. D.H. prepared the figures. D.H. wrote and revised the manuscript.

2.1 Introduction

For more than 100 years,^[1] understanding the Maillard reaction (MR) has been of great interest in food science. The MR refers to a non-enzymatic reaction between reducing carbohydrates and amino compounds. It can be understood as a complex network of chemical reaction series, rather than a single reaction. Hundreds or even thousands of distinct Maillard reaction products (MRPs) are generated, in particular through thermal processing. Many of the molecules contribute significantly to the aroma, taste and color of food.^[2] In 1953, Hodge divided the MR into three essential steps^[16]: (i) In the initial phase the carbonyl moiety of a sugar condenses with an amino compound; (ii) the subsequent rearrangement and breakdown of the Amadori compound (intermediate phase) leads to a reaction cascade involving dehydration, deamination, Strecker degradation, and many other fragmentation steps^[191]; and (iii) high-molecular weight and colored compounds are produced from the low molecular weight intermediates.^[16] In order to control the MR to produce desired molecules (*e.g.* flavors, antioxidants) and to avoid loss in nutritional value of food, it is essential to understand this entire chemical “collective”.

Traditionally, MRPs are analyzed by targeted methods. However, in targeted approaches only a small set of known (or predicted) compounds are studied at the same time. The bulk of the many unknown compounds remain ignored. By comparison, non-targeted analytical methods aim to investigate the entire complexity of a sample and provide the opportunity to solve yet unanswered issues.^[166] Ultrahigh-resolution ion cyclotron resonance mass spectrometry (FT-ICR-MS) was recently used in several studies to fingerprint, classify and describe the chemical composition of several foods^[192] and beverages.^[193–195] Jeandet *et al.* identified 5-hydroxymethylfurfural (HMF) and other caramelization markers by a combination of non-targeted FT-ICR-MS and NMR in 170-year-old champagne found in a shipwreck in the Baltic Sea.^[139] Golon *et al.* reported a considerably higher number of resolved analytes in heated sucrose-amino acid mixtures analyzed by FT-ICR-MS compared to TOF-MS.^[196] Despite the growing number of non-targeted approaches, the majority of MRPs, produced even when only one sugar is heated together with a single amino acid, still remain unknown. Despite decades of structural studies on the MR, a comprehensive picture of the composition of the reaction system and coherences between the intermediates has not been resolved. The aim of this study was to use non-targeted analysis and data visualization to deliver more insights into the overall chemical changes occurring in a ribose-glycine reaction.

2.2 Experimental procedures

2.2.1 Maillard model systems

D-(-)-Ribose (Rib, $\geq 99\%$) was purchased from Sigma-Aldrich (Steinheim, Germany). Glycine (Gly, $\geq 98.5\%$) was obtained from Merck (Darmstadt, Germany). Equimolar mixtures of ribose and glycine (0.1 M) were prepared in Milli-Q purified water (Millipore, Germany) immediately prior to thermal treatment. Samples were heated in a closed glass vial for two, four, six and ten hours (100 °C, waterbath). Additionally, blank samples containing only 0.1 M ribose or 0.1 M glycine were prepared. All experiments on Maillard model systems were carried out in triplicate ($n = 3$).

2.2.2 Direct-infusion FT-ICR mass spectrometry

Ultrahigh-resolution FT-ICR mass spectra were acquired with a 12 T Bruker Solarix mass spectrometer (Bruker Daltonics, Bremen, Germany) equipped with an APOLLO II electrospray source in negative ionization mode. For MS analysis the thermally processed Maillard model systems were diluted 1:500 (v/v) with methanol (LC-MS grade, Fluka, Germany). The diluted samples were infused into the electrospray ion source with a flow rate of $2 \mu\text{L min}^{-1}$. Settings for the ion source were: drying gas temperature 180 °C, drying gas flow 4.0 L min^{-1} , capillary voltage 3 600 V. Spectra were first externally calibrated by ion clusters of arginine (57 nmol mL^{-1} in methanol). Next, internal calibration of each spectrum was conducted with a reference list including selected Maillard reaction markers and ubiquitous fatty acids. The spectra were acquired with a time-domain of 4 megawords and 300 scans were accumulated within a mass range of m/z 92 to 1 000. A resolving power of 400 000 at m/z 300 was achieved. Raw spectra were post-processed by Compass DataAnalysis 4.2 (Bruker Daltonics, Bremen, Germany) and peaks with a signal-to-noise ratio (S/N) of at least 8 were exported to mass lists.

2.2.3 Processing of FT-ICR-MS data

All exported m/z features were aligned in a matrix containing averaged m/z -values (peak alignment window width: ± 1 ppm, Figure B.1 in Appendix Chapter 2) and corresponding peak intensities of all analyzed samples.^[197] Molecular formulae were assigned to the exact m/z -values by mass difference network analysis using an in-house developed software tool.^[198] For further processing, only those molecular

formulae were considered which were found in all three replicates of at least one sample. In total, 373 detected features could be assigned to distinct and unique molecular formulae. More than 90% of all assignments were found within an error range of ± 0.2 ppm (Figure B.2 in Appendix Chapter 2). All further calculations and filtering were done in Microsoft Excel 2010 and R Statistical Language (version 3.1.1).^[199]

2.2.4 Classification into reaction pools

Molecular formulae were classified according to Yaylayan into three different reaction pools (Figure B.3 in Appendix Chapter 2):^[159] (i) Maillard reaction products (MRPs, Table B.1 in Appendix Chapter 2), (ii) thermal induced carbohydrate degradation products, and (iii) amino acid degradation products. Ion signals which were found exclusively in all three replicates of the model systems but not in the blank samples (ribose and glycine heated alone) were classified as MRPs. Features also found in the ribose blank sample were classified as carbohydrate decomposition product. When signals were found in the model systems and both blank samples, they were considered to be contaminants. In total, eight different contaminants were detected known by us as trace contaminants omnipresent in solvents and sample preparation (Table B.2 in Appendix Chapter 2). Glycine degradation products could not be detected by our analytical platform.

2.2.5 Average carbon oxidation state

Carbon oxidation state of molecular formulae was calculated as suggested by Kroll *et al.* (2011):^[183]

$$\overline{OS}_C = - \sum_i OS_i \frac{n_i}{n_C} \quad (2.1)$$

in which OS_C is determined by non-carbon atoms (H, O, and N) in the molecular formulae. The quotient n_i/n_C is the molar ratio of element i to carbon and OS_i the oxidation state of element i set to +1, -2, and -3 for hydrogen, oxygen, and nitrogen, respectively.

2.3 Results and discussion

2.3.1 Compositional characterization of ribose-glycine MRPs

Here, an equimolar mixture of ribose and glycine was heated under the same conditions L. C. Maillard used in his original experiments in 1912 (100 °C, unbuffered).^[1] We monitored the formation of MRPs over time in a non-targeted approach by FT-ICR-MS. Extracts of the model system were subjected to analysis using direct-infusion FT-ICR-MS and a vast and complex pool of hundreds of distinct ion signals was observed (Figure 2.1a). Starting with two initial reactants, the number of intermediates produced throughout the course of the MR increased with time. Reaction products were recorded using negative electrospray ionization to achieve higher selectivity for oxygen-rich analytes,^[161] which are preferentially formed in the early MR. The instrument's high resolving power (400 000 at m/z 300) and mass accuracy enabled the assignment of the individual mass peaks to their corresponding unique elemental compositions. According to Yaylayan's classification approach,^[159] three kinds of reactions can occur when a sugar is heated in the presence of amino acids: (i) Degradation of the Amadori rearrangement product (ARP), Maillard reaction; (ii) carbohydrate degradation, caramelization type reactions; and (iii) amino acid degradation; (detailed classification approach is described in Chapter 2.2.4). Formation of reactive intermediates which constantly feed the reaction pool, leads to an exponential increase in production of MRPs (Figure 2.1b). After ten hours, we found hundreds of distinct molecular formulae which were not produced when ribose or glycine were heated alone. The shape of the curve (Figure 2.1b) indicates that, even after ten hours, an end point of the reaction was not reached. By comparison, ribose caramelization (ribose heated alone; Figure 2.1b) led to a linear increase in the number of decomposition products but only a few tens of compounds were formed. Sugar decomposition is known to predominantly occur at high temperatures (>120 °C) or under strongly alkaline or acidic conditions^[200] whereas the MR requires less energy.^[9] Nevertheless, these ribose decomposition products (and some smaller ones outside our analytical window; <100 Da) may also be reactive intermediates which can contribute to the overall MR cascade. Most of the MRPs detected have a molecular mass below 400 Da. However, after two hours a large number of molecular formulae were found at a higher molecular weight than the initial ARP *N*-(1-deoxy-D-erythro-2-pentulos-1-yl)glycine (structure 2 in Figure 2.2). Thus, MRPs are not only formed by degradation of the ARP into smaller molecules, also molecules of higher molecular weight are produced, which contribute to the diversity observed in the MR.

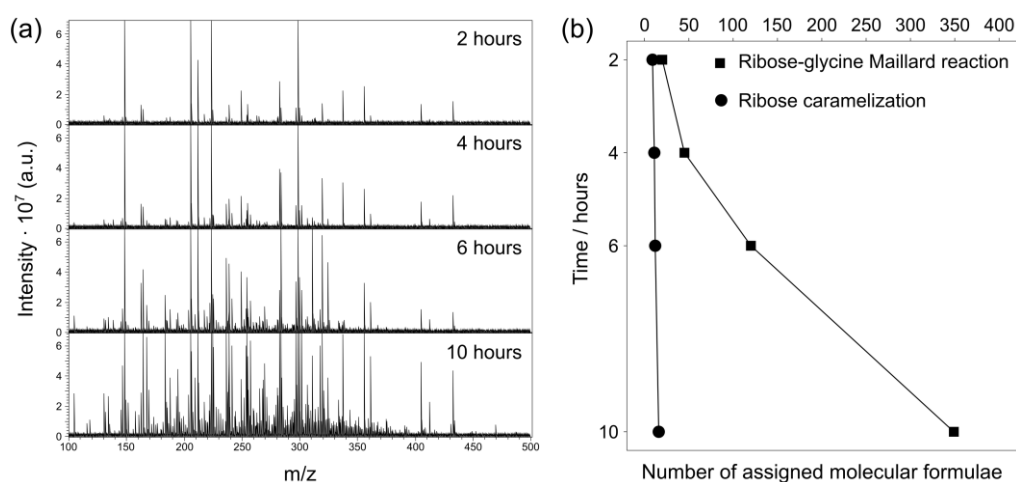


Figure 2.1 | Progression of reaction products in a ribose-glycine Maillard model system after thermal treatment at 100 °C for two, four, six, and ten hours. (a) Raw FT-ICR mass spectra with fixed peak intensity scale. (b) Classification of the detected signals into Maillard reaction products (square) and carbohydrate degradation products (circle). Glycine degradation products were not detected.

Molecular formulae retrieved for MRPs (and ribose) were projected into 2D van Krevelen plots (Figure 2.2a-d).^[179] After two hours, the compound pool was almost exclusively made up of MRPs containing one nitrogen atom (Figure 2.2e). After ten hours the number of detected CHNO and CHO compounds was 18 times as many as found after two hours (19 MRPs found after 2 h, 348 after 10 h). However, the formation of MRPs containing two nitrogen atoms showed a noticeably greater increase after six hours compared to MRPs containing only one or no nitrogen atoms. Starting with condensation of ribose (O/C: 1, H/C: 2) and glycine the MR begins in the top right corner of the van Krevelen diagrams. The initial condensation is followed by an extended series of dehydration reactions leading to MRPs with a higher degree of unsaturation and aromaticity (lower H/C and O/C ratios) as a function of time. After four hours, more than half of the MRPs produced were found in a very narrow range ($1 \leq \text{H/C} \leq 1.5$ and $0.35 \leq \text{O/C} \leq 0.65$), so, although the number of MRPs produced is high, they are found in a very discrete chemical compositional space. Within the first four hours, we observed that extended series of dehydration reactions were the most dominant in the formation of nitrogen-containing (CHNO) species. Interestingly, when nitrogen-free (CHO) compounds were considered separately, dehydration reactions did not play a significant role in the first six hours, neither in Maillard reactions (Figure B.4 in Appendix Chapter 2) nor when ribose was heated alone. This leads us to propose that dehydration of the carbohydrate backbone is favored when the sugar is covalently bound to amino compounds. These nitrogen-free (CHO) MRPs detected in the first six hours all revealed an average carbon oxidation state^[183] (OS_c) higher than ribose (Figure B.4 in Appendix Chapter 2). Many of these intermediates

may be formed by oxidative cleavage of dicarbonyl structures.^[31] By comparison, the predominant CHNO-containing MRPs in the first four hours mostly revealed an OSC similar to that of the ARP (Figure B.5 in Appendix Chapter 2). Consequently, reactions of other type than oxidation reactions (*e.g.* dehydration) predominate the formation of CHNO-MRPs at the beginning of the MR. After six hours, both oxidized and reduced CHNO species were also observed. After ten hours, nitrogen-free (CHO) intermediates also showed pronounced dehydration series (Figure B.4 in Appendix Chapter 2). By comparison, when ribose was heated alone, there was little evidence of dehydration reactions playing a meaningful role over the entire ten-hour cooking period. In this context, nitrogen-free (CHO) and nitrogen containing (CHNO) MRPs act very differently in their reactive behavior.

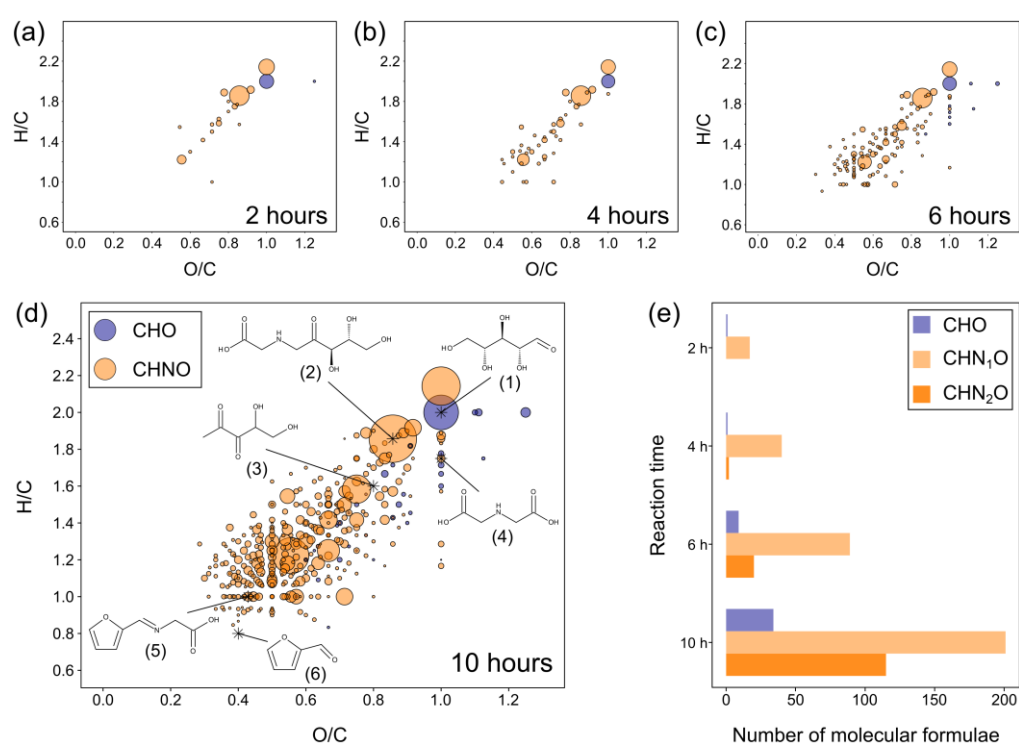


Figure 2.2 | Compositional characteristics of MRPs and ribose. (a–d) Van Krevelen diagrams (H/C vs. O/C) were used to visualize the reaction progression. Features on imaginary lines with a slope of 2 indicate dehydration series, those on vertical and horizontal lines represent redox reaction series.^[179] Selected known marker compounds illustrate the position in the diagrams depending on structural characteristics: ribose 1, Amadori product (ARP, 2), 1-deoxypentose 3, *N*-(carboxymethyl)glycine 4, *N*-(2-furanylmethylene)glycine 5, and furfural 6. (e) The bar chart illustrates the absolute number of assigned molecular formulae for each reaction time classified into compositional spaces (CHO, CHN₁O, and CHN₂O).

2.3.2 Time-resolved interplay between MRPs

As all features which were detected after two, four, or six hours were still detectable in the samples heated for ten hours, the chemical pathways leading to these intermediates must be present in the mass spectra and can be characterized by studying the exact mass differences (MDs) between compounds which represent chemical transitions in the early stages of the MR such as dehydration, oxidation, *etc.*^[16] This type of data analysis shows the chemical relationships between the compounds and probes the data in a more reactivity-related context. It was possible to connect 98% of the observed compounds (MRPs, carbohydrate decomposition products, and ribose) with just seven types of transformations. A network graph was constructed (Figure 2.3) where the nodes represent assigned molecular formulae which are connected to each other by accurate MDs representing possible chemical transformations. In fact, the network in Figure 2.3a offers a broad picture of simple and repetitive reaction series occurring in parallel. Moreover, the decomposition of the ARP can be completely followed as a time dependent pathway until the formation of the furfural and Strecker imine (Figure 2.3b). This confirms the comprehensive acquisition of early MRPs with the method applied. However, the ARP degradation as described in the Hodge scheme (Figure 2.3c) constitutes only a small subpart of our network.

In Figure 2.4 we applied a modified Kendrick mass defect analysis^[179] in order to visualize the role of dehydration reactions as well as the relationships between each other. At the beginning, dehydration series are connected to each other by simple carbohydrate type fragments of type $C_n(H_2O)_m$. After the initial ribose-glycine condensation, the ARP was formed and subsequently dehydrated. At the same time, we observed another glycation of the ARP by $C_5H_{10}O_5$ leading probably to *N,N*-bis(1-deoxy-D-erythro-2-pentulos-1-yl)-glycine. The formation of diketosamines has apparently been only reported for difructosamines. Mossine *et al.* showed that the degradation rate of difructosamines is much higher than for monofructosamines.^[201] Consequently, the two further dehydration series (C+2 and C+3), detected after four hours, could arise from direct cleavage of dicarbonyl intermediates produced from the diketosamine. The amino intermediates formed from this reaction, potentially offer a new reducing end, which is able to undergo new glycine condensation, thus opening the CHN_2O space, or aldol-type reactions with other carbonyl intermediates to extend the carbon backbone. Little is known about C-C bond formation in the MR. The elongation of carbohydrates by aldol-type reactions is still under debate. However, intermolecular C-C bond formation between ketones and aldehydes may be catalyzed by the action of amino acids.^[202] Recently, Pfeiffer *et al.* reported an aldol-based polymerization of methylglyoxal produced during the decomposition of

3-deoxy-D-erythro-hexos-2-ulose leading to reactive aldehydes with extended carbon chains.^[203] Additionally, oxidation of the ARP led to a further dehydration series (4 h, Figure 2.4). Both, fragmentation of the carbohydrate backbone and redox reactions, were found to be mainly responsible for the complete set of dehydration series found after ten hours. We found series ranging from ARP-C1 to ARP+C9 (Figure 2.4). It is worth noting that all series greater than ARP+C5 must involve the formation of new C-C bonds in at least one stage of the reaction cascade and not only a breakdown into smaller fragments.

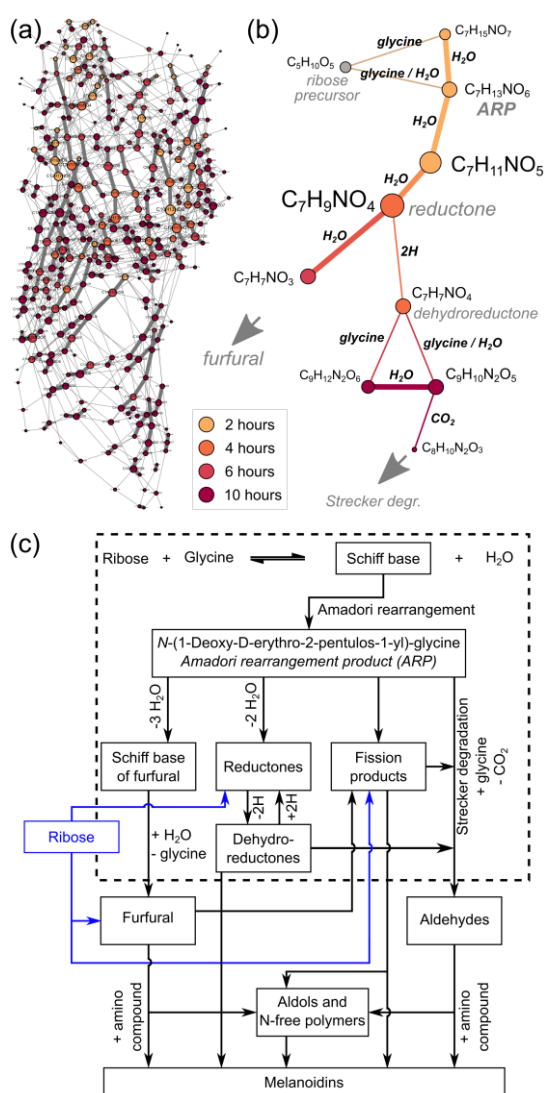


Figure 2.3 | Time-resolved coherences between MRPs. (a) Mass difference network of MRPs, carbohydrate decomposition products and the ribose precursor. 98% of assigned ion signals (357/366) could be connected in the network by allowing only a set of seven simple transformations from the Hodge scheme: 2.01565 (2H), 12.00000 (Strecker degradation, + H_2O /- CH_2O), 18.01057 (H_2O , in bold), 43.98983 (CO_2), 57.02146 (glycine condensation), 75.03203 (glycine addition), 150.05283 (pentose addition). The transformations (edges) in the graph are undirected, reverse reactions are also possible. (b) The selection shows the coherences between observed molecular formulae as expected for the initial and intermediate phase by the reaction scheme (dashed box in c). (c) Fundamental Maillard reaction scheme adapted from Hodge.^[16]

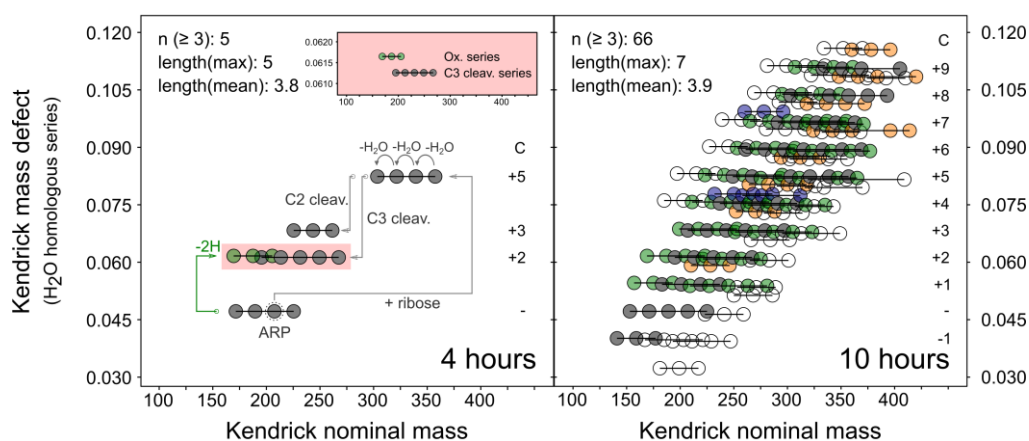


Figure 2.4 | Visualization of dehydration series by Kendrick mass defect (KMD) analysis.^[179] Conversion of the IUPAC mass to a Kendrick mass scale ($\text{IUPAC} \times 18/18.01057$) projects dehydration series onto horizontal lines. Only series including at least three intermediates ($n \geq 3$) are shown. Most series can be formed from the ARP by condensation with carbohydrate type ($\text{C}_c(\text{H}_2\text{O})_n$) fragments (grey), redox reactions (green) or a combination of both. Formation of nitrogen-free compounds (blue) and MRPs containing two nitrogen atoms (orange) must involve further release or addition/condensation of glycine.

2.4 Conclusions

In summary, this study emphasized the complexity of hundreds of distinct early MRPs produced in a simple two reactant system. Although isomers could not be resolved by our methods, we achieved a comprehensive coverage of intermediates involved in the early Maillard reaction. Those intermediates can be formed within a network of parallel reactions following repetitive patterns. Among others, dehydration, fragmentation of the carbohydrate backbone and redox reactions turned out to have a large impact on the diversity. Not only decomposition of the ARP but also the formation of initial intermediates with higher molecular weight than the ARP is involved in the reaction cascade. Extending these experiments by multiple amino or carbohydrate sources as in the case of food products would certainly amplify the diversity to new dimensions reaching thousands of distinct compounds.

Chapter 3 |

Insights into the Chemistry of Non-Enzymatic Browning Reactions in Different Ribose-Amino Acid Model Systems

Reactions between sugars and amino acids in the Maillard reaction produce a multitude of compounds through interconnected chemical pathways. The course of the pathways changes depending on the nature of the amino acids and sugars as well as the processing conditions (e.g. temperature, water activity). Some partial pathways have been elucidated using labelled precursors but the process is very time intensive. Here, we use rapid, non-targeted analysis with Fourier transform ion cyclotron resonance mass spectrometry (FT-ICR-MS) to deliver the molecular formulae and ion intensities of the compounds generated from reaction of four amino acids with ribose (10 h at 100 °C) to study the effect of amino acid side chains on the reaction pathways. Using van Krevelen diagrams, known chemical changes during the reaction (e.g. dehydration or decarboxylation) can be studied. Comparison of the data from the four amino acids studied, showed a common pathway, which involved 73 Maillard reaction products (MRPs) where the differences were due only to the nature of the amino acid side chain. From the more than 1 400 different molecular formulae found, pathways unique to the amino acids were also identified and the order of reactivity was lysine > cysteine > isoleucine ≈ glycine. While unequivocal identification of the compounds cannot be achieved with FT-ICR-MS, applying known chemical transformations found in the Maillard reaction, not only identifies new and known pathways, but also integrates the MRPs into a general Maillard reaction scheme that better represents the totality of the Maillard reaction.

This chapter has been published as [Hemmler, D.](#), Roullier-Gall, C., Marshall, J. W., Rychlik, M., Taylor, A. J. & Schmitt-Kopplin, P. Insights into the Chemistry of Non-Enzymatic Browning Reactions in Different Ribose-Amino Acid Model Systems. *Scientific Reports* **8**, 16879 (2018).

Reprint permitted under the Creative Commons Attribution 4.0 International License (<http://creativecommons.org/licenses/by/4.0/>).

Candidate's contributions: D.H. designed the research. D.H. performed the experiments and analyzed the data. D.H. prepared the figures. D.H. wrote and revised the manuscript.

3.1 Introduction

Non-enzymatic browning between reducing carbohydrates and amines, also known as the Maillard reaction (MR), is of crucial importance in food science where it significantly contributes to taste, aroma and color.^[2] Additionally, it is now established that the MR takes place *in vivo* under physiological conditions, where non-enzymatic reactions between carbohydrates and proteins lead to irreversible protein modifications associated with a wide range of diseases, such as *diabetes mellitus*.^[2,204,205] The initial condensation between an amine compound (*e.g.* amino acid) and carbonyls leads to the relatively stable Amadori rearrangement product (ARP). Subsequent breakdown of the ARP (intermediate phase) initiates a flood of chemical reactions continuously producing new intermediates which are fed into the Maillard reaction pool. Many of the breakdown intermediates produced are highly reactive, such as reductones and other (di)carbonyl compounds,^[16] which then may react to form new Maillard reaction products (MRPs), thus increasing the chemodiversity exponentially. Among many other factors, type and concentration of precursors, temperature, pH and time have a major impact on the type of reactions and intermediates as well as the end products produced. This makes the MR certainly one of the most complex reaction “collectives” which is able to produce thousands of distinct chemical compounds from only a few initial precursors.

To date, detailed knowledge of reaction mechanisms has been achieved for the some specific steps of the MR, mainly from studies of sugar-amino acid model systems but no overall view of the reaction pathways has been published. By means of non-targeted GC-MS methods, many volatile, often flavor-active molecules or precursors thereof, have been identified, and important formation pathways proposed.^[89,206] By comparison, non-volatiles of the intermediate phase are still unknown to a large extent. The high diversity in chemical properties makes a simultaneous analysis especially challenging.^[93,207] Although several reported methods have successfully separated and detected multiple reaction products, non-targeted analysis exploring the non-volatiles, produced throughout the course of the MR, are rare.^[208] The large number of reaction products, reactive intermediates and transition species, often

having very similar retention properties, do not allow sufficient isolation and structure elucidation of all of the compounds involved in the MR. Hence, most of the described analytical approaches focus on quantification of selected target molecules. For example, Davidek *et al.* proposed a derivatization-free anion exchange chromatography method for the simultaneous quantitation of sugar and amino acid precursors together with the Amadori rearrangement product (ARP) and three cyclic intermediates.^[208] More recently, Katayama *et al.* developed an LC-MS/MS method for quantification of twenty fructose-derived ARPs.^[209]

Although mass spectrometry alone cannot provide sufficient structural information for unequivocal identification, it is an irreplaceable tool for the holistic analysis of complex samples on a molecular level. In recent years, ultrahigh-resolution Fourier transform ion cyclotron resonance mass spectrometry (FT-ICR-MS) has prevailed as a method of choice in the compositional characterization of utmost complex samples in many scientific disciplines.^[161,194,210] We have recently shown that direct-infusion FT-ICR-MS provides deep insights into initial and intermediate MRPs produced in a ribose-glycine Maillard model system. We found more than 300 distinct elemental compositions, produced in the ribose-glycine Maillard reaction cascade.^[211] In the present study, we extend our experiment using multiple amino acid precursors. The aim is to demonstrate the chemodiversity in the molecular characteristics among different model systems on the level of accurate molecular formulae in order to generate new hypotheses, which could help to improve the understanding of the chemistry of MRPs and their formation processes.

3.2 Experimental procedures

3.2.1 Chemicals

D-(-)-Ribose (Rib, 98%), L-lysine (Lys, $\geq 99\%$), L-cysteine (Cys, $\geq 97\%$), and L-isoleucine (Ile, 99%) were purchased from Sigma-Aldrich (Steinheim, Germany). Glycine (Gly, $\geq 98.5\%$) was obtained from Merck (Darmstadt, Germany).

3.2.2 Model systems

Mixtures of ribose and amino acids (0.1 mol L⁻¹ respectively) were prepared in Milli-Q purified water (Millipore, Germany) immediately prior to thermal treatment. 1 mL of each mixture was heated in 2 mL glass vials sealed with temperature and pressure

resistant crimp caps to exclude additional air/gas exchange for two, four, six and ten hours in a boiling water bath (100 °C). For the identification of ribose and amino acid degradation products, blank samples containing 0.1 mol L⁻¹ ribose or amino acid were prepared. All Maillard model systems were prepared and analyzed in triplicate.

3.2.3 Direct-infusion FT-ICR mass spectrometry

All samples were diluted 1:500 (*v/v*) with methanol (LC-MS grade, Fluka, Germany) and analyzed by direct-infusion FT-ICR-MS as recently described.^[211] Direct-infusion FT-ICR mass spectra were acquired with a 12 Tesla Bruker Solarix FT-ICR mass spectrometer (Bruker Daltonics, Bremen, Germany). The mass analyzer was first calibrated by means of arginine ion clusters (57 nmol mL⁻¹ in methanol). Next, raw spectra were further internally calibrated using a reference list including known Maillard reaction markers and ubiquitous fatty acids to achieve best possible mass accuracy and precision among the samples. Raw spectra were post-processed by Compass DataAnalysis 4.2 (Bruker Daltonics, Bremen, Germany) and peaks with a signal-to-noise ratio (S/N) of at least 8 were exported to mass lists. All exported features were aligned in a matrix containing averaged *m/z*-values (maximum peak alignment window width: ± 1 ppm) and corresponding peak intensities of all analyzed samples.^[197] Only *m/z* features of monoisotopic candidates and features with feasible mass defect were retained in the matrix. Identification of heavy isotope candidates was performed as described elsewhere.^[212] Remaining *m/z*-values were assigned to their unambiguous molecular formulae as recently described.^[211] Chloride adducts [M+Cl]⁻ were only retained in the final data matrix when no corresponding [M-H]⁻ ion was found. In general, chloride adduct formation played only a minor role. In the ribose-lysine model systems 26 and in the ribose-cysteine model systems one [M+Cl]⁻ adducts could be detected which were not recorded as [M-H]⁻. No such unique chloride adducts were found for ribose-glycine and ribose-isoleucine MRPs.

3.2.4 UV-absorbance

Samples were diluted 1:100 (*v/v*) with Milli-Q purified water (Millipore, Germany). Immediately after dilution, the absorbance at 294 nm was measured using a μ Quant Spectrophotometer (Bio-Tek Instruments, USA).

3.2.5 Data analysis

All further data processing was done in Microsoft Excel 2010 and R Statistical Language (version 3.4.1).^[199] Only those molecular features, which were detected in all three replicates ($S/N \geq 8$) of one sample group, were considered for further data analysis and interpretation. The number of double-bond equivalents (sum of rings and double bonds in a molecule) per carbon atom (DBE/C) can be calculated according to Eqn. 3.1 from the number of atoms (n_i) and the valence (v_i) of each element i .

$$\text{DBE/C} = \frac{1 + \frac{1}{2} \sum n_i (v_i - 2)}{n_c} \quad (3.1)$$

3.3 Results and discussion

3.3.1 Reaction monitoring by direct-infusion FT-ICR mass spectrometry

Four different amino acids (glycine, isoleucine, lysine, and cysteine) were reacted with ribose in equimolar (0.1 M) mixtures at 100 °C. We monitored the formation of intermediates and reaction products by direct-infusion FT-ICR-MS after a reaction time of two, four, six, and ten hours. In this fundamental proof-of-principle study, we used a well-known but uncontrolled reaction system (unbuffered solutions). The amino acids were chosen to cover a wide range of physicochemical properties. Ribose was selected as the major carbohydrate precursor to study because of its high reactivity among the common pentoses and hexoses.^[213]

Here, we focus on results obtained after negative electrospray (ESI(-)) ionization which allows detection of polar and oxygen-rich MRPs of the initial and intermediate phase of the MR. Hundreds of distinct ion signals could be recorded in each model system (Figure C.1a in Appendix Chapter 3). Comparing the four amino acids, lysine showed a considerably higher signal density after ten hours compared to the other amino acids. Most of the reaction products were found in a mass range between m/z 100 – 600. While the high resolving power (400 000 at m/z 300) allowed an unambiguous differentiation of the recorded ion signals, high mass accuracy and precision allowed us to assign detected m/z -values to their unambiguous molecular formulae. If only $C_cH_hO_o$ element compositions are considered it would be possible, with the achieved mass accuracy, to accurately assign molecular formulae using only

the exact ion masses. However, when non-oxygen heteroatoms, such as nitrogen or sulfur, are also taken into account, the number of possible solutions increases dramatically with the number of heteroatoms and ion mass.^[175] Hence, we used a combination of compositional network-based formulae annotation and isotopic fine structure validation (Figure C.1b in Appendix Chapter 3) in order to eliminate false assignments.^[178,198,214] After ten hours, we found in total 1 493 distinct molecular formulae among the four investigated model systems. More than 90% of all features were found within a maximum error of ± 0.2 ppm (99% with maximum error of ± 0.5 ppm, Figure C.1c in Appendix Chapter 3).

Here, we report only features, which were found in all three replicates. This guarantees highest accuracy and reproducibility of the discussed compounds. Spectra were always dominated by a few high-intensity principal components while the majority of produced compounds were found with considerably lower peak intensities (Figure C.1c in Appendix Chapter 3). Overall, we observed analytes in a range covering approximately four orders of magnitude in peak intensity. This intensity range, covered by the ICR mass analyzer, can also be interpreted as an approximation for the relative concentration range in which compounds occur in the MR. The similarity in chemical properties together with the complexity and high dynamic range in concentrations makes a simultaneous or comprehensive analysis with conventional analytical approaches, such as LC-MS, very challenging.^[93,207]

3.3.2 Formation of reaction products monitored over time

With the help of blank samples (ribose and amino acids heated alone, respectively), the recorded reaction products were classified into thermally synthesized MRPs, sugar and amino acid degradation products according to the classification approach suggested by Yaylayan^[159] and as recently described.^[211] Most reaction products could be clearly assigned to MRPs, which require for their formation the presence of both, an amino acid and a sugar precursor. Among the tested amino acids, lysine produced most MRPs. After ten hours of thermal treatment, we could detect more than 700 different molecular formulae assigned to MRPs. By comparison, for glycine, isoleucine and cysteine we found 300-400 MRPs, respectively. The order of MRPs produced after ten hours was lysine > cysteine > isoleucine \approx glycine (Figure 3.1a). Lysine was also shown in many other studies to be the most reactive amino acid in Maillard model systems^[83,160,215] and the key contributor to MRPs produced through protein glycation. Interestingly, cysteine and lysine both showed a high number of produced MRPs after heating the samples for only two hours. Compared to glycine and isoleucine, these amino acids have reactive functional side chains. It is very likely that the strong

nucleophilicity of the thiol side chain^[216] leads to many of the observed MRPs produced in the ribose-cysteine model. Further, Munch *et al.* showed that, when the side chains were protected, the reactivity of N-terminal amino acids in dipeptides towards glucose and fructose addition is almost similar among the twenty proteinogenic amino acids.^[217] Only cysteine revealed slightly lower reactivity. However, when the side chains were unprotected cysteine and lysine showed by far highest reactivity.^[217]

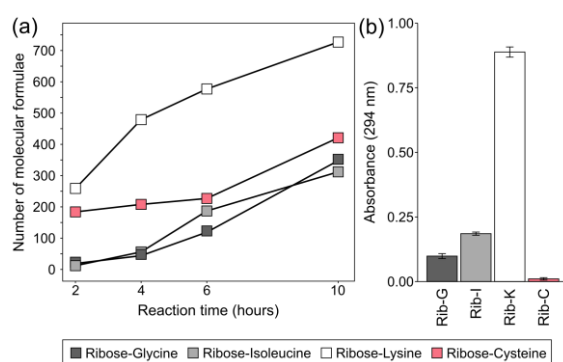


Figure 3.1 | Formation of MRPs and UV absorbing products. (a) Number of MRPs produced in four different ribose-amino acid model systems heated for two, four, six, and ten hours (100 °C). (b) Absorbance at 294 nm of ribose-amino acid models heated for ten hours (100 °C). Error bars indicate the standard deviation of the mean absorbance value (n = 3).

A simple and fast method to assess the progress of Maillard reactions is to measure the degree of browning. In the intermediate stage, non-enzymatic browning leads to chromophores showing good absorbance at 294 nm while 420 nm indicates reaction products of the final stage.^[97,218] Here, after ten hours, the order in degree of browning found at 294 nm was: lysine > isoleucine > glycine > cysteine as shown in Figure 3.1b. The same order was reported by Hwang *et al.* when they heated unbuffered amino acid – glucose mixtures for two hours at 130 °C.^[219] For cysteine, we observed only a minor amount of browning over the entire reaction timescale. It has been reported in many studies that cysteine does not lead to extensively colored compounds, but rather suppresses the formation of chromophores. The suppressing effect of cysteine has so far been mostly explained by the formation of relatively stable thiazolidines^[220] and its ability to effectively trap (di)carbonyls to form hemi- or thioacetals.^[221] Although cysteine does not contribute to the characteristic browning in Maillard reactions, it is responsible for a huge diversity in reaction products as shown in our FT-ICR-MS data (Figure 3.1a). Furthermore, cysteine is known to produce many meat-like aroma compounds including S-containing heterocyclic molecules which are often formed from cysteine degradation products such as H₂S or cysteamine.^[4,222,223] However, non-volatile Maillard intermediates, which are

produced by cysteine, are largely unknown. With more than 400 MRPs observed in electrospray MS, we here report a large pool of chemical compounds which could act as non-volatile precursors in the formation of aromas. Moreover, although cysteine is often considered as relatively unreactive in the MR^[220] we could show that it is responsible for a variety of non-volatile intermediates, consequently having quite a remarkable reactivity.

Compared to the multitude of MRPs produced in the model systems, we observed only a few amino acid degradation products for lysine and cysteine (Figure C.2 in Appendix Chapter 3). No amino acid degradation products were observed for glycine and isoleucine in the covered mass range. Cysteine showed highest thermal instability resulting in 27 amino acid degradation products, which could be formed without the interaction with ribose. Some of those cysteine degradation products may also contribute to the total diversity in reaction products we observed in the ribose-cysteine MR. The number of sugar degradation products observed in the model systems is very similar for glycine, isoleucine and lysine (16 ± 2 ; Figure C.2 in Appendix Chapter 3). However, in the cysteine model system, the number of ribose decomposition products produced was considerably smaller than for the other amino acids. After ten hours, we found only nine ribose degradation products in the ribose-cysteine mixture. Thus, cysteine seems not only to suppress the browning in Maillard reactions but also has a suppressing effect on sugar decomposition. Sugar degradation products, such as furfural or dicarbonyls, significantly contribute to the degree of browning.^[16] As a result, it can be assumed that suppression of sugar degradation products in cysteine-containing Maillard systems is a part of the suppression effect of cysteine on browning.

Degradation of the ARP and hence the composition and number of formed MRPs strongly depends, among many other factors, on the reaction pH.^[26,224] In our reaction systems, pH values dropped with increasing reaction time. After ten hours, the pH decreased by approximately 2-3 pH units compared to unheated model systems. Acidification has a significant impact on the availability of amino groups and, to a lesser degree, an effect on the acyclic form of the sugar precursor.^[225] The relative proportion of unprotonated amino groups, which is essential for nucleophilic reactions in the initial phase of the MR, increases with increasing pH. Lysine showed a strong increase in the formation of MRPs within the first four hours (Figure 3.1a) which can be attributed to the availability of more amino groups in the early phase of the reaction.

3.3.3 Compositional characteristics of MRPs

Among the many visualization tools used for high-resolution MS data, the van Krevelen diagram is a very valuable tool for the representation of hundreds or thousands of molecular compounds in a two-dimensional space.^[179] The van Krevelen diagrams of the four investigated Maillard model systems show an extraordinary high molecular diversity in produced MRPs (Figure 3.2). Primarily, the amino acid precursor is responsible for the individual characteristics of the detected MRPs. By comparison, when six different sugars were heated together with glycine for 24 h, the element compositions were very similar among the different sugars (Figure C.3 in Appendix Chapter 3). Different sugar precursors mainly revealed differences in the number of produced MRPs (ribose > arabinose > fructose \approx xylose > galactose > glucose) but no substantial differences in their characteristic positions in the van Krevelen diagrams could be observed. Specifically, the sugar reactivity order can be attributed to a combination of factors, such as the proportion of free carbonyls in the sugar precursor^[226,227] and faster reaction rates of pentoses than hexoses.^[228]

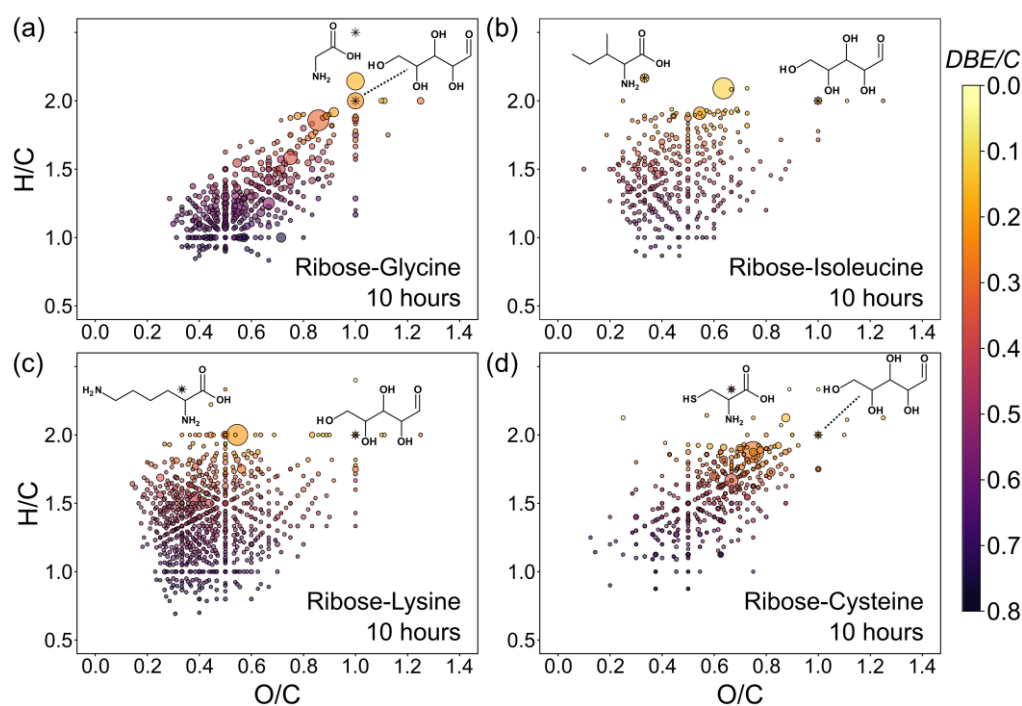


Figure 3.2 | Compositional characterization of MRPs. (a-d) Van Krevelen diagrams (H/C vs. O/C atomic ratios) of four ribose-amino acid model systems heated for ten hours at 100 °C. Scaling of points is according to their relative peak intensity in the mass spectra. Color gradient according to the degree in unsaturation (number of double bond equivalents per carbon atom (DBE/C)).

Interestingly, when comparing the molecular formulae of all four ribose-amino acid model systems, there was no single molecular formula that was common to all four samples among the >1 000 MRPs identified. This demonstrates how difficult it is to find general Maillard reaction markers, which are independent of the amino acid and sugar precursors. It is worth noting, that ESI(-) analysis mainly targets oxygen-rich and polar MRPs of the initial and intermediate phase. In later stages of the MR an increasing similarity in chemical structures, *e.g.* after Strecker degradation can be expected. By comparison, molecular formulae retrieved for the different sugar-glycine model systems showed more similarity. After 24 h, 88%, 95%, 75%, and 78% of all observed MRPs in the arabinose- and xylose-, galactose-, and fructose-glycine mixtures were also found in the ribose-glycine mixture, respectively. Only the glucose-glycine model showed a smaller number of common formulae (45%) which is mainly because of the lower reactivity of glucose (Figure C.3 in Appendix Chapter 3). After 24 h we observed only a few initial MRPs formed in the glucose-glycine model. A longer reaction time might be required to initiate fragmentation of the sugar backbone and may increase the molecular formulae intersect. Although chemical information obtained from direct-infusion FT-ICR-MS is restricted to accurate molecular formulae, the high proportion of common formulae between the different sugar systems indicates that different sugar precursors react to form similar or even identical MRPs. The many cleavage reactions might easily convert hexose-derived MRPs into smaller derivatives, which can also be formed directly from smaller carbohydrate precursors.

Compared to the glycine and cysteine mixtures, isoleucine and lysine showed a large number of MRPs with high H/C and low O/C ratios (aliphatic area, Figure 3.2). The aliphatic parts of the side chains of isoleucine and lysine are mainly responsible for these specific molecular characteristics. However, the van Krevelen diagrams do not show a shift of all produced MRPs of the isoleucine and lysine models towards higher aliphaticity. We rather found a widespread distribution of MRPs over a large part of the van Krevelen space including also many unsaturated compounds (low H/C and O/C ratios, high DBE/C) similar to the MRPs produced in the ribose-glycine model system. Compounds with such low H/C ratios cannot contain original or intact lysine or isoleucine residues. More precisely, they must be produced either (i) by elimination of the amino acid side chain in one step of the reaction cascade, or (ii) by Maillard-type condensations of small amine intermediates with carbonyls. Indeed, 90% of the detected lysine-MRPs containing only one nitrogen atom showed H/C and O/C ratios not exceeding 1.5 and 0.6, respectively. Consequently, a part of the amino acid's side chain must have been eliminated during the reaction. Enaminols and amino ketones formed during the Strecker degradation (Scheme C.1 in Appendix Chapter 3) could be an important class of compounds, which contain less aliphatic parts than the original

amino acid and hence, would fit in the van Krevelen space of such low H/C and O/C ratios.

Fundamentally, the contribution of MRPs of higher unsaturation increases with reaction time in all four model systems (Figure 3.3a). However, glycine showed the highest tendency to form unsaturated compounds, followed by isoleucine and lysine. Cysteine showed only a very slow decrease in H/C and O/C ratios over time (Figure 3.3a). This could be due to a much faster degradation of the ribose-glycine ARP. After ten hours, the relative intensities of the glycine-ARP decreased by 66% compared to the relative intensity observed after two hours. The degradation rates for the ARPs formed by the other amino acids were significantly lower (Figure 3.3a). Extrapolation of the regression lines in Figure 3.3a would lead to an intersection in an area of low H/C and O/C atomic ratios. There, highly unsaturated compounds, such as heterocycles like furfural, pyrazine, or pyrrole derivatives are found. Although these compounds are not detectable by ESI(-) the intersection represents an area where final products of the Maillard reaction (volatiles and polymer-type melanoidins) can be expected, including common MRPs, which can be produced by various amino acids. For example, Strecker degraded amino acids have been shown in the reaction with carbonyls to produce common pyrazine derivatives.^[92,229]

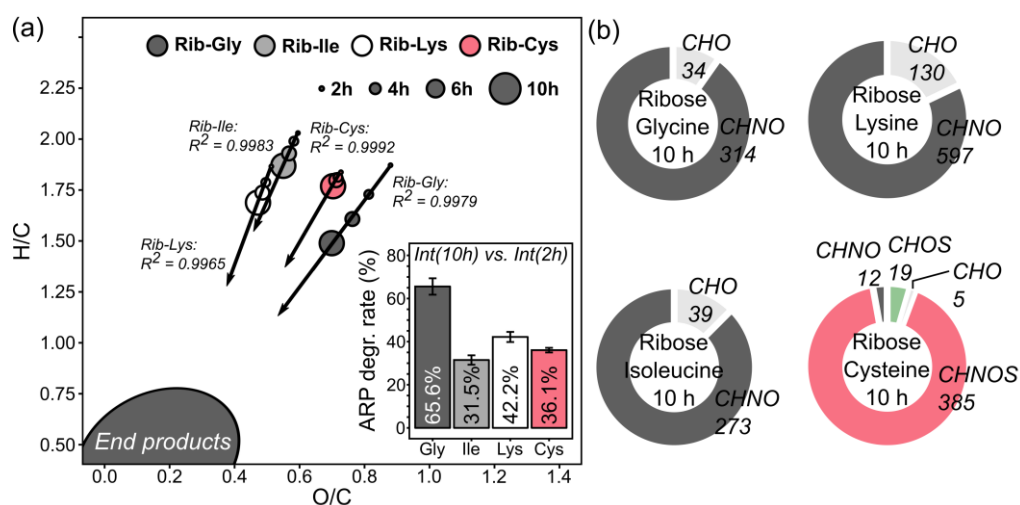


Figure 3.3 | Changes in unsaturation over time and characteristics of compositional spaces. (a) Progression of H/C and O/C atomic ratios over time for ribose-glycine (dark grey), ribose-isoleucine (grey), ribose-lysine (white) and ribose-cysteine (red) MRPs. Points represent intensity weighted mean values of the H/C and O/C ratios, respectively. Linear regression lines visualize the direction of MRPs moving with increasing reaction time. (b) Absolute number of MRPs depicted for different chemical spaces.

We further divided and characterized the MRPs by their compositional spaces (Figure 3.3b). Based on the amino acid precursor, glycine, isoleucine, and lysine can only produce MRPs containing carbon, hydrogen, oxygen, and nitrogen, thus compounds of the CHO and CHNO space. On the contrary, cysteine can additionally produce sulfur-containing MRPs (CHOS and CHNOS space). After ten hours, 89% of all detected MRPs (1 268/1 431) contained at least one nitrogen atom (CHNO or CHNOS space, Figure 3.3b). Most of the N-containing MRPs in the cysteine Maillard reaction also contained sulfur. Only 12 sulfur-free but nitrogen containing MRPs could be identified contributing < 1% to the total peak intensity. Thus, release of the cysteine side chain (*e.g.* by Strecker degradation) seems to have less impact than side chain elimination for example in the lysine Maillard reaction. We found 346 different molecular formulae in the ribose-lysine MR, accounting for 20% of the relative peak intensity, containing an odd number of nitrogen atoms (Figure C.4 in Appendix Chapter 3) indicating fragmentation of the amino acid in any step of the reaction progress. We also noticed significant differences in produced nitrogen-free (CHO) compounds among the four model systems (Figure 3.3b). The number of different CHO-compounds was 34, 39, 130, and 5 for glycine, isoleucine, lysine, and cysteine, respectively. This again demonstrates the strong ability of cysteine to trap free carbonyl compounds.

3.3.4 General Maillard reaction scheme

Next, we analyzed the MRPs based on their carbon backbone (Figure 3.4). We found for all model systems highest intensities for the carbon chain lengths which result from the reaction of one molecule of ribose with one molecule of amino acid (glycine: C₇, isoleucine/lysine: C₁₁, and cysteine: C₈) indicating that the formation and direct degradation pathway of the ARP contributes most to the formation of MRPs. Furthermore, much higher intensity contributions, divergent from an assumed normal distribution, were found for several carbon chain lengths: the reaction of two molecules of ribose with one amino acid molecule (glycine: C₁₂, isoleucine/lysine: C₁₆, and cysteine: C₁₃) accounted for 16% to the total ribose-glycine MR intensity. Additionally, we found higher intensities for ribose + amino acid + C₂ (or 2 ribose + amino acid - C₃) in the glycine, isoleucine, and lysine models (Figure 3.4a-c) as well as for ribose + amino acid + C₃ (or 2 ribose + amino acid - C₂) in the ribose-cysteine model (Figure 3.4d). The latter observation revealed that approx. half of the produced MRPs with C₁₁ contained two nitrogen atoms. In the other model systems (glycine, isoleucine, and lysine), MRPs resulting from the reaction of one molecule ribose with two molecules of amino acid did not contribute significantly to the total intensity. We

assume that the C_{11} reaction products containing two nitrogen atoms found in the cysteine model arise from the reaction of earlier formed cystine and ribose or the oxidation of C_8 -MRPs with another molecule of cysteine under formation of a disulfide link. This also explains the higher intensity contribution found for C_{16} in the ribose-cysteine samples.

Most of the MRPs bearing the discussed carbon chain lengths turned out to follow identical reactivity patterns and have compositional similarities. All MRPs, which were found in at least three out of the four model systems, heated for ten hours, followed identical reactivity rules and had the same core composition, are summarized in Figure 3.5 (see also Table C.1-Table C.4 in Appendix Chapter 3). We found more than 70 different molecular compositions (molecular formulae) which only differ in the amino acid side chain. In sum, they explained 45%, 73%, 55%, and 46% of the total peak intensity found for the ribose-glycine, -isoleucine, -lysine, and -cysteine MRPs, respectively. The candidates can be further subdivided into four pathways of similar assembly. First, the reaction between one molecule of ribose and an amino acid molecule builds the Amadori product formation and degradation scheme (Figure 3.5a). The ARP then may react with a second molecule of ribose leading to highly reactive diketosamines (Figure 3.5b). Diketosamines, such as *N,N*-bis(1-deoxy-D-erythro-2-pentulos-1-yl)-glycine, are assumed to decompose much faster than the initial ARP^[201] and may thereby subsequently undergo C_2 - and C_3 -cleavage reactions (Figure 3.5c-d).

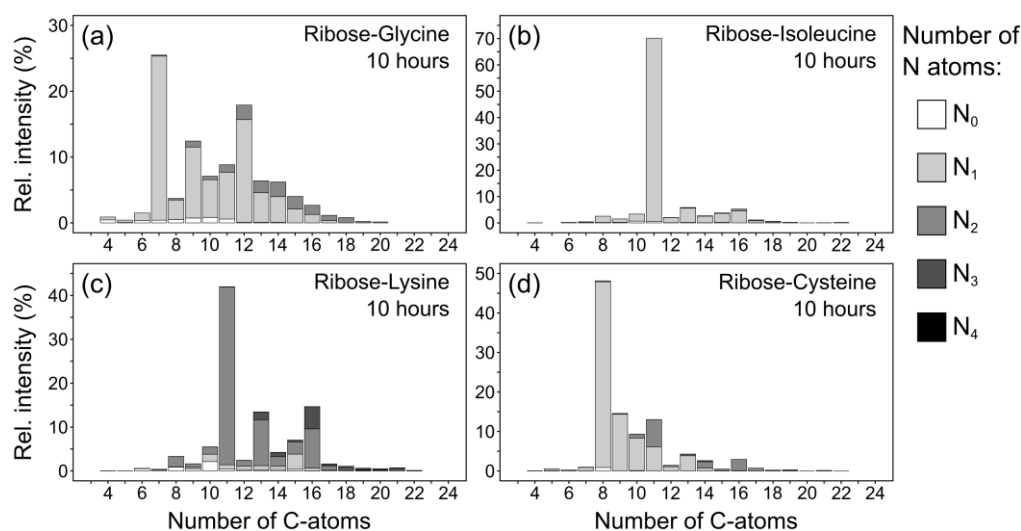


Figure 3.4 | Number of carbon atoms in MRPs. Relative peak intensities classified by the number of carbon atoms of thermally synthesized (10 h, 100 °C) (a) ribose-glycine, (b) ribose-isoleucine, (c) ribose-lysine, and (d) ribose-cysteine MRPs.

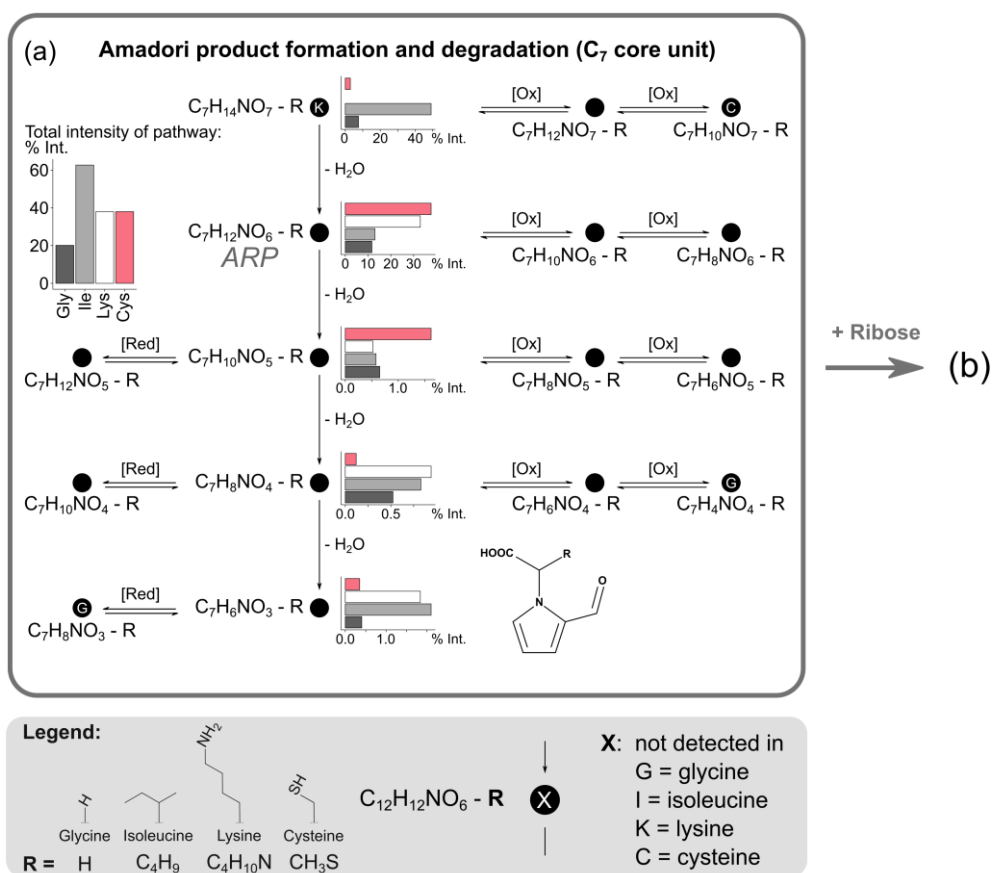


Figure 3.5 | General Maillard reaction product formation and degradation pathways. Maillard reaction products with identical element core compositions detected (S/N ratio ≥ 8) in at least three of the four investigated Maillard model systems revealed identical reaction behavior following a well-defined series of dehydration and redox reactions. The scheme could be subdivided into four pathways of similar assembly: (a) ARP formation and degradation, (b) diketosamine degradation, (c-d) C2- and C3-cleavage. Molecular formulae shown have the same core composition but differ in the amino acid residues (-R). Embedded bar charts illustrate the relative peak intensity contributions after ten hours.

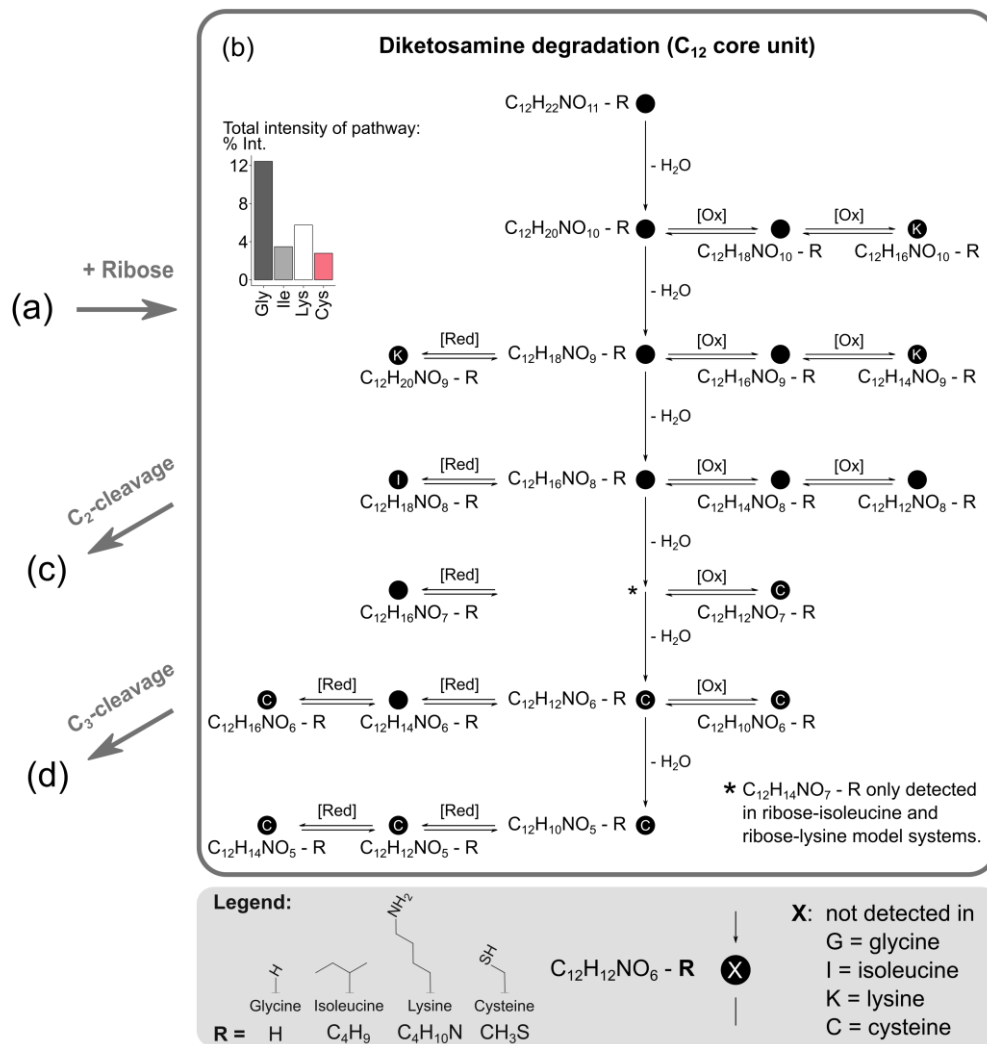


Figure 3.5 (continued) | General Maillard reaction product formation and degradation pathways. Maillard reaction products with identical element core compositions detected (S/N ratio ≥ 8) in at least three of the four investigated Maillard model systems revealed identical reaction behavior following a well-defined series of dehydration and redox reactions. The scheme could be sub-divided into four pathways of similar assembly: (a) ARP formation and degradation, (b) diketosamine degradation, (c-d) C_2 - and C_3 -cleavage. Molecular formulae shown have the same core composition but differ in the amino acid residues (-R). Embedded bar charts illustrate the relative peak intensity contributions after ten hours.

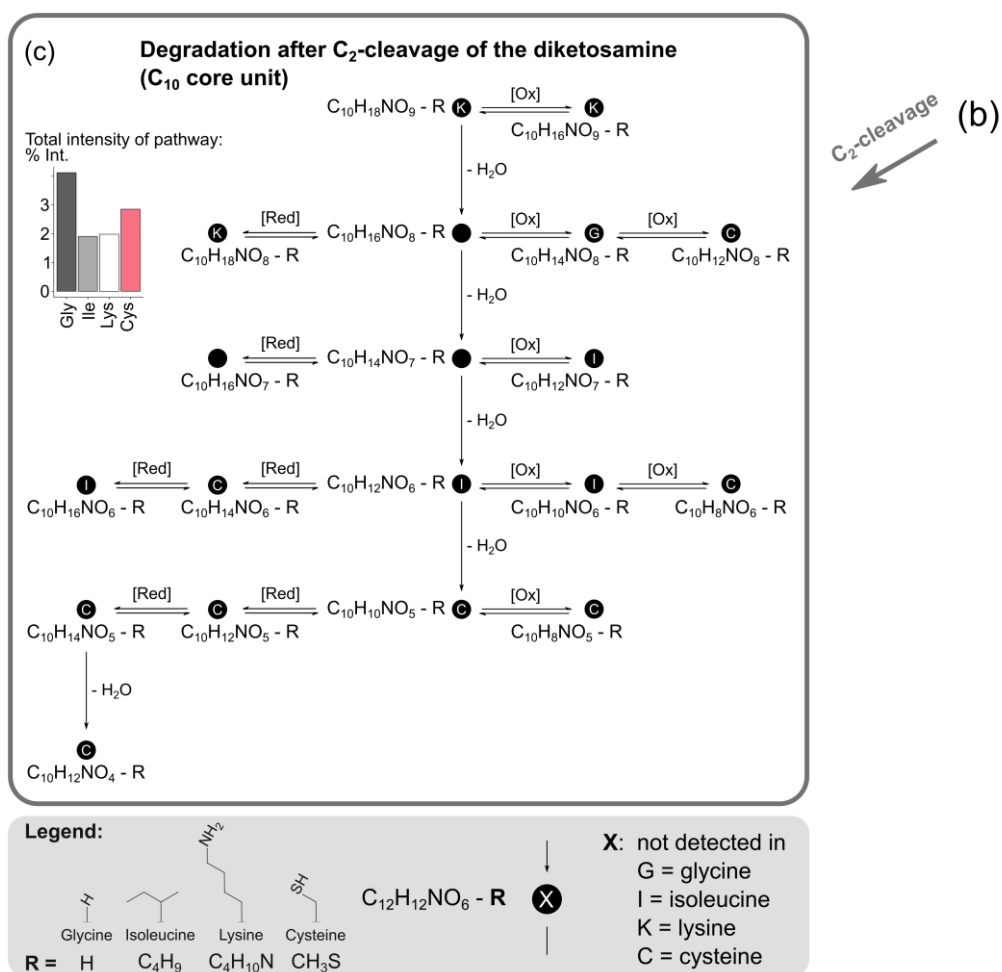


Figure 3.5 (continued) | General Maillard reaction product formation and degradation pathways. Maillard reaction products with identical element core compositions detected (S/N ratio ≥ 8) in at least three of the four investigated Maillard model systems revealed identical reaction behavior following a well-defined series of dehydration and redox reactions. The scheme could be sub-divided into four pathways of similar assembly: (a) ARP formation and degradation, (b) diketosamine degradation, (c-d) C₂- and C₃-cleavage. Molecular formulae shown have the same core composition but differ in the amino acid residues (-R). Embedded bar charts illustrate the relative peak intensity contributions after ten hours.

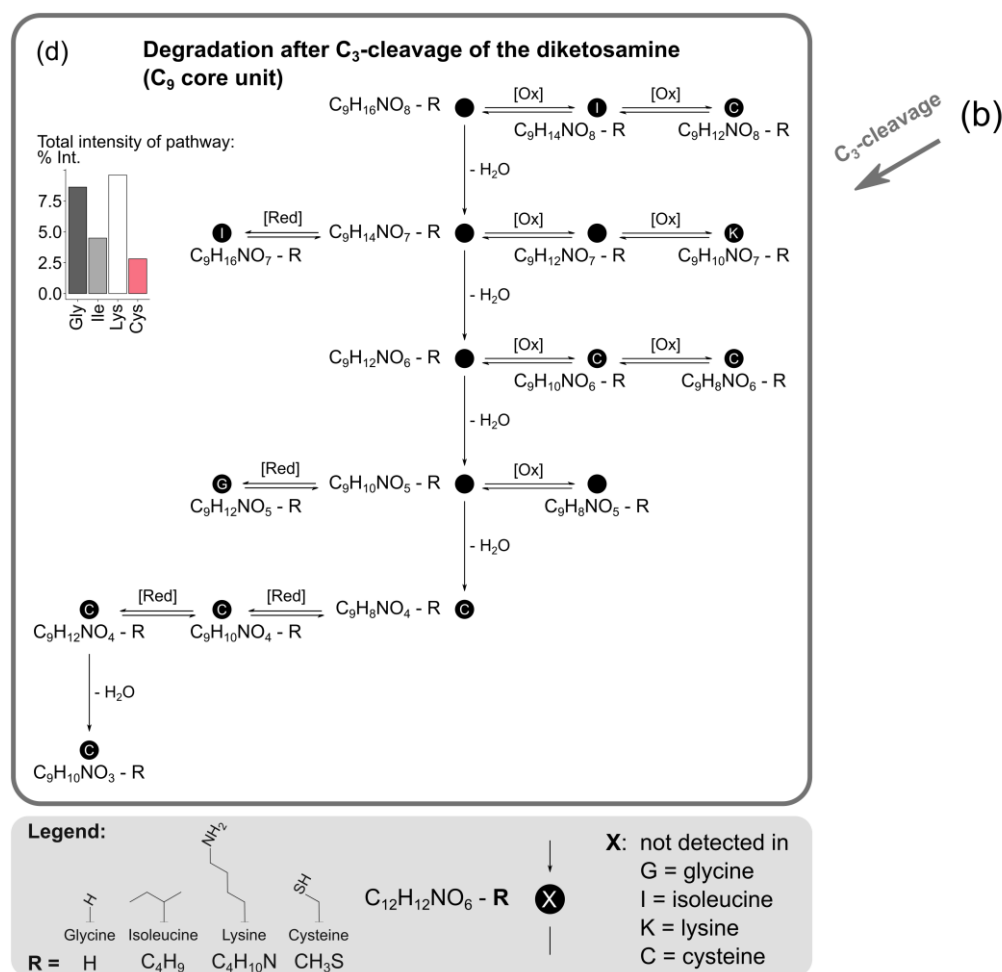


Figure 3.5 (continued) | General Maillard reaction product formation and degradation pathways. Maillard reaction products with identical element core compositions detected (S/N ratio ≥ 8) in at least three of the four investigated Maillard model systems revealed identical reaction behavior following a well-defined series of dehydration and redox reactions. The scheme could be sub-divided into four pathways of similar assembly: (a) ARP formation and degradation, (b) diketosamine degradation, (c-d) C2- and C3-cleavage. Molecular formulae shown have the same core composition but differ in the amino acid residues (-R). Embedded bar charts illustrate the relative peak intensity contributions after ten hours.

Each of the reaction schemes in Figure 3.5 comprises of a series of dehydration reactions. Additionally, several redox reactions may arise from the dehydrated intermediates. Carbonyls produced during dehydration can rapidly interconvert to enaminol and endiol structures which are known to undergo reversible redox behavior.^[230] As for most of the intermediates in the dehydration series, both reduced and oxidized compounds were found; it is very likely, that behind each of the 73 “general” MR compounds several different chemical isomers are conceivable. Although the relative intensities of the oxidized and reduced MRPs were always lower

than those depicted as dehydration products, it is possible that oxidation products especially, act as important intermediates in the dehydration process. Oxidation of hydroxyl groups could lead to carbonyls acting as targets for intramolecular nucleophilic additions with subsequent dehydration, finally, increasing the dehydration reaction rates.

ARP formation and degradation scheme (Figure 3.5a): With exception of the isoleucine-ARP, all ARPs were observed as base peaks in the respective mass spectra. With increasing reaction time, we observed up to three ARP-dehydration products. Relative intensities of the ARP-dehydration products decreased with increasing dehydration progress. However, intensities of the ARP-3-H₂O were again higher than for the ARP-2-H₂O indicating a more stable molecule such as the substituted 2-formyl-1-pyrrole-1-acetate as shown in Figure 3.5a. 2-Formyl-1-pyrrole-1-acetate derivatives could be isolated when xylose was heated with glycine^[231] and isoleucine.^[17] Higher relative peak intensities (>30%) were observed for the cysteine- and lysine-ARPs as compared to the glycine- and isoleucine-ARPs. This shows that the initial condensation rates of cysteine and lysine are, due to the reactive side chain, higher than for glycine and isoleucine which is in agreement with the findings of Munch *et al.*^[217]

Diketosamine degradation scheme (Figure 3.5b): While ribose-glycine MRPs accounted for only 20% of the total intensity in the Amadori degradation pathway MRPs in the diketosamine degradation scheme were found to explain up to three times more of the total intensity than the other amino acids. This could be due to steric hindrance caused by the bulky isoleucine residue or intramolecular cyclization through the nucleophilic lysine and cysteine residues hindering further carbonyl condensation. The starting point of the diketosamine degradation pathway results from the addition of the ARP (C₇H₁₂NO₆-R) to a second ribose molecule. In total, we found six possible dehydration products which could arise from this initial addition reaction. However, the structural variety of molecules is expected to be even higher than in the Amadori degradation pathway. Several combining possibilities exist which could lead to stable molecules involved in this pathway. It is worth noting, that there is no evidence for a complete series of successive dehydration events actually taking place. The pathways must rather be understood as a conceptual summary of dominating and regular patterns we observed between the identified molecular formulae. For instance, it is also conceivable that the last dehydration product in Figure 3.5b (C₁₂H₁₀NO₅-R) results from a condensation reaction between the substituted 2-formyl-1-pyrrole-1-acetate (C₇H₆NO₃-R in Figure 3.5a) and norfuranol as shown by Ledl and Severin.^[231]

C₂- and C₃- cleavage schemes (Figure 3.5c-d): The C₂- and C₃-cleavage pathways arise most likely from α - and β -dicarbonyl cleavage of intermediates from the diketosamine degradation pathway (Figure 3.5b). Different cleavage mechanisms can be taken into account to explain the resulting molecular compositions of the pathways in Figure 3.5c-d, such as retro-aldolization^[26] or many other putative or proven (di)carbonyl cleavage mechanisms. For example, in a C₂-cleavage reaction, C₂H₄O₂, acetic or glycolic acid could be possible by-products. For glycine, isoleucine, and lysine C₃-cleavage reactions seem to be preferred relative to C₂-cleavage, which is exemplified by the higher peak intensities. By comparison, cysteine derived MRPs showed similar or slightly higher intensities explained by the C₂-pathway. Interestingly, late dehydration products and the linked oxidized and reduced MRPs in Figure 3.5b-d could not be detected in the ribose-cysteine samples indicating a different reactivity of cysteine MRPs in the final steps of the chemical pathways. Cysteine is known to react somewhat differently compared to other amino acids. It can be assumed that the strong ability of the cysteine side chain to undergo redox reactions is in competition with redox activities on the carbohydrate backbone. This can explain lower intensities of ribose-cysteine MRPs and the different reactivity particularly in steps involving oxidation or reducing steps.

3.4 Conclusions

In the present fundamental study, we showed that non-volatile initial and intermediate MRPs can be comprehensively analyzed using direct-infusion FT-ICR-MS, hence, bypassing the restricted selectivity of LC-based methods and finally delivering accurate molecular formulae for the entire reaction products. Here, we mainly compared four ribose-amino acid Maillard model systems using amino acids with very different side chains (glycine, isoleucine, lysine, and cysteine). Depending on the amino acid precursor, we observed wide disparity in the absolute number and compositional characteristics of produced MRPs. The order of reactivity we found after heating the model systems for ten hours at 100 °C was: ribose-lysine > -cysteine > -isoleucine \approx -glycine. While the amino acid precursors are responsible for the molecular characteristics of MRPs, sugar precursors drive the reaction rates. Even though cysteine is often considered as relatively unreactive in the Maillard reaction, surprisingly, it produced more than 400 distinct MRPs. Many of those MRPs are apparently produced through condensation reactions between the nucleophilic thiol residue and carbonyls as well as oxidative formation of disulfide links resulting

in reaction products, which, in this way, cannot be produced by any other proteinogenic amino acid. Further studies in a more complex environment, such as mixtures of several amino acids or protein hydrolysates, may help to better understand the particular role of cysteine derived MRPs and the ability of thiols to effectively suppress browning.

Although we could not detect a single molecular formula, apart from ribose degradation products, which was found in all four model systems, more than 70 MRPs were identified that followed similar reactivity behavior. These “general” MRPs have identical element core compositions differing only in the amino acid side chain and could be further classified into Amadori product degradation, diketosamine degradation and two different carbonyl cleavage pathways. To date, little is known about the role of diketosamines in the MR. However, based on our findings, we can conclude that the early formation and subsequent degradation of diketosamines contribute to a large extent to the overall MRPs. Mechanistic studies should be performed in order to fully understand exact reaction routes and rates between the MRPs in the proposed degradation pathways. Furthermore, it is yet unclear whether other reaction conditions (*e.g.* pH, temperature, water content), which are relevant under physiological conditions or in food samples, would lead to similar ARP degradation behavior. Hence, further studies are required, which specifically investigate the formation of MRPs under the reaction conditions of interest.

Chapter 4 |

Sunlight Selectively Modifies Maillard Reaction Products in a Wide Array of Chemical Reactions

We report the photochemical transformation of Maillard reaction products (MRPs) under simulated sunlight into mostly unexplored photoproducts. Non-enzymatic glycation of amino acids leads to a heterogeneous class of intermediates with extreme chemical diversity, which is of particular relevance in processed and stored food products as well as in diabetic and age-related protein damage. We here reacted three amino acids (lysine, arginine, and histidine) with ribose at 100 °C for ten hours. Exposing these model systems to simulated sunlight led to a fast decay of MRPs. We studied the photo-degradation of MRPs and the formation of new compounds by fluorescence spectroscopy and non-targeted (ultra)high-resolution mass spectrometry. Photoreactions showed strong selectivity towards the degradation of electron-rich aromatic heterocycles, such as pyrroles and pyrimidines. Our data show that oxidative cleavage mechanisms dominate the formation of photoproducts. The photochemical transformations differed fundamentally from “traditional” thermal Maillard reactions and indicated a high amino acid specificity.

This chapter has been published as [Hemmler, D.](#), Gonsior, M., Powers, L. C., Marshall, J. W., Rychlik, M., Taylor, A. J. & Schmitt-Kopplin, P. Simulated Sunlight Selectively Modifies Maillard Reaction Products in a Wide Array of Chemical Reactions. *Chemistry – A European Journal* **25**, 13208–13217 (2019).

Reprint permitted under the Creative Commons Attribution 4.0 International License (CC BY 4.0; <http://creativecommons.org/licenses/by/4.0/>).

Candidate’s contributions: D.H. designed the research. D.H. performed the experiments and analyzed the data. D.H. prepared the figures. D.H. wrote and revised the manuscript.

4.1 Introduction

Non-enzymatic browning reactions have been of great interest in food science and health. In food products, reactions between amino acids and carbonyl moieties (Maillard reaction, MR) are the main contributors to flavor and color formation.^[2,40] Under physiological conditions, non-enzymatic glycation leads to irreversible protein damage (by formation of advanced glycation end products (AGEs)), associated with a wide range of diseases.^[204] Non-enzymatic browning leads to a heterogeneous class of compounds including chromophores and fluorophores that absorb and fluoresce in the ultraviolet (UV) and visible (Vis) spectral range. Aromatic and often heterocyclic colored compounds are formed mainly in the final phase of the MR by a series of condensation reactions, many of which are only partly understood.^[67,152,232]

During their shelf life, food products are often unavoidably exposed to sunlight. In a similar way, AGEs, *e.g.* in eye lenses or skin, continuously experience solar exposure. Chromophores formed as part of the advanced glycation have been suggested as possible photosensitizers producing reactive oxygen species (ROS), which lead to age-related protein photodamage. Major targets for photooxidation reactions in proteins are aromatic amino acids (tryptophan (Trp), tyrosine (Tyr), and phenylalanine (Phe)) as well as histidine (His), cysteine (Cys) and methionine (Met) residues.^[233] The amino acids lysine and arginine, which are of greatest relevance in non-enzymatic glycation reactions on proteins, do not show significant absorption at >230 nm^[234] and photooxidation on these amino acids has only been observed at high pH values for their unprotonated species.^[235] Increased levels of AGE photosensitizers have been found in aged and diabetic lenses^[236,237] as well as on long-lived skin proteins.^[238] It is well accepted that the predominating mechanism involves the AGE sensitized formation of ROS, such as singlet oxygen ($^1\text{O}_2$), superoxide anion radicals ($\cdot\text{O}_2^-$) and hydroxyl radicals ($\cdot\text{OH}$).^[239-241] Further, Wondrak and co-workers showed that AGEs can act as photosensitizers to DNA damage. Besides reactions of ROS, they also proposed other photosensitization reactions involved in phototoxicity mechanisms.^[242]

Because of the chemical nature of reducing sugars, the initial condensation with amine compounds and subsequent downstream reactions lead to a wide range of compounds with carbonyl functional groups, including dicarbonyl moieties and α -hydroxy ketones.^[40,243] When irradiated with UV-B light, carbonyl functional groups can form acyl radicals in aqueous solutions, predominantly by Norrish-type-I photofragmentation reactions.^[244-246] The α -cleavage and subsequent decarbonylation is about an order of magnitude faster for α -hydroxy ketones compared to their alkyl counterparts.^[245] Although the nature of compound classes formed during the MR

suggests a strong photochemical reactivity, to date, the effect of solar radiation on the direct chemical alteration of MRPs is only partially explored. Bohart and Carson were the first to report decolorization in glucose-glycine Maillard model systems when they were exposed to illumination under oxygen in the laboratory.^[247] Later, Kessel and co-workers showed that UV-A radiation readily degrades purified argpyrimidine.^[248]

Here we report photochemical effects on MRPs using holistic non-targeted analysis. More precisely, we exposed reaction products, initially formed by heating different amino acid-ribose mixtures at 100 °C for ten hours, to a simulated solar spectrum. Chemical changes were analyzed by optical spectroscopy and (ultra)high resolution mass spectrometry. We focus on three different amino acids (lysine, arginine, and histidine), the MRPs of which provide abundant chromophores. While lysine and arginine are the main contributors to non-enzymatic glycation reactions in foods and on proteins under physiological conditions, histidine is among the major protein residues for ROS driven cellular photodamage. Ribose has been chosen because of its high reactivity, readily leading to a large number of MRPs upon thermal processing.

4.2 Experimental procedures

4.2.1 Chemicals and reagents

L-Arginine ($\geq 98\%$), L-asparagine ($>99\%$), L-histidine (98%), L-lysine ($>98\%$), and D-(-)-ribose (98%) were purchased from Sigma-Aldrich (Steinheim, Germany). Urea (100%) was obtained from Beckmann Coulter (Krefeld, Germany). LC-MS grade methanol and acetonitrile were purchased from Merck (Darmstadt, Germany). Formic acid (LC-MS grade) and ammonium formate (10 M stock solution) were obtained from Sigma-Aldrich (Steinheim, Germany). MilliQ-purified water (18.2 M Ω ; Millipore, Germany) was used throughout the experiments.

4.2.2 Maillard model systems

Equimolar mixtures of ribose and amino acids (0.1 mol L⁻¹ respectively) were prepared in MilliQ-purified water. 1 mL of each mixture was heated in closed glass vials as recently described at 100 °C for ten hours.^[211] Model systems were stored at -20 °C until usage.

4.2.3 Irradiation experiments

All Maillard model systems were diluted 1:800 (v/v) with MilliQ-purified water prior to irradiation. Aliquots of the model systems were irradiated in a custom-built photolysis system, as described in detail elsewhere.^[249,250] Irradiation experiments were performed for 20 h with a 1 000 W Xe arc lamp equipped with an air mass filter (AM 1.5). Before each irradiation experiment, the lamp intensity was controlled to ensure that the irradiated sample receives a radiation dose, which is equivalent to the sun at Earth's surface (45° north, midsummer, at noon). The temperature was controlled at 25 °C using Peltier units and a circulating water bath. The pH value was monitored throughout the irradiation process (Table D.1 in Appendix Chapter 4).

For subsequent Fourier transform ion cyclotron resonance mass spectrometry (FT-ICR-MS) and liquid chromatography-mass spectrometry (LC-MS/MS) experiments, larger sample amounts were irradiated, with the same dilution as above (1:800 (v/v)), in quartz vessels in a Suntest CPS system (Heraeus, Hanau, Germany) equipped with an NXE xenon lamp (Atlas Material Testing Technology, Gelnhausen, Germany) for four and eight hours. The temperature was maintained at 25 °C using an air conditioning unit and the pH was recorded before and after irradiation (Table D.2 in Appendix Chapter 4), respectively. Additionally, control samples in lightproof vessels were placed under the xenon lamp. All samples were irradiated in two independent experiments (n = 2).

4.2.4 Excitation emission matrix fluorescence

Online EEM measurements during the irradiation were performed every 20 min using a 4 × 10 mm flow cell and an Aqualog spectrofluorometer (Horiba Instruments, New Jersey, USA). Excitation ranged from 230 to 600 nm and emission was recorded between 211 to 617 nm. All fluorescence spectra were corrected for scatter and inner filter effects. Normalization to a 1 mg L⁻¹ quinine sulfate standard (Starna reference material RM-QS00, 1.28 × 10⁻⁶ mol L⁻¹) was used to express all fluorescence intensities in quinine sulfate units (ppm). Independently for each irradiated model system, Parallel factor analysis (PARAFAC) models were built using the drEEM toolbox for MATLAB.^[251] The data best fitted four-component PARAFAC models, which were split-half validated, explaining 99.8%, 99.8%, and 99.7% of the spectral variance in the ribose-lysine, -arginine, and -histidine model system, respectively.

4.2.5 FT-ICR-MS analysis

All irradiated Maillard model systems were further diluted with methanol to achieve a final dilution of 1:2 500 (v/v) immediately prior to FT-ICR-MS analysis. Each sample was analyzed in three independent injections ($n = 2 \times 3 = 6$ MS measurements). Direct-infusion FT-ICR mass spectra were acquired with a 12 T Bruker Solarix mass spectrometer (Bruker Daltonics, Bremen, Germany). Samples were infused with a flow rate of $2 \mu\text{L min}^{-1}$ into an APOLLO II electrospray source operated in negative ionization mode. Ion source settings and spectra calibration were the same as recently described.^[211] Spectra were acquired with a time-domain of 4 megawords and 300 scans were accumulated within a mass range of m/z 123 to 1 000.

Peaks with a signal-to-noise ratio of at least eight were exported to mass lists. Data prefiltering was used to remove FT artifacts,^[177] features with unusual mass defects and ^{13}C isotope signals. Peaks were then aligned into a matrix containing averaged m/z -values and corresponding peak intensities allowing a maximum alignment window of 1 ppm.^[197] Only those m/z -values were retained in the matrix, which were reproducibly found in all three replicate injections of at least one sample. Zero values in the matrix then were replaced by the recorded absolute intensity values found in the raw spectra at that m/z -value, respectively. Finally, molecular formulae were computed for all averaged m/z -values as recently described.^[252]

4.2.6 Tandem HILIC-RP LC-MS/MS

16 mL aliquots of the irradiated samples were lyophilized until dryness and immediately reconstituted in 200 μL of an aqueous solution containing 2% acetonitrile prior to LC-MS/MS analysis. Instrumental setup and chromatographic conditions were the same as recently described.^[189] Each sample was injected and analyzed in triplicate. The MS data were recorded with a high resolution Bruker maXis qTOF-MS equipped with an APOLLO II electrospray ion source (Bruker Daltonics, Bremen, Germany), which was operated in electrospray positive mode to achieve maximum compound coverage.^[189] Precursor and product ion scans were recorded in a mass range from m/z 50 – 1 500 with a scanning rate of 5 Hz. For data-dependent fragmentation, after each precursor scan, the two most abundant precursors were isolated and subjected to collision induced fragmentation. Maximum coverage of MS/MS data was achieved by excluding precursor masses from fragmentation after three successful MS/MS spectra for five minutes. The collision energy was set to 35 eV. All mass spectra were internally calibrated by infusing a tuning mix solution (Agilent Technologies, Waldbronn, Germany) prior to each chromatographic run.

Raw data were post-processed using the XCMS R package (version 3.2.0).^[253] Chromatographic features were detected by the *centWave* algorithm^[254] using an expected approximate peak width in the range from 10 – 80 s and a maximum tolerated *m/z* deviation of 10 ppm. Retention time alignment was done with the *Orbiwarp* algorithm^[255] as integrated in XCMS. Peaks within and between samples then were grouped into chromatographic features (retention time–*m/z*-pairs) based on time dimension densities.^[253] In the obtained matrix, only those features were retained, which were reproducibly detected in all three replicate injections of at least one sample.

4.2.7 Data analysis

All further statistical analysis and filtering was done in R Statistical Language and Microsoft Excel 2016. All p-values were calculated based on heteroscedastic Student's t-Tests. The number of double bond equivalents per carbon atom (DBE/C) and average carbon oxidation state (OS_c) was computed as recently described.^[211,252]

4.3 Results and discussion

4.3.1 Effect of simulated solar irradiation on absorption and fluorescent properties of MRPs

Excitation emission matrix measurements of MRPs and during photo-degradation experiments. After an induction period, heating reducing sugars in the presence of amino acids leads to the formation of chromophores and fluorophores.^[256] Among the proteinogenic amino acids, especially those with basic functional side chains show significant color formation in unbuffered solutions while not being affected by amino acid autofluorescence.^[257] After heating three different model systems (ribose-lysine, ribose-arginine, and ribose-histidine) for ten hours at 100 °C excitation-emission-matrices (EEM) were constructed from fluorescence measurements (Figure 4.1a-c). Fluorescence intensities and excitation/emission wavelengths strongly depended on the amino acid precursor. Interestingly, ribose-histidine showed the most complex fluorescence behavior with at least two major emitting regions indicating multiple chemical structures and moieties participating in the overall fluorescence behavior. In the ribose-lysine and -arginine model systems we observed dominating fluorescence peaks with emission maxima at 440 nm

(excitation: ≤ 245 nm and 350 nm) and 400 nm (excitation: ≤ 245 nm and 320 nm), respectively. Only a few fluorescent MRPs have been previously fully characterized. Most of them were isolated from model systems containing the amino acids lysine and arginine.^[258] Many of the studied fluorescent MRPs are involved in the crosslinking of proteins and are used as important markers in the formation of AGEs. Pentodilysine (LM-1), a fluorescent molecule cross-linking lysine residues, has excitation/emission wavelengths that would match the dominating fluorescence peak in the ribose-lysine model-system (Figure 4.1a).^[259,260] In a similar way, argpyrimidine shows excitation/emission corresponding to the major peak found in the ribose-arginine model system (Figure 4.1b).^[151] While pentodilysine can be formed directly from ribose and lysine, argpyrimidine is formed from arginine and methylglyoxal.^[151,260] Fluorophores formed in the Maillard reaction by other amino acids than lysine and arginine have received only minor attention^[258] even though some studies support that fluorescent MRPs may be related to the formation of brown pigments.^[257]

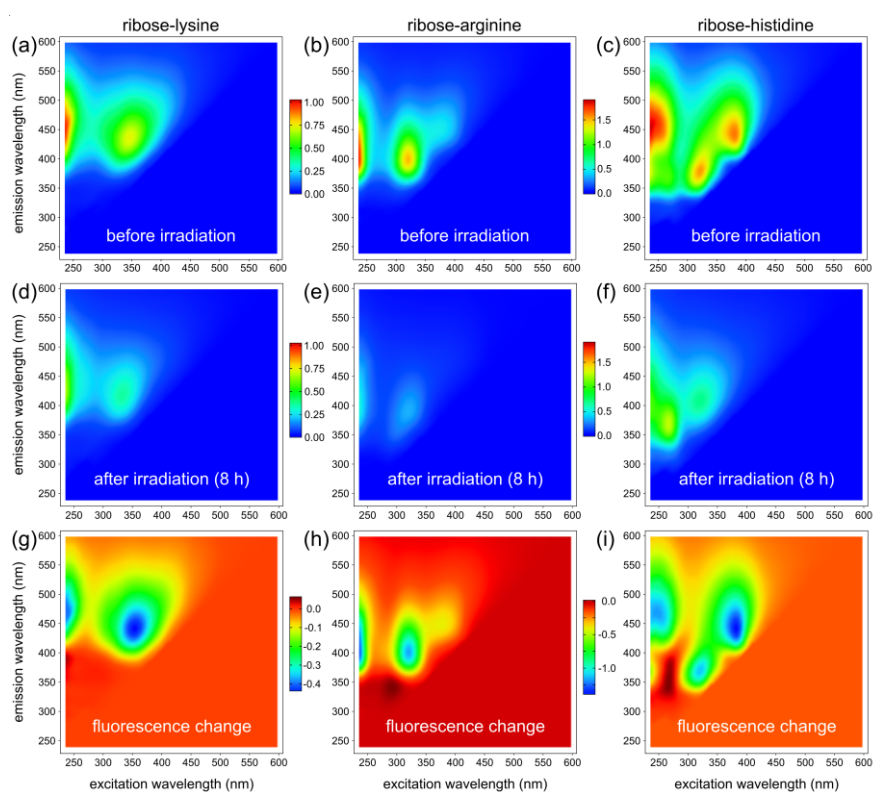


Figure 4.1 | Photolytic degradation of MRPs in three model systems (ribose-lysine, -arginine, and -histidine) heated for ten hours at 100 °C. Excitation-emission-matrices retrieved from diluted model systems (1:800 v/v in H₂O) (a-c) before irradiation and (d-f) after solar irradiation for 8 h. (g-i) Changes in fluorescence intensity after an irradiation time of 8 h. All fluorescence intensity values are expressed in quinine sulfate units (ppm).

The same model systems (ribose-lysine, -arginine, and -histidine) were then exposed to solar irradiation to initiate photo-decomposition (e.g. photobleaching and photo-transformations). Upon solar irradiation, we observed a fast decay in fluorescence intensities in all model systems (Figure 4.1d-i). Besides the decrease in fluorescence, however, the EEM maps in Figure 4.1g-i also indicate formation of new fluorescent compounds, which were formed during the photolysis or which have been quenched by other compounds prior to irradiation. PARAFAC was used to decompose fluorescence spectra into distinct statistical components.^[251] For all three model systems, four component PARAFAC models could be developed and split-half validated. Besides the above-mentioned characteristic spectral regions, the PARAFAC models give evidence for the existence of additional fluorophores, even though with lower quantum yields (Table 4.1 and Figure 4.2). For all model systems, three components were retrieved which showed a decrease in fluorescence and one fluorescent component which increased over time, respectively. These components (Lys: C2, Arg: C2, His: C1) show very different excitation/emission positions and different Stoke's shifts between the model systems indicating different chemical structures and fluorescent moieties, respectively. In the ribose-lysine model system, the increase of C2 showed remarkable correlation to the decreasing fluorescence of C3 and C4. Hence, C2 may be formed by photochemical reactions of C3 and/or C4, or these fluorophores may have quenched the fluorescence of C2 before irradiation. A similar correlation could be found for C2 and C3/C4 in the ribose-arginine reaction system. Very similar fluorescence peaks further indicate the possibility of similar substructures (fluorophoric groups) between C4 of the ribose-lysine and C4 of the ribose-arginine systems. In general, the photo kinetics derived from the PARAFAC components are very similar between the lysine and arginine reaction systems. By comparison, fluorophores degraded and potentially formed in the ribose-histidine model system behaved differently. For example, the increasing component (C1) showed a nearly linear increase in fluorescence over the entire irradiation period indicating zero order photochemical synthesis.

Table 4.1 | Fluorescence local maxima obtained by EEM-PARAFAC analysis.

Component	Lysine	Arginine	Histidine
C1: Ex Em	350 440 nm	320 400 nm	265 365 nm
C2: Ex Em	270 430 nm	295 350 nm	330 420 nm
C3: Ex Em	330 395 nm	355 430 nm	245 470 nm
			380 470 nm
C4: Ex Em	240 485 nm	245 480 nm	325 370 nm
	395 485 nm	395 480 nm	

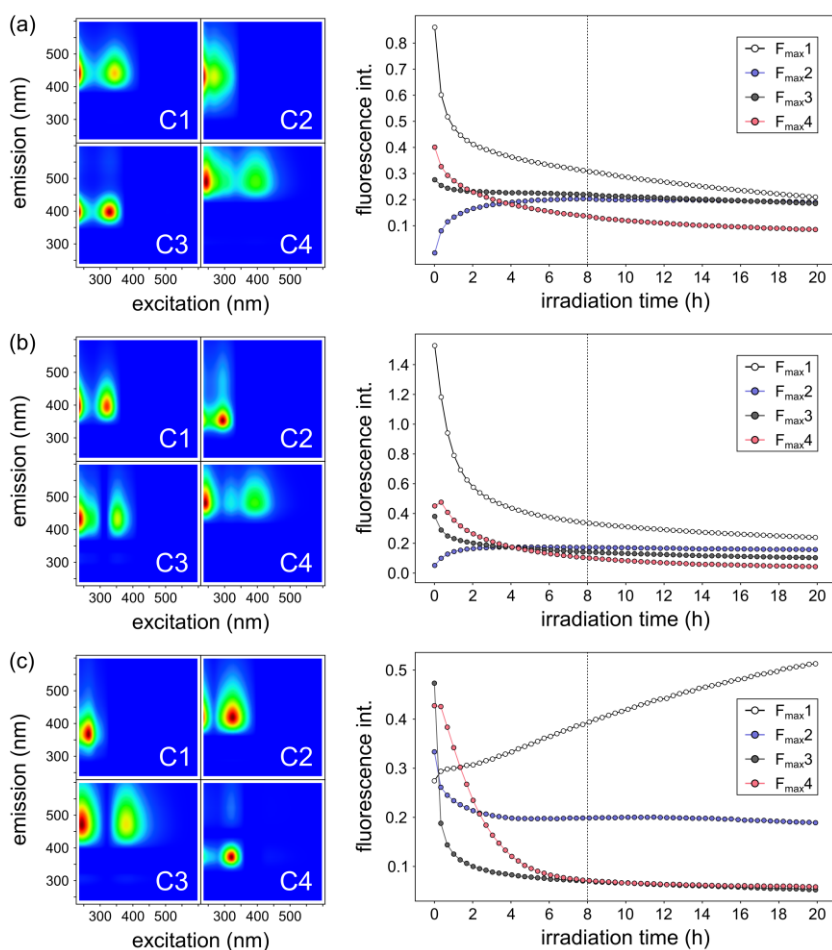


Figure 4.2 | Four component EEM-PARAFAC models obtained from EEM measurements. (a) Ribose-lysine, (b) ribose-arginine, and (c) ribose-histidine model systems. All model systems were irradiated for 20 h. EEM spectra were recorded every 20 min.

Absorbance measurements. After heating the ribose-amino acid mixtures for ten hours at 100 °C, we found maximum absorbance at 265 nm in the ribose-lysine and -histidine mixture (Figure 4.3). The arginine reaction system showed maximum absorbance < 240 nm but indicated a second maximum at about 300 nm. Irradiation of the samples led to an exponential decrease in absorbance with maximum decrease found at 336 nm, 327 nm, and 294 nm for the ribose-lysine, -arginine, and -histidine model system, respectively (Figure 4.3). The discrete maxima indicate a selectivity of photochemical reactions rather than random degradation of all chromophores absorbing in the irradiated energy range. A red-shifted shoulder in Figure 4.3c (ribose-histidine model system) indicated an underlying curve with a second maximum decrease in absorbance at approx. 340 nm, which was in the range found for the ribose-lysine and ribose-arginine model systems, and could represent degradation reactions on chromophoric groups, similar to those in the lysine and arginine systems. The relative degradation rates of the two maxima found at 294 nm and 340 nm in the ribose-histidine model system were different. Especially at the beginning of the irradiation process, degradation rates at 340 nm were faster than for chromophores showing greatest changes at 294 nm (Figure 4.3c). This suggests at least two different groups of chromophores and potentially different degradation mechanisms.

4.3.2 Holistic characterization of photosensitive MRPs

We additionally irradiated larger amounts of sample in a suntester solar-simulation system equipped with a xenon arc lamp, also simulating the solar spectrum. Irradiation was performed for four and eight hours while the temperature was maintained at 25 °C. Control samples, which were protected from light exposure, were also placed in the suntester system for four and eight hours. Subsequently, we analyzed the samples by direct-infusion FT-ICR-MS and Tandem HILIC-RP LC-MS/MS, which combines hydrophilic interaction chromatography (HILIC) and reversed-phase (RP) liquid chromatography (LC) in a single chromatographic run.^[189] Direct-Infusion FT-ICR-MS allows a highly sensitive and holistic non-targeted screening of complex samples on the level of accurate molecular formulae.^[211] To provide further data for comparison, LC-MS/MS was used to monitor irradiation effects for specific candidate compounds and to study effects on the chemical structures. Principal component analysis (PCA) of the obtained FT-ICR-MS raw data could clearly separate irradiated model systems from controls on PC1 (exemplarily shown for the ribose-histidine model in Figure D.1 in Appendix Chapter 4). Samples irradiated for four hours could also be distinguished from samples exposed to sunlight for eight hours by PC2. Moreover, we could not observe a difference between the

control samples kept for four and eight hours in the suntester (while protected from light exposure) and freshly prepared model systems. This indicates that no significant thermal or time effects on the formation of new MRPs took place during irradiation experiments.

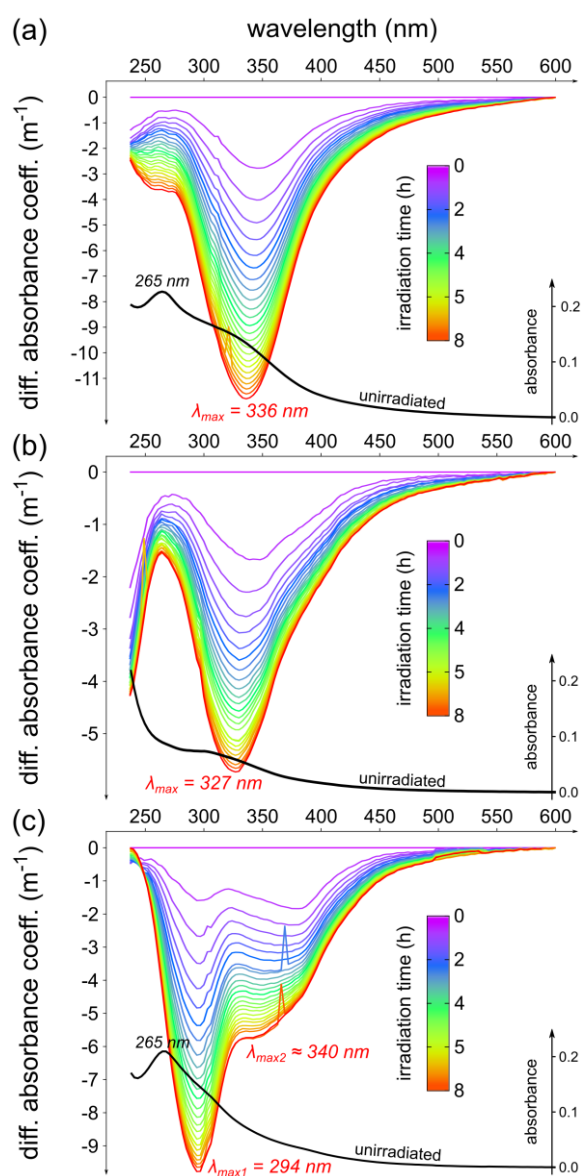


Figure 4.3 | Changes in the absorption spectra upon irradiation. Differential absorbance spectra of (a) ribose-lysine, (b) ribose-arginine, and (c) ribose-histidine model systems irradiated for eight hours. UV/Vis spectra were recorded every 20 minutes simultaneously with EEMs presented above. Embedded black curves represent UV/Vis absorption spectra of unirradiated model systems (10 h, 100 °C), respectively.

Photochemical degradation of MRPs. Using FT-ICR-MS, we could detect 1 446, 1 945, and 2 066 monoisotopic signals in unirradiated ribose-histidine, -lysine, and -arginine model systems (thermally formed reaction products and precursor molecules), respectively. Upon solar irradiation, we observed the largest changes in the ribose-histidine model system. Here, 391 elemental compositions (27%) showed a significant decrease in peak intensities after an irradiation time of eight hours ($p < 0.01$ and $\log_2FC < -1$ in both replicate experiments) (Figure 4.4). By comparison, in ribose-lysine and -arginine model systems irradiation led to 42 (2.2%) and 88 (4.3%) elemental compositions, which showed a significant decrease in ion intensities (Figure D.2 and Figure D.3 in Appendix Chapter 4).

Photooxidation of MRPs by singlet oxygen. Histidine residues are well known to easily undergo photooxidation reactions.^[233,261,262] However, direct light absorption by the imidazole function is not the major mechanism.^[262] In oxygen-rich atmospheres histidine photooxidation mainly occurs via Type II photo reactions.^[263] In a Type II reaction, the energy absorbed by a sensitizer is transferred onto ground state molecular oxygen to produce singlet oxygen (1O_2) and to a lesser extent other ROS.^[241] Singlet oxygen then may form unstable endoperoxide intermediates on imidazole residues, which further decompose into a complex mixture of as yet mostly unknown products.^[264,265] Among the proteinogenic amino acids, only Trp, Tyr, Phe, His, Cys, and Met show noteworthy rate constants in the reaction with 1O_2 with the highest values found for histidine oxidation,^[266,267] which might explain the greater number of photolabile MRPs in the ribose-histidine model compared to the two other model systems investigated. Nevertheless, formation of 1O_2 , and subsequent reactions of MRPs with 1O_2 may also play a role in the ribose-lysine and arginine model systems, particularly due to photosensitizers that can be produced in the course of the MR. We could detect significantly elevated levels of urea and asparagine in the irradiated histidine model systems (Figure D.4 in Appendix Chapter 4), which are formed in the decomposition of histidine via 1O_2 .^[265,268] Assuming that urea and asparagine are exclusively formed from photooxidation reactions, quantification (by LC-MS) of the formed urea and asparagine, suggested up to 0.06 – 0.09% and 0.002% of the initial histidine amount being transferred into urea and asparagine, respectively (Figure D.4 in Appendix Chapter 4). While urea can also be formed by α -NH₂-substituted histidines, asparagine can only be formed by degradation of the free amino acid.^[265]

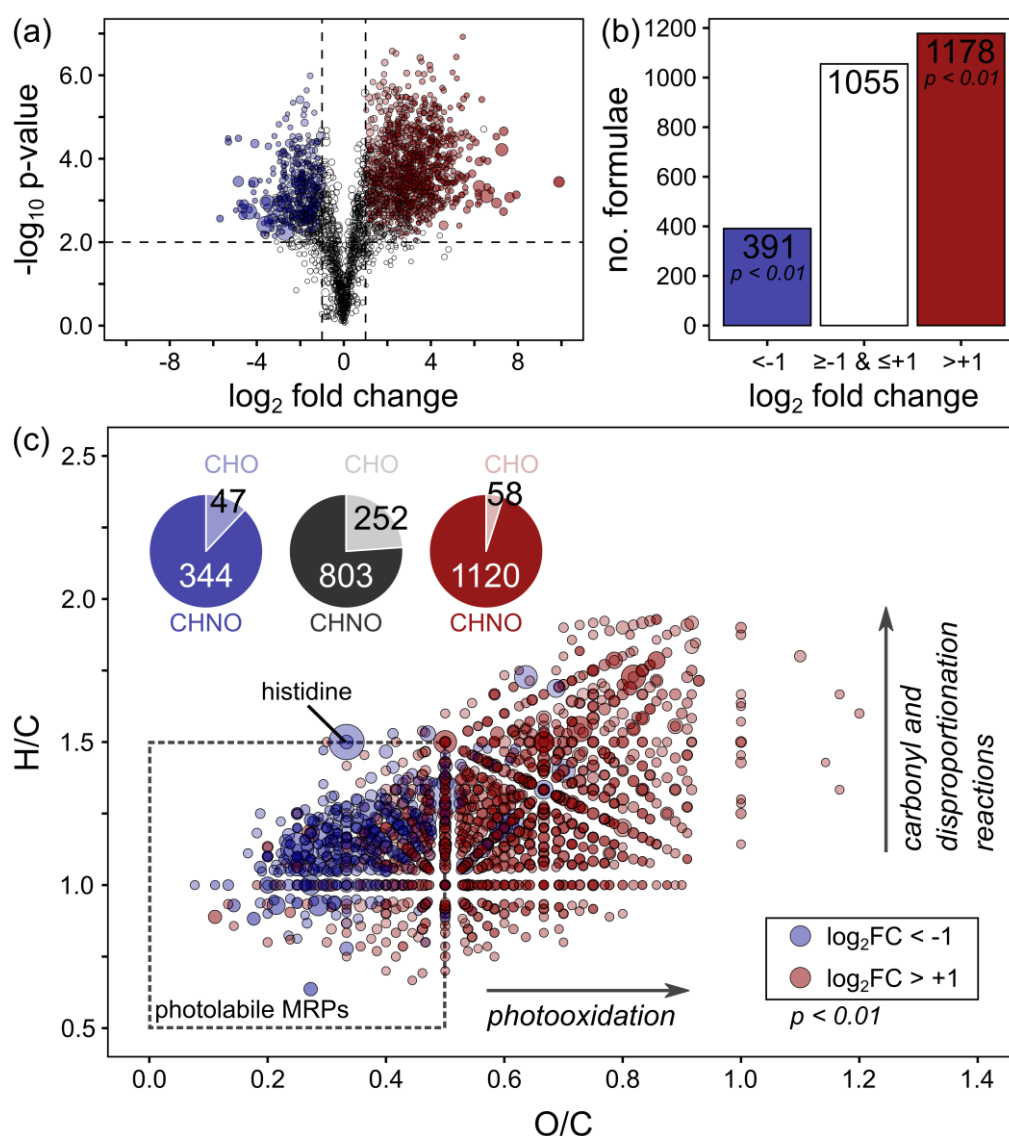


Figure 4.4 | Effect of solar irradiation on elemental compositions of ribose-histidine MRPs. Model systems were irradiated for eight hours and compared to unirradiated control samples. Irradiation experiments were performed in duplicate. Each sample then was analyzed by FT-ICR-MS in triplicate injections ($N = 2 \times 3$). Peak intensities of all features found in irradiated samples were compared to the same features in the unirradiated control samples by Student's t-Test ($n = 3$): Features, which showed a significant decrease in peak intensities in both independent irradiation experiments are colored in blue. Features, which showed a significant increase or were newly formed upon irradiation are highlighted in red, respectively. (a) Volcano plot. (b) Number of molecular formulae showing significant changes in peak intensities. (c) Van Krevelen diagram of all significantly affected molecular formulae. Pie charts illustrate the reduced occurrence of nitrogen-free (CHO) MRPs in photochemical reactions. Black pie chart represents elemental compositions, which did not show a significant change in peak intensities upon irradiation.

Several studies showed that rate constants for $^1\text{O}_2$ -photooxygenation reactions on α - NH_2 -substituted histidines are in the same order of magnitude as for the free amino acid indicating that the major target for photooxidation is the imidazole group of histidine.^[265,269,270] Notwithstanding this, many of the compositions that remained unchanged after irradiation, such as the Amadori rearrangement product (ARP) and other MRPs of the initial and intermediate phase (Figure 4.5), also contain intact histidine residues. Furthermore, when screening for imidazole fragments in MS/MS data, we could not observe a preferred degradation selectivity when MRPs contained intact imidazole groups (Figure D.5 in Appendix Chapter 4). The MS/MS spectra further revealed that most of the molecules formed upon irradiation still contained intact imidazole functions (Figure D.5 in Appendix Chapter 4). Conclusively, imidazoles cannot be the dominating targets for photooxidation reactions but the nature of substituents at the α - NH_2 position seems to play a decisive role in the reactivity towards photons. It has been shown that the pH in aqueous solutions strongly affects the $^1\text{O}_2$ oxygenation of histidine residues, indicating that oxygenation mainly occurs on unprotonated imidazole residues.^[271,272] The initial pH of the histidine model systems used in this study was equal to the pKa value of the histidine side chain (pH 6). Within eight hours of irradiation, the pH value had dropped exponentially to about pH 5.5 (Table D.1 and Table D.2 in Appendix Chapter 4). Consequently, the amount of unprotonated imidazoles in the model systems strongly decreased and it is conceivable that other moieties predominate in the photochemical degradation of histidine derived MRPs.

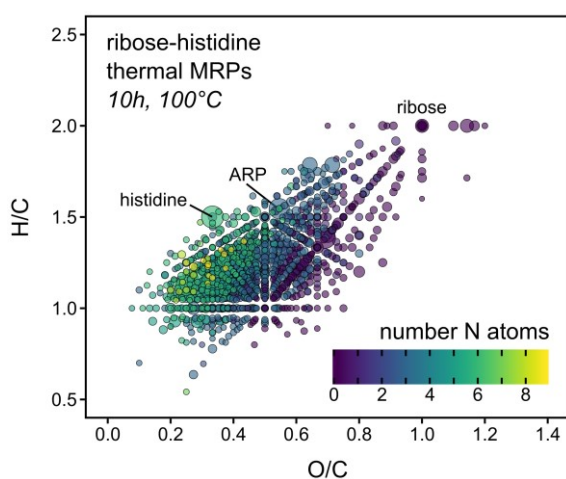


Figure 4.5 | Van Krevelen diagram of all molecular formulae reproducibly found in two independent replicate experiments (each analyzed in triplicate) after heating a ribose-histidine model system for ten hours at 100 °C. Color indicates the number of nitrogen atoms in the formulae. Scaling is relative to the average peak intensity recorded by FT-ICR-MS.

Photochemical selectivity. Interestingly, molecular formulae of the photochemically degraded species cover a discrete area in the van Krevelen space (Figure 4.4c; Figure D.2c and Figure D.3c in Appendix Chapter 4). The majority of degraded compounds have small H/C and O/C ratios, which are characteristic of unsaturated and aromatic compounds. In all model systems, most of the photochemically degraded compounds were characterized by an O/C-ratio ≤ 0.5 and an H/C-ratio ≤ 1.5 . Even though the different amino acids led to the formation of very different, largely amino acid specific MRPs (Figure D.6 in Appendix Chapter 4), this “photolabile area” was the same for all model systems. In the photolabile area, we reproducibly found 617, 611, and 851 molecular formulae, accounting for 34%, 21% and 57% of the total peak intensity, in the ribose-lysine, -arginine, and -histidine model systems, respectively. This somewhat higher number and higher molar amounts (estimated as relative peak intensities) found in the ribose-histidine MR may explain to a certain extent the higher number of degraded MRPs found in the histidine MR.

Several studies reported significantly greater antioxidant activity of MRPs formed from histidine compared to other amino acids.^[273,274] Indeed, antioxidants exhibit compositional characteristics (H/C and O/C-ratios; Figure D.7 in Appendix Chapter 4) similar to the compounds found in the photolabile area shown in Figure 4.4. Hence, increased active oxygen and radical scavenging activity^[275,276] found for these MRPs may also play a role in the photochemical selectivity and the greater number of photo-modified MRPs in the histidine model system.

Only a few AGE markers, which can be formed in the ribose-lysine and -arginine MR, have been described previously.^[12] We could identify seven compounds in our LC-MS/MS data (Figure 4.6), and we used fragmentation spectra to substantiate chemical structures (Figure D.8 and Figure D.9 in Appendix Chapter 4). Among the seven identified candidates, only formylidine^[153] and argpyrimidine^[151] showed significant degradation ($\log_2FC < -1$ and $p < 0.01$, Student's t-Test ($n = 3$)) after an irradiation time of eight hours in both irradiation experiments. Heterocyclic aromatic groups (pyrrole and pyrimidine) characterize these markers. In the two imidazole derivatives, GOLD and MOLD,^[277] both nitrogen atoms are substituted leading to a positive charge and therefore a reduced electron density in the aromatic ring structure, similar to protonated histidine residues. This indicates a selectivity of photochemical degradation reactions, towards the degradation of electron-rich aromatic heterocycles, which are preferentially formed in the final phase of the MR and which are often responsible for the characteristic browning (melanoidins).^[2,16]

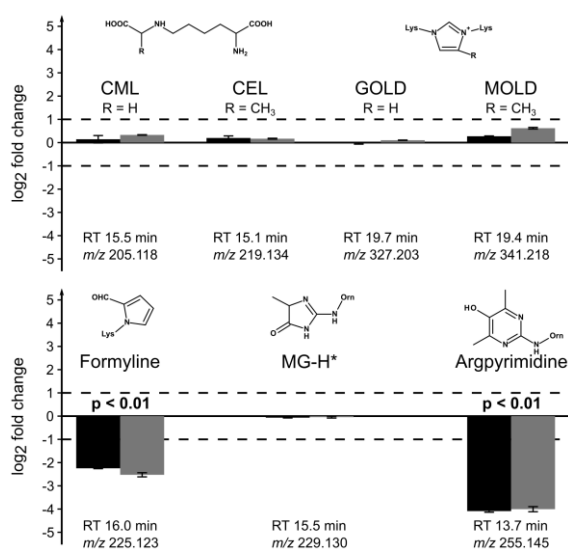


Figure 4.6 | LC-MS/MS analysis of known AGEs and MRPs that can be formed in the ribose-lysine and arginine Maillard reaction, respectively. Log₂ fold changes represent the changes in peak intensities between irradiated (8 h) and unirradiated control samples. Two independent irradiation experiments (experiment A: dark grey, experiment B: grey) were carried out. Each experiment was analyzed in triplicate injections by LC-MS/MS.

Photo-induced formation of MRPs. In all model systems, we found far more compounds, which were produced upon solar-simulated irradiation than MRPs that were degraded. More precisely, analysis of the ribose-histidine model system showed 1 178 compounds after irradiation, which significantly increased in their ion intensities ($\log_2\text{FC} > 1$, $p < 0.01$, Student's *t*-Test ($n = 3$)) or were newly formed (Figure 4.4). By comparison, the ribose-lysine and arginine model systems showed 167 and 525 elemental compositions increasing in intensity after an irradiation time of eight hours, respectively (Figure D.2 and Figure D.3 in Appendix Chapter 4). Compared to the degraded MRPs, the photochemically formed products showed a clear shift towards higher O/C-ratios indicating that oxidation reactions are involved in the photochemical modification of MRPs. While most of the photooxidation products can be formed by successive oxidation of double bonds ($\text{O/C} > 0.5$ and $\text{H/C} \leq 1.5$), we also found a considerable number of photoproducts with an H/C-ratio greater than 1.5 (Figure 4.4c). These reaction products might be formed by disproportionation reactions or by reactions on carbonyl groups, such as hydroxyl carbonyls or deoxyosones, with nucleophilic components of the system. Many of the degraded MRPs in the photolabile area may also serve as good scavengers for (hydroxy)acyl radicals formed by Norrish-type reactions during the irradiation process.^[244] In general, these type of photoproducts have similar elemental compositions as thermally formed MRPs found in the initial and intermediate phase of the MR (Figure 4.5).

We further studied the behavior of different compositional descriptors, which can be retrieved from the computed molecular formulae (Figure 4.7; Figure D.10 and Figure D.11 in Appendix Chapter 4). Interestingly, all model systems showed similar behavior, which can be summarized as follows:

(i) MRPs with a greater number of carbon atoms preferably undergo photolytic reactions. By comparison, photochemical products tend to be smaller molecules with a reduced number of carbon atoms (Figure 4.7a-b), indicating that cleavage mechanisms are likely to be involved in photochemical reactions on MRPs.

(ii) Upon photolytic reactions, the number of oxygen atoms per molecule increased on average by 1.5 oxygen atoms per molecule (Figure 4.7c). Together with the increase in the average carbon oxidation state (Figure 4.7f), it can be concluded that exogenous ROS, such as $^1\text{O}_2$ or hydroxyl radicals, must play a key role in the photochemical reaction mechanisms.

(iii) Photosensitive MRPs have a higher number of double bond equivalents (sum of double bonds and rings) per carbon atom (DBE/C) than MRPs that are stable towards light exposure (Figure 4.7e). However, we could not observe a noticeable difference between the DBE/C-values of the degraded and the photochemically produced compounds. For example, after cleavage of a carbon-carbon double bond each of the two carbon atoms must still contain a double bond to maintain the DBE/C value. Because the average carbon oxidation state of the photolysis products tends to have higher values than that of the other MRPs, it is likely that double bonds undergo photooxidative cleavage reactions leading to the formation of carbonyl moieties such as aldehydes or carboxylic acids. A decrease of the pH-value during the irradiation experiments (Table D.1 and Table D.2 in Appendix Chapter 4) further supports the formation of carboxylic acids in the course of photolysis.

(iv) Photolabile MRPs tend to be nitrogen-rich compounds (Figure 4.7d). When irradiated, the number of nitrogen atoms in the reaction products decreased. This substantiates photochemical targets, such as nitrogen containing heterocyclic structures or Schiff bases that might undergo oxidative degradation similar to the Karstens and Rossbach mechanism.^[278]

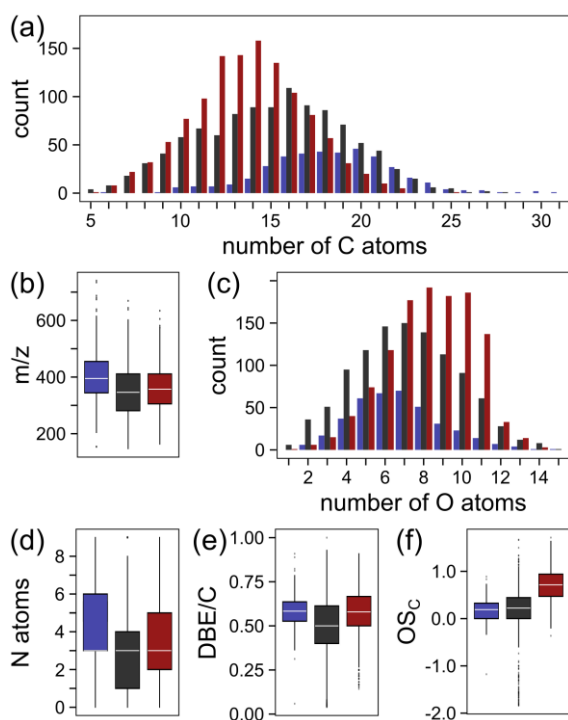


Figure 4.7 | Overview of compositional descriptors retrieved for the ribose-histidine model system after molecular formulae computation from FT-ICR-MS data. Bar charts are grouped into features, which showed a significant decrease (blue; $\log_2FC < -1$ and $p < 0.01$, Student's t-Test ($n = 3$)) and significant increase (red; $\log_2FC > 1$ and $p < 0.01$, Student's t-Test ($n = 3$)) in peak intensities in both independent irradiation experiments, respectively. Features that did not show a significant change in peak intensities after an irradiation time of eight hours are colored in black. Represented descriptors are (a) number of carbon atoms per formula, (b) measured m/z -values, (c) number of oxygen atoms per formula, (d) number of nitrogen atoms per formula, (e) average number of double bond equivalents per carbon atom, and (f) average carbon oxidation state.

Amino acid-specific photochemical reactions and their orthogonality to thermal reactions. Non-targeted analysis aims to comprehensively investigate a sample's chemical composition. Although we are unlikely to be able to resolve and detect the entire chemistry of very complex samples, we can potentially find many precursor-product pairs in the mass spectra obtained from non-targeted experiments of reaction systems. The mass difference between a potential reaction precursor and product can provide information about their net chemical transformation.^[212,279] Even though not all mass differences correspond to a real chemical transformation, they can provide useful information about the compositional connectivity between the observed reaction products.^[161] We computed pairwise all mass differences between all monoisotopic ions observed in the FT-ICR mass spectra and used their relative incidences to elucidate meaningful mass differences (Figure 4.8). For example, an incidence rate of 54%, as found for the mass difference 18.010565 Da (compositional equivalent: $\pm H_2O$) in the unirradiated ribose-histidine model system (Figure 4.8), means that 54% of all monoisotopic ion signals in the spectra can be connected to another signal by this mass difference and suggests (de)hydration reactions.

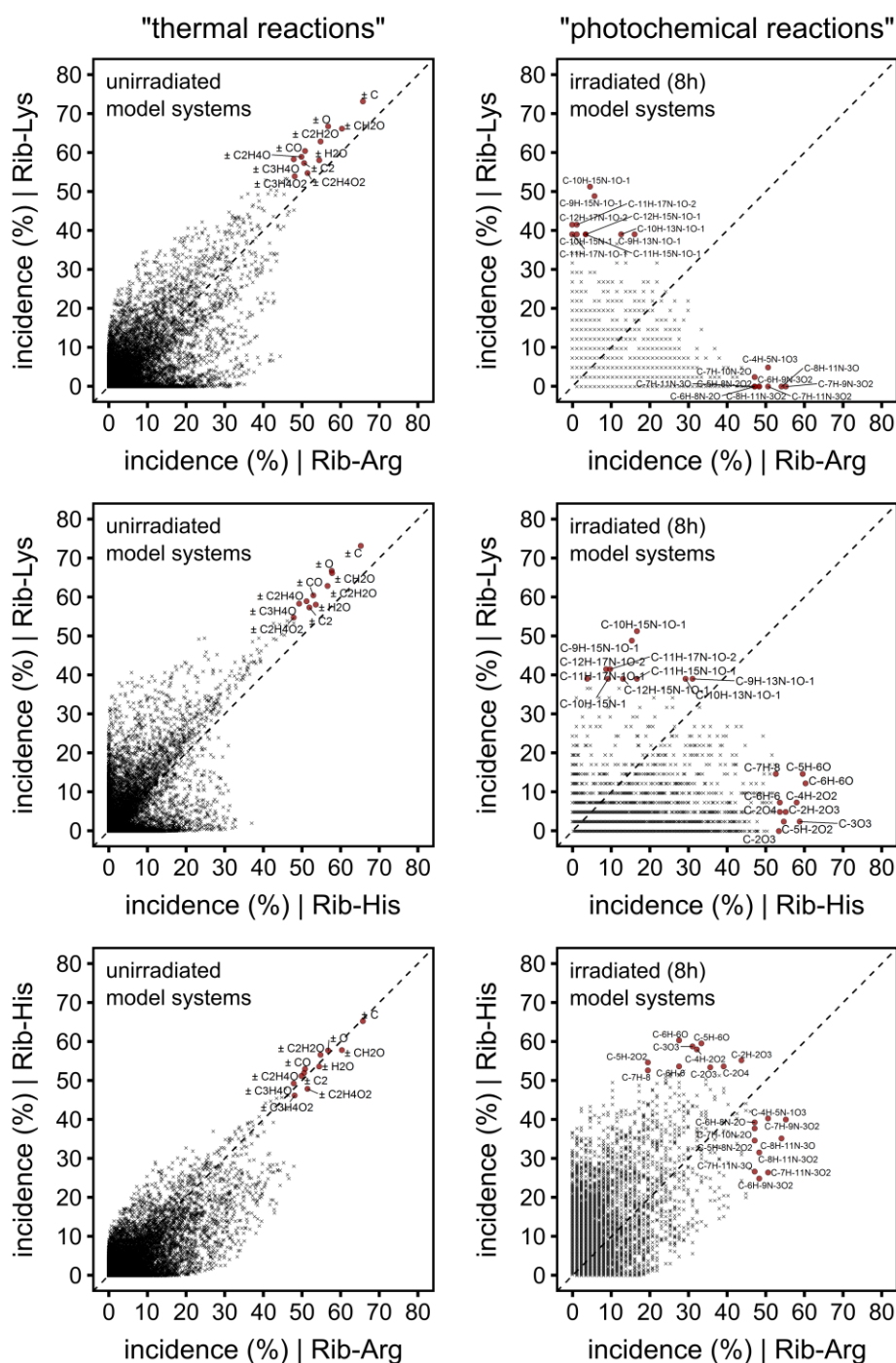


Figure 4.8 | Pairwise comparison of mass difference incidences. Incidence rates were computed from all recorded mass differences in the mass spectra of thermally synthesized MRPs (left panel) and photochemically synthesized products (right panel). The top ten of the most frequently occurring mass differences were assigned to their element compositional equivalents representing possible net chemical transformations. Incidences represent the relative probability by which a monoisotopic signal in the mass spectrum can be linked to another monoisotopic signal with a given mass difference md_i .

Pairwise comparison of the different unirradiated control model systems showed good correlation of mass differences, especially those with high incidence rates, indicating very similar chemical reactions in the thermal formation of MRPs. These mass differences involved chemical transformations, such as (de)hydration ($\pm \text{H}_2\text{O}$) and oxidation/reduction ($\pm \text{O}$), which are known to play a crucial role in the thermal synthesis of MRPs. This data agrees with our recent study, which showed that different amino acid precursors follow consistent reactivity behavior, even though the different amino acid precursors lead to very different chemical compositions.^[252] By comparison, when comparing mass differences, which were exclusively found between degraded MRPs (“photo-precursors”) and compounds formed upon irradiation (“photoproducts”) we received a completely different picture (Figure 4.8). Firstly, compared to the thermally formed MRPs, we observed poor correlation of reactivity patterns between the different model systems, indicating photochemical reactions of MRPs are very specific to the parent amino acids. Secondly, net chemical transformations that are dominating the MR in thermal processing seem to play only a minor role in the photochemical reactions of the MRPs. It is worth noting, that intermediate reactions, which do not lead to stable molecules that can be detected by MS, are not considered with this approach. Conclusively, while major chemical reactions in the thermal synthesis of MRPs are very consistent and independent of the amino acid precursor, the same systems show strong amino acid specificity in the photochemical degradation of MRPs.

4.4 Conclusions

We studied the effects of solar-simulated radiation on the modification of MRPs, formed in a typical non-enzymatic browning reaction at moderate temperature (100 °C). Upon photon absorption, hundreds of MRPs readily underwent degradation reactions leading to a complex mixture of newly formed photoproducts. Our data provides evidence for a strong selectivity of photo-degradation reactions, mainly towards electron-rich and nitrogen-containing heterocycles, which are preferentially formed in the advanced and final phase of the Maillard reaction. Photoreactions on these structures break down the molecules into smaller but strongly oxidized compounds. While the “traditional” (thermal) synthesis of amino acid glycation products follows general chemical reactions, such as dehydration, carbonyl cleavage and redox reactions, photoreactions are a lot more diverse and show strong amino acid specificity. This fundamental study is of special importance in the shelf-life of

foods, phototoxicity mechanisms in diabetic and aged tissues and may, under certain conditions, also play a role in prebiotic molecular synthesis. Lack of current comprehensive database information on MRPs and photochemical products did not allow identification of most of the structures, but also suggests a great pool of as yet unexplored chemical compounds, which need detailed characterization in future studies. Studies on purified reaction products may help to understand some specific photo-degradation mechanisms. However, it must be taken into consideration that many of the formed photoproducts are likely to be produced only in a complex interplay of reactive intermediates and products. Hence, further improvements in holistic approaches are required to gain better understanding.

Chapter 5 |

Concluding Discussion and Outlook

The presented thesis reports on the non-targeted monitoring of Maillard reaction products (MRPs) in sugar-amino acid model systems. Analytical methods, data analysis, and visualization strategies were developed and implemented to comprehensively study MRPs and their chemical interplay in the entire reaction network. (Ultra)high-resolution mass spectrometry methods in combination with complementary optical spectroscopy proved to be excellent tools to investigate the formation and subsequent degradation of reaction intermediates and products under thermal (Chapter 2-3) and photochemical conditions (Chapter 4). The approaches used were able to resolve and monitor hundreds of MRPs simultaneously on a molecular level. To understand this entire chemical “collective” is of great importance and the fundamental prerequisite to control the Maillard reaction (MR) towards the formation of desired reaction products. Data analysis and visualization tools, such as van Krevelen diagrams, mass difference (MD) analysis, reaction network graphs, and Kendrick mass defect analysis were decisive to decipher compositional characteristics and probe samples in a reactivity-related context.

Even very simple model systems, containing only one sugar and one amino acid precursor, were able to produce several hundreds of reaction products. In all model systems studied, by far the most intermediates and reaction products could be formed only by the interaction of sugars and amino acids. By comparison, at the moderate reaction conditions used (100 °C in unbuffered model systems), sugar and amino acid degradation products only played a minor role. Despite the large number of different reaction products recorded in the model systems, most of these can be formed by very simple chemical transformations, including dehydration, carbonyl cleavage, and redox reactions. The resulting interconnected reaction network ultimately leads to an extraordinarily high chemical diversity and complexity. We could discover such general reactions not only in ribose-glycine mixtures but also when different amino acid precursors were used in the model systems. This allowed a general reaction scheme to be conceptualized, which involves more than 70 MRPs of general composition, which only differ in the amino acids’ side chain and eventually

expands known reaction pathways. In addition to Amadori products, other compounds, especially diketosamines, seem to play a crucial role in the early MR and significantly contribute to the diversity in reaction products. However, it must be pointed out that diketosamines and their direct degradation products are to be expected in significantly lower concentrations. This may also be the reason why these intermediates have, so far, received only little attention. In general, amino acid precursors were mainly responsible for the chemical diversity observed while different sugar precursors mainly had an influence on the reaction rates but led to similar or even identical MRPs. As expected,^[280] the reactivity of pentoses was higher compared to hexoses, which was reflected in a noticeably larger number of reaction products. Likewise, the proportion of free carbonyl groups in the sugar precursors had an influence on the reactivity. More precisely, ribose was more reactive than arabinose and xylose. However, the findings from the comparison of different amino acids were surprising. Above all, cysteine, contrary to our expectations, showed a very high reactivity and eventually led to more reaction products than other amino acids, including glycine and isoleucine.

One of the most obvious characteristics of the MR is the formation of chromophores and fluorophores. Such subunits make MRPs potential targets for photochemical reactions. Irradiation of heated sugar-amino acid mixtures with simulated sunlight resulted in a rapid degradation of multiple MRPs. Nitrogen-containing and electron-rich heterocycles were preferentially degraded, whereas early MRPs showed high stability towards the exposed radiation. The data also showed that the formation of reactive oxygen species played a significant role in degradation reactions. Exogenous oxygen initiated oxidative cleavage reactions and ultimately cleaved photolabile MRPs into a large number of yet unexplored photoproducts. While reactions in thermal Maillard systems are largely independent of the precursor molecules, photochemical reactions showed a much higher amino acid specificity and differed fundamentally from “classical” Maillard transformations.

The presented analytical and data science approaches build a solid basis for future non-targeted and holistic studies on the MR. While the approaches used in this work mainly aimed to holistically explore the composition of reaction products on a molecular level, future work should also include characterization of chemical structures and elucidation of exact reaction mechanisms. It is clear that the high complexity and similarity in physicochemical properties make it impossible to elucidate structures of all intermediates and reaction products formed, even if only simple model systems are considered. Isolation of multiple MRPs is very time-consuming and it must be assumed that isolation of the many unstable compounds is impossible. Hence, it would be more efficient to focus on reasonably stable and/or key intermediates (*e.g.* diketosamines). Mass difference analysis as presented in Chapter 2

is a promising tool to identify such key intermediates. Connecting mass spectral features with exact MDs, corresponding to relevant chemical transformations, eventually leads to reaction networks where key intermediates are represented as highly connected nodes. These intermediates can be considered as secondary precursors for many of the downstream reaction products. A promising analytical setup for the isolation of MRPs was presented in the Appendix of Chapter 1.

Studying chemical (degradation) mechanisms based on purified or synthesized MRPs would allow a more precise understanding of specific reaction mechanisms under both, thermal and photochemical conditions.^[9] However, when studied individually and isolated from other MRPs in the reaction pool, such an approach only allows us to gain insights into linear downstream reactions while the interplay with other MRPs and the role in the entire reaction cascade remains overlooked. A more promising approach would be to study degradation mechanisms using isotopically labeled MRPs. The use of isotopically enriched (secondary) precursors or solvents in model systems is a powerful way to trace back the atoms to their original position in the parent molecule.^[26,95] Model systems using labeled components in combination with mass spectrometry or nuclear magnetic resonance spectroscopy became the most successful approaches in studying underlying reaction mechanisms.^[281] For example, synthesis of fully labeled key intermediates can be achieved in model systems followed by targeted isolation and purification. In a carbon module labeling (CAMOLA) approach,^[281] these intermediates can then be spiked into model systems containing differentially labeled precursors or precursors with natural isotope abundances, which can decipher direct degradation products from those which are interconnected to other components in the reaction pool.

In this fundamental work, we used throughout the experiments unbuffered aqueous model systems, which allowed straightforward analysis by direct-infusion mass spectrometry without an additional cleanup step. Nevertheless, it is well known that other reaction conditions, such as pH, temperature and water activity, have a great influence on the type and concentrations of MRPs formed (see also Chapter 1.2). Especially with regard to application-oriented issues, such as the formation of MRPs under food-relevant conditions, it would be of great value to know the effects of various factors on the entire reaction process. In an experimental design, studying multiple factors at once, response models for all detected MRPs can be computed.^[282] These models would allow the effects of different reaction conditions on hundreds of MRPs in the same time to be studied. Such models would be of great importance to efficiently reduce unwanted reaction products while maintaining desired MRPs.

The presented results showed large differences in the formation of nitrogen-free (CHO) compounds. For example, only 1% of the detected compounds in a ribose-

cysteine system were CHO compounds, while ribose-lysine systems produced 18% of such CHO compounds. However, in all model systems studied, most of the observed MRPs contained nitrogen originating from the amino acid precursor, respectively. The exact reasons for the different proportions in CHO compounds remain largely unclear. Reactive dicarbonyls are considered as key components in the intermediate phase of the MR (see also Chapter 1.1.2). Interestingly, most of the known dicarbonyl structures (e.g. deoxyosones, glyoxal, or methylglyoxal) can be formed independently of the type of amino acid. By comparison, amino acid specific dicarbonyls and hence nitrogen-containing dicarbonyls are largely unknown. It is clear that in a complex interplay of multiple amine sources, higher concentrations for those reaction products can be expected, which are formed independently of a specific nitrogen source. However, the sum of many trace-level and amino acid specific dicarbonyls may significantly impact subsequent dicarbonyl-triggered reactions (e.g. protein crosslinking). It would therefore be of great value to evaluate the amount and type of nitrogen-containing dicarbonyls. Efficient trapping reagents, such as *o*-phenylenediamine, readily allow to transfer these reactive intermediates into stable derivatives,^[283] which can be comprehensively analyzed using the here presented methods.

Cysteine is known to react somewhat differently compared to other amino acids. The reduced formation of colored compounds during the MR has often been explained by the formation of stable thiazolidines during the initial condensation reaction and by the ability of cysteine to efficiently trap dicarbonyl structures.^[220,221] On the one hand, the data presented here clearly indicate that cysteine readily forms a multitude of reaction products. On the other hand, different behavior was also observed in our results, especially in the later steps of the advanced phase (see also Chapter 3.3.4). Further research is needed to exactly understand the mechanism of action of cysteine and other thiols in the early stages of the reaction cascade.

Comprehensive analysis of MRPs and AGEs in real samples, such as food extracts or biological material, is still a major challenge. Due to the current lack of comprehensive MS/MS databases, standard-free identification of MRPs or AGEs in high-throughput screenings is largely impossible. Although, in recent years, *in silico* prediction of MS fragmentation patterns has made huge progress in metabolomics,^[284] the high similarity in chemical structures and substructures of MRPs does not currently allow accurate structure assignments. A possibility to overcome these limitations would be to build a database that contains experimental MS/MS data by analyzing various model systems, which were produced from multiple carbonyl and amine precursors, respectively. Although most of the chemical structures of the features in such a database will remain unknown, the database can be used to identify MRPs and their potential precursors in real samples. Then, selected MRP candidates can be specifically synthesized in model experiments, which provide a well-controlled

and less complex environment and therefore would allow better structure elucidation and confirmation. The tandem LC setup presented in the Appendix of Chapter 1 is an ideal platform for such an approach. In non-targeted screenings, it can resolve hundreds of MRPs in model systems. Data-dependent acquisition can be used to subject most of the recorded precursor ions to automated MS/MS experiments, which would build the core of the database.

Another future approach that may help to identify possible MRPs in real samples benefits from the high mass accuracy provided by ultrahigh-resolution mass spectrometers and the fact that different reaction precursors in the MR go through the same reaction pathways: Each compound i in a complex sample containing N compounds is represented in a mass spectrum by its accurate mass. Each of the N compounds can also be described by a vector of $N-1$ MDs, which represents all exact mass spacings between compound i and all other $N-1$ compounds in the spectrum. In a similar way, each MRP of the general Maillard reaction scheme, presented in Chapter 3.3.4, can be described by a vector of MDs relative to the other MRPs in the scheme. Such a vector (*e.g.* the vector that describes the interconnectivity of the Amadori product in the general pathway), can be used in an inverse approach to identify possible and unexpected MRPs (*e.g.* Amadori products) in real samples. This approach assumes that, regardless of the type of precursor molecules, general reaction pathways take place. If a compound in the real sample shows a high overlap to the theoretical MD-vector, this compound is more likely to be an MRP than compounds, which do not match the pattern of the template vector. By comparison, searching mass spectra of real samples for theoretical m/z -values of all possible MRPs would go along with searching for an immense number of theoretical m/z -values if all possible amine-sugar combinations were taken into account. In any case, such an approach would drastically increase false discovery rates, which are assumed to be much lower if instead multiple values (a vector approach) are used.

A Appendix Chapter 1: Tandem HILIC-RP Liquid Chromatography for Increased Polarity Coverage in Food Analysis

Comprehensive non-targeted analysis of food products normally requires two complementary chromatographic runs to achieve maximum compound coverage. In this study, we present a sensitive tandem-LC method, which combines RP and HILIC separation in a single run. The setup consists of a C18 trap column and two subsequently coupled analytical columns (HILIC and C18) which are operated in parallel. First, hydrophobic compounds are retained on the RP trap column while rather hydrophilic compounds are directly transferred onto a HILIC phase. Next, the pre-fractionated sample composition is analyzed by HILIC or RP chromatography, respectively. The presented setup allows individual and independent gradient elution as well as interfacing with mass spectrometry. The performance of the method has been proven by means of food relevant standards and analysis of complex food samples (e.g. red wine, meat extract). The simple and robust setup provides high flexibility in the selection of column combinations and does not require sophisticated instrumental setups or software. The method significantly increases the covered polarity range compared to classical one-dimensional chromatography. Our results indicate that tandem-LC is a valuable and universal tool in the non-targeted screening of various types of complex food samples.

This chapter has been published as [Hemmler, D., Heinzmann, S. S., Wöhr, K., Schmitt-Kopplin, P. & Witting, M. Tandem HILIC-RP liquid chromatography for increased polarity coverage in food analysis. *Electrophoresis* 39, 1645–1653 \(2018\).](#)

Reprinted with permission. Copyright 2018 Wiley-VCH.

Candidate's contributions: D.H. designed the research. D.H. performed the experiments and analyzed the data. D.H. prepared the figures. D.H. wrote and revised the manuscript.

A.1 Introduction

The integration of biotic and abiotic processes makes foods very complex chemical systems. For example, the chemical complexity of wine combines biochemical impacts, such as plant, microorganism and secondary metabolisms, with environmental and viticultural impacts.^[193,285] Typical small molecular constituents of wine are primary metabolites (e.g. carbohydrates, organic acids, lipids, and amino acids) and phytochemicals (e.g. phenols, lignans, sterols, and alkaloids).^[286,287] It is assumed that secondary metabolism leads to more than 200 000 natural products present in the plant kingdom.^[288] Although application of metabolomics tools to food fingerprinting has rapidly emerged in recent years, only a small number of these compounds have been identified and listed in databases. Liquid chromatography coupled to high-resolution mass spectrometry (LC-MS) has prevailed as an excellent method in metabolomics.^[166,289] However, when aiming to identify as many compounds as possible, selection of an appropriate stationary phase is difficult because of a wide range of chemical and physical properties (e.g. polarity, pK_a) of the metabolites.^[166,290] Arubulu *et al.* have recently shown for red wine samples that a maximum metabolite coverage requires reversed-phase (RP) and hydrophilic liquid interaction chromatography (HILIC). While organic acids and carbohydrates were preferentially retained on the HILIC column, for most other compound classes no preferred separation phase could be found.^[286] Two independent chromatographic runs, however, are time consuming and require larger sample amounts. Additionally, accurate alignment of unknown compounds that show retention on multiple stationary phases, such as RP and HILIC, is a challenging task.

To overcome these limitations, several setups have been developed which combine RP chromatography and HILIC in a single run. A first type of setup uses serial coupling of HILIC and RP columns.^[291–296] Greco *et al.* showed an increased polarity range covered when a zwitterionic HILIC column was serially coupled to a C18 RP column in the analysis of phenolic compounds.^[291] However, serial coupling of columns does not allow independent gradient elution^[297] and restricts the selection of columns due to an increase in back pressure. Good summaries of serial couplings have recently been published in comprehensive reviews by Haggarty and Burgess^[298] and Alvarez-Segura *et al.*^[299] The second type of setup (tandem LC) uses first a trap column to divide the sample composition into hydrophilic and hydrophobic compounds. The pre-fractionated sample can then be analyzed on two different stationary phases (e.g. HILIC and RP). Due to the pre-fractionation step, analytes are separated either on the HILIC or on the RP column using independent gradient elution.^[297,300] Pyke *et al.* recently reported a tandem method, which combines aqueous normal phase (ANP)

chromatography with RP separation for the analysis of urine metabolites.^[297] They showed that the number of detected compounds using the tandem method is comparable to results when the same sample was analyzed in two independent chromatographic runs.

The aim of this study was to develop a HILIC-RP tandem coupling which allows analysis of highly polar to nonpolar food constituents in a single chromatographic run. Online pre-fractionation of the sample composition and subsequent analysis on two orthogonal stationary phases enhances the covered polarity range compared to traditional one-dimensional LC systems. Compared to serial couplings the here presented setup can be operated with individual gradients and bypasses limitations due to an increased column backpressure. By means of a second switching valve effluates of the two analytical columns enter the mass spectrometer individually, thus, avoiding possible loss in ionization efficiency.

A.2 Experimental procedures

A.2.1 Reagents

LC-MS grade methanol and acetonitrile (ACN) were purchased from Merck (Darmstadt, Germany). Formic acid (LC-MS grade) and ammonium formate (10 M stock solution) were obtained from Sigma-Aldrich (Steinheim, Germany). MilliQ-purified water (18.2 M Ω ; Millipore, Germany) was used throughout the experiments.

A.2.2 Reference standards

Reference standards L-Alanine (99%), L-arginine (\geq 98%), L-asparagine monohydrate (>99%), L-aspartic acid (>98%), p-cresol (analytical standard), L-cysteine (>98%), D-(-)-fructose (>99%), fumaric acid (>99%), D-(+)-glucose (>99.5%), L-glutamic acid (>99%), L-glutamine (>99%), glycine (>99%), L-histidine (98%), L-isoleucine (99%), L-leucine (>99.5%), L-lysine (>98%), L-(-)-malic acid (>99.5%), L-methionine (>98%), myricetin (\geq 98%), L-phenylalanine (99%), L-proline (>99%), pyrocatechol (>99%), quercetin (\geq 95%), D-(-)-ribose (98%), L-serine (99%), succinic acid (\geq 99%), sucrose (>99.5%), syringic acid (analytical standard), L-threonine (>98%), D-(+)-trehalose dihydrate (>99%), L-tyrosine (>99%), and L-valine (>98%) were obtained from Sigma-Aldrich (Steinheim, Germany). Malvin chloride (Rotichrom[®] HPLC) was purchased from Roth (Karlsruhe, Germany) and malvidine chloride was purchased from Biomol

(Hamburg, Germany). Individual stock solutions (1 mg mL^{-1}) were prepared of each reference standard. Amino acid standards were dissolved in methanol/water (1:1) *v/v*, sugar and dicarboxylic acids were dissolved in water, and phenolic compounds were dissolved in methanol, respectively. Stock solutions were diluted with water/ACN (98:2) *v/v* prior to injection. Concentration of the injected standards was $20 \text{ } \mu\text{g mL}^{-1}$ (amino acids: $10 \text{ } \mu\text{g mL}^{-1}$), respectively.

A.2.3 Sample preparation

Red wine. A wine sample from the grape variety “Lemberger” with an alcohol content of 13.0% was diluted (1:5) *v/v* with water/ACN (98:2) *v/v* prior to injection.

Meat extract. 5 g minced beef were extracted in a blender with 30 mL methanol/water/hexane (1:1:1) *v/v/v* for 2.5 min. After centrifugation, 1 mL of the clear methanol/water-phase was vacuum dried and reconstituted in water/ACN (98:2) *v/v* before injection.

Brewed coffee (Italian espresso). 10 g freshly grinded coffee beans (100% Arabica beans) were brewed with 30 mL hot water. After centrifugation, the supernatant was diluted 1:10 with water/ACN (98:2) *v/v*.

Prior to each food sample, blank samples (water/ACN (98:2) *v/v*) were analyzed in order to subtract impurities and chemical noise from the sample results. Only features were reported which were exclusively found in food samples but not in the blank chromatograms.

A.2.4 Instrumental setup

Chromatographic analysis was carried out on a Thermo Scientific Dionex Ultimate 3000 system (Dreieich, Germany) equipped with two vacuum degassers, dual gradient pump (P1 and P2), a temperature controlled autosampler (AS), a thermostat-controlled column oven containing two 10-port 2-position valves, and a variable wavelength detector (UV). The autosampler temperature was set to $5 \text{ } ^\circ\text{C}$. Column temperature was maintained at $40 \text{ } ^\circ\text{C}$. Connections were made using stainless-steel Viper capillaries ($180 \text{ } \mu\text{m}$ ID; Thermo Scientific, Dreieich, Germany) with shortest possible lengths. A Kinetex C18 column ($2.1 \times 30 \text{ mm}$, $2.6 \text{ } \mu\text{m}$; Phenomenex, Aschaffenburg, Germany) was used for trapping hydrophobic analytes. For chromatographic separations, a ZIC-chILIC column ($2.1 \times 100 \text{ mm}$, $3 \text{ } \mu\text{m}$, Merck, Darmstadt, Germany) and a Kinetex C18 column ($2.1 \times 100 \text{ mm}$, $2.6 \text{ } \mu\text{m}$, Phenomenex, Aschaffenburg, Germany) were used. Samples and blanks were injected in the LC flow stream via full-loop-injection

(20 μL). The LC system was coupled to a Bruker maXis qTOF-MS equipped with an APOLLO II electrospray ion source (Bruker Daltonics, Bremen, Germany). Detection was run in both electrospray modes (ESI(-) and ESI(+)). Source settings in ESI(-) mode were: nebulizer pressure = 2 bar, dry gas flow = 10 L min^{-1} , dry gas temperature = 200 $^{\circ}\text{C}$, capillary voltage = 4.0 kV, end plate offset = -500 V, mass range = 50 – 1 500 m/z . Source settings in ESI(+) mode were: nebulizer pressure = 2 bar, dry gas flow = 10 L min^{-1} , dry gas temperature = 200 $^{\circ}\text{C}$, capillary voltage = 4.5 kV, end plate offset = +500 V, mass range = 50 – 1 500 m/z . The time-of-flight mass analyzer was calibrated by means of a commercial ESI Low Concentration Tune Mix (Agilent Technologies, Waldbronn, Germany). Additionally, prior to each chromatographic run, the same calibrants were injected for internal recalibration of each analyzed sample.

A.2.5 Chromatographic conditions

The RP mobile phase (P1) was a composition of 0.1% formic acid (solvent P1-A) and ACN + 0.1% formic acid (solvent P1-B). The HILIC mobile phase (P2) was a mixture of 5 mM ammonium formate/ACN (95:5) v/v (eluent P2-A) and ACN (eluent P2-B). Trapping phase (0-5 min) was run with isocratic conditions while RP and HILIC separations were run in gradient mode as shown in Table A.1. Columns were re-equilibrated for 15 min after each chromatographic run to reach initial conditions.

A.2.6 Data processing

Raw data were post-processed with Genedata Expressionist for MS 11.0 (Genedata, Basel, Switzerland). After chromatogram smoothing and noise subtraction, mass spectra were internally calibrated. For internal calibration, the same Tune Mix as above was injected prior to each sample injection. Next, retention times were aligned to correct for shifts between chromatograms. Peak picking was done based on a curvature-based algorithm and heavy isotopes were identified and removed. The final data matrix consists of grouped chromatographic features (aligned m/z -values and retention times) and peak intensities. Original values, such as retention times and m/z -values were retained in the matrix and used for method validation purposes. All further data processing and statistics were done in Microsoft Excel 2016 and R Statistical Language (version 3.4.1).^[199]

Table A.1 | Chromatographic conditions of the tandem HILIC-RP coupling

	Pump 1 (P1)			Pump 2 (P2)		Valve position
	Time (min)	%B	Flow ($\mu\text{L}/\text{min}$)	%B	Flow ($\mu\text{L}/\text{min}$)	Left right
Trap.	0.0	2.5	50	100.0	350	1_2 1_2
	5.0	↓	↓	↓	350	1_2 1_2
HILIC	5.1	↓	50	100.0	400	1_2 10_1
	18.0	↓	↓	40.0	↓	↓
	24.0	↓	↓	40.0	400	↓
	24.9	↓	400	↓	↓	1_2 10_1
RP	25.0	↓	↓	↓	↓	10_1 10_1
	26.0	2.5	↓	90.0	200	↓
	40.0	100.0	↓	↓	↓	↓
	45.0	100.0	↓	↓	↓	↓
Equil.	48.0	2.5	↓	↓	↓	↓
	60.0	2.5	400	90.0	200	10_1 10_1

A.3 Results and discussion

A.3.1 Principle setup

The here introduced tandem LC system is build up of a short C18 RP-column (trap column) and two analytical separation columns (zwitterionic HILIC and C18 RP). HILIC phases are known to retain hydrophilic compounds (*e.g.* carbohydrates, amino acids) while RP columns have a complementary retention preference for nonpolar substances. In addition, Chalcraft *et al.* showed that the combination of HILIC and RP columns provides maximum orthogonality.^[293] The system consists of three major steps: (i) loading/trapping phase (0-5 min), (ii) HILIC (5-25 min) and, (ii) RP separation (25–45 min). In a first step (0-5 min, Figure A.1a), the sample composition is passed through the trap column in isocratic mode. While hydrophobic analytes are retained on the C18 trap column more hydrophilic compounds are directly passed onto a HILIC phase. A T-piece and addition of high organic mobile phase ensures the immediate binding of hydrophilic analytes on the HILIC column. The combined eluent

composition during the trapping step at the HILIC column is 87.8% at a total flow rate of $400 \mu\text{L min}^{-1}$. A trapping time of five minutes ($50 \mu\text{L min}^{-1}$ flow rate) was found to be sufficient to remove most disturbing salts and other sample components, which cannot be separated neither by HILIC nor by RP. Two 10-port valves allow subsequent and independent chromatographic runs of the divided sample composition. First, compounds retained on the HILIC phase are separated running a linear gradient (5–25 min, Figure A.1b and Table A.1). In this time, the composition of the pump 1 flow (passes trap column and RP separation column) is hold at initial conditions. We could not observe considerable band broadening when the flow of P1 was kept at initial conditions during HILIC separation. After the HILIC separation, analytes trapped on the C18 trap column are consecutively separated by a linear gradient (25–45 min, Figure A.1c and Table A.1) by the two C18 RP columns. At the end of each run, the system is re-equilibrated to reach initial conditions. This type of instrumental setup allows two independent chromatographic runs, after dividing the analytes of a sample into a hydrophobic and hydrophilic part during the trapping phase, on two different analytical columns. By comparison, Pyke *et al.* used only one valve to switch between the three steps.^[297] In their setup, effluates of the HILIC and RP column were continuously recombined by a T-piece before entering the detector. By using a second valve, it was possible to transfer the column effluates individually into the mass spectrometer. Hence, conditions in the ion source are the same as in single one-dimensional LC and loss in ionization efficiency can be avoided.

A.3.2 Analysis of food-relevant reference standards

A selection of 34 food-relevant reference standards was analyzed with the HILIC-RP tandem coupling method as described above (chromatographic conditions are given in Table A.1). Standards included amino acids, carbohydrates, small dicarboxylic acids, and phenolic compounds covering a logP range from -3.5 to 2.1. Amino acids were injected with a concentration of $10 \mu\text{g mL}^{-1}$. All other standards were analyzed with a concentration of $20 \mu\text{g mL}^{-1}$, respectively. As shown in Figure A.2a rather hydrophilic compounds (amino acids, sugars, and dicarboxylates) were directly transferred onto the HILIC column during the loading phase and subsequently separated by HILIC. It is worth noting that succinate and ribose showed only weak retention on the HILIC phase and thus eluted already at the end of the trapping phase. By comparison, with except of pyrocatechol, all tested phenolic compounds were retained on the C18 trap column and consequently separated in the RP part. Although not all standards revealed baseline separated peaks, mass selective detection was able to resolve all tested standards with exception of isoleucine and leucine.

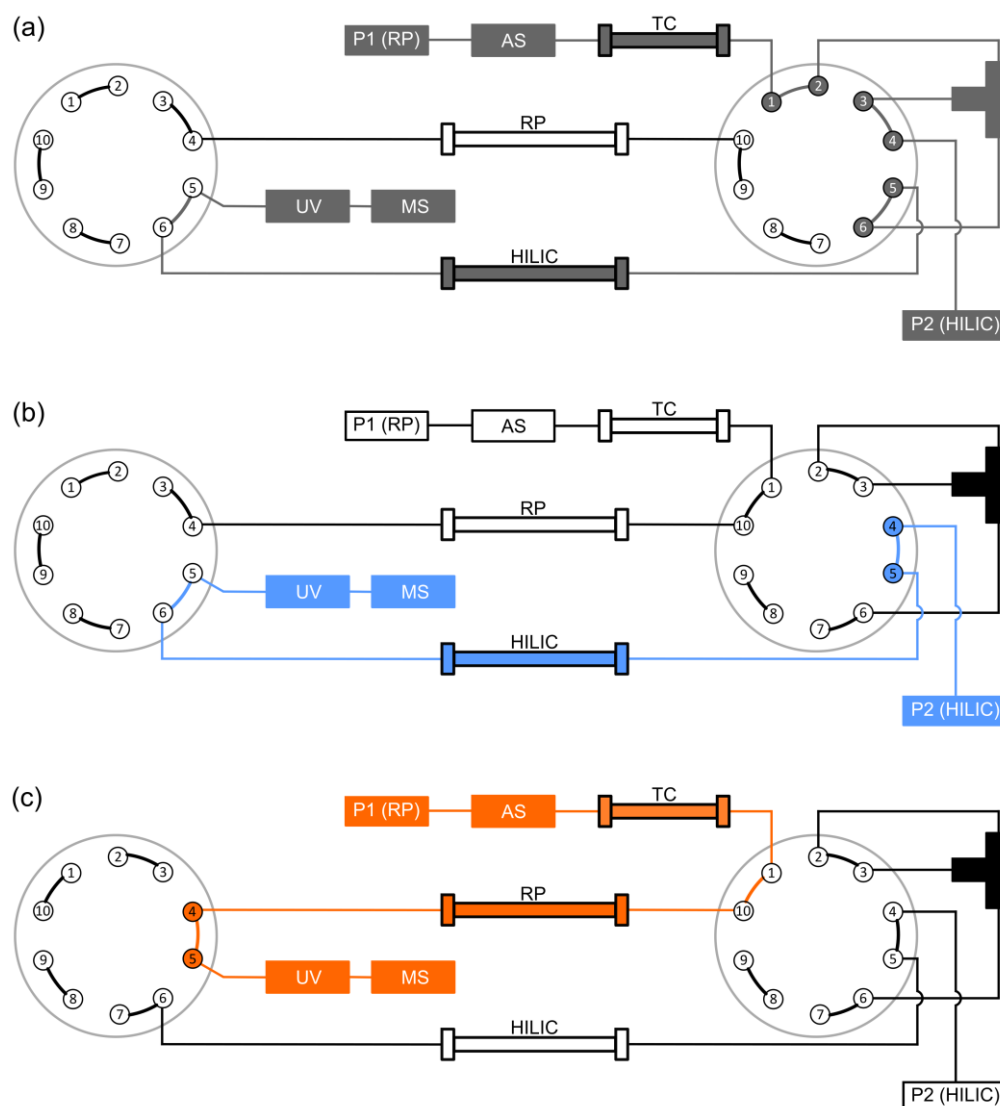


Figure A.1 | Configuration of the tandem HILIC-RP system. (a) Pre-fractionation of the sample in a first loading (trapping) step (0–5 min) into hydrophobic and hydrophilic compounds. Addition of high organic mobile phase via pump 2 and a T-piece ensures retention of hydrophilic compounds on the HILIC column. (b) Independent gradient elution of hydrophilic components retained on the HILIC column (5–25 min). (c) Independent gradient elution of hydrophobic components trapped on the RP column (25–45 min).

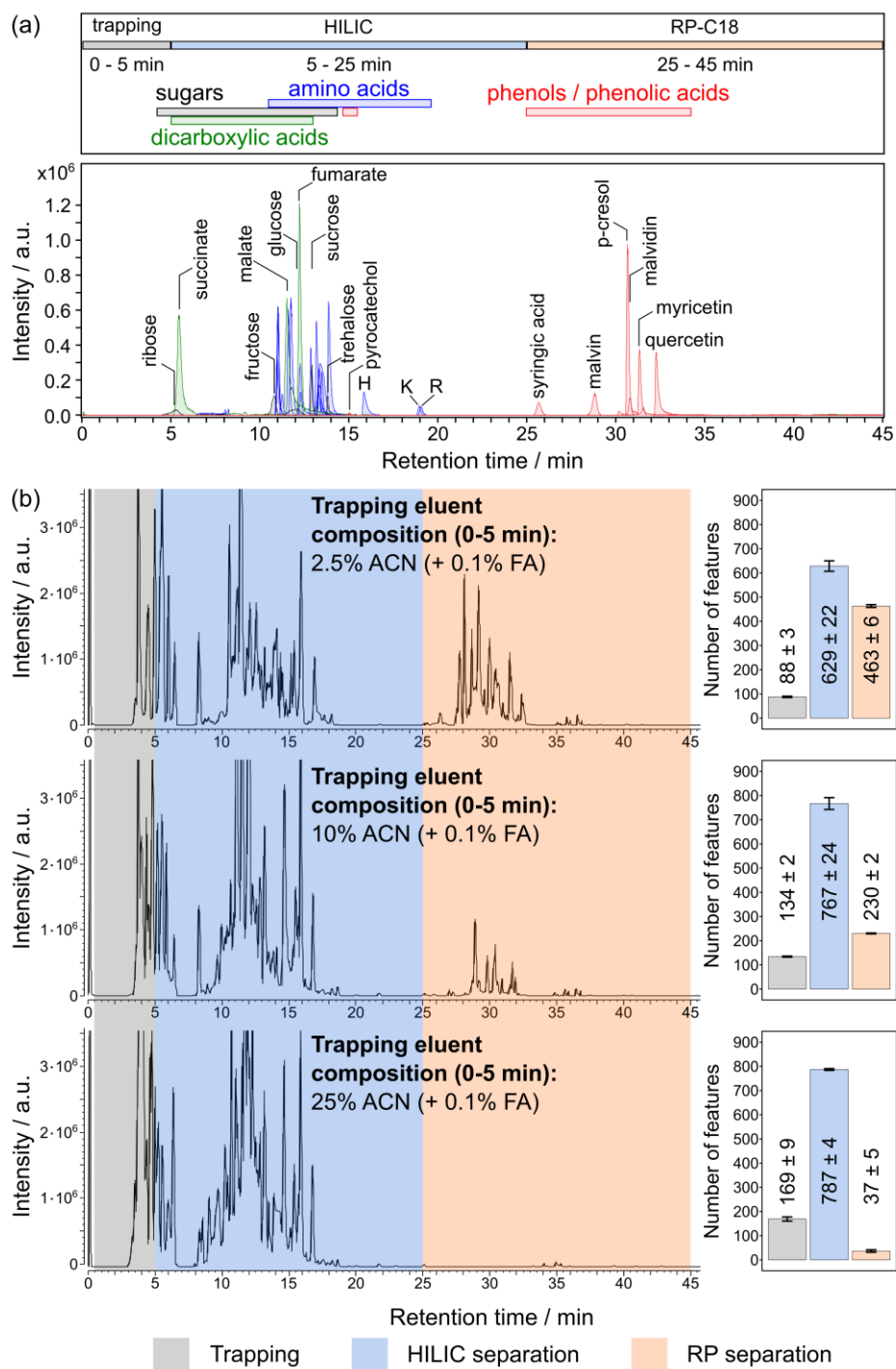


Figure A.2 | (a) Analysis of 34 food relevant reference standards including amino acids, mono- and disaccharides, dicarboxylic acids, and phenols. (b) Influence of the acetonitrile content in the eluent composition during the loading step (0–5 min) on the distribution of red wine components onto the HILIC or RP stationary phase. Bar charts illustrate the number of detected features ($S/N > 3$) in the three sections of the chromatogram, respectively. Error bars indicate the standard deviation of the mean ($n = 3$).

A.3.3 Online pre-fractionation of sample components (loading step)

The eluent composition during the trapping phase is crucial for the partitioning of sample analytes between the two analytical columns. The high chemical diversity^[287,301] and the simple and loss-free sample preparation (dilution) make wine an ideal food representative in the development and validation of non-targeted methods. Figure A.2b shows chromatograms of a red wine sample analyzed by three different eluent compositions during the trapping phase (0–5 min). Increasing the organic content of the eluent of P1 increases also the organic content of the combined eluent composition at the HILIC phase, thus, enhances the retention of more hydrophilic compounds on the HILIC column. Increasing the organic content of P1, however, counteracts with the capability of retaining hydrophobic compounds on the C18 trap column. Most equal distribution of analytes was achieved when the organic content was kept at a minimum (2.5% ACN, Figure A.2b). Increasing the ACN content of P1 reduced the number of analytes retained on the trap column dramatically. The number of features ($S/N > 3$) detected in ESI(-) after RP separation is halved when the ACN content of P1 is increased from 2.5% to 10%. Here, a feature is an analytical signal characterized by a unique retention time and ion mass.^[166,302] When using a P1-ACN content of 2.5% 463 ± 6 features could be detected after RP separation compared to 230 ± 2 at P1=10% ACN. Although the total number of detected features was very similar (1 180 at P1=2.5% ACN, 1 131 at P1=10% ACN) an uneven distribution of the analytes increases the number of co-eluting compounds, thus, complicating subsequent detection, e.g. by an increased chance of ion suppression in mass spectrometry. Moreover, when using a low ACN concentration during the trapping period, the number of weakly resolved signals in the first five minutes can be minimized. In this region of the chromatogram highest effects of ion suppression must be expected.^[293] Signals eluting during the first five minutes result from compounds that are not or only weakly retained on the C18 trap column and the HILIC column. A P1-ACN content of 25% was found to be already high enough to minimize wine analytes retained on the trap column to less than 10% (37 ± 5 detected features) compared to P1=2.5% ACN (463 ± 6).

A.3.4 Non-targeted analysis of red wines

Next, we analyzed a red wine sample (1:5 dilution, v/v) in $n = 9$ replicate measurements with the optimized conditions as described before. Using both electrospray modes, ESI(-) and ESI(+), in total 4 400 different features were found in all nine replicate measurements but not in blank samples, respectively (Figure A.3a-c). Only 255 features, having the same neutral monoisotopic mass (± 10 ppm) and retention time

(± 0.3 min) could be detected likewise in both ionization modes (Figure A.3c). 147 of the features found in both ionization modes could be separated by RP chromatography compared to 101 features separated by HILIC. Overall, in ESI(+) mode we could detect approx. twice the number of features as compared to ESI(-). However, the number of features was 1.7 and 2.4 times higher in ESI(+) after HILIC and RP separation, respectively. The different factors could arise from the type of compounds separated by the two stationary phases and the eluent composition. Here, we used in both electrospray modes addition of 0.1% formic acid to the RP eluent which is known to enhance MS response in positive ionization mode. By comparison, the HILIC separation was performed using an almost neutral eluent composition of 5 mM ammonium formate and ACN.

Precision of the method. The precision of retention times was evaluated by injection of $n = 9$ replicates of a red wine sample. The relative standard deviation (RSD) was $<2\%$ for all 4 400 detected features derived from the original retention times (none-aligned retention times). This is in good agreement with other dual-column methods.^[293,297] Additionally, the majority ($>98\%$) of detected features showed a random distribution of retention time values among the nine replicates and none of the retention times showed a relative deviation greater 3% from its mean, respectively (Figure A.3d). In general, features detected during the RP separation revealed slightly better run-to-run repeatability than those detected during the HILIC separation.

Retention characteristics of the stationary phase. We searched for possible compound classes in FooDB (<http://foodb.ca>, release: 06/29/2017) to gain more information about the retention behavior of the two columns. Database searches were done only based on the experimental monoisotopic mass (± 10 ppm) and multiple annotations were allowed. This results in a list of possible compound annotations and the corresponding compound classes. Although this approach does not provide unambiguous identifications, it gives valuable information about the distribution of compound classes between the two columns. Most of the putatively metabolites found in the database belong to compound classes that are known for their relevance in wine (Figure A.4). The majority of compounds separated by the RP column were assigned as phenylpropanoids, polyketides, lipids and lipid-like molecules (68% of database findings) indicating especially a strong selectivity of the RP column for flavonoids. The number of possibly detected flavonoids was slightly higher in positive ionization (Figure A.4b), even though in most studies ESI(-) is the method of choice for the analysis of these type of compounds.^[303,304] On the one hand, it must be noted that we used addition of 0.1% formic acid consistently in both ionization modes for the RP mobile phase which could play a role in the preferred ionization efficiency in ESI(+). On the other hand, however, quite a remarkable number of flavonoids, such as anthocyanins, per se are positively charged.

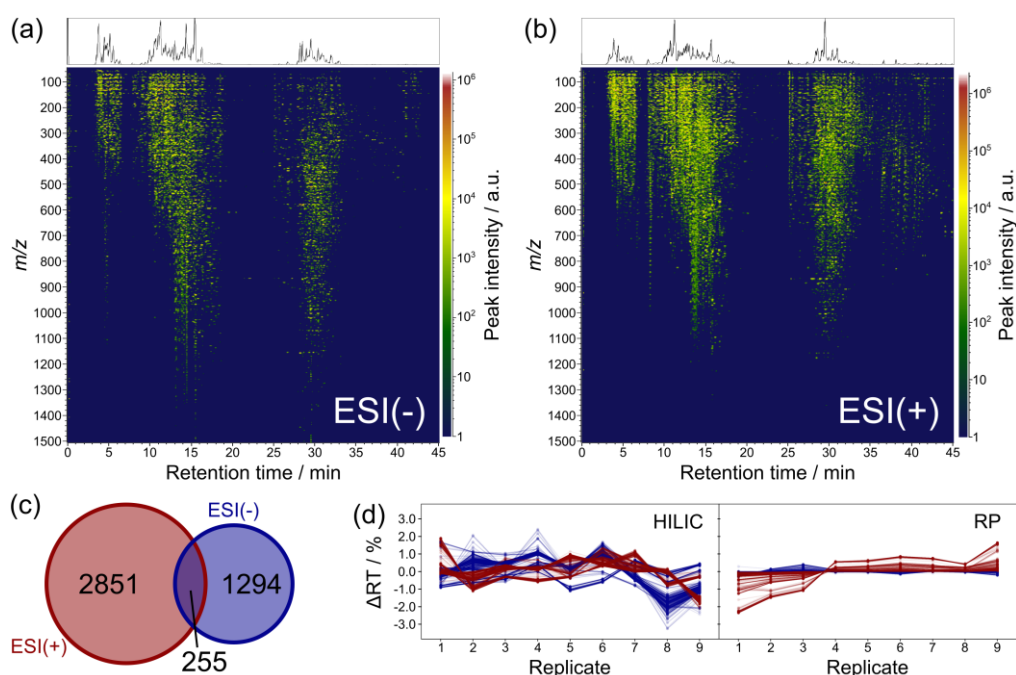


Figure A.3 | Non-target analysis of a red wine sample by tandem HILIC-RP chromatography. (a-b) Retention time versus m/z -value plots of processed results obtained in electrospray negative (ESI(-)) and positive (ESI(+)) mode, respectively. Each dot represents an analytical signal (feature) colored according to the observed peak intensity. (c) Comparison of detected features in ESI(+) and ESI(-) mode. (d) Relative deviation of the retention times of all detected features from the mean for nine replicate measurements detected during HILIC (left) and RP separation (right); ESI(+) = red; ESI(-) = blue.

While rather hydrophobic compounds showed a clear preference for the RP column, HILIC revealed stronger retention selectivity for polar compounds, such as carbohydrates and organic acids (Figure A.4). Interestingly, we observed a clear difference in selectivity of the ionization modes for the number of carbohydrates and organic acids putatively annotated in the database. Negative ionization mode could reveal more carbohydrates while carboxylic acids were preferentially detected by ESI(+). Further subdivision revealed that carboxylic acid derivatives detected in ESI(+) were exclusively annotated as amino acids or peptides. By comparison, around 30% of annotated carboxylic acid derivatives found in ESI(-) were mono-, or oligo-carboxylates (17/56) while the remaining 70% were amino acids and peptides (39/56).

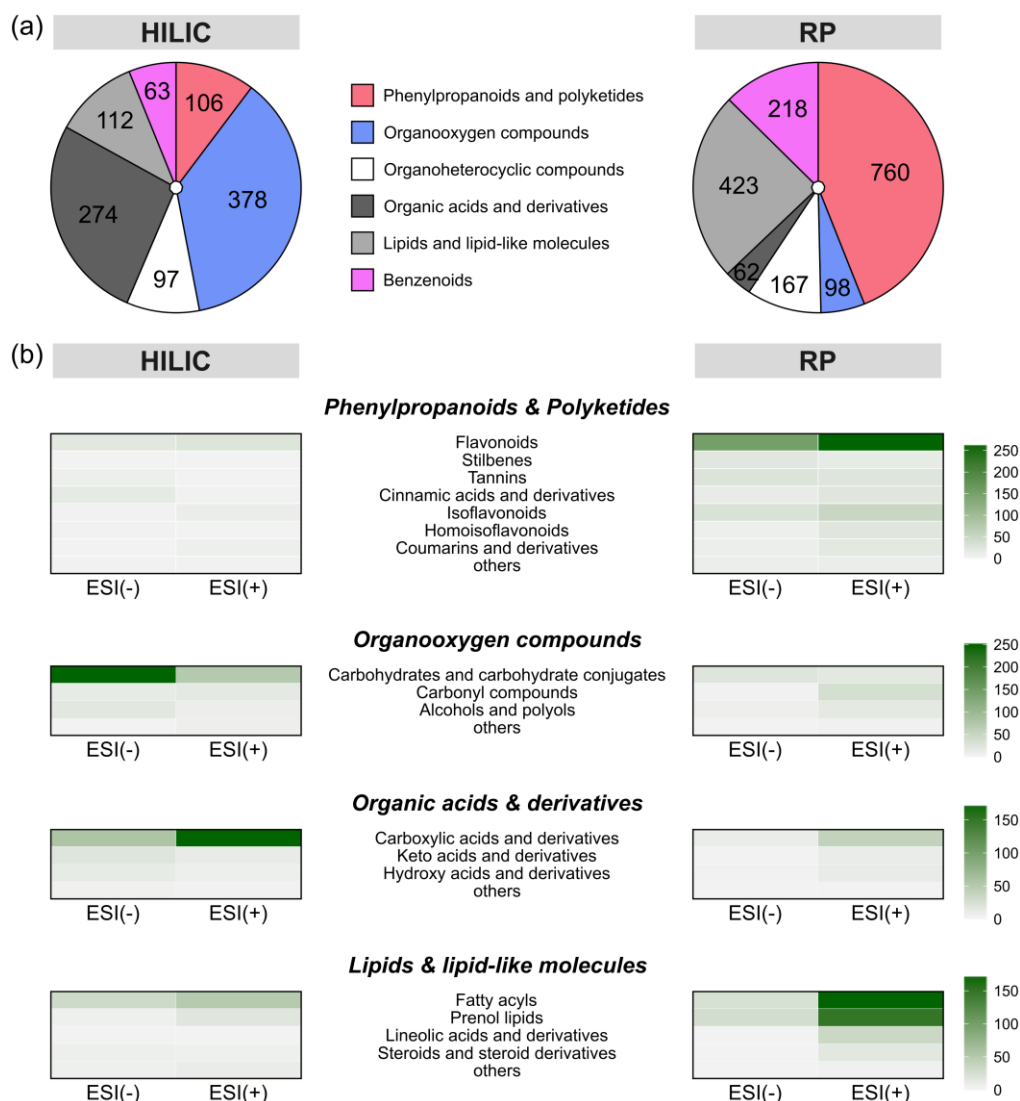


Figure A.4 | Selectivity of the two analytical columns used in the tandem LC system and selectivity of ionization modes for food relevant compound classes. (a) Pie charts illustrating the preferred selectivity of the HILIC and RP column. (b) Sub-classification of major compound classes.

A.3.5 Application to other food samples

We applied the above-described HILIC-RP tandem method to the non-targeted analysis of additional food samples. In this proof-of-concept test, we measured a beef meat extract and a diluted Italian espresso (coffee extract). After chromatographic separation, food components were recorded by MS in ESI(+) mode. Both samples showed a comparable number of recorded features (Table A.2 and Figure A.5). The total number of detected features was 1 633 and 1 797 found in the meat extract and

brewed coffee, respectively. Similar to the results we obtained for the red wine sample, in both samples approx. 50% of the features were recorded after HILIC separation indicating an equal distribution of sample compounds. Hence, the method presented here is not limited to the analysis of wine samples. It rather can be used as a routine platform in the non-target screening of different food samples.

Table A.2 | Number of features (retention time–*m/z*-pairs) detected in a beef meat extract and brewed coffee by ESI(+)-MS.

Sample	Total number of features	Trapping (0-5 min)	HILIC (5-25 min)	RP (25-45 min)
Beef meat extract	1 633	109	875	649
Coffee extract	1 797	216	936	645

The same database search as described above revealed that most of the features detected in the meat extract could be attributed to lipid- and organic acid derivatives, including amino acids and peptides (Figure A.6). Although fatty acids were partially removed in the sample preparation, more than 70% of database findings of those compounds retained on the RP column were lipid-type molecules. Main compound classes found for coffee metabolites were lipid-like molecules, benzenoids, phenylpropanoids, phenylketides, and heterocyclic compounds (*e.g.* furans, pyrans and pyrazines; Figure A.6).

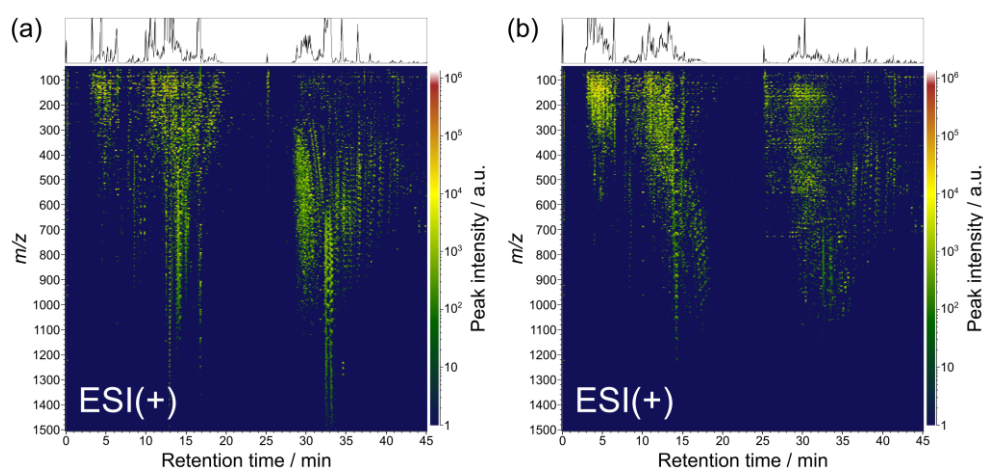


Figure A.5 | Non-target analysis of a (a) beef meat extract and (b) coffee extract by tandem HILIC-RP chromatography, respectively. Retention time versus m/z -value plots of processed results obtained in electrospray positive (ESI(+)) mode. Each dot represents an analytical signal (feature) colored according to the observed peak intensity.

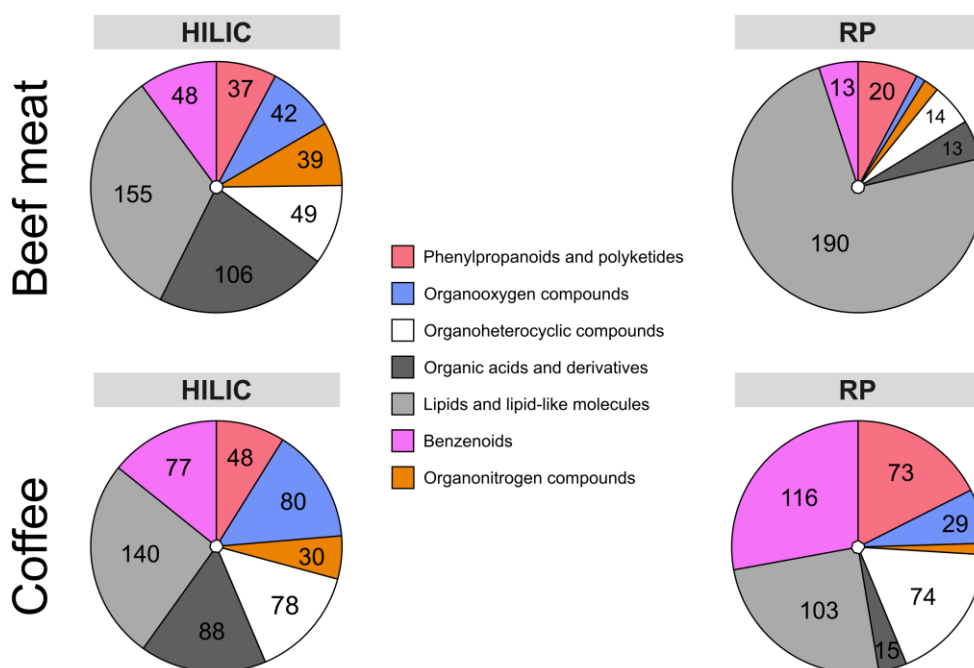


Figure A.6 | Selectivity of the two analytical columns used in the tandem LC system for food relevant compound classes. Compound classes were obtained from searching possible metabolites in FooDB database (<http://foodb.ca>, release: 06/29/2017) based on the experimental mass (± 10 ppm). Pie charts illustrating the preferred selectivity of the HILIC and RP column for a measured meat and coffee extract.

A.4 Conclusions

The presented HILIC-RP tandem coupling allows sensitive and precise analysis of food metabolites covering a large polarity range in a single chromatographic run. We showed that the combination of two columns with high orthogonality (HILIC and RP) increases the polarity range covered from highly polar (*e.g.* carbohydrates, oligo-carboxylic acids) to nonpolar compounds (*e.g.* flavonoids) which is of particular importance in comprehensive non-targeted studies. Analysis of a red wine sample revealed more than 4 000 features detected by high-resolution MS. Although we mainly used a red wine sample for method development and validation, the potential of this method in the application to other types of food samples has been proven. Moreover, there is no reason to be restricted to foods. We believe that this method is valuable for the analysis of small molecules (metabolites) in a wide range of different sample matrices.

Dual-column tandem chromatography does not require complicated instrumentation and software setups, such as in comprehensive 2D-LC. Compared to serial couplings individual gradients for each separation column can be used independently. In theory, there is no limitation in the types of columns, which are connected in the system. When the aim is to measure as many compounds as possible in a single run, columns of highest possible orthogonality (complementary columns) should be favored. Nevertheless, combination of less complementary columns could have also specific advantages. For example, coupling of two RP columns with different surface chemistries (*e.g.* Phenyl/C18 or C8/C18) could enhance the total peak capacity, selectivity and separation efficiency specifically for hydrophobic compound classes (*e.g.* lipids and lipid-type molecules) compared to single column LC. Depending on the sample extraction, in some cases it could be useful to change the order of the two columns. Sample extracts containing high amounts of organic solvent (*e.g.* after protein precipitation) could benefit from a reversed column order and a hydrophilic trap column. Optimization regarding high-throughput and run-time reduction was not the aim of this study. Further method development is needed to reduce sections in the chromatogram of poor peak capacity. Additionally, the use of columns with smaller particles (UPLC) may further reduce the overall run time.

B Appendix Chapter 2

B.1 Processing of FT-ICR-MS data

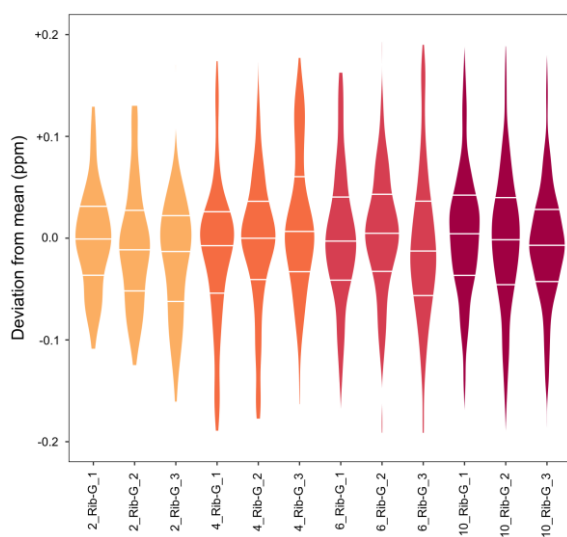


Figure B.1 | Peak alignment based on experimental m/z -values with maximum of 1 ppm alignment window. Violin plots illustrate the quality of the alignment. Violins are horizontally divided into 25%, 50%, and 75% quantiles.

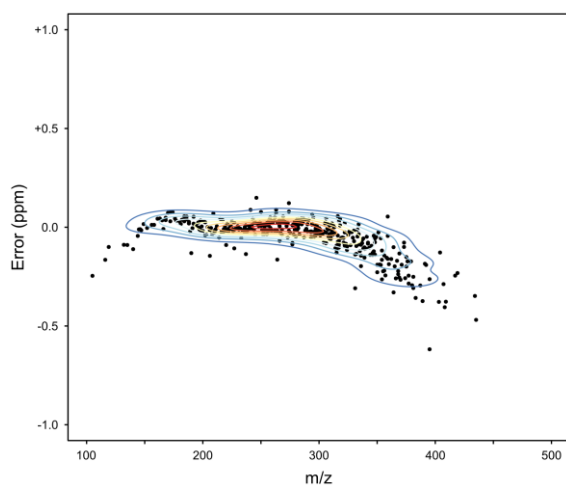


Figure B.2 | Error plot retrieved after molecular formula assignment. More than 90% of all molecular formulae were found within an error range of ± 200 ppb, more than 75% within ± 100 ppb.

B.2 Classification into reaction pools

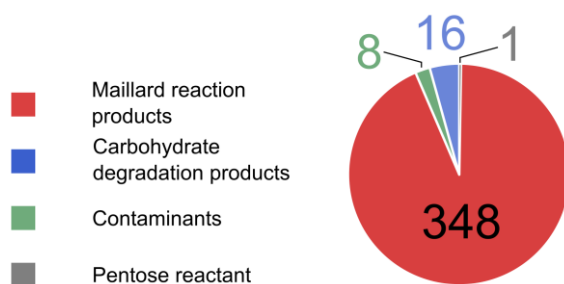
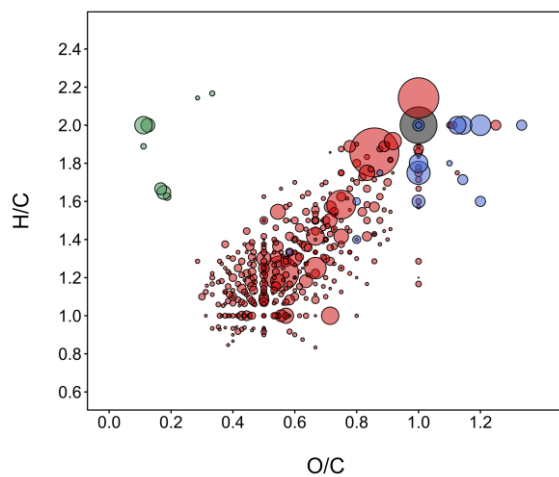


Figure B.3 | Classification of a ribose-glycine model system (10 h) into reaction pools according to the approach of Yaylayan.^[159]

B.3 Assigned molecular formulae

Table B.1 | List of assigned molecular formulae classified as Maillard reaction products and ribose.

Peak no.	<i>m/z</i>	Error (ppm)	Molecular formula (neutral)	Time (h)	Peak no.	<i>m/z</i>	Error (ppm)	Molecular formula (neutral)	Time (h)
1	116.03530	-0.17	C4H7NO3	6	34	191.05611	-0.01	C7H12O6	10
2	132.03022	-0.09	C4H7NO4	6	35	192.05137	0.02	C6H11NO6	10
3	135.02989	-0.09	C4H8O5	2	36	192.06663	0.05	C10H11NO3	6
4	140.03530	-0.11	C6H7NO3	10	37	194.04589	0.01	C9H9NO4	4
5	144.03023	-0.04	C5H7NO4	10	38	196.02515	0.00	C8H7NO5	10
6	145.01425	-0.01	C5H6O5	10	39	196.06154	0.02	C9H11NO4	4
7	146.04588	-0.01	C5H9NO4	2	40	197.05678	-0.01	C8H10N2O4	6
8	149.04555	0.02	C5H10O5	2	41	198.04081	0.04	C8H9NO5	6
9	152.03532	0.00	C7H7NO3	6	42	198.07718	-0.02	C9H13NO4	6
10	156.03024	0.01	C6H7NO4	10	43	199.03605	0.00	C7H8N2O5	10
11	158.04588	0.01	C6H9NO4	6	44	200.05644	-0.02	C8H11NO5	6
12	161.04556	0.04	C6H10O5	10	45	201.04047	0.03	C8H10O6	10
13	166.05097	-0.01	C8H9NO3	10	46	202.03571	-0.04	C7H9NO6	6
14	168.03024	0.04	C7H7NO4	4	47	202.07210	0.03	C8H13NO5	10
15	168.06663	0.05	C8H11NO3	6	48	203.05611	-0.04	C8H12O6	10
16	170.04590	0.07	C7H9NO4	4	49	204.05136	0.00	C7H11NO6	2
17	172.02515	0.03	C6H7NO5	10	50	206.04585	-0.15	C10H9NO4	10
18	172.06155	0.08	C7H11NO4	10	51	206.06701	-0.02	C7H13NO6	2
19	174.04081	0.08	C6H9NO5	6	52	207.05103	0.00	C7H12O7	6
20	176.05646	0.04	C6H11NO5	10	53	208.06153	-0.04	C10H11NO4	6
21	177.04047	0.03	C6H10O6	6	54	209.05680	0.07	C9H10N2O4	10
22	180.06662	0.03	C9H11NO3	10	55	210.04079	-0.02	C9H9NO5	4
23	181.06187	0.02	C8H10N2O3	10	56	210.07718	-0.03	C10H13NO4	10
24	182.04589	0.04	C8H9NO4	6	57	211.07243	-0.01	C9H12N2O4	10
25	184.02516	0.06	C7H7NO5	2	58	212.05645	0.01	C9H11NO5	2
26	184.06154	0.03	C8H11NO4	6	59	214.03570	-0.05	C8H9NO6	6
27	185.04556	0.04	C8H10O5	10	60	215.05612	0.04	C9H12O6	10
28	186.04081	0.04	C7H9NO5	4	61	216.05136	-0.02	C8H11NO6	6
29	186.07719	0.05	C8H13NO4	10	62	216.08776	0.04	C9H15NO5	10
30	188.02007	0.02	C6H7NO6	6	63	217.04662	0.04	C7H10N2O6	10
31	188.05645	0.03	C7H11NO5	2	64	218.03063	-0.01	C7H9NO7	10
32	189.04046	-0.02	C7H10O6	10	65	218.06701	-0.02	C8H13NO6	2
33	190.07207	-0.13	C7H13NO5	10	66	219.05103	0.00	C8H12O7	6

Time: Reaction time when MRP was detected (SN >= 8) for the first time.

Table B.1 (continued) | List of assigned molecular formulae classified as Maillard reaction products and ribose.

Peak no.	<i>m/z</i>	Error (ppm)	Molecular formula (neutral)	Time (h)	Peak no.	<i>m/z</i>	Error (ppm)	Molecular formula (neutral)	Time (h)
67	220.04627	-0.02	C7H11NO7	10	102	245.06667	-0.04	C10H14O7	10
68	220.06151	-0.09	C11H11NO4	10	103	245.07792	0.02	C9H14N2O6	6
69	220.08266	-0.01	C8H15NO6	6	104	246.06193	0.02	C9H13NO7	10
70	222.04079	-0.02	C10H9NO5	10	105	246.09835	0.15	C10H17NO6	10
71	222.06192	-0.02	C7H13NO7	6	106	248.05645	0.01	C12H11NO5	10
72	222.07718	-0.01	C11H13NO4	10	107	248.07758	0.01	C9H15NO7	4
73	224.05645	0.01	C10H11NO5	4	108	249.06160	0.02	C9H14O8	10
74	224.07758	-0.01	C7H15NO7	2	109	249.08809	0.02	C12H14N2O4	10
75	225.05170	0.03	C9H10N2O5	10	110	250.07212	0.08	C12H13NO5	10
76	226.03571	-0.01	C9H9NO6	10	111	250.09323	0.01	C9H17NO7	2
77	226.07209	-0.02	C10H13NO5	4	112	251.06734	-0.01	C11H12N2O5	10
78	227.05609	-0.11	C10H12O6	10	113	252.05135	-0.04	C11H11NO6	6
79	227.06735	0.02	C9H12N2O5	10	114	252.07249	-0.03	C8H15NO8	4
80	228.05136	-0.01	C9H11NO6	4	115	252.08775	0.01	C12H15NO5	6
81	228.08775	-0.01	C10H15NO5	6	116	253.05651	0.00	C8H14O9	6
82	230.06701	0.01	C9H13NO6	4	117	253.08299	-0.02	C11H14N2O5	10
83	231.05103	-0.01	C9H12O7	10	118	254.06702	0.01	C11H13NO6	4
84	232.04628	-0.01	C8H11NO7	10	119	255.05102	-0.04	C11H12O7	10
85	233.06667	-0.05	C9H14O7	10	120	256.04627	-0.02	C10H11NO7	10
86	234.06193	-0.01	C8H13NO7	6	121	256.08267	0.01	C11H15NO6	4
87	236.05644	-0.02	C11H11NO5	10	122	257.06668	0.02	C11H14O7	10
88	236.07758	0.00	C8H15NO7	6	123	257.07792	0.04	C10H14N2O6	6
89	237.05169	-0.02	C10H10N2O5	10	124	258.06194	0.05	C10H13NO7	6
90	237.08805	-0.14	C11H14N2O4	10	125	258.09831	0.00	C11H17NO6	2
91	238.03571	-0.01	C10H9NO6	10	126	259.04594	-0.02	C10H12O8	10
92	238.07209	-0.02	C11H13NO5	4	127	259.05717	-0.02	C9H12N2O7	10
93	240.05136	-0.01	C10H11NO6	6	128	260.05646	0.03	C13H11NO5	10
94	240.08775	0.01	C11H15NO5	6	129	260.07758	0.02	C10H15NO7	4
95	241.04663	0.09	C9H10N2O6	10	130	262.05686	0.05	C9H13NO8	10
96	241.08300	0.00	C10H14N2O5	10	131	262.07209	-0.02	C13H13NO5	10
97	242.06702	0.01	C10H13NO6	2	132	262.09322	-0.02	C10H17NO7	10
98	243.05103	-0.01	C10H12O7	10	133	263.06737	0.07	C12H12N2O5	10
99	243.06227	0.04	C9H12N2O6	10	134	264.05137	0.03	C12H11NO6	10
100	244.04628	0.02	C9H11NO7	10	135	264.07245	-0.16	C9H15NO8	10
101	244.08266	-0.01	C10H15NO6	6	136	264.08774	-0.02	C13H15NO5	10

Time: Reaction time when MRP was detected (SN >= 8) for the first time.

Appendix B | Assigned molecular formulae

Table B.1 (continued) | List of assigned molecular formulae classified as Maillard reaction products and ribose.

Peak no.	<i>m/z</i>	Error (ppm)	Molecular formula (neutral)	Time (h)	Peak no.	<i>m/z</i>	Error (ppm)	Molecular formula (neutral)	Time (h)
137	265.08300	0.02	C12H14N2O5	6	172	285.07284	0.05	C11H14N2O7	10
138	266.06702	0.04	C12H13NO6	6	173	285.08273	0.02	C9H18O10	6
139	266.08814	0.01	C9H17NO8	4	174	285.10922	0.02	C12H18N2O6	10
140	266.10338	-0.07	C13H17NO5	10	175	286.05685	0.02	C11H13NO8	10
141	267.07215	-0.03	C9H16O9	6	176	286.09324	0.05	C12H17NO7	6
142	267.09865	0.02	C12H16N2O5	10	177	287.08846	-0.05	C11H16N2O7	10
143	268.04627	-0.04	C11H11NO7	10	178	288.07250	0.04	C11H15NO8	6
144	268.08266	-0.01	C12H15NO6	4	179	288.10887	-0.02	C12H19NO7	10
145	269.07793	0.05	C11H14N2O6	6	180	289.08299	-0.01	C14H14N2O5	10
146	270.06193	0.02	C11H13NO7	4	181	290.06701	-0.02	C14H13NO6	10
147	270.09832	0.03	C12H17NO6	10	182	290.08815	0.02	C11H17NO8	6
148	272.07758	0.01	C11H15NO7	4	183	291.06227	0.04	C13H12N2O6	10
149	273.06158	-0.05	C11H14O8	10	184	292.08266	-0.02	C14H15NO6	10
150	273.07283	0.02	C10H14N2O7	10	185	293.07790	-0.03	C13H14N2O6	10
151	274.05688	0.12	C10H13NO8	10	186	293.11428	-0.05	C14H18N2O5	10
152	274.07209	-0.02	C14H13NO5	10	187	294.06193	0.01	C13H13NO7	10
153	274.09325	0.08	C11H17NO7	6	188	294.08306	0.02	C10H17NO9	6
154	275.07724	-0.03	C11H16O8	10	189	294.09833	0.07	C14H17NO6	10
155	277.05649	-0.09	C10H14O9	10	190	295.05717	-0.02	C12H12N2O7	10
156	277.08297	-0.08	C13H14N2O5	10	191	295.06707	-0.02	C10H16O10	6
157	277.11939	0.01	C14H18N2O4	10	192	295.09358	0.05	C13H16N2O6	6
158	278.06700	-0.04	C13H13NO6	6	193	296.07756	-0.05	C13H15NO7	6
159	278.08815	0.01	C10H17NO8	2	194	296.09869	-0.05	C10H19NO9	10
160	279.06227	0.03	C12H12N2O6	10	195	297.07282	-0.02	C12H14N2O7	10
161	279.09864	-0.01	C13H16N2O5	10	196	297.10920	-0.04	C13H18N2O6	10
162	280.04628	0.01	C12H11NO7	10	197	298.05683	-0.03	C12H13NO8	6
163	280.08267	0.02	C13H15NO6	6	198	298.09323	0.01	C13H17NO7	4
164	280.10378	-0.05	C10H19NO8	10	199	299.08847	-0.02	C12H16N2O7	4
165	281.03029	-0.02	C12H10O8	10	200	300.07249	-0.02	C12H15NO8	4
166	281.07792	0.04	C12H14N2O6	6	201	300.10888	-0.01	C13H19NO7	10
167	282.06193	0.01	C12H13NO7	6	202	301.08299	-0.04	C15H14N2O5	6
168	282.08307	0.04	C9H17NO9	10	203	301.10412	-0.01	C12H18N2O7	10
169	282.09831	-0.01	C13H17NO6	10	204	302.06701	-0.02	C15H13NO6	10
170	283.09355	-0.04	C12H16N2O6	10	205	302.08814	-0.03	C12H17NO8	2
171	285.03645	0.04	C10H10N2O8	10	206	303.08338	-0.03	C11H16N2O8	4

Time: Reaction time when MRP was detected (SN >= 8) for the first time.

Table B.1 (continued) | List of assigned molecular formulae classified as Maillard reaction products and ribose.

Peak no.	<i>m/z</i>	Error (ppm)	Molecular formula (neutral)	Time (h)	Peak no.	<i>m/z</i>	Error (ppm)	Molecular formula (neutral)	Time (h)
207	304.08266	-0.02	C15H15NO6	10	242	321.07281	-0.05	C14H14N2O7	10
208	304.10377	-0.08	C12H19NO8	10	243	321.10919	-0.08	C15H18N2O6	6
209	305.11430	0.02	C15H18N2O5	10	244	322.07794	-0.09	C11H17NO10	10
210	306.06190	-0.08	C14H13NO7	10	245	322.09322	-0.03	C15H17NO7	6
211	306.08305	-0.03	C11H17NO9	6	246	322.11437	0.02	C12H21NO9	10
212	306.09833	0.04	C15H17NO6	10	247	323.08845	-0.08	C14H16N2O7	6
213	307.06708	0.02	C11H16O10	10	248	324.07246	-0.12	C14H15NO8	10
214	307.09356	-0.01	C14H16N2O6	6	249	324.10885	-0.10	C15H19NO7	10
215	308.07758	-0.01	C14H15NO7	6	250	325.10411	-0.04	C14H18N2O7	6
216	308.09869	-0.05	C11H19NO9	10	251	326.08814	-0.02	C14H17NO8	10
217	309.06158	-0.06	C14H14O8	10	252	327.08336	-0.09	C13H16N2O8	10
218	309.07282	-0.03	C13H14N2O7	10	253	328.06740	-0.03	C13H15NO9	10
219	309.10922	0.01	C14H18N2O6	6	254	329.09902	-0.05	C13H18N2O8	10
220	310.05683	-0.05	C13H13NO8	10	255	330.08305	-0.02	C13H17NO9	10
221	310.09321	-0.06	C14H17NO7	6	256	330.11942	-0.07	C14H21NO8	10
222	311.08848	0.02	C13H16N2O7	10	257	331.07821	-0.31	C12H16N2O9	10
223	311.09837	-0.01	C11H20O10	10	258	331.09352	-0.14	C16H16N2O6	10
224	312.07250	0.01	C13H15NO8	10	259	332.07753	-0.14	C16H15NO7	10
225	312.10887	-0.04	C14H19NO7	10	260	332.09868	-0.10	C13H19NO9	10
226	313.10412	-0.03	C13H18N2O7	10	261	333.07282	-0.01	C15H14N2O7	10
227	314.08811	-0.11	C13H17NO8	6	262	333.10920	-0.05	C16H18N2O6	10
228	315.08336	-0.11	C12H16N2O8	10	263	334.07794	-0.09	C12H17NO10	6
229	315.09326	-0.09	C10H20O11	10	264	334.09322	-0.04	C16H17NO7	10
230	315.09861	-0.13	C16H16N2O5	10	265	334.11436	0.02	C13H21NO9	10
231	316.06743	0.06	C12H15NO9	10	266	335.08844	-0.12	C15H16N2O7	10
232	316.08264	-0.07	C16H15NO6	10	267	336.07246	-0.09	C15H15NO8	10
233	316.10378	-0.04	C13H19NO8	4	268	336.09356	-0.20	C12H19NO10	6
234	317.07789	-0.07	C15H14N2O6	10	269	336.10883	-0.14	C16H19NO7	10
235	317.08778	-0.10	C13H18O9	10	270	337.06772	-0.08	C14H14N2O8	6
236	317.09901	-0.09	C12H18N2O8	6	271	337.10411	-0.06	C15H18N2O7	6
237	317.11431	0.03	C16H18N2O5	10	272	338.08812	-0.06	C15H17NO8	10
238	318.08306	0.01	C12H17NO9	4	273	338.10924	-0.11	C12H21NO10	2
239	318.09833	0.04	C16H17NO6	10	274	339.08336	-0.10	C14H16N2O8	10
240	319.09355	-0.05	C15H16N2O6	10	275	339.10447	-0.15	C11H20N2O10	10
241	320.09869	-0.05	C12H19NO9	2	276	339.11974	-0.11	C15H20N2O7	10

Time: Reaction time when MRP was detected (SN >= 8) for the first time.

Appendix B | Assigned molecular formulae

Table B.1 (continued) | List of assigned molecular formulae classified as Maillard reaction products and ribose.

Peak no.	<i>m/z</i>	Error (ppm)	Molecular formula (neutral)	Time (h)	Peak no.	<i>m/z</i>	Error (ppm)	Molecular formula (neutral)	Time (h)
277	340.10376	-0.11	C15H19NO8	10	312	364.12480	-0.33	C14H23NO10	10
278	341.09903	-0.05	C14H18N2O8	10	313	365.09897	-0.20	C16H18N2O8	10
279	342.08303	-0.08	C14H17NO9	10	314	366.08296	-0.26	C16H17NO9	10
280	342.11942	-0.08	C15H21NO8	10	315	367.11463	-0.17	C16H20N2O8	10
281	343.09353	-0.10	C17H16N2O6	10	316	368.09863	-0.22	C16H19NO9	10
282	344.09866	-0.14	C14H19NO9	6	317	368.11975	-0.24	C13H23NO11	2
283	345.10918	-0.09	C17H18N2O6	10	318	369.09386	-0.26	C15H18N2O9	10
284	346.09318	-0.13	C17H17NO7	10	319	369.13029	-0.13	C16H22N2O8	10
285	346.11431	-0.14	C14H21NO9	10	320	370.11426	-0.27	C16H21NO9	10
286	347.08846	-0.04	C16H16N2O7	10	321	371.10954	-0.19	C15H20N2O9	10
287	347.12482	-0.12	C17H20N2O6	10	322	373.10409	-0.10	C18H18N2O7	10
288	348.07247	-0.08	C16H15NO8	10	323	373.14048	-0.08	C19H22N2O6	10
289	348.09360	-0.06	C13H19NO10	10	324	374.10918	-0.26	C15H21NO10	10
290	348.12996	-0.14	C14H23NO9	10	325	375.10447	-0.15	C14H20N2O10	6
291	349.10411	-0.05	C16H18N2O7	10	326	375.11970	-0.20	C18H20N2O7	10
292	350.08806	-0.23	C16H17NO8	10	327	376.12486	-0.17	C15H23NO10	6
293	350.10921	-0.19	C13H21NO10	10	328	377.09895	-0.25	C17H18N2O8	10
294	351.08338	-0.03	C15H16N2O8	10	329	377.13532	-0.29	C18H22N2O7	10
295	352.10373	-0.19	C16H19NO8	10	330	379.11463	-0.17	C17H20N2O8	10
296	353.09902	-0.06	C15H18N2O8	10	331	380.09860	-0.29	C17H19NO9	10
297	353.13536	-0.19	C16H22N2O7	10	332	381.09384	-0.31	C16H18N2O9	10
298	354.08300	-0.17	C15H17NO9	10	333	381.13025	-0.25	C17H22N2O8	10
299	354.10415	-0.12	C12H21NO11	10	334	383.10947	-0.36	C16H20N2O9	10
300	354.11935	-0.26	C16H21NO8	10	335	387.11966	-0.30	C19H20N2O7	10
301	355.11461	-0.22	C15H20N2O8	10	336	389.09890	-0.37	C18H18N2O8	10
302	356.09863	-0.22	C15H19NO9	10	337	391.11462	-0.19	C18H20N2O8	10
303	356.11979	-0.14	C12H23NO11	2	338	392.11976	-0.19	C15H23NO11	10
304	357.09387	-0.24	C14H18N2O9	10	339	395.10936	-0.62	C17H20N2O9	10
305	358.11430	-0.15	C15H21NO9	10	340	395.13063	-0.26	C14H24N2O11	10
306	359.08850	0.05	C17H16N2O7	10	341	403.11454	-0.38	C19H20N2O8	10
307	359.10955	-0.16	C14H20N2O9	10	342	404.11979	-0.13	C16H23NO11	10
308	359.12485	-0.04	C18H20N2O6	10	343	407.10949	-0.29	C18H20N2O9	10
309	360.09356	-0.19	C14H19NO10	10	344	408.15097	-0.41	C16H27NO11	10
310	362.10922	-0.16	C14H21NO10	2	345	409.12510	-0.38	C18H22N2O9	10
311	364.10376	-0.10	C17H19NO8	10	346	417.13024	-0.25	C20H22N2O8	10

Time: Reaction time when MRP was detected (SN >= 8) for the first time.

Table B.1 (continued) | List of assigned molecular formulae classified as Maillard reaction products and ribose.

Peak no.	<i>m/z</i>	Error (ppm)	Molecular formula (neutral)	Time (h)	Peak no.	<i>m/z</i>	Error (ppm)	Molecular formula (neutral)	Time (h)
347	419.13064	-0.23	C ₁₆ H ₂₄ N ₂ O ₁₁	10	349	435.14070	-0.47	C ₂₀ H ₂₄ N ₂ O ₉	10
348	434.13025	-0.35	C ₁₇ H ₂₅ NO ₁₂	10					

Time: Reaction time when MRP was detected (SN >= 8) for the first time.

Table B.2 | List of detected contaminants.

<i>m/z</i>	Error (ppm)	Molecular formula (neutral)	Source
255.23296	0.02	C ₁₆ H ₃₂ O ₂	Fatty acid 16:0
265.14791	0.02	C ₁₂ H ₂₆ O ₄ S	Alkyl sulfate
281.24861	0.03	C ₁₈ H ₃₄ O ₂	Fatty acid 18:1
283.26426	0.02	C ₁₈ H ₃₆ O ₂	Fatty acid 18:0
293.1792	-0.02	C ₁₄ H ₃₀ O ₄ S	Alkyl sulfate
297.15299	0.01	C ₁₆ H ₂₆ O ₃ S	Benzenesulfonic acid
311.16863	-0.02	C ₁₇ H ₂₈ O ₃ S	Benzenesulfonic acid
325.18428	-0.03	C ₁₈ H ₃₀ O ₃ S	Benzenesulfonic acid

B.4 Average carbon oxidation state

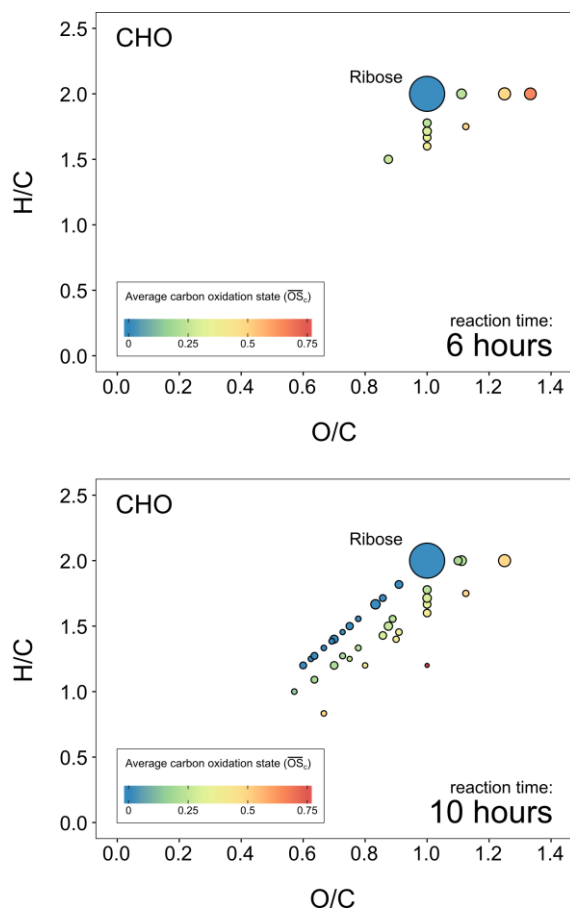


Figure B.4 | Van Krevelen diagrams (H/C vs. O/C) for nitrogen-free MRPs detected after six (top) and ten hours (bottom). Color code illustrates the average carbon oxidation state (\overline{OS}_C). Bubble size is scaled to relative peak intensity. $C_3H_6O_4$ (probably glyceric acid) was only detected in the Maillard model systems after six hours. However, it could also be produced when ribose was heated alone for ten hours.

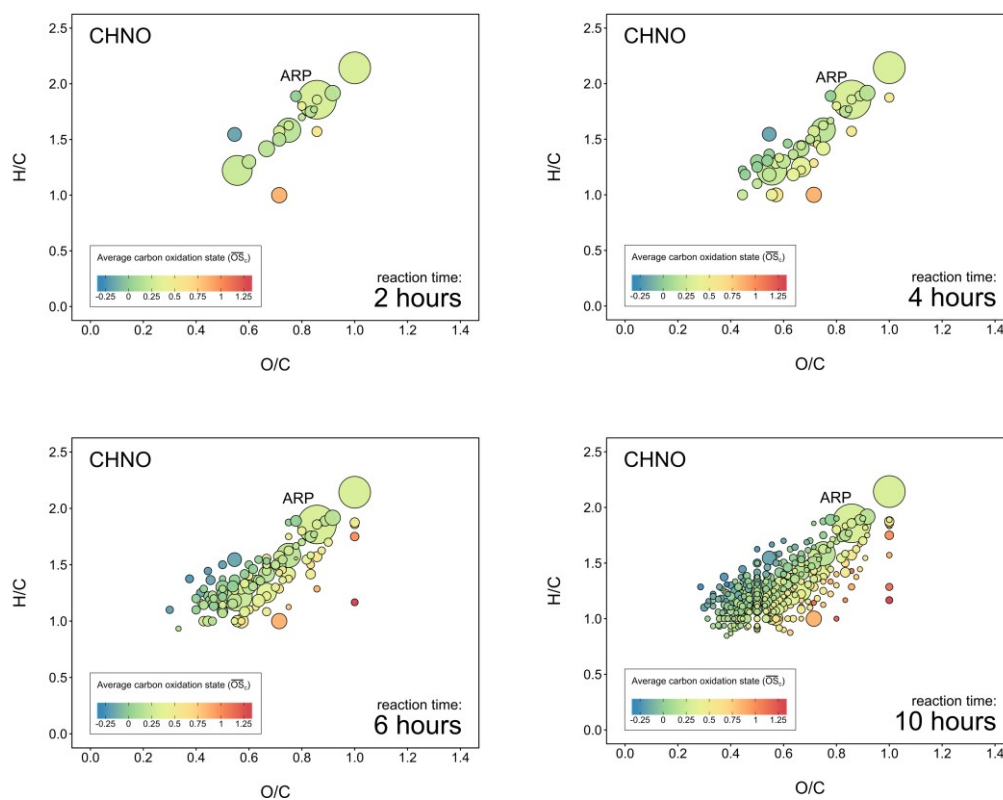


Figure B.5 | Van Krevelen diagrams (H/C vs. O/C) for nitrogen-containing MRPs detected at four different reaction times (two, four, six, and ten hours). Color code illustrates the average carbon oxidation state (OS_C). Bubble size is scaled to relative peak intensity.

C Appendix Chapter 3

C.1 Direct-infusion FT-ICR mass spectra

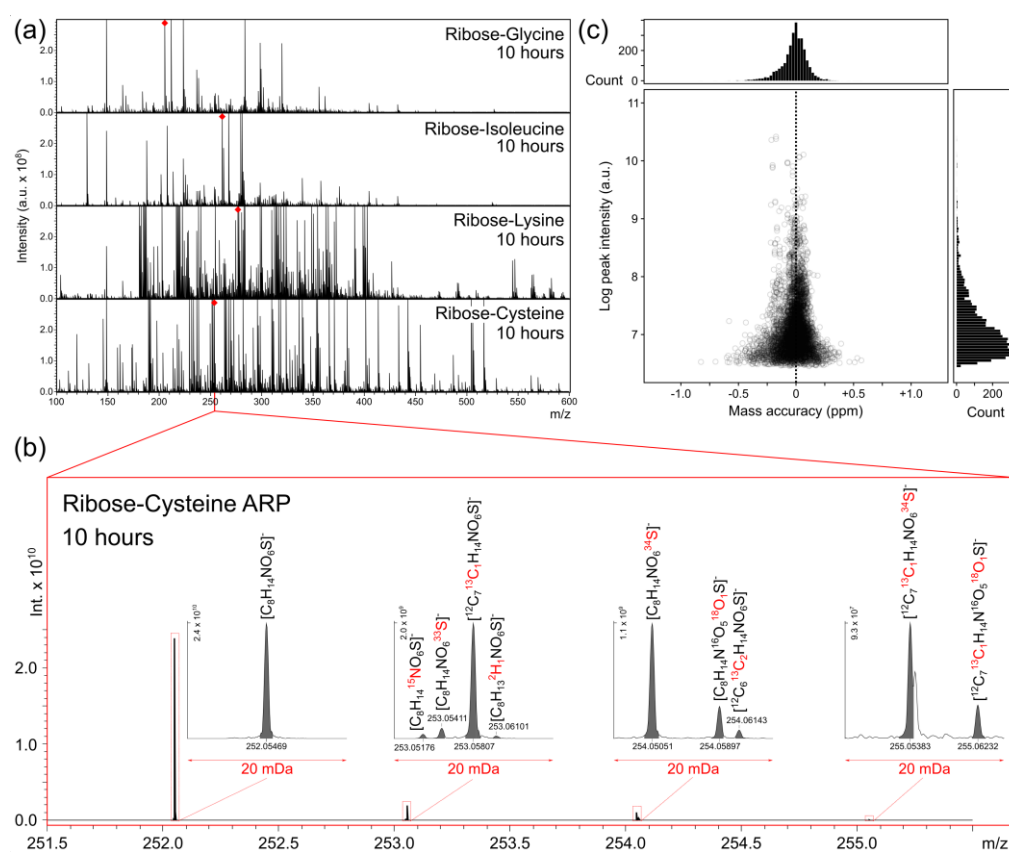


Figure C.1 | Direct-infusion FT-ICR-MS spectra. (a) Raw spectra of four different ribose-amino acid model systems heated for ten hours (100 °C). Red diamonds indicate the position of the Amadori rearrangement products in the mass spectra. (b) Isotopic fine structure validation of the ribose-cysteine Amadori product ion ($C_8H_{14}NO_6S^-$) by means of the exact masses and relative abundances of nine isotope signals. (c) Mass accuracy and peak intensity of 1 493 monoisotopic peaks assigned to their molecular formulae.

C.2 Classification of reaction products

Molecular formulae were classified according to Yaylayan into three different reaction product pools:^[159] (i) Maillard reaction products (MRPs), (ii) thermal induced carbohydrate degradation products, and (iii) amino acid degradation products. Ion signals, which were found exclusively in all three replicates of the model systems but not in the blank samples (ribose and amino acids heated alone) were classified as MRPs. Features also found in the ribose blank sample were classified as carbohydrate decomposition products. Those features, which were found in the model systems and the amino acid blank sample, were classified as amino acid decomposition products.

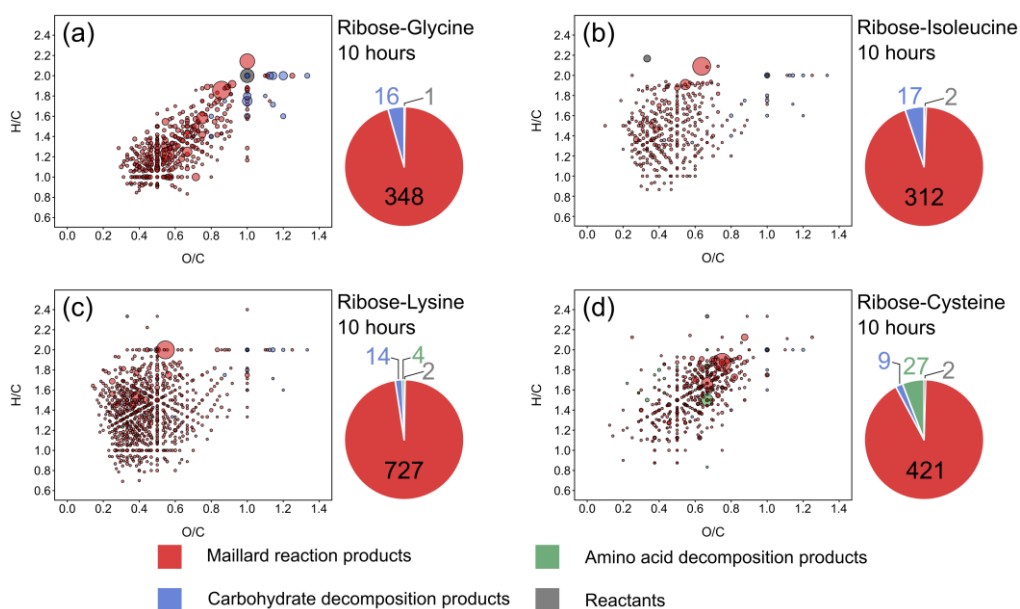


Figure C.2 | Classification of detected reaction products as Maillard reaction products (MRPs), carbohydrate and amino acid degradation products.

C.3 Consideration of different sugar precursors

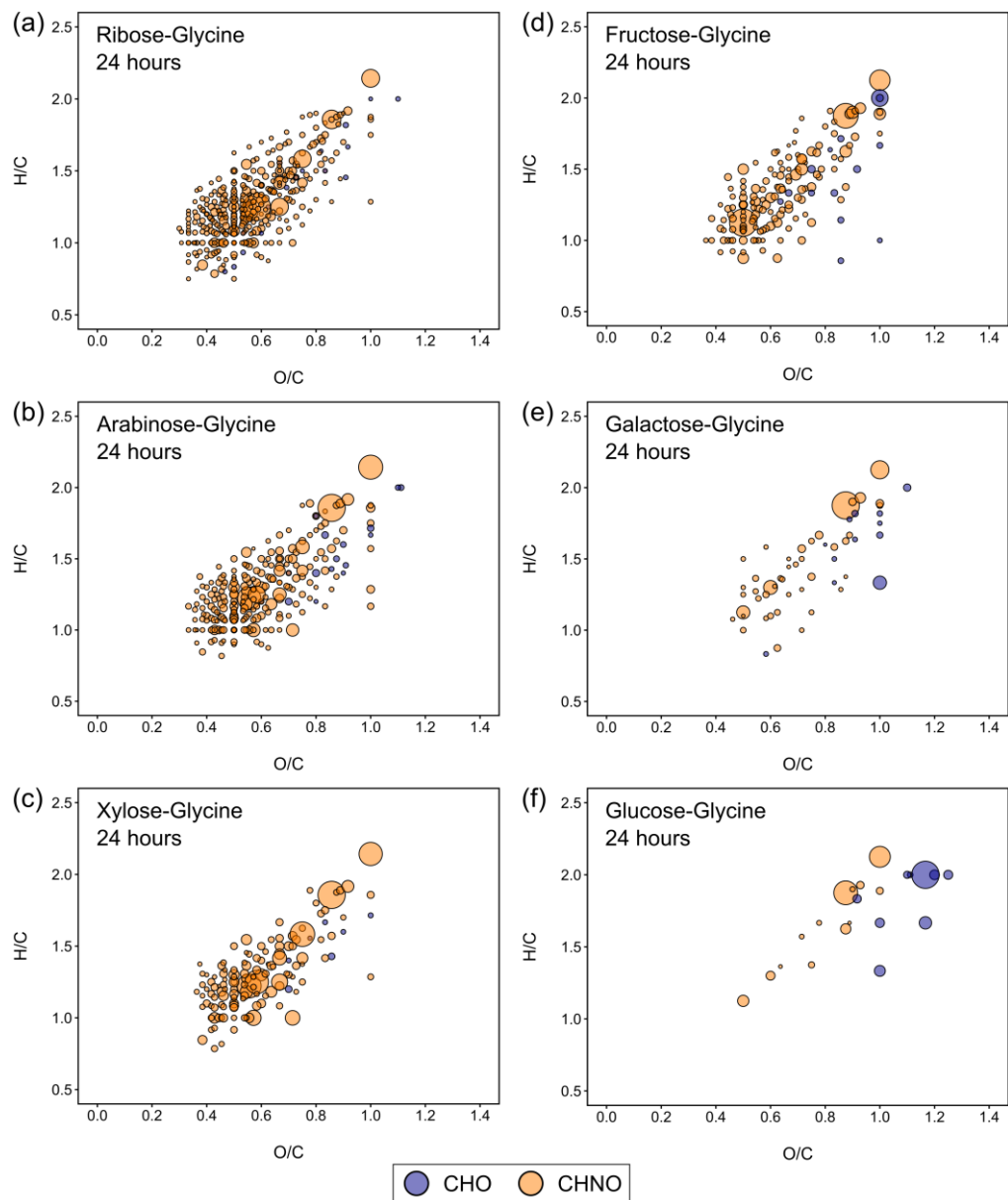
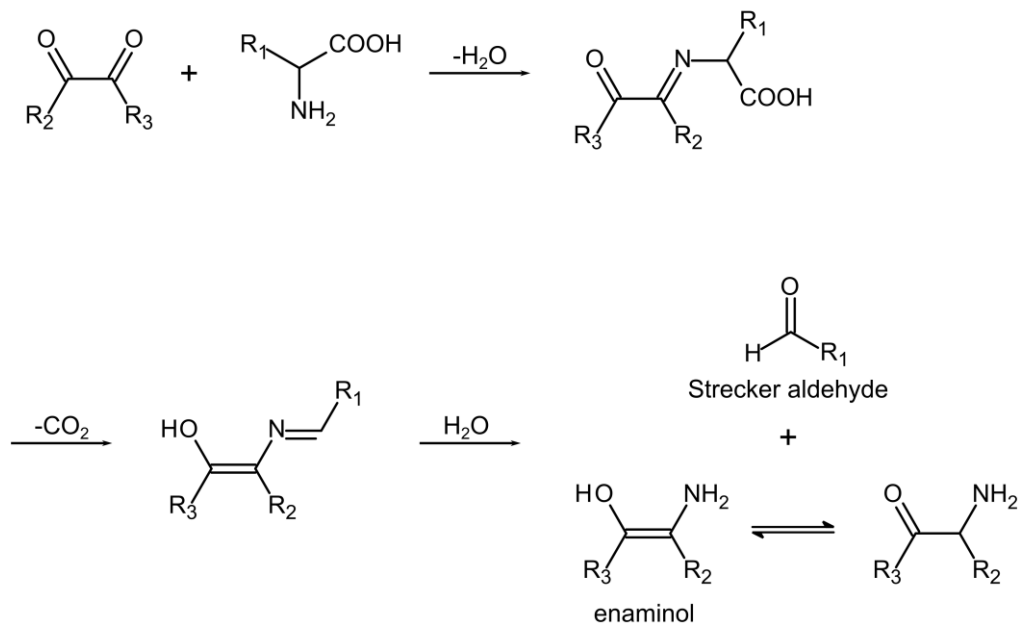


Figure C.3 | Van Krevelen diagrams of MRPs found in (a-c) three different pentose-glycine and (d-f) three hexose-glycine Maillard reaction model systems heated for 24 h at 100 °C.

C.4 Formation of enamminols and amino ketones



Scheme C.1 | Strecker degradation in the Maillard reaction. Enaminols and amino ketones formed in the Strecker degradation of amino acids by dicarbonyls could be a class of compounds with low H/C and O/C ratios as observed in the lysine and isoleucine Maillard reaction.

C.5 Compositional characterization of MRPs

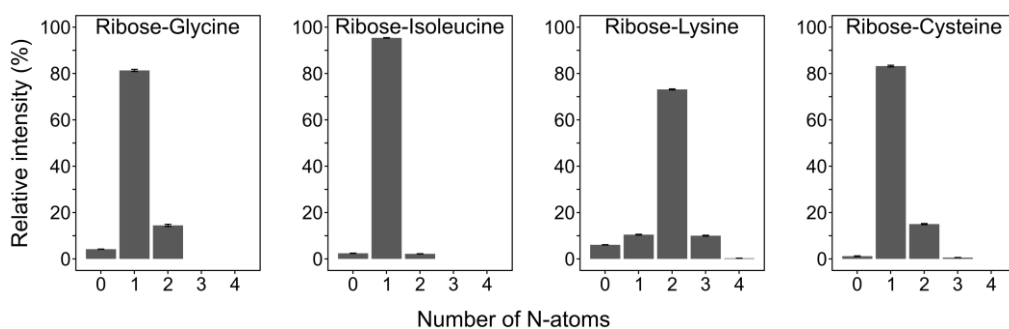


Figure C.4 | Relative peak intensities explained by MRPs classified by the number of nitrogen atoms in the molecular formulae of model systems heated for ten hours (100 °C).

C.6 General formation and degradation pathways of MRPs

Table C.1 | Ribose-glycine derived Maillard reaction products, which appear in the "general" Maillard reaction products formation and degradation pathways shown in Figure 3.5; (n.d.) not detected or S/N < 8.

General Formula	Ribose-glycine	m/z (avg.)	error (ppm)	Relative peak intensity (mean ± sd, n = 3)			
				2 h	4 h	6 h	10 h
C7H12NO6 - R	C7H13NO6	206.067007	-0.029	0.4091 ± 0.0098	0.3096 ± 0.0159	0.1929 ± 0.0144	0.1168 ± 0.0103
C7H14NO7 - R	C7H15NO7	224.077577	-0.003	0.2573 ± 0.0105	0.1622 ± 0.0043	0.1075 ± 0.0036	0.0758 ± 0.0049
C7H6NO4 - R	C7H7NO4	168.030239	0.036	n.d.	0.0083 ± 0.0005	0.0101 ± 0.0011	0.0107 ± 0.0004
C7H6NO3 - R	C7H7NO3	152.035318	-0.003	n.d.	n.d.	0.0034 ± 0.0002	0.0040 ± 0.0003
C7H10NO5 - R	C7H11NO5	188.056450	0.008	0.0110 ± 0.0000	0.0106 ± 0.0008	0.0095 ± 0.0009	0.0065 ± 0.0000
C7H6NO5 - R	C7H7NO5	184.025158	0.056	0.0054 ± 0.0007	0.0100 ± 0.0009	0.0140 ± 0.0018	0.0138 ± 0.0010
C7H8NO4 - R	C7H9NO4	170.045892	0.053	n.d.	0.0060 ± 0.0004	0.0048 ± 0.0003	0.0052 ± 0.0001
C7H10NO6 - R	C7H11NO6	204.051363	0.001	0.0055 ± 0.0010	0.0078 ± 0.0011	0.0080 ± 0.0012	0.0047 ± 0.0001
C7H12NO7 - R	C7H13NO7	222.061924	-0.019	n.d.	n.d.	0.0034 ± 0.0008	0.0028 ± 0.0002
C7H8NO5 - R	C7H9NO5	186.040806	0.040	n.d.	0.0044 ± 0.0004	0.0046 ± 0.0002	0.0031 ± 0.0002
C7H10NO4 - R	C7H11NO4	172.061541	0.048	n.d.	n.d.	n.d.	0.0014 ± 0.0001
C7H8NO6 - R	C7H9NO6	202.035705	-0.040	n.d.	n.d.	0.0020 ± 0.0002	0.0013 ± 0.0001
C7H10NO7 - R	C7H11NO7	220.046274	-0.018	n.d.	n.d.	n.d.	0.0009 ± 0.0001
C7H12NO5 - R	C7H13NO5	190.072082	-0.084	n.d.	n.d.	n.d.	0.0006 ± 0.0000
C7H4NO4 - R	C7H5NO4	n.d.	n.d.	n.d.	n.d.	n.d.	n.d.
C7H8NO3 - R	C7H9NO3	n.d.	n.d.	n.d.	n.d.	n.d.	n.d.
C12H18NO9 - R	C12H19NO9	320.098692	-0.052	0.0287 ± 0.0015	0.0442 ± 0.0009	0.0431 ± 0.0033	0.0411 ± 0.0008
C12H14NO8 - R	C12H15NO8	300.072498	0.018	n.d.	0.0157 ± 0.0008	0.0240 ± 0.0018	0.0247 ± 0.0020
C12H16NO8 - R	C12H17NO8	302.088135	-0.025	0.0127 ± 0.0018	0.0203 ± 0.0012	0.0180 ± 0.0006	0.0154 ± 0.0004
C12H22NO11 - R	C12H23NO11	356.119789	-0.138	0.0543 ± 0.0035	0.0372 ± 0.0023	0.0213 ± 0.0020	0.0139 ± 0.0015
C12H16NO9 - R	C12H17NO9	318.083061	0.009	n.d.	0.0067 ± 0.0009	0.0087 ± 0.0008	0.0100 ± 0.0001
C12H20NO10 - R	C12H21NO10	338.109237	-0.107	0.0248 ± 0.0157	0.0168 ± 0.0201	0.0057 ± 0.0013	0.0062 ± 0.0046
C12H14NO6 - R	C12H15NO6	268.082673	0.037	n.d.	0.0049 ± 0.0007	0.0051 ± 0.0002	0.0054 ± 0.0003
C12H12NO6 - R	C12H13NO6	266.067022	0.033	n.d.	n.d.	0.0040 ± 0.0002	0.0054 ± 0.0004
C12H12NO7 - R	C12H13NO7	282.061931	0.009	n.d.	n.d.	0.0048 ± 0.0006	0.0048 ± 0.0002
C12H16NO10 - R	C12H17NO10	334.077944	-0.086	n.d.	n.d.	0.0039 ± 0.0010	0.0041 ± 0.0001
C12H16NO7 - R	C12H17NO7	286.093228	-0.002	n.d.	n.d.	0.0032 ± 0.0007	0.0035 ± 0.0001

Appendix C | General formation and degradation pathways of MRPs

Table C.1 (continued) | Ribose-glycine derived Maillard reaction products, which appear in the "general" Maillard reaction products formation and degradation pathways shown in Figure 3.5; (n.d.) not detected or S/N < 8.

General Formula	Ribose-glycine	<i>m/z</i> (avg.)	error (ppm)	Relative peak intensity (mean ± sd, n = 3)			
				2 h	4 h	6 h	10 h
C12H12NO8 - R	C12H13NO8	298.056833	-0.033	n.d.	n.d.	0.0035 ± 0.0006	0.0027 ± 0.0001
C12H14NO5 - R	C12H15NO5	252.087752	0.016	n.d.	n.d.	0.0024 ± 0.0003	0.0026 ± 0.0001
C12H20NO9 - R	C12H21NO9	322.114365	0.022	n.d.	n.d.	n.d.	0.0019 ± 0.0000
C12H18NO10 - R	C12H19NO10	336.093557	-0.196	n.d.	n.d.	0.0025 ± 0.0003	0.0018 ± 0.0001
C12H12NO5 - R	C12H13NO5	250.072107	0.037	n.d.	n.d.	n.d.	0.0018 ± 0.0001
C12H14NO9 - R	C12H15NO9	316.067426	0.057	n.d.	n.d.	n.d.	0.0017 ± 0.0001
C12H16NO6 - R	C12H17NO6	270.098322	0.031	n.d.	n.d.	n.d.	0.0016 ± 0.0000
C12H10NO5 - R	C12H11NO5	248.056447	-0.005	n.d.	n.d.	n.d.	0.0015 ± 0.0001
C12H10NO6 - R	C12H11NO6	264.051353	-0.038	n.d.	n.d.	n.d.	0.0015 ± 0.0001
C12H18NO8 - R	C12H19NO8	304.103791	-0.006	n.d.	n.d.	n.d.	0.0012 ± 0.0003
C10H12NO6 - R	C10H13NO6	242.067014	0.003	0.0077 ± 0.0011	0.0144 ± 0.0004	0.0144 ± 0.0006	0.0103 ± 0.0003
C10H12NO5 - R	C10H13NO5	226.072077	-0.094	n.d.	0.0126 ± 0.0007	0.0142 ± 0.0005	0.0099 ± 0.0002
C10H10NO5 - R	C10H11NO5	224.056419	-0.129	n.d.	0.0048 ± 0.0006	0.0049 ± 0.0004	0.0042 ± 0.0003
C10H14NO7 - R	C10H15NO7	260.077585	0.026	n.d.	0.0045 ± 0.0002	0.0043 ± 0.0001	0.0032 ± 0.0000
C10H10NO6 - R	C10H11NO6	240.051366	0.013	n.d.	n.d.	0.0037 ± 0.0004	0.0030 ± 0.0001
C10H16NO9 - R	C10H17NO9	294.083063	0.018	n.d.	n.d.	0.0031 ± 0.0005	0.0027 ± 0.0001
C10H12NO7 - R	C10H13NO7	258.061938	0.038	n.d.	n.d.	0.0032 ± 0.0006	0.0026 ± 0.0002
C10H14NO5 - R	C10H15NO5	228.087729	-0.083	n.d.	n.d.	0.0025 ± 0.0005	0.0025 ± 0.0002
C10H14NO6 - R	C10H15NO6	244.082659	-0.018	n.d.	n.d.	0.0028 ± 0.0003	0.0024 ± 0.0001
C10H16NO8 - R	C10H17NO8	278.088150	0.027	0.0056 ± 0.0017	n.d.	0.0028 ± 0.0008	0.0017 ± 0.0003
C10H12NO4 - R	C10H13NO4	210.077175	-0.037	n.d.	n.d.	n.d.	0.0016 ± 0.0001
C10H16NO7 - R	C10H17NO7	262.093232	0.016	n.d.	n.d.	n.d.	0.0011 ± 0.0001
C10H18NO9 - R	C10H19NO9	296.098694	-0.046	n.d.	n.d.	n.d.	0.0010 ± 0.0001
C10H8NO5 - R	C10H9NO5	222.040775	-0.102	n.d.	n.d.	n.d.	0.0010 ± 0.0000
C10H8NO6 - R	C10H9NO6	238.035718	0.022	n.d.	n.d.	n.d.	0.0009 ± 0.0001
C10H18NO8 - R	C10H19NO8	280.103780	-0.046	n.d.	n.d.	n.d.	0.0009 ± 0.0001
C10H12NO8 - R	C10H13NO8	274.056877	0.123	n.d.	n.d.	n.d.	0.0009 ± 0.0001
C10H16NO6 - R	C10H17NO6	246.098312	-0.004	n.d.	n.d.	n.d.	0.0008 ± 0.0001
C10H14NO8 - R	C10H15NO8	n.d.	n.d.	n.d.	n.d.	n.d.	n.d.

Table C.1 (continued) | Ribose-glycine derived Maillard reaction products, which appear in the "general" Maillard reaction products formation and degradation pathways shown in Figure 3.5; (n.d.) not detected or S/N < 8.

General Formula	Ribose-glycine	<i>m/z</i> (avg.)	error (ppm)	Relative peak intensity (mean ± sd, n = 3)			
				2 h	4 h	6 h	10 h
C9H16NO8 - R	C9H17NO8	266.088145	0.006	n.d.	0.0081 ± 0.0009	0.0060 ± 0.0006	0.0049 ± 0.0004
C9H12NO8 - R	C9H13NO8	262.056857	0.052	n.d.	n.d.	n.d.	0.0007 ± 0.0001
C9H14NO8 - R	C9H15NO8	264.072450	-0.163	n.d.	n.d.	n.d.	0.0007 ± 0.0001
C9H16NO7 - R	C9H17NO7	250.093235	0.026	0.0486 ± 0.0027	0.0347 ± 0.0059	0.0227 ± 0.0025	0.0058 ± 0.0007
C9H14NO7 - R	C9H15NO7	248.077580	0.008	n.d.	0.0042 ± 0.0005	0.0024 ± 0.0003	0.0015 ± 0.0001
C9H12NO7 - R	C9H13NO7	246.061933	0.022	n.d.	n.d.	n.d.	0.0012 ± 0.0001
C9H10NO7 - R	C9H11NO7	244.046283	0.022	n.d.	n.d.	n.d.	0.0010 ± 0.0001
C9H12NO6 - R	C9H13NO6	230.066995	-0.076	n.d.	0.0051 ± 0.0010	0.0048 ± 0.0005	0.0032 ± 0.0002
C9H10NO6 - R	C9H11NO6	228.051337	-0.113	n.d.	0.0059 ± 0.0012	0.0054 ± 0.0002	0.0031 ± 0.0002
C9H8NO6 - R	C9H9NO6	226.035710	-0.013	n.d.	n.d.	n.d.	0.0007 ± 0.0001
C9H10NO5 - R	C9H11NO5	212.056446	-0.011	0.0794 ± 0.0048	0.1106 ± 0.0022	0.0907 ± 0.0044	0.0664 ± 0.0050
C9H8NO5 - R	C9H9NO5	210.040793	-0.026	n.d.	0.0053 ± 0.0004	0.0079 ± 0.0004	0.0064 ± 0.0003
C9H12NO5 - R	C9H13NO5	n.d.	n.d.	n.d.	n.d.	n.d.	n.d.
C9H8NO4 - R	C9H9NO4	194.045881	-0.010	n.d.	0.0071 ± 0.0010	0.0056 ± 0.0003	0.0047 ± 0.0003
C9H10NO4 - R	C9H11NO4	196.061525	-0.041	n.d.	0.0041 ± 0.0003	0.0031 ± 0.0001	0.0030 ± 0.0002
C9H12NO4 - R	C9H13NO4	198.077179	-0.018	n.d.	n.d.	0.0022 ± 0.0002	0.0021 ± 0.0001

Appendix C | General formation and degradation pathways of MRPs

Table C.2 | Ribose-isoleucine derived Maillard reaction products, which appear in the "general" Maillard reaction products formation and degradation pathways shown in Figure 3.5; (n.d.) not detected or S/N < 8.

General Formula	Ribose-isoleucine	m/z (avg.)	error (ppm)	Relative peak intensity (mean ± sd, n = 3)			
				2 h	4 h	6 h	10 h
C7H12NO6 - R	C11H21NO6	262.129606	-0.028	0.1929 ± 0.0051	0.1830 ± 0.0019	0.1591 ± 0.0012	0.1304 ± 0.0006
C7H14NO7 - R	C11H23NO7	280.140171	-0.026	0.7262 ± 0.0045	0.6436 ± 0.0035	0.5611 ± 0.0055	0.4913 ± 0.0062
C7H6NO4 - R	C11H15NO4	224.092808	-0.112	n.d.	0.0063 ± 0.0003	0.0099 ± 0.0003	0.0135 ± 0.0003
C7H6NO3 - R	C11H15NO3	208.097909	-0.042	0.0028 ± 0.0003	0.0071 ± 0.0002	0.0124 ± 0.0002	0.0210 ± 0.0011
C7H10NO5 - R	C11H19NO5	244.119044	-0.016	0.0069 ± 0.0005	0.0069 ± 0.0002	0.0063 ± 0.0001	0.0058 ± 0.0001
C7H6NO5 - R	C11H15NO5	240.087744	-0.018	n.d.	0.0021 ± 0.0002	0.0031 ± 0.0002	0.0042 ± 0.0001
C7H8NO4 - R	C11H17NO4	226.108455	-0.126	0.0083 ± 0.0005	0.0075 ± 0.0002	0.0069 ± 0.0001	0.0083 ± 0.0004
C7H10NO6 - R	C11H19NO6	260.113955	-0.031	n.d.	0.0019 ± 0.0000	0.0020 ± 0.0001	0.0015 ± 0.0000
C7H12NO7 - R	C11H21NO7	278.124531	0.010	0.0033 ± 0.0002	0.0045 ± 0.0002	0.0041 ± 0.0002	0.0038 ± 0.0002
C7H8NO5 - R	C11H17NO5	242.103397	-0.002	n.d.	0.0020 ± 0.0002	0.0021 ± 0.0001	0.0020 ± 0.0000
C7H10NO4 - R	C11H19NO4	228.124111	-0.096	n.d.	0.0014 ± 0.0003	0.0031 ± 0.0001	0.0063 ± 0.0003
C7H8NO6 - R	C11H17NO6	258.098316	0.010	n.d.	0.0012 ± 0.0002	0.0011 ± 0.0001	0.0011 ± 0.0001
C7H10NO7 - R	C11H19NO7	276.108884	0.023	n.d.	n.d.	0.0005 ± 0.0000	0.0005 ± 0.0000
C7H12NO5 - R	C11H21NO5	246.134704	0.024	n.d.	n.d.	n.d.	0.0004 ± 0.0000
C7H4NO4 - R	C11H13NO4	222.077157	-0.117	n.d.	n.d.	0.0005 ± 0.0000	0.0007 ± 0.0001
C7H8NO3 - R	C11H17NO3	210.113548	-0.098	n.d.	n.d.	n.d.	0.0004 ± 0.0000
C12H18NO9 - R	C16H27NO9	376.161292	-0.043	0.0032 ± 0.0002	0.0043 ± 0.0003	0.0049 ± 0.0001	0.0054 ± 0.0002
C12H14NO8 - R	C16H23NO8	356.135089	-0.010	n.d.	n.d.	0.0014 ± 0.0001	0.0017 ± 0.0001
C12H16NO8 - R	C16H25NO8	358.150741	-0.006	n.d.	0.0032 ± 0.0000	0.0048 ± 0.0002	0.0067 ± 0.0002
C12H22NO11 - R	C16H31NO11	412.182426	-0.030	n.d.	0.0028 ± 0.0004	0.0026 ± 0.0002	0.0022 ± 0.0000
C12H16NO9 - R	C16H25NO9	374.145641	-0.045	n.d.	0.0011 ± 0.0000	0.0019 ± 0.0001	0.0026 ± 0.0001
C12H20NO10 - R	C16H29NO10	394.171860	-0.033	n.d.	n.d.	0.0011 ± 0.0001	0.0012 ± 0.0000
C12H14NO6 - R	C16H23NO6	324.145264	0.004	n.d.	n.d.	0.0005 ± 0.0002	0.0011 ± 0.0001
C12H12NO6 - R	C16H21NO6	322.129617	0.013	n.d.	0.0016 ± 0.0002	0.0023 ± 0.0002	0.0038 ± 0.0003
C12H12NO7 - R	C16H21NO7	338.124539	0.032	n.d.	n.d.	0.0012 ± 0.0001	0.0014 ± 0.0001
C12H16NO10 - R	C16H25NO10	390.140582	0.024	n.d.	n.d.	n.d.	0.0003 ± 0.0000
C12H16NO7 - R	C16H25NO7	342.155810	-0.053	n.d.	n.d.	0.0004 ± 0.0000	0.0011 ± 0.0001

Table C.2 (continued) | Ribose-isoleucine derived Maillard reaction products, which appear in the "general" Maillard reaction products formation and degradation pathways shown in Figure 3.5; (n.d.) not detected or S/N < 8.

General Formula	Ribose-isoleucine	m/z (avg.)	error (ppm)	Relative peak intensity (mean ± sd, n = 3)			
				2 h	4 h	6 h	10 h
C12H12NO8 - R	C16H21NO8	354.119417	-0.073	n.d.	n.d.	0.0011 ± 0.0001	0.0016 ± 0.0001
C12H14NO5 - R	C16H23NO5	308.150373	0.080	n.d.	n.d.	n.d.	0.0006 ± 0.0001
C12H20NO9 - R	C16H29NO9	378.176952	-0.017	n.d.	n.d.	0.0011 ± 0.0001	0.0021 ± 0.0002
C12H18NO10 - R	C16H27NO10	392.156230	0.018	n.d.	n.d.	n.d.	0.0003 ± 0.0001
C12H12NO5 - R	C16H21NO5	306.134707	0.029	n.d.	n.d.	0.0007 ± 0.0003	0.0012 ± 0.0001
C12H14NO9 - R	C16H23NO9	372.129979	-0.079	n.d.	n.d.	0.0005 ± 0.0000	0.0006 ± 0.0000
C12H16NO6 - R	C16H25NO6	326.160920	0.021	n.d.	n.d.	0.0004 ± 0.0001	0.0007 ± 0.0001
C12H10NO5 - R	C16H19NO5	304.119057	0.029	n.d.	n.d.	0.0011 ± 0.0000	0.0021 ± 0.0001
C12H10NO6 - R	C16H19NO6	320.113964	0.002	n.d.	n.d.	0.0010 ± 0.0000	0.0017 ± 0.0001
C12H18NO8 - R	C16H27NO8	n.d.	n.d.	n.d.	n.d.	n.d.	n.d.
C10H12NO6 - R	C14H21NO6	n.d.	n.d.	n.d.	n.d.	n.d.	n.d.
C10H12NO5 - R	C14H21NO5	282.134694	-0.015	0.0055 ± 0.0006	0.0077 ± 0.0002	0.0084 ± 0.0002	0.0095 ± 0.0002
C10H10NO5 - R	C14H19NO5	280.119055	0.025	n.d.	0.0010 ± 0.0001	0.0012 ± 0.0001	0.0016 ± 0.0001
C10H14NO7 - R	C14H23NO7	316.140128	-0.158	n.d.	n.d.	0.0008 ± 0.0000	0.0008 ± 0.0000
C10H10NO6 - R	C14H19NO6	n.d.	n.d.	n.d.	n.d.	n.d.	n.d.
C10H16NO9 - R	C14H25NO9	350.145643	-0.042	n.d.	n.d.	0.0006 ± 0.0000	0.0007 ± 0.0001
C10H12NO7 - R	C14H21NO7	n.d.	n.d.	n.d.	n.d.	n.d.	n.d.
C10H14NO5 - R	C14H23NO5	284.150337	-0.040	n.d.	n.d.	0.0005 ± 0.0001	0.0006 ± 0.0000
C10H14NO6 - R	C14H23NO6	300.145273	0.034	n.d.	n.d.	0.0004 ± 0.0000	0.0005 ± 0.0000
C10H16NO8 - R	C14H25NO8	334.150736	-0.020	n.d.	n.d.	0.0008 ± 0.0000	0.0008 ± 0.0001
C10H12NO4 - R	C14H21NO4	266.139770	-0.049	n.d.	n.d.	0.0005 ± 0.0000	0.0008 ± 0.0000
C10H16NO7 - R	C14H25NO7	318.155808	-0.064	n.d.	n.d.	n.d.	0.0003 ± 0.0001
C10H18NO9 - R	C14H27NO9	352.161293	-0.043	n.d.	0.0013 ± 0.0002	0.0009 ± 0.0001	0.0005 ± 0.0000
C10H8NO5 - R	C14H17NO5	278.103412	0.052	n.d.	n.d.	0.0005 ± 0.0000	0.0006 ± 0.0000
C10H8NO6 - R	C14H17NO6	294.098320	0.025	n.d.	0.0011 ± 0.0001	0.0019 ± 0.0001	0.0023 ± 0.0001
C10H18NO8 - R	C14H27NO8	336.166383	-0.030	n.d.	n.d.	0.0009 ± 0.0001	0.0011 ± 0.0001
C10H12NO8 - R	C14H21NO8	330.119453	0.031	n.d.	n.d.	0.0004 ± 0.0001	0.0004 ± 0.0000
C10H16NO6 - R	C14H25NO6	n.d.	n.d.	n.d.	n.d.	n.d.	n.d.
C10H14NO8 - R	C14H23NO8	332.135081	-0.035	n.d.	n.d.	0.0005 ± 0.0001	0.0005 ± 0.0000

Appendix C | General formation and degradation pathways of MRPs

Table C.2 (continued) | Ribose-isoleucine derived Maillard reaction products, which appear in the "general" Maillard reaction products formation and degradation pathways shown in Figure 3.5; (n.d.) not detected or S/N < 8.

General Formula	Ribose-isoleucine	<i>m/z</i> (avg.)	error (ppm)	Relative peak intensity (mean ± sd, n = 3)			
				2 h	4 h	6 h	10 h
C9H16NO8 - R	C13H25NO8	322.150740	-0.009	n.d.	0.0024 ± 0.0001	0.0024 ± 0.0001	0.0022 ± 0.0000
C9H12NO8 - R	C13H21NO8	318.119450	0.022	n.d.	n.d.	n.d.	0.0003 ± 0.0000
C9H14NO8 - R	C13H23NO8	n.d.	n.d.	n.d.	n.d.	n.d.	n.d.
C9H16NO7 - R	C13H25NO7	n.d.	n.d.	n.d.	n.d.	n.d.	n.d.
C9H14NO7 - R	C13H23NO7	304.140185	0.023	n.d.	n.d.	0.0005 ± 0.0000	0.0005 ± 0.0001
C9H12NO7 - R	C13H21NO7	302.124555	0.089	n.d.	n.d.	0.0004 ± 0.0000	0.0004 ± 0.0001
C9H10NO7 - R	C13H19NO7	300.108884	0.020	n.d.	n.d.	0.0011 ± 0.0000	0.0011 ± 0.0001
C9H12NO6 - R	C13H21NO6	286.129613	0.000	n.d.	n.d.	0.0010 ± 0.0001	0.0010 ± 0.0000
C9H10NO6 - R	C13H19NO6	284.113955	-0.027	n.d.	0.0014 ± 0.0002	0.0017 ± 0.0001	0.0018 ± 0.0001
C9H8NO6 - R	C13H17NO6	282.098311	-0.006	n.d.	0.0010 ± 0.0001	0.0012 ± 0.0000	0.0015 ± 0.0001
C9H10NO5 - R	C13H19NO5	268.119055	0.028	0.0231 ± 0.0004	0.0260 ± 0.0007	0.0286 ± 0.0012	0.0293 ± 0.0011
C9H8NO5 - R	C13H17NO5	266.103395	-0.011	n.d.	n.d.	0.0011 ± 0.0000	0.0013 ± 0.0001
C9H12NO5 - R	C13H21NO5	270.134688	-0.036	n.d.	n.d.	0.0006 ± 0.0001	0.0007 ± 0.0001
C9H8NO4 - R	C13H17NO4	250.108485	0.008	n.d.	n.d.	0.0010 ± 0.0001	0.0012 ± 0.0000
C9H10NO4 - R	C13H19NO4	252.124122	-0.044	n.d.	0.0012 ± 0.0002	0.0015 ± 0.0001	0.0017 ± 0.0001
C9H12NO4 - R	C13H21NO4	254.139764	-0.075	n.d.	0.0019 ± 0.0002	0.0030 ± 0.0000	0.0051 ± 0.0002

Appendix C | General formation and degradation pathways of MRPs

Table C.3 | Ribose-lysine derived Maillard reaction products, which appear in the "general" Maillard reaction products formation and degradation pathways shown in Figure 3.5; (n.d.) not detected or S/N < 8.

General Formula	Ribose-lysine	m/z (avg.)	error (ppm)	Relative peak intensity (mean ± sd, n = 3)			
				2 h	4 h	6 h	10 h
C7H12NO6 - R	C11H22N2O6	277.140515	0.011	0.6223 ± 0.0038	0.4832 ± 0.0070	0.4049 ± 0.0028	0.3298 ± 0.0013
C7H14NO7 - R	C11H24N2O7	n.d.	n.d.	n.d.	n.d.	n.d.	n.d.
C7H6NO4 - R	C11H16N2O4	239.103728	-0.019	0.0080 ± 0.0004	0.0159 ± 0.0004	0.0219 ± 0.0010	0.0253 ± 0.0020
C7H6NO3 - R	C11H16N2O3	223.108778	-0.177	0.0053 ± 0.0002	0.0088 ± 0.0002	0.0120 ± 0.0002	0.0184 ± 0.0008
C7H10NO5 - R	C11H20N2O5	259.129957	0.037	0.0084 ± 0.0001	0.0070 ± 0.0002	0.0058 ± 0.0000	0.0052 ± 0.0001
C7H6NO5 - R	C11H16N2O5	255.098659	0.045	0.0007 ± 0.0000	0.0013 ± 0.0001	0.0018 ± 0.0001	0.0020 ± 0.0001
C7H8NO4 - R	C11H18N2O4	241.119376	-0.023	0.0051 ± 0.0001	0.0045 ± 0.0001	0.0051 ± 0.0002	0.0094 ± 0.0004
C7H10NO6 - R	C11H20N2O6	275.124882	0.072	0.0037 ± 0.0002	0.0059 ± 0.0001	0.0077 ± 0.0001	0.0072 ± 0.0002
C7H12NO7 - R	C11H22N2O7	293.135435	0.029	0.0008 ± 0.0000	0.0009 ± 0.0000	0.0008 ± 0.0000	0.0008 ± 0.0000
C7H8NO5 - R	C11H18N2O5	257.114308	0.041	0.0030 ± 0.0001	0.0030 ± 0.0000	0.0027 ± 0.0001	0.0022 ± 0.0001
C7H10NO4 - R	C11H20N2O4	243.135033	0.005	0.0008 ± 0.0000	0.0007 ± 0.0000	0.0009 ± 0.0000	0.0014 ± 0.0001
C7H8NO6 - R	C11H18N2O6	273.109228	0.057	0.0012 ± 0.0001	0.0013 ± 0.0000	0.0012 ± 0.0001	0.0009 ± 0.0001
C7H10NO7 - R	C11H20N2O7	291.119781	0.013	0.0012 ± 0.0001	0.0011 ± 0.0000	0.0009 ± 0.0001	0.0005 ± 0.0001
C7H12NO5 - R	C11H22N2O5	261.145613	0.062	0.0003 ± 0.0000	0.0003 ± 0.0000	0.0002 ± 0.0000	0.0003 ± 0.0000
C7H4NO4 - R	C11H14N2O4	237.088069	-0.055	n.d.	n.d.	0.0002 ± 0.0000	0.0001 ± 0.0000
C7H8NO3 - R	C11H18N2O3	225.124433	-0.150	0.0003 ± 0.0000	0.0002 ± 0.0000	0.0002 ± 0.0000	0.0002 ± 0.0000
C12H18NO9 - R	C16H28N2O9	391.172176	-0.080	0.0179 ± 0.0002	0.0255 ± 0.0003	0.0272 ± 0.0006	0.0266 ± 0.0013
C12H14NO8 - R	C16H24N2O8	371.145971	-0.057	0.0026 ± 0.0000	0.0052 ± 0.0001	0.0067 ± 0.0001	0.0072 ± 0.0001
C12H16NO8 - R	C16H26N2O8	373.161623	-0.052	0.0087 ± 0.0002	0.0099 ± 0.0001	0.0091 ± 0.0003	0.0080 ± 0.0005
C12H22NO11 - R	C16H32N2O11	427.193270	-0.157	0.0007 ± 0.0001	0.0006 ± 0.0000	0.0004 ± 0.0000	0.0003 ± 0.0000
C12H16NO9 - R	C16H26N2O9	389.156533	-0.061	0.0012 ± 0.0000	0.0019 ± 0.0000	0.0020 ± 0.0000	0.0019 ± 0.0000
C12H20NO10 - R	C16H30N2O10	409.182703	-0.169	0.0074 ± 0.0015	0.0059 ± 0.0009	0.0044 ± 0.0001	0.0024 ± 0.0000
C12H14NO6 - R	C16H24N2O6	339.156168	0.018	0.0005 ± 0.0000	0.0008 ± 0.0000	0.0009 ± 0.0000	0.0015 ± 0.0001
C12H12NO6 - R	C16H22N2O6	337.140523	0.031	0.0011 ± 0.0000	0.0019 ± 0.0000	0.0025 ± 0.0000	0.0042 ± 0.0002
C12H12NO7 - R	C16H22N2O7	353.135408	-0.054	0.0010 ± 0.0000	0.0021 ± 0.0001	0.0025 ± 0.0000	0.0027 ± 0.0000
C12H16NO10 - R	C16H26N2O10	n.d.	n.d.	n.d.	n.d.	n.d.	n.d.
C12H16NO7 - R	C16H26N2O7	357.166730	0.008	0.0004 ± 0.0001	0.0006 ± 0.0000	0.0006 ± 0.0000	0.0009 ± 0.0001

Appendix C | General formation and degradation pathways of MRPs

Table C.3 (continued) | Ribose-lysine derived Maillard reaction products, which appear in the "general" Maillard reaction products formation and degradation pathways shown in Figure 3.5; (n.d.) not detected or S/N < 8.

General Formula	Ribose-lysine	m/z (avg.)	error (ppm)	Relative peak intensity (mean ± sd, n = 3)			
				2 h	4 h	6 h	10 h
C12H12NO8 – R	C16H22N2O8	369.130309	-0.090	0.0003 ± 0.0000	0.0006 ± 0.0000	0.0008 ± 0.0000	0.0008 ± 0.0001
C12H14NO5 – R	C16H24N2O5	323.161258	0.033	0.0002 ± 0.0000	0.0003 ± 0.0001	0.0005 ± 0.0001	0.0008 ± 0.0001
C12H20NO9 – R	C16H30N2O9	n.d.	n.d.	n.d.	n.d.	n.d.	n.d.
C12H18NO10 – R	C16H28N2O10	407.167061	-0.150	0.0007 ± 0.0000	0.0009 ± 0.0000	0.0010 ± 0.0000	0.0007 ± 0.0000
C12H12NO5 – R	C16H22N2O5	321.145598	0.004	0.0003 ± 0.0000	0.0006 ± 0.0000	0.0008 ± 0.0000	0.0012 ± 0.0001
C12H14NO9 – R	C16H24N2O9	n.d.	n.d.	n.d.	n.d.	n.d.	n.d.
C12H16NO6 – R	C16H26N2O6	341.171801	-0.031	n.d.	0.0003 ± 0.0000	0.0004 ± 0.0000	0.0006 ± 0.0000
C12H10NO5 – R	C16H20N2O5	355.106619	-0.017	n.d.	0.0003 ± 0.0000	0.0004 ± 0.0000	0.0006 ± 0.0000
C12H10NO6 – R	C16H20N2O6	371.101507	-0.090	n.d.	n.d.	0.0001 ± 0.0000	0.0001 ± 0.0000
C12H18NO8 – R	C16H28N2O8	375.177288	-0.010	n.d.	0.0003 ± 0.0000	0.0004 ± 0.0000	0.0005 ± 0.0000
C10H12NO6 – R	C14H22N2O6	313.140525	0.042	0.0062 ± 0.0001	0.0064 ± 0.0002	0.0059 ± 0.0001	0.0050 ± 0.0001
C10H12NO5 – R	C14H22N2O5	297.145612	0.049	0.0021 ± 0.0000	0.0030 ± 0.0001	0.0034 ± 0.0001	0.0032 ± 0.0000
C10H10NO5 – R	C14H20N2O5	295.129967	0.067	0.0025 ± 0.0001	0.0026 ± 0.0001	0.0027 ± 0.0001	0.0028 ± 0.0001
C10H14NO7 – R	C14H24N2O7	331.151081	0.011	0.0023 ± 0.0000	0.0027 ± 0.0001	0.0026 ± 0.0001	0.0024 ± 0.0001
C10H10NO6 – R	C14H20N2O6	311.124875	0.041	0.0013 ± 0.0001	0.0018 ± 0.0000	0.0017 ± 0.0000	0.0016 ± 0.0001
C10H16NO9 – R	C14H26N2O9	n.d.	n.d.	n.d.	n.d.	n.d.	n.d.
C10H12NO7 – R	C14H22N2O7	329.135423	-0.011	0.0008 ± 0.0000	0.0009 ± 0.0000	0.0009 ± 0.0000	0.0008 ± 0.0001
C10H14NO5 – R	C14H24N2O5	299.161249	0.007	n.d.	n.d.	n.d.	0.0003 ± 0.0000
C10H14NO6 – R	C14H24N2O6	315.156181	0.059	0.0005 ± 0.0000	0.0004 ± 0.0000	0.0004 ± 0.0000	0.0004 ± 0.0000
C10H16NO8 – R	C14H26N2O8	349.161637	-0.015	0.0011 ± 0.0001	0.0010 ± 0.0000	0.0010 ± 0.0000	0.0011 ± 0.0000
C10H12NO4 – R	C14H22N2O4	281.150678	-0.013	n.d.	n.d.	n.d.	0.0003 ± 0.0000
C10H16NO7 – R	C14H26N2O7	333.166731	0.011	0.0005 ± 0.0000	0.0007 ± 0.0000	0.0009 ± 0.0000	0.0009 ± 0.0001
C10H18NO9 – R	C14H28N2O9	n.d.	n.d.	n.d.	n.d.	n.d.	n.d.
C10H8NO5 – R	C14H18N2O5	293.114294	-0.011	0.0003 ± 0.0000	0.0005 ± 0.0001	0.0005 ± 0.0000	0.0006 ± 0.0000
C10H8NO6 – R	C14H18N2O6	309.109220	0.024	0.0003 ± 0.0000	0.0005 ± 0.0000	0.0006 ± 0.0000	0.0005 ± 0.0000
C10H18NO8 – R	C14H28N2O8	n.d.	n.d.	n.d.	n.d.	n.d.	n.d.
C10H12NO8 – R	C14H22N2O8	345.130348	0.016	0.0002 ± 0.0000	0.0003 ± 0.0000	0.0002 ± 0.0000	0.0002 ± 0.0000
C10H16NO6 – R	C14H26N2O6	317.171802	-0.032	0.0002 ± 0.0000	0.0002 ± 0.0000	0.0001 ± 0.0000	0.0001 ± 0.0000
C10H14NO8 – R	C14H24N2O8	347.145978	-0.039	0.0005 ± 0.0001	0.0007 ± 0.0000	0.0007 ± 0.0000	0.0007 ± 0.0000

Table C.3 (continued) | Ribose-lysine derived Maillard reaction products, which appear in the "general" Maillard reaction products formation and degradation pathways shown in Figure 3.5; (n.d.) not detected or S/N < 8.

General Formula	Ribose-lysine	m/z (avg.)	error (ppm)	Relative peak intensity (mean ± sd, n = 3)			
				2 h	4 h	6 h	10 h
C9H16NO8 - R	C13H26N2O8	337.161643	0.004	0.0005 ± 0.0001	0.0004 ± 0.0000	0.0004 ± 0.0000	0.0003 ± 0.0000
C9H12NO8 - R	C13H22N2O8	333.130350	0.024	0.0002 ± 0.0000	0.0002 ± 0.0000	0.0002 ± 0.0000	0.0002 ± 0.0000
C9H14NO8 - R	C13H24N2O8	335.145990	-0.006	0.0010 ± 0.0001	0.0017 ± 0.0002	0.0021 ± 0.0001	0.0023 ± 0.0001
C9H16NO7 - R	C13H26N2O7	321.166723	-0.012	0.0049 ± 0.0004	0.0026 ± 0.0002	0.0011 ± 0.0000	0.0003 ± 0.0000
C9H14NO7 - R	C13H24N2O7	319.151081	0.012	0.0014 ± 0.0001	0.0014 ± 0.0001	0.0014 ± 0.0000	0.0013 ± 0.0000
C9H12NO7 - R	C13H22N2O7	317.135434	0.023	0.0006 ± 0.0000	0.0007 ± 0.0000	0.0008 ± 0.0000	0.0007 ± 0.0000
C9H10NO7 - R	C13H20N2O7	n.d.	n.d.	n.d.	n.d.	n.d.	n.d.
C9H12NO6 - R	C13H22N2O6	301.140516	0.014	0.0014 ± 0.0000	0.0015 ± 0.0000	0.0015 ± 0.0000	0.0014 ± 0.0000
C9H10NO6 - R	C13H20N2O6	299.124875	0.043	0.0011 ± 0.0000	0.0015 ± 0.0001	0.0015 ± 0.0001	0.0014 ± 0.0001
C9H8NO6 - R	C13H18N2O6	297.109218	0.021	0.0010 ± 0.0000	0.0012 ± 0.0000	0.0012 ± 0.0000	0.0010 ± 0.0001
C9H10NO5 - R	C13H20N2O5	283.129937	-0.036	0.0896 ± 0.0010	0.0937 ± 0.0018	0.0930 ± 0.0010	0.0842 ± 0.0012
C9H8NO5 - R	C13H18N2O5	281.114299	0.008	0.0011 ± 0.0000	0.0020 ± 0.0000	0.0024 ± 0.0001	0.0027 ± 0.0001
C9H12NO5 - R	C13H22N2O5	285.145590	-0.025	0.0013 ± 0.0000	0.0009 ± 0.0001	0.0009 ± 0.0000	0.0009 ± 0.0000
C9H8NO4 - R	C13H18N2O4	265.119396	0.053	0.0026 ± 0.0000	0.0030 ± 0.0001	0.0030 ± 0.0000	0.0031 ± 0.0001
C9H10NO4 - R	C13H20N2O4	267.135045	0.049	0.0010 ± 0.0000	0.0010 ± 0.0000	0.0010 ± 0.0000	0.0009 ± 0.0000
C9H12NO4 - R	C13H22N2O4	269.150693	0.042	0.0002 ± 0.0000	0.0006 ± 0.0000	0.0008 ± 0.0000	0.0011 ± 0.0001

Appendix C | General formation and degradation pathways of MRPs

Table C.4 | Ribose-cysteine derived Maillard reaction products, which appear in the "general" Maillard reaction products formation and degradation pathways shown in Figure 3.5; (n.d.) not detected or S/N < 8.

General Formula	Ribose-cysteine	m/z (avg.)	error (ppm)	Relative peak intensity (mean ± sd, n = 3)			
				2 h	4 h	6 h	10 h
C7H12NO6 - R	C8H15NO6S	252.054714	-0.081	0.5114 ± 0.0106	0.4447 ± 0.0170	0.4223 ± 0.0033	0.3769 ± 0.0069
C7H14NO7 - R	C8H17NO7S	270.065273	-0.095	0.0464 ± 0.0022	0.0390 ± 0.0033	0.0347 ± 0.0008	0.0291 ± 0.0007
C7H6NO4 - R	C8H9NO4S	214.017952	-0.011	0.0002 ± 0.0000	0.0006 ± 0.0001	0.0010 ± 0.0001	0.0023 ± 0.0001
C7H6NO3 - R	C8H9NO3S	198.023031	-0.042	0.0003 ± 0.0000	0.0009 ± 0.0001	0.0019 ± 0.0001	0.0035 ± 0.0001
C7H10NO5 - R	C8H13NO5S	234.044165	-0.017	0.0041 ± 0.0002	0.0080 ± 0.0001	0.0108 ± 0.0010	0.0162 ± 0.0004
C7H6NO5 - R	C8H9NO5S	230.012870	0.004	0.0010 ± 0.0001	0.0025 ± 0.0003	0.0038 ± 0.0006	0.0070 ± 0.0005
C7H8NO4 - R	C8H11NO4S	216.033604	0.001	0.0001 ± 0.0000	0.0004 ± 0.0000	0.0006 ± 0.0001	0.0012 ± 0.0000
C7H10NO6 - R	C8H13NO6S	250.039088	0.016	0.0012 ± 0.0001	0.0021 ± 0.0002	0.0028 ± 0.0002	0.0035 ± 0.0002
C7H12NO7 - R	C8H15NO7S	268.049620	-0.108	0.0039 ± 0.0002	0.0043 ± 0.0004	0.0048 ± 0.0004	0.0058 ± 0.0004
C7H8NO5 - R	C8H11NO5S	232.028520	0.004	0.0013 ± 0.0001	0.0028 ± 0.0001	0.0036 ± 0.0005	0.0051 ± 0.0002
C7H10NO4 - R	C8H13NO4S	218.049256	0.007	n.d.	n.d.	n.d.	0.0003 ± 0.0000
C7H8NO6 - R	C8H11NO6S	248.023439	0.021	0.0004 ± 0.0000	0.0008 ± 0.0000	0.0010 ± 0.0001	0.0014 ± 0.0001
C7H10NO7 - R	C8H13NO7S	n.d.	n.d.	n.d.	n.d.	n.d.	n.d.
C7H12NO5 - R	C8H15NO5S	236.059826	0.031	0.0001 ± 0.0000	0.0001 ± 0.0000	0.0002 ± 0.0000	0.0002 ± 0.0000
C7H4NO4 - R	C8H7NO4S	212.002291	-0.060	n.d.	n.d.	0.0001 ± 0.0000	0.0002 ± 0.0000
C7H8NO3 - R	C8H11NO3S	200.038672	-0.085	n.d.	n.d.	n.d.	0.0001 ± 0.0000
C12H18NO9 - R	C13H21NO9S	366.086426	-0.008	0.0015 ± 0.0001	0.0034 ± 0.0000	0.0055 ± 0.0003	0.0093 ± 0.0002
C12H14NO8 - R	C13H17NO8S	346.060205	-0.026	0.0001 ± 0.0000	0.0001 ± 0.0000	0.0002 ± 0.0000	0.0005 ± 0.0000
C12H16NO8 - R	C13H19NO8S	348.075877	0.037	0.0005 ± 0.0000	0.0012 ± 0.0000	0.0020 ± 0.0002	0.0028 ± 0.0000
C12H22NO11 - R	C13H25NO11S	402.107485	-0.184	0.0137 ± 0.0007	0.0112 ± 0.0009	0.0105 ± 0.0003	0.0097 ± 0.0002
C12H16NO9 - R	C13H19NO9S	364.070775	-0.012	0.0001 ± 0.0000	0.0003 ± 0.0000	0.0004 ± 0.0000	0.0008 ± 0.0001
C12H20NO10 - R	C13H23NO10S	384.096983	-0.029	0.0031 ± 0.0001	0.0061 ± 0.0006	0.0055 ± 0.0002	0.0073 ± 0.0001
C12H14NO6 - R	C13H17NO6S	314.070417	0.104	n.d.	n.d.	n.d.	0.0001 ± 0.0000
C12H12NO6 - R	C13H15NO6S	n.d.	n.d.	n.d.	n.d.	n.d.	n.d.
C12H12NO7 - R	C13H15NO7S	n.d.	n.d.	n.d.	n.d.	n.d.	n.d.
C12H16NO10 - R	C13H19NO10S	380.065698	0.009	0.0001 ± 0.0000	0.0002 ± 0.0000	0.0003 ± 0.0000	0.0004 ± 0.0000
C12H16NO7 - R	C13H19NO7S	332.080988	0.116	n.d.	n.d.	n.d.	0.0002 ± 0.0000

Table C.4 (continued) | Ribose-cysteine derived Maillard reaction products, which appear in the "general" Maillard reaction products formation and degradation pathways shown in Figure 3.5; (n.d.) not detected or S/N < 8.

General Formula	Ribose-cysteine	m/z (avg.)	error (ppm)	Relative peak intensity (mean ± sd, n = 3)			
				2 h	4 h	6 h	10 h
C12H20NO9 - R	C13H23NO9S	368.102063	-0.043	n.d.	n.d.	n.d.	0.0001 ± 0.0000
C12H18NO10 - R	C13H21NO10S	382.081338	-0.017	0.0005 ± 0.0000	0.0009 ± 0.0001	0.0012 ± 0.0001	0.0016 ± 0.0001
C12H12NO5 - R	C13H15NO5S	n.d.	n.d.	n.d.	n.d.	n.d.	n.d.
C12H14NO9 - R	C13H17NO9S	362.055128	-0.002	n.d.	n.d.	0.0001 ± 0.0000	0.0002 ± 0.0000
C12H16NO6 - R	C13H19NO6S	n.d.	n.d.	n.d.	n.d.	n.d.	n.d.
C12H10NO5 - R	C13H13NO5S	n.d.	n.d.	n.d.	n.d.	n.d.	n.d.
C12H10NO6 - R	C13H13NO6S	n.d.	n.d.	n.d.	n.d.	n.d.	n.d.
C12H18NO8 - R	C13H21NO8S	350.091536	0.062	n.d.	n.d.	0.0002 ± 0.0000	0.0003 ± 0.0000
C10H12NO6 - R	C11H15NO6S	288.054753	0.067	n.d.	n.d.	n.d.	0.0001 ± 0.0000
C10H12NO5 - R	C11H15NO5S	n.d.	n.d.	n.d.	n.d.	n.d.	n.d.
C10H10NO5 - R	C11H13NO5S	n.d.	n.d.	n.d.	n.d.	n.d.	n.d.
C10H14NO7 - R	C11H17NO7S	306.065316	0.055	0.0001 ± 0.0000	0.0002 ± 0.0000	0.0003 ± 0.0000	0.0005 ± 0.0000
C10H10NO6 - R	C11H13NO6S	286.039127	0.149	n.d.	n.d.	n.d.	0.0001 ± 0.0000
C10H16NO9 - R	C11H19NO9S	340.070787	0.023	0.0052 ± 0.0001	0.0125 ± 0.0007	0.0185 ± 0.0010	0.0289 ± 0.0012
C10H12NO7 - R	C11H15NO7S	304.049673	0.079	n.d.	n.d.	0.0002 ± 0.0000	0.0007 ± 0.0000
C10H14NO5 - R	C11H17NO5S	n.d.	n.d.	n.d.	n.d.	n.d.	n.d.
C10H14NO6 - R	C11H17NO6S	n.d.	n.d.	n.d.	n.d.	n.d.	n.d.
C10H16NO8 - R	C11H19NO8S	324.075874	0.032	n.d.	n.d.	n.d.	0.0006 ± 0.0000
C10H12NO4 - R	C11H15NO4S	n.d.	n.d.	n.d.	n.d.	n.d.	n.d.
C10H16NO7 - R	C11H19NO7S	308.080964	0.048	0.0002 ± 0.0000	0.0002 ± 0.0000	0.0003 ± 0.0000	0.0004 ± 0.0000
C10H18NO9 - R	C11H21NO9S	342.086435	0.017	0.0004 ± 0.0000	0.0006 ± 0.0000	0.0008 ± 0.0000	0.0011 ± 0.0001
C10H8NO5 - R	C11H11NO5S	n.d.	n.d.	n.d.	n.d.	n.d.	n.d.
C10H8NO6 - R	C11H11NO6S	n.d.	n.d.	n.d.	n.d.	n.d.	n.d.
C10H18NO8 - R	C11H21NO8S	326.091529	0.045	0.0002 ± 0.0000	0.0002 ± 0.0000	0.0002 ± 0.0001	0.0001 ± 0.0000
C10H12NO8 - R	C11H15NO8S	n.d.	n.d.	n.d.	n.d.	n.d.	n.d.
C10H16NO6 - R	C11H19NO6S	292.086051	0.059	0.0010 ± 0.0000	0.0011 ± 0.0000	0.0010 ± 0.0001	0.0008 ± 0.0000
C10H14NO8 - R	C11H17NO8S	322.060229	0.047	0.0001 ± 0.0000	0.0003 ± 0.0000	0.0003 ± 0.0000	0.0007 ± 0.0000
C9H16NO8 - R	C10H19NO8S	312.075873	0.029	0.0003 ± 0.0000	0.0005 ± 0.0000	0.0008 ± 0.0001	0.0013 ± 0.0000
C9H12NO8 - R	C10H15NO8S	n.d.	n.d.	n.d.	n.d.	n.d.	n.d.

Appendix C | General formation and degradation pathways of MRPs

Table C.4 (continued) | Ribose-cysteine derived Maillard reaction products, which appear in the "general" Maillard reaction products formation and degradation pathways shown in Figure 3.5; (n.d.) not detected or S/N < 8.

General Formula	Ribose-cysteine	<i>m/z</i> (avg.)	error (ppm)	Relative peak intensity (mean ± sd, n = 3)			
				2 h	4 h	6 h	10 h
C9H14NO8 - R	C10H17NO8S	310.060220	0.019	0.0001 ± 0.0000	0.0002 ± 0.0000	0.0002 ± 0.0000	0.0003 ± 0.0000
C9H16NO7 - R	C10H19NO7S	296.080953	0.015	0.0426 ± 0.0017	0.0411 ± 0.0026	0.0372 ± 0.0011	0.0294 ± 0.0007
C9H14NO7 - R	C10H17NO7S	294.065310	0.037	0.0005 ± 0.0000	0.0007 ± 0.0000	0.0008 ± 0.0001	0.0011 ± 0.0000
C9H12NO7 - R	C10H15NO7S	292.049665	0.055	0.0002 ± 0.0000	0.0004 ± 0.0000	0.0004 ± 0.0000	0.0005 ± 0.0000
C9H10NO7 - R	C10H13NO7S	290.034000	0.003	n.d.	n.d.	n.d.	0.0001 ± 0.0000
C9H12NO6 - R	C10H15NO6S	276.054736	0.007	0.0001 ± 0.0000	0.0002 ± 0.0000	0.0003 ± 0.0000	0.0006 ± 0.0000
C9H10NO6 - R	C10H13NO6S	n.d.	n.d.	n.d.	n.d.	n.d.	n.d.
C9H8NO6 - R	C10H11NO6S	n.d.	n.d.	n.d.	n.d.	n.d.	n.d.
C9H10NO5 - R	C10H13NO5S	258.044138	-0.122	n.d.	n.d.	n.d.	0.0002 ± 0.0000
C9H8NO5 - R	C10H11NO5S	256.028480	-0.152	n.d.	n.d.	n.d.	0.0001 ± 0.0000
C9H12NO5 - R	C10H15NO5S	260.059822	0.010	n.d.	n.d.	n.d.	0.0001 ± 0.0000
C9H8NO4 - R	C10H11NO4S	n.d.	n.d.	n.d.	n.d.	n.d.	n.d.
C9H10NO4 - R	C10H13NO4S	n.d.	n.d.	n.d.	n.d.	n.d.	n.d.
C9H12NO4 - R	C10H15NO4S	n.d.	n.d.	n.d.	n.d.	n.d.	n.d.

D Appendix Chapter 4

D.1 Changes in pH during irradiation experiments

Table D.1 | Measured pH values during irradiation of Maillard model systems in the custom-built photolysis system used for online EEM measurements.

Irradiation time	pH ribose-lysine	pH ribose-arginine	pH ribose-histidine
0 h (before irradiation)	6.06	6.64	6.01
4 h	5.48	6.29	5.64
8 h	5.30	6.14	5.48
12 h	5.19	6.10	5.42
16 h	5.14	6.07	5.38
20 h	5.10	6.07	5.37

Table D.2 | Measured pH values (mean from n = 2 irradiation experiments) before and after irradiation of Maillard model systems in the Suntest CPS system.

Irradiation time	pH ribose-lysine	pH ribose-arginine	pH ribose-histidine
0 h (before irradiation)	6.0	6.6	6.0
8 h (after irradiation)	5.2	6.1	5.4

D.2 Holistic characterization of photosensitive MRPs

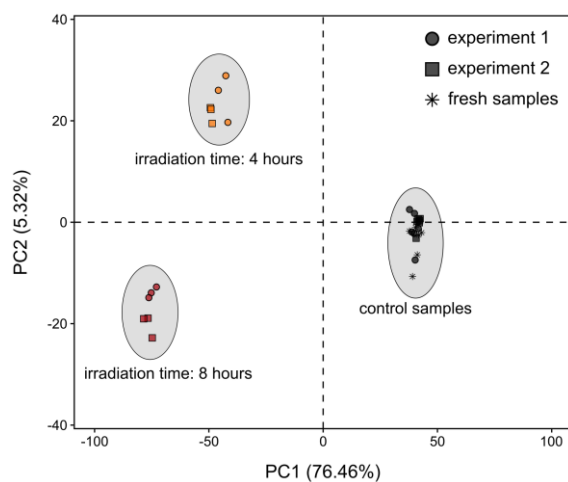


Figure D.1 | Principal component analysis of ribose-histidine FT-ICR-MS raw data. Samples were irradiated for four and eight hours in a suntester system. Additionally, control samples, which were kept under the same conditions, however, protected from light exposure, as well as freshly prepared model systems were analyzed. All experiments were carried out in two independent experiments. Each sample was injected in triplicate measurements (total number of samples per treatment = 6). Samples and replicate injections were measured in randomized order.

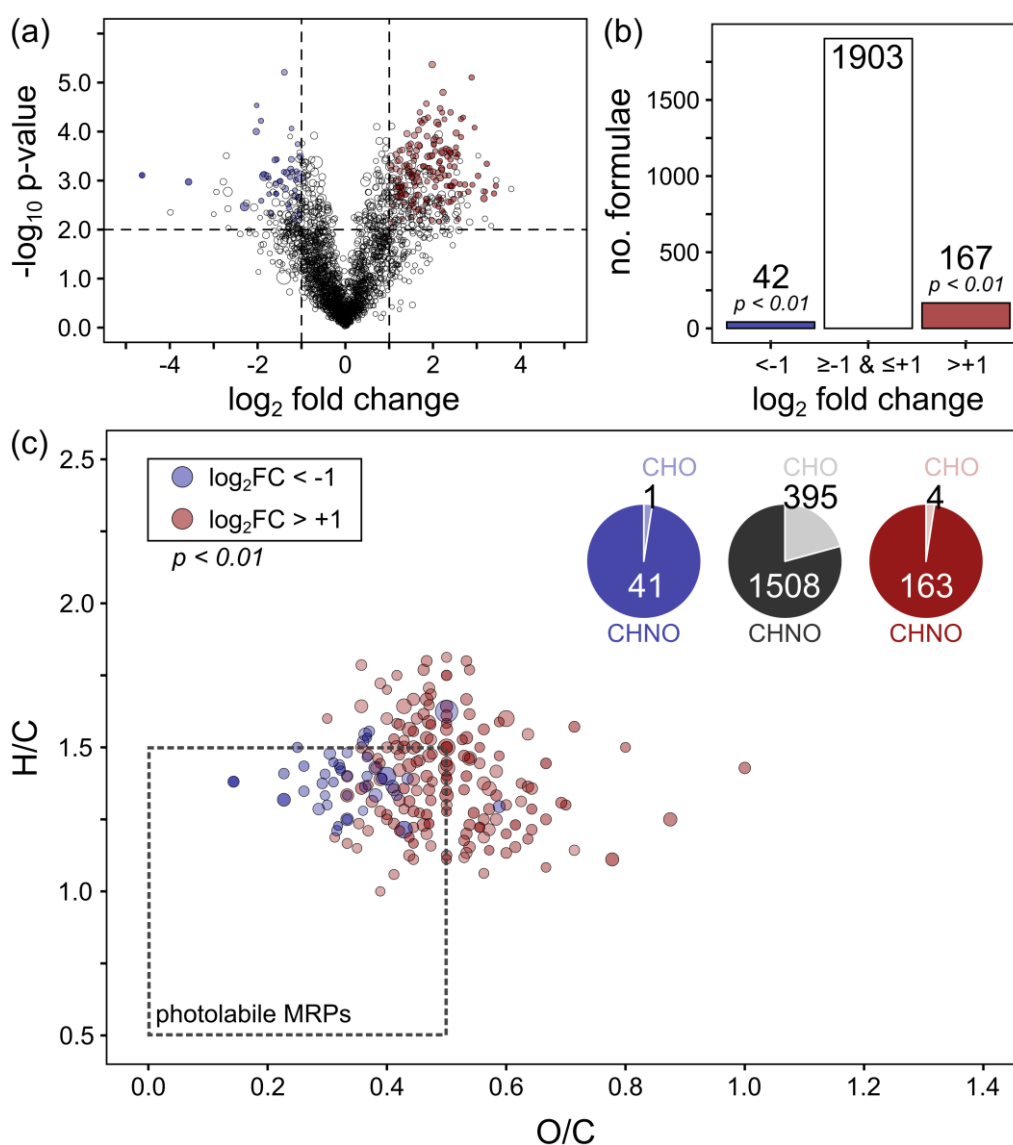


Figure D.2 | Effect of solar irradiation on elemental compositions of ribose-lysine MRPs. Model systems were irradiated for eight hours and compared to unirradiated control samples. Irradiation experiments were performed in duplicate. Each sample then was analyzed by FT-ICR-MS in triplicate injections ($N = 2 \times 3$). Peak intensities of all features found in irradiated samples were compared to the same features in the unirradiated control samples by Student's t-Test ($n = 3$): Features, which showed a significant decrease in peak intensities in both independent irradiation experiments are colored in blue. Features, which showed a significant increase or were newly formed upon irradiation are highlighted in red, respectively. (a) Volcano plot. (b) Number of molecular formulae showing significant changes in peak intensities. (c) Van Krevelen diagram of all significantly affected molecular formulae. Pie charts illustrate the reduced occurrence of nitrogen-free (CHO) MRPs in photochemical reactions. Black pie chart represents elemental compositions, which did not show a significant change in peak intensities upon irradiation.

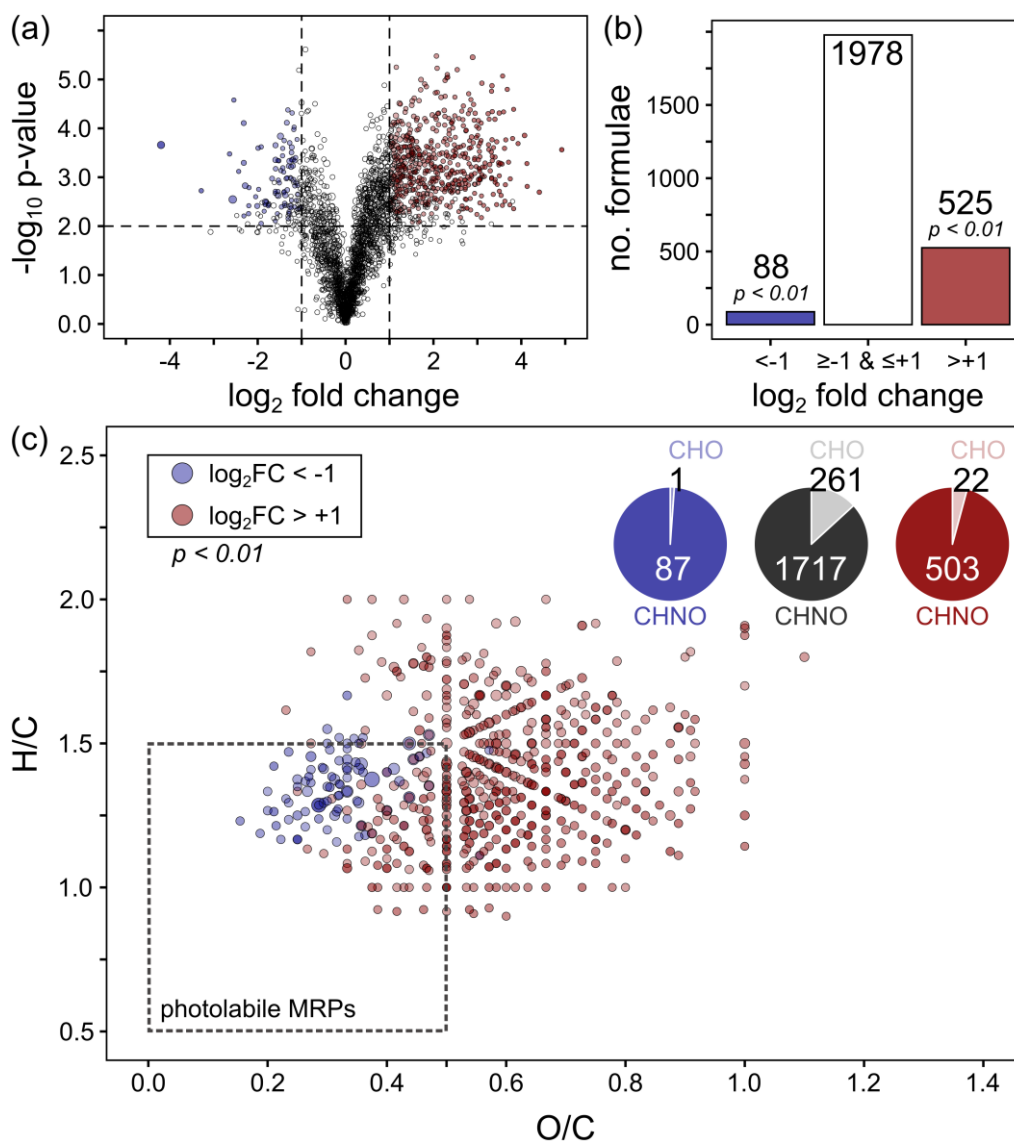


Figure D.3 | Effect of solar irradiation on elemental compositions of ribose-arginine MRPs. Model systems were irradiated for eight hours and compared to unirradiated control samples. Irradiation experiments were performed in duplicate. Each sample then was analyzed by FT-ICR-MS in triplicate injections ($N = 2 \times 3$). Peak intensities of all features found in irradiated samples were compared to the same features in the unirradiated control samples by Student's t-Test ($n = 3$): Features, which showed a significant decrease in peak intensities in both independent irradiation experiments are colored in blue. Features, which showed a significant increase or were newly formed upon irradiation are highlighted in red, respectively. (a) Volcano plot. (b) Number of molecular formulae showing significant changes in peak intensities. (c) Van Krevelen diagram of all significantly affected molecular formulae. Pie charts illustrate the reduced occurrence of nitrogen-free (CHO) MRPs in photochemical reactions. Black pie chart represents elemental compositions, which did not show a significant change in peak intensities upon irradiation.

D.3 Photooxidation of MRPs by singlet oxygen

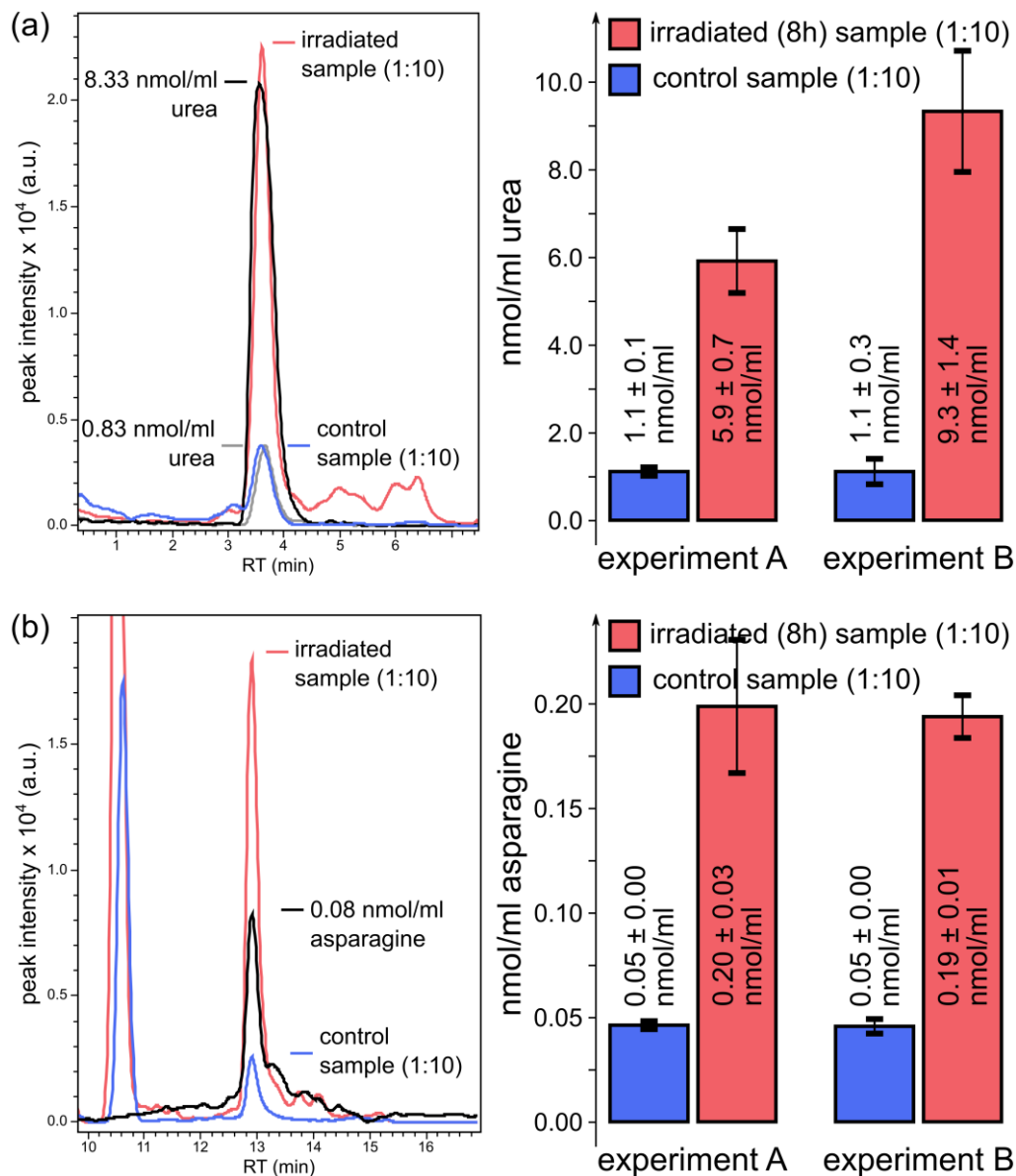


Figure D.4 | Quantification of (a) urea and (b) asparagine in ribose-histidine model systems. After lyophilization, the model systems were reconstituted in 2% acetonitrile solution to achieve a dilution factor of 1:10 (v/v) with respect to the original model system. Calibration curves were computed from analyzed standard solutions as shown below.

Table D.3 | Calibration standards used for quantification of urea and asparagine in ribose-histidine model systems. Standards were prepared in 2% acetonitrile solution. Concentration values are given in nmol mL⁻¹.

calibrant	urea	L-asparagine
1	0.08	0.04
2	0.17	0.08
3	0.83	0.38
4	1.67	0.76
5	8.33	3.78
6	16.65	

D.4 The role of imidazole groups in photochemical reactions

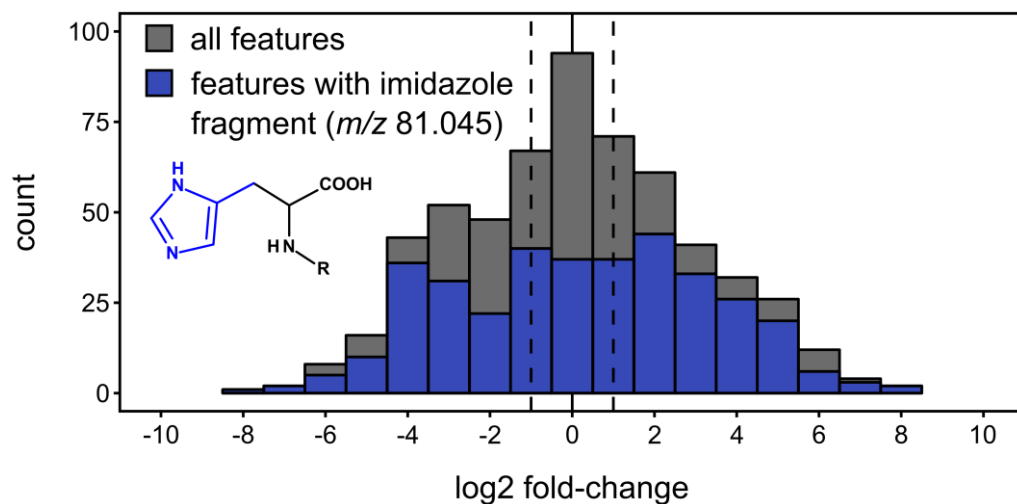


Figure D.5 | Screening of fragment spectra containing imidazole specific fragments at $m/z = 81.045$. Fragment spectra were acquired by data-dependent LC-MS/MS. Histograms illustrate the \log_2 fold change (irradiated samples vs. control samples) calculated from the peak intensities of the precursor ions, respectively, which represent the effect of irradiation on ribose-histidine samples after eight hours. Gray histogram represents all chromatographic features with available MS/MS spectra (N = 580). Blue histogram shows only features, which contained an imidazole characteristic fragment ($m/z = 81.045$) in their MS/MS spectra (N = 355).

D.5 Chemical diversity of thermally formed MRPs

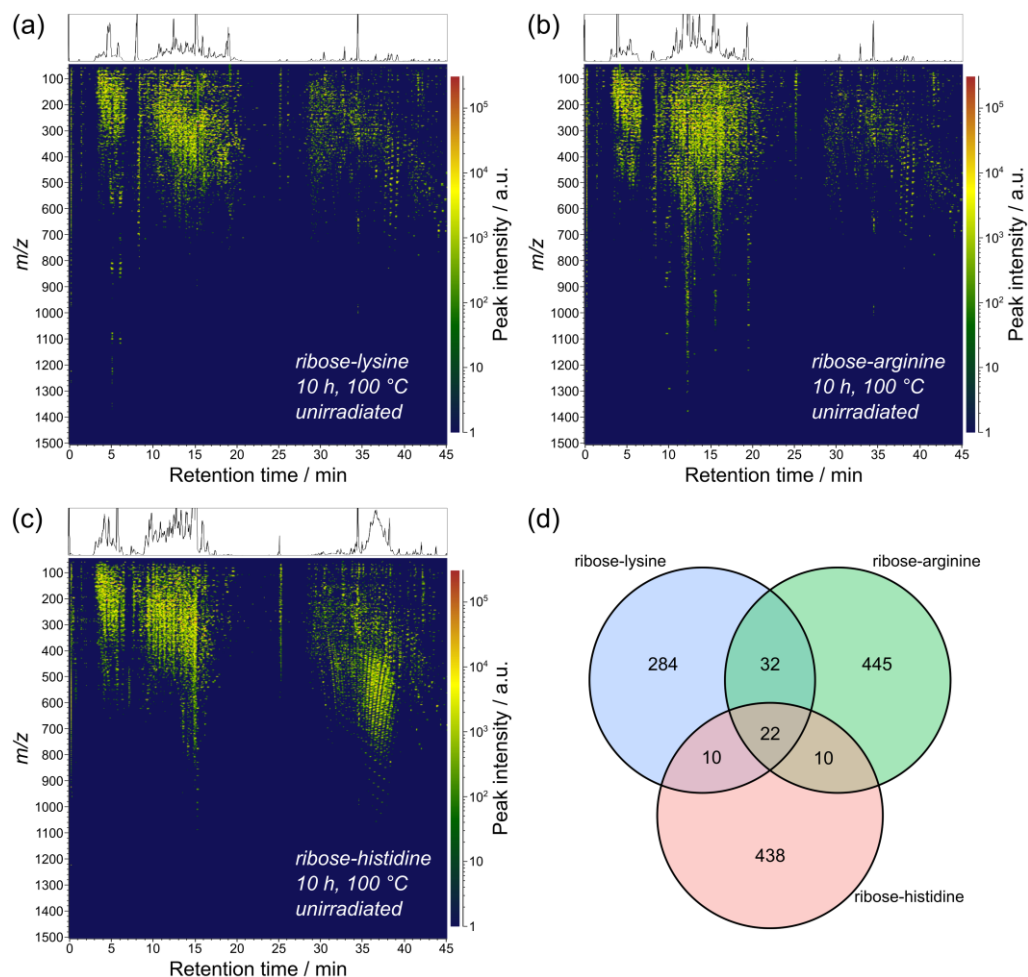


Figure D.6 | Non-targeted analysis of unirradiated model systems by tandem HILIC-RP chromatography. Retention time versus m/z -value plots of (a) a ribose-lysine, (b) a ribose-arginine, (c) and a ribose-histidine model system, heated for ten hours at 100 °C. Each dot in (a-c) represents an analytical signal (feature) colored according to the observed peak intensity. (d) Venn diagram illustrates the amino acid specific chemical diversity in produced MRPs. Between the three model systems, chromatographic features were considered as the same chemical compound when m/z -values and retention times were equal (m/z -alignment: ± 10 ppm and $\Delta RT \leq 30$ s).

D.6 Compositional description of antioxidants

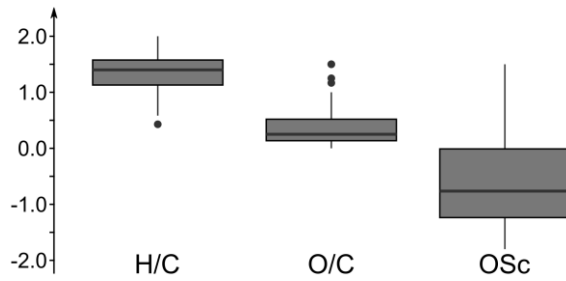


Figure D.7 | Compositional descriptors retrieved for 125 antioxidants containing no more than C, H, N, and O elements. Antioxidants were taken from FooDB (Release June 29, 2017).

D.7 LC-MS/MS analysis of AGE markers

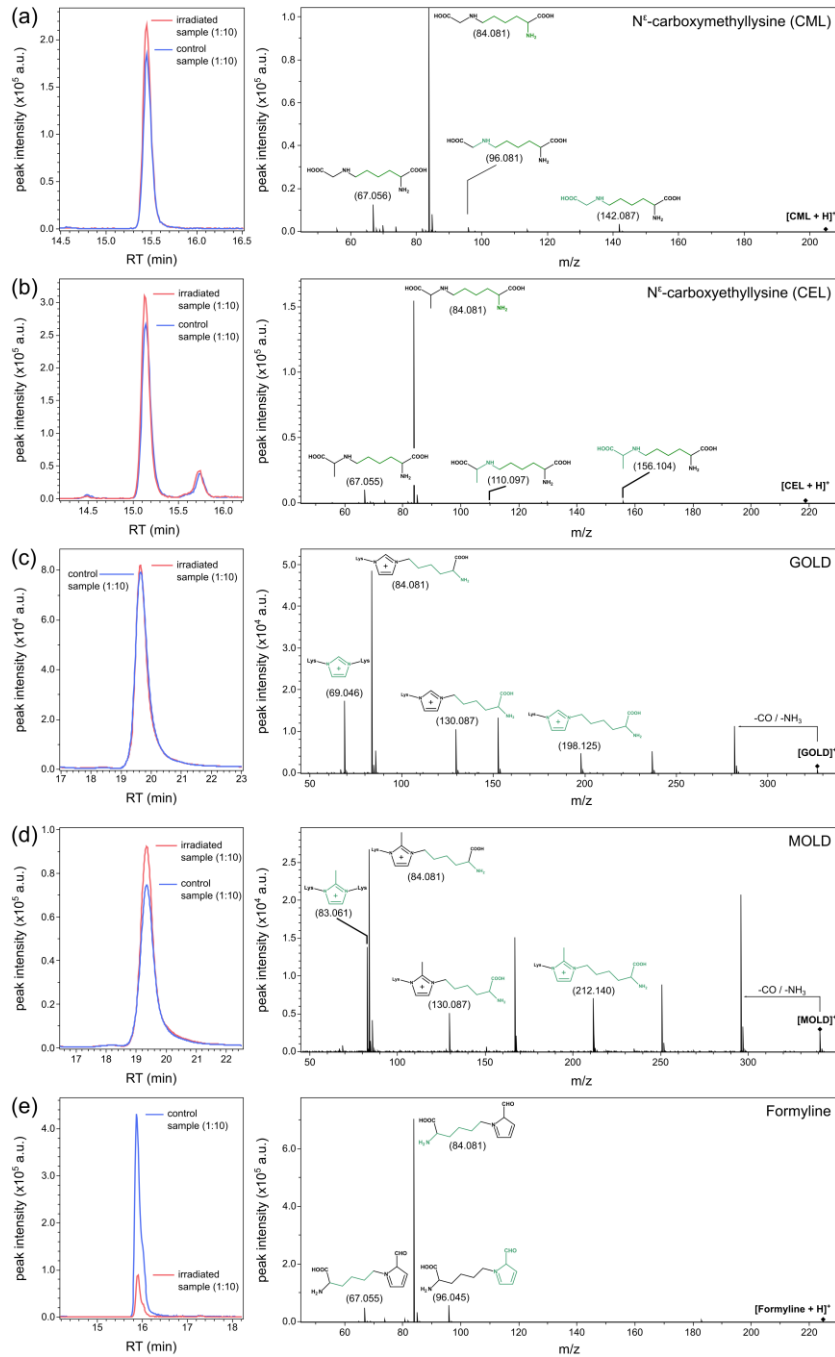


Figure D.8 | LC-MS/MS analysis of AGE markers in unirradiated ribose-lysine model systems (blue) and ribose-lysine model systems irradiated for eight hours (red). Structures were confirmed by MS/MS spectra. Detected markers were: (a) carboxymethyllysine (CML), (b) carboxyethyllysine (CEL), (c) GOLD, (d) MOLD, and (e) formyllysine.

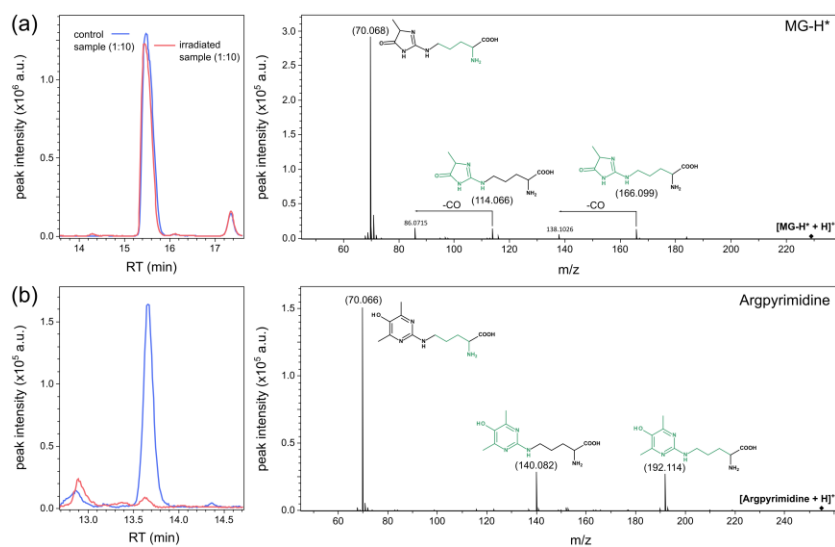


Figure D.9 | LC-MS/MS analysis of AGE markers in unirradiated ribose-arginine model systems (blue) and ribose-arginine model systems irradiated for eight hours (red). Structures were confirmed by MS/MS spectra. Detected markers were: (a) one hydroimidazolone isomer MG-H* (assignment of the three possible isomers MG H1 – MG H3 based on MS/MS data not possible), and (b) argpyrimidine.

D.8 Compositional descriptors

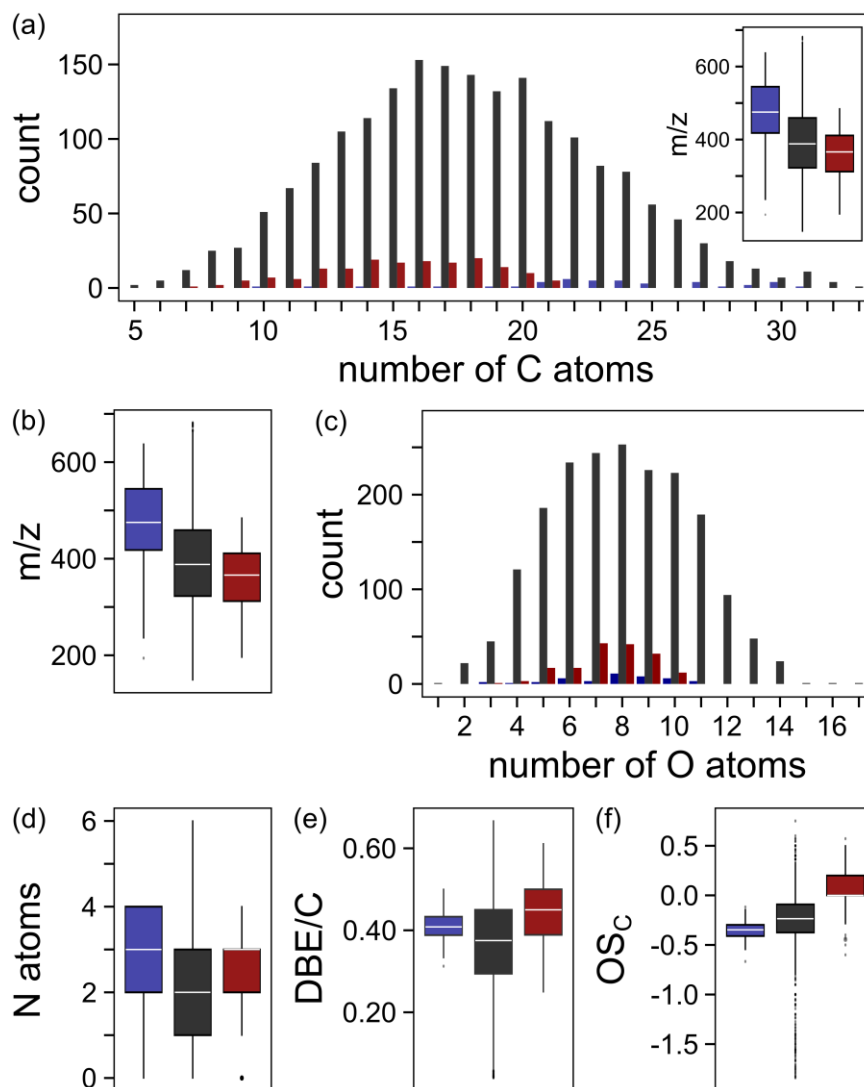


Figure D.10 | Overview of compositional descriptors retrieved for the ribose-lysine model system after molecular formulae computation from FT-ICR-MS data. Bar charts are grouped into features, which showed a significant decrease (blue; $\log_2\text{FC} < -1$ and $p < 0.01$, Student's t-Test ($n = 3$)) and significant increase (red; $\log_2\text{FC} > 1$ and $p < 0.01$, Student's t-Test ($n = 3$)) in peak intensities in both independent irradiation experiments, respectively. Features that did not show a significant change in peak intensities after an irradiation time of eight hours are colored in dark gray. Represented descriptors are (a) number of carbon atoms per formula, (b) measured m/z -values, (c) number of oxygen, and (d) number of nitrogen atoms per formula, as well as (e) average number of double bond equivalents per carbon atom and (f) average carbon oxidation state.

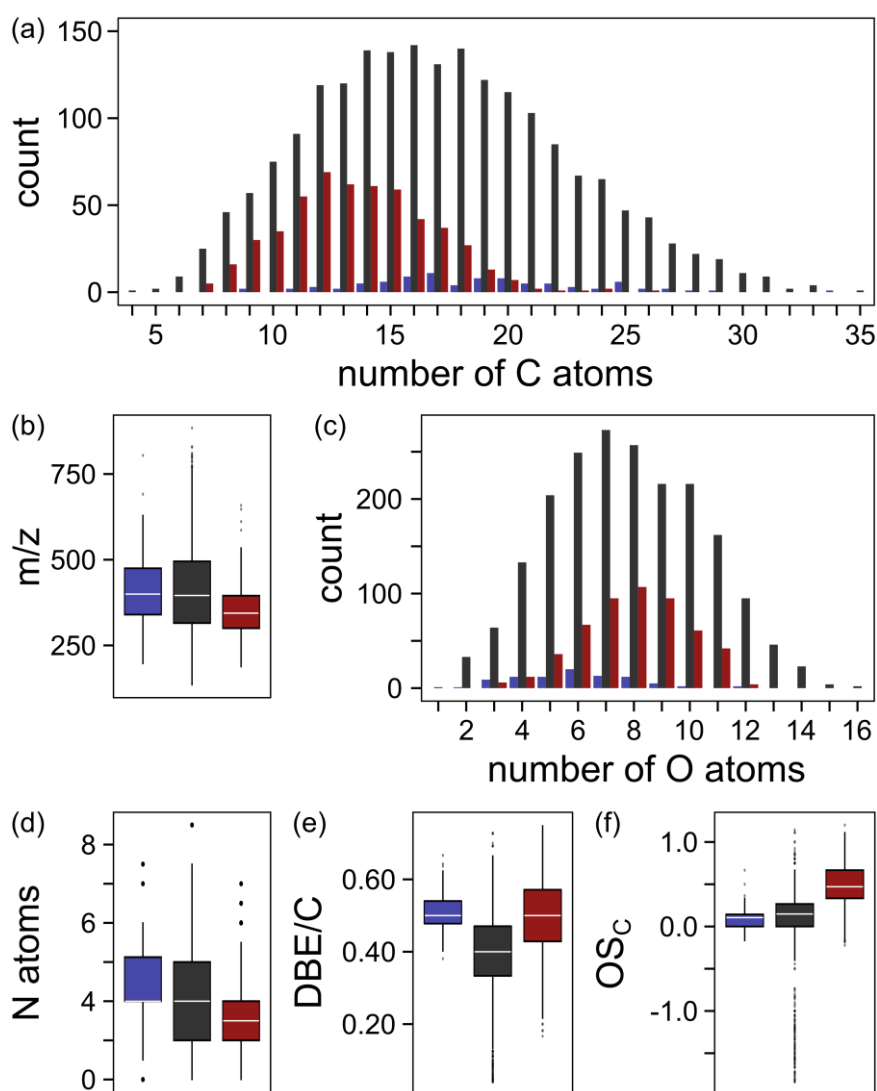


Figure D.11 | Overview of compositional descriptors retrieved for the ribose-arginine model system after molecular formulae computation from FT-ICR-MS data. Bar charts are grouped into features, which showed a significant decrease (blue; $\log_2FC < -1$ and $p < 0.01$, Student's t-Test ($n = 3$)) and significant increase (red; $\log_2FC > 1$ and $p < 0.01$, Student's t-Test ($n = 3$)) in peak intensities in both independent irradiation experiments, respectively. Features that did not show a significant change in peak intensities after an irradiation time of eight hours are colored in dark gray. Represented descriptors are (a) number of carbon atoms per formula, (b) measured m/z -values, (c) number of oxygen, and (d) number of nitrogen atoms per formula, as well as (e) average number of double bond equivalents per carbon atom and (f) average carbon oxidation state.

Bibliography

1. Maillard, L.C. *Comptes Rendus hebdomadaires de l'Académie des Sciences* **1912**, *154*, 66–68.
2. Hellwig, M.; Henle, T. *Angewandte Chemie International Edition* **2014**, *53*, 10316–10329.
3. Labuza, T.P.; Monnier, V.M.; Baynes, J.; O'Brien, J. *Maillard Reactions in Chemistry, Food and Health*. 1st ed. (Elsevier, 1998).
4. Ledl, F.; Schleicher, E. *Angewandte Chemie International Edition* **1990**, *29*, 565–594.
5. Erbersdobler, H.F.; Somoza, V. *Molecular Nutrition & Food Research* **2007**, *51*, 423–430.
6. Dyer, D.G.; Blackledge, J.A.; Thorpe, S.R.; Baynes, J.W. *Journal of Biological Chemistry* **1991**, *266*, 11654–11660.
7. Schleicher, E.D.; Wagner, E.; Nerlich, A.G. *The Journal of Clinical Investigation* **1997**, *99*, 457–468.
8. Wrodnigg, T.M.; Eder, B. in *Glycoscience: Epimerisation, Isomerisation and Rearrangement Reactions of Carbohydrates*, edited by Stütz, A.E. (Springer, 2001), pp. 115–152.
9. Davídek, T.; Clety, N.; Aubin, S.; Blank, I. *Journal of Agricultural and Food Chemistry* **2002**, *50*, 5472–5479.
10. Yaylayan, V.A.; Huyghues-Despointes, A. *Carbohydrate Research* **1996**, *286*, 179–187.
11. Ames, J. in *Biochemistry of Food Proteins*, edited by Hudson, B. (Springer US, 1992), pp. 99–153.
12. Vistoli, G.; De Maddis, D.; Cipak, A.; Zarkovic, N.; Carini, M.; Aldini, G. *Free Radical Research* **2013**, *47*, 3–27.
13. Namiki, M. in *Advances in Food Research. Volume 32*, edited by Chichester, C.O. & Schweigert, B.S. (Academic Press, 1988), pp. 115–184.
14. Nursten, H. *The Maillard Reaction. Chemistry, Biochemistry and Implications* (Royal Society of Chemistry, 2005).
15. Fayle, S.E.; Gerrard, J.A. *The Maillard Reaction* (Royal Society of Chemistry, 2002).
16. Hodge, J.E. *Journal of Agricultural and Food Chemistry* **1953**, *1*, 928–943.
17. Tressl, R.; Nittka, C.; Kersten, E.; Rewicki, D. *Journal of Agricultural and Food Chemistry* **1995**, *43*, 1163–1169.

18. Hayashi, T.; Namiki, M. *Agricultural and Biological Chemistry* **1986**, *50*, 1965–1970.
19. Davídek, T.; Devaud, S.; Robert, F.; Blank, I. *Journal of Agricultural and Food Chemistry* **2006**, *54*, 6667–6676.
20. Thornalley, P.J. *Annals of the New York Academy of Sciences* **2005**, *1043*, 111–117.
21. Smuda, M.; Glomb, M.A. *Journal of Agricultural and Food Chemistry* **2013**, *61*, 10198–10208.
22. Weenen, H. *Food Chemistry* **1998**, *62*, 393–401.
23. Weenen, H.; Apeldoorn, W. in *Flavour science: Recent developments*, edited by Taylor, A.J. & Mottram, D.S. (The Royal Society of Chemistry, 1996), pp. 211–216.
24. Biemel, K.M.; Conrad, J.; Lederer, M.O. *Angewandte Chemie International Edition* **2002**, *41*, 801–804.
25. Tressl, R.; Rewicki, D. in *Flavor Chemistry: Thirty Years of Progress*, edited by Teranishi, R.; Wick, E.L. & Hornstein, I. (Springer Science+Business Media, 1999), pp. 305–325.
26. Huyghues-Despointes, A.; Yaylayan, V.A. *Journal of Agricultural and Food Chemistry* **1996**, *44*, 672–681.
27. Hollnagel, A.; Kroh, L.W. *Zeitschrift für Lebensmittel-Untersuchung und Forschung* **1998**, *207*, 50–54.
28. Thornalley, P.J.; Langborg, A.; Minhas, H.S. *Biochemical Journal* **1999**, *344*, 109–116.
29. Cämmerer, B.; Wedzicha, B.L.; Kroh, L.W. *European Food Research and Technology* **1999**, *209*, 261–265.
30. de Bruijn, J.M.; Kieboom, A.P.G.; van Bekkum, H. *Starch - Stärke* **1987**, *39*, 23–28.
31. Davídek, T.; Robert, F.; Devaud, S.; Vera, F.A.; Blank, I. *Journal of Agricultural and Food Chemistry* **2006**, *54*, 6677–6684.
32. Martins, S.I.F.S.; Marcelis, A.T.M.; van Boekel, M.A.J.S. *Carbohydrate Research* **2003**, *338*, 1651–1663.
33. Ginz, M.; Balzer, H.H.; Bradbury, A.G.W.; Maier, H.G. *Zeitschrift für Lebensmittel-Untersuchung und Forschung* **2000**, *211*, 404–410.
34. Kim, M.-O.; Baltes, W. *Journal of Agricultural and Food Chemistry* **1996**, *44*, 282–289.
35. Brands, C.M.J.; van Boekel, M.A.J.S. *Journal of Agricultural and Food Chemistry* **2001**, *49*, 4667–4675.
36. Smuda, M.; Voigt, M.; Glomb, M.A. *Journal of Agricultural and Food Chemistry* **2010**, *58*, 6458–6464.

37. Davidek, T.; Devaud, S.; Robert, F.; Blank, I. *Annals of the New York Academy of Sciences* **2005**, *1043*, 73–79.
38. Davidek, T.; Gouézec, E.; Devaud, S.; Blank, I. *Annals of the New York Academy of Sciences* **2008**, *1126*, 241–243.
39. Rizzi, G.P. *Food Reviews International* **2008**, *24*, 416–435.
40. Yaylayan, V.A. *Food Science and Technology Research* **2003**, *9*, 1–6.
41. Yaylayan, V.A.; Keyhani, A. *Journal of Agricultural and Food Chemistry* **2001**, *49*, 800–803.
42. Cremer, D.R.; Vollenbroeker, M.; Eichner, K. *Zeitschrift für Lebensmittel-Untersuchung und Forschung* **2000**, *211*, 400–403.
43. Hofmann, T.; Schieberle, P. *Journal of Agricultural and Food Chemistry* **2000**, *48*, 4301–4305.
44. Yaylayan, V.A.; Keyhani, A. *Food Chemistry* **2001**, *74*, 1–9.
45. Yaylayan, V.A.; Haffenden, L.J.W. *Food Chemistry* **2003**, *81*, 403–409.
46. Adams, A.; Kitryte, V.; Venskutonis, R.; de Kimpe, N. *Journal of Agricultural and Food Chemistry* **2011**, *59*, 1449–1456.
47. Adams, A.; Polizzi, V.; van Boekel, M.A.J.S.; de Kimpe, N. *Journal of Agricultural and Food Chemistry* **2008**, *56*, 2147–2153.
48. Yaylayan, V.A.; Haffenden, L.J.W. *Food Research International* **2003**, *36*, 571–577.
49. van Boekel, M.A.J.S. *Biotechnology Advances* **2006**, *24*, 230–233.
50. Umamo, K.; Hagi, Y.; Nakahara, K.; Shyoji, A.; Shibamoto, T. *Journal of Agricultural and Food Chemistry* **1995**, *43*, 2212–2218.
51. Yu, A.-N.; Tan, Z.-W.; Wang, F.-S. *Food Chemistry* **2012**, *132*, 1316–1323.
52. Yaylayan, V.A.; Keyhani, A.; Wnorowski, A. *Journal of Agricultural and Food Chemistry* **2000**, *48*, 636–641.
53. Farmar, J.G.; Ulrich, P.C.; Cerami, A. *The Journal of Organic Chemistry* **1988**, *53*, 2346–2349.
54. Hofmann, T. *Journal of Agricultural and Food Chemistry* **1998**, *46*, 3902–3911.
55. Kort, M.J. in *Advances in Carbohydrate Chemistry and Biochemistry, Volume 25*, edited by Tipson, R.S. & Horton, D. (Academic Press, 1970), pp. 311–349.
56. Chellan, P.; Nagaraj, R.H. *Archives of Biochemistry and Biophysics* **1999**, *368*, 98–104.
57. Mesías, M.; Delgado-Andrade, C. *Current Opinion in Food Science* **2017**, *14*, 37–42.
58. Delgado-Andrade, C.; Rufián-Henares, J.A.; Morales, F.J. *Journal of Agricultural and Food Chemistry* **2005**, *53*, 7832–7836.

59. Borrelli, R.C.; Mennella, C.; Barba, F.; Russo, M.; Russo, G.L.; Krome, K.; Erbersdobler, H.F.; Faist, V.; Fogliano, V. *Food and Chemical Toxicology* **2003**, *41*, 1367–1374.
60. Pastoriza, S.; Rufián-Henares, J.A. *Food Chemistry* **2014**, *164*, 438–445.
61. Rivero, D.; Pérez-Magariño, S.; González-Sanjosé, M.L.; Valls-Belles, V.; Codoñer, P.; Muñoz, P. *Journal of Agricultural and Food Chemistry* **2005**, *53*, 3637–3642.
62. Langner, E.; Rzeski, W. *International Journal of Food Properties* **2014**, *17*, 344–353.
63. Fogliano, V.; Morales, F.J. *Food & Function* **2011**, *2*, 117–123.
64. Rizzi, G.P. *Food Reviews International* **1997**, *13*, 1–28.
65. Clark, A.V.; Tannenbaum, S.R. *Journal of Agricultural and Food Chemistry* **1974**, *22*, 1089–1093.
66. Tressl, R.; Wondrak, G.T.; Krüger, R.-P.; Rewicki, D. *Journal of Agricultural and Food Chemistry* **1998**, *46*, 104–110.
67. Hofmann, T. *Journal of Agricultural and Food Chemistry* **1998**, *46*, 3891–3895.
68. Hofmann, T.; Bors, W.; Stettmaier, K. *Journal of Agricultural and Food Chemistry* **1999**, *47*, 391–396.
69. Hofmann, T. in *The Maillard Reaction in Foods and Medicine*, edited by John O'Brien; Harry E. Nursten; M. James C. Crabbe & Jennifer M. Ames (Woodhead Publishing, 2005), pp. 82–88.
70. Hofmann, T. *Zeitschrift für Lebensmittel-Untersuchung und Forschung* **1998**, *206*, 251–258.
71. Mottram, D.S.; Wedzicha, B.L.; Dodson, A.T. *Nature* **2002**, *419*, 448–449.
72. Friedman, M. *Food & Function* **2015**, *6*, 1752–1772.
73. Duda-Chodak, A.; Tarko, T.; Sroka, P.; Satora, P. *Food & Function* **2016**, *7*, 1282–1295.
74. Yaylayan, V.A.; Locas, C.P.; Wnorowski, A.; O'Brien, J. *Journal of Agricultural and Food Chemistry* **2004**, *52*, 5559–5565.
75. Feather, M.S.; Nelson, D. *Journal of Agricultural and Food Chemistry* **1984**, *32*, 1428–1432.
76. Morales, F.J.; Somoza, V.; Fogliano, V. *Amino Acids* **2012**, *42*, 1097–1109.
77. Chu, F.L.; Yaylayan, V.A. *Annals of the New York Academy of Sciences* **2008**, *1126*, 30–37.
78. Cerny, C. *Annals of the New York Academy of Sciences* **2008**, *1126*, 66–71.
79. Blank, I.; Davidek, T.; Devaud, S.; Clety, N. *International Congress Series* **2002**, *1245*, 263–267.
80. Blank, I.; Devaud, S.; Matthey-Doret, W.; Robert, F. *Journal of Agricultural and Food Chemistry* **2003**, *51*, 3643–3650.

81. Hofmann, T. *European Food Research and Technology* **1999**, *209*, 113–121.
82. Saltmarch, M.; Labuza, T. *Diabetes* **1982**, *31*, 29–36.
83. Kwak, E.-J.; Lim, S.-I. *Amino Acids* **2004**, *27*, 85–90.
84. Moreno, F.J.; Molina, E.; Olano, A.; López-Fandiño, R. *Journal of Agricultural and Food Chemistry* **2003**, *51*, 394–400.
85. Jousse, F.; Jongen, T.; Agterof, W.; Russell, S.; Braat, P. *Journal of Food Science* **2002**, *67*, 2534–2542.
86. Coleman III, W.M. *Journal of Chromatographic Science* **1996**, *34*, 213–218.
87. Yu, A.-N.; Zhang, A.-D. *Food Chemistry* **2010**, *119*, 214–219.
88. Cerny, C.; Davídek, T. *Journal of Agricultural and Food Chemistry* **2003**, *51*, 2714–2721.
89. Lojzova, L.; Riddellova, K.; Hajslova, J.; Zrostlikova, J.; Schurek, J.; Cajka, T. *Analytica chimica acta* **2009**, *641*, 101–109.
90. Yi, J.; Kebede, B.T.; Dang, D.N.H.; Buvé, C.; Grauwet, T.; van Loey, A.; Hu, X.; Hendrickx, M. *LWT - Food Science and Technology* **2017**, *75*, 85–92.
91. Ruiz-Matute, A.I.; Hernández-Hernández, O.; Rodríguez-Sánchez, S.; Sanz, M.L.; Martínez-Castro, I. *Journal of Chromatography B* **2011**, *879*, 1226–1240.
92. Keyhani, A.; Yaylayan, V.A. *Journal of Agricultural and Food Chemistry* **1996**, *44*, 2511–2516.
93. Benson, L.M.; Naylor, S.; Tomlinson, A.J. *Food Chemistry* **1998**, *62*, 179–183.
94. Fay, L.B.; Brevard, H. *Mass Spectrometry Reviews* **2005**, *24*, 487–507.
95. Tressl, R.; Helak, B.; Kersten, E.; Rewicki, D. *Journal of Agricultural and Food Chemistry* **1993**, *41*, 547–553.
96. Yaylayan, V.A.; Keyhani, A. *Journal of Agricultural and Food Chemistry* **2000**, *48*, 2415–2419.
97. Ajandouz, E.H.; Tchiakpe, L.S.; Ore, F.D.; Benajiba, A.; Puigserver, A. *Journal of Food Science* **2001**, *66*, 926–931.
98. Andersen, C.M.; Mortensen, G. *Journal of Agricultural and Food Chemistry* **2008**, *56*, 720–729.
99. Lakowicz, J.R. *Principles of Fluorescence Spectroscopy*. 3rd ed. (Springer US, 2006).
100. Birlouez-Aragon, I.; Nicolas, M.; Metais, A.; Marchond, N.; Grenier, J.; Calvo, D. *International Dairy Journal* **1998**, *8*, 771–777.
101. Meerwaldt, R.; Graaff, R.; Oomen, P.H.; Links, T.P.; Jager, J.J.; Alderson, N.L.; Thorpe, S.R.; Baynes, J.W.; Gans, R.O.; Smit, A.J. *Diabetologia* **2004**, *47*, 1324–1330.
102. Meerwaldt, R.; Lutgers, H.L.; Links, T.P.; Graaff, R.; Baynes, J.W.; Gans, R.O.B.; Smit, A.J. *Diabetes Care* **2007**, *30*, 107–112.

103. Roullier-Gall, C.; Heinzmann, S.S.; Garcia, J.-P.; Schmitt-Kopplin, P.; Gougeon, R.D. *npj Science of Food* **2017**, *1*, 1.
104. Staempfli, A.A.; Blank, I.; Fumeaux, R.; Fay, L.B. *Biological Mass Spectrometry* **1994**, *23*, 642–646.
105. Prabhakaram, M.; Smith, J.B.; Ortwerth, B.J. *IUBMB Life* **1996**, *40*, 315–325.
106. Lapolla, A.; Gerhardinger, C.; Baldo, L.; Fedele, D.; Keane, A.; Seraglia, R.; Catinella, S.; Traldi, P. *Biochimica et Biophysica Acta (BBA) - Molecular Basis of Disease* **1993**, *1225*, 33–38.
107. Lapolla, A.; Fedele, D.; Aronica, R.; Garboglio, M.; D'Alpaos, M.; Seraglia, R.; Traldi, P. *Rapid Communications in Mass Spectrometry* **1997**, *11*, 1342–1346.
108. Lapolla, A.; Fedele, D.; Garboglio, M.; Martano, L.; Tonani, R.; Seraglia, R.; Favretto, D.; Fedrigo, M.A.; Traldi, P. *Journal of the American Society for Mass Spectrometry* **2000**, *11*, 153–159.
109. Cataldi, T.R.I.; Campa, C.; Benedetto, G.E. de. *Fresenius' Journal of Analytical Chemistry* **2000**, *368*, 739–758.
110. Antonio, C.; Larson, T.; Gilday, A.; Graham, I.; Bergström, E.; Thomas-Oates, J. *Rapid Communications in Mass Spectrometry* **2008**, *22*, 1399–1407.
111. Milkovska-Stamenova, S.; Schmidt, R.; Frolov, A.; Birkemeyer, C. *Journal of Agricultural and Food Chemistry* **2015**, *63*, 5911–5919.
112. ISO 18329:2004. *Milk and milk products - Determination of furosine content – Ion-pair reverse-phase high-performance liquid chromatography method.*
113. Degen, J.; Hellwig, M.; Henle, T. *Journal of Agricultural and Food Chemistry* **2012**, *60*, 7071–7079.
114. Wenzl, T.; de la Calle, M.B.; Anklam, E. *Food Additives & Contaminants* **2003**, *20*, 885–902.
115. Scheijen, J.L.; Clevers, E.; Engelen, L.; Dagnelie, P.C.; Brouns, F.; Stehouwer, C.D.A.; Schalkwijk, C.G. *Food Chemistry* **2016**, *190*, 1145–1150.
116. Tomlinson, A.J.; Mlotkiewicz, J.A.; Lewis, I.A.S. *Food Chemistry* **1994**, *49*, 219–223.
117. Ames, J.M.; Arnoldi, A.; Bates, L.; Negroni, M. *Journal of Agricultural and Food Chemistry* **1997**, *45*, 1256–1263.
118. Vallejo-Cordoba, B.; Mazorra-Manzano, M.A.; González-Córdova, A.F. *Journal of Agricultural and Food Chemistry* **2004**, *52*, 5787–5790.
119. Corradini, D.; Cannarsa, G.; Corradini, C.; Nicoletti, I.; Pizzoferrato, L.; Vivanti, V. *Electrophoresis* **1996**, *17*, 120–124.
120. Bermudo, E.; Nunez, O.; Moyano, E.; Puignou, L.; Galceran, M.T. *Journal of Chromatography A* **2007**, *1159*, 225–232.
121. Bermudo, E.; Núñez, O.; Puignou, L.; Galceran, M.T. *Journal of Chromatography A* **2006**, *1129*, 129–134.

122. Morales, F.J.; Babbel, M.-B. *Journal of Agricultural and Food Chemistry* **2002**, *50*, 4657–4661.
123. Moreno, F.J.; López-Fandiño, R.; Olano, A. *Journal of Agricultural and Food Chemistry* **2002**, *50*, 5179–5184.
124. Block, J. de; Merchiers, M.; Mortier, L.; Braekman, A.; Ooghe, W.; van Renterghem, R. *International Dairy Journal* **2003**, *13*, 87–94.
125. Johnson, P.; Philo, M.; Watson, A.; Mills, E.N.C. *Journal of Agricultural and Food Chemistry* **2011**, *59*, 12420–12427.
126. Schmidt, A.-C.; Fahlbusch, B.; Otto, M. *Journal of Mass Spectrometry* **2009**, *44*, 898–910.
127. Miyata, S.; Monnier, V.M. *The Journal of Clinical Investigation* **1992**, *89*, 1102–1112.
128. Hayase, F.; Nagaraj, R.H.; Miyata, S.; Njoroge, F.G.; Monnier, V.M. *The Journal of Biological Chemistry* **1989**, *264*, 3758–3764.
129. Takeuchi, M.; Iwaki, M.; Takino, J.-i.; Shirai, H.; Kawakami, M.; Bucala, R.; Yamagishi, S.-i. *Laboratory Investigation* **2010**, *90*, 1117–1127.
130. Hein, G.; Wiegand, R.; Lehmann, G.; Stein, G.; Franke, S. *Rheumatology* **2003**, *42*, 1242–1246.
131. Tareke, E.; Forslund, A.; Lindh, C.H.; Fahlgren, C.; Östman, E. *Food Chemistry* **2013**, *141*, 4253–4259.
132. Gómez-Ojeda, A.; Jaramillo-Ortíz, S.; Wrobel, K.; Wrobel, K.; Barbosa-Sabanero, G.; Luevano-Contreras, C.; La Maza, M.P. de; Uribarri, J.; del Castillo, M.D.; Garay-Sevilla, M.E. *Food Chemistry* **2018**, *243*, 11–18.
133. Fiehn, O. *Plant Molecular Biology* **2002**, *48*, 155–171.
134. Oliver, S.G.; Winson, M.K.; Kell, D.B.; Baganz, F. *Trends in Biotechnology* **1998**, *16*, 373–378.
135. Cifuentes, A. *Journal of Chromatography A* **2009**, *1216*, 7109.
136. Cifuentes, A. *Trends in Analytical Chemistry* **2017**, *96*, 1.
137. León, C.; Cifuentes, A.; Valdés, A. in *Data Analysis for Omic Sciences: Methods and Applications*, edited by Jaumot, J.; Bedia, C. & Tauler, R. (Elsevier, 2018), pp. 643–685.
138. Beleggia, R.; Platani, C.; Papa, R.; Di Chio, A.; Barros, E.; Mashaba, C.; Wirth, J.; Fammartino, A.; Sautter, C.; Conner, S.; Rauscher, J.; Stewart, D.; Cattivelli, L. *Journal of Agricultural and Food Chemistry* **2011**, *59*, 9366–9377.
139. Jeandet, P.; Heinzmann, S.S.; Roullier-Gall, C.; Cilindre, C.; Aron, A.; Deville, M.A.; Moritz, F.; Karbowski, T.; Demarville, D.; Brun, C.; Moreau, F.; Michalke, B.; Liger-Belair, G.; Witting, M.; Lucio, M.; Steyer, D.; Gougeon, R.D.; Schmitt-Kopplin, P. *Proceedings of the National Academy of Sciences of the United States of America* **2015**, *112*, 5893–5898.

140. Moritz, F.; Hemmler, D.; Kanawati, B.; Schnitzler, J.-P.; Schmitt-Kopplin, P. in *Fundamentals and Applications of Fourier Transform Mass Spectrometry*, edited by Schmitt-Kopplin, P. & Kanawati, B. (Elsevier, 2019), Vol. 1, in press.
141. Grauwet, T.; Vervoort, L.; Colle, I.; van Loey, A.; Hendrickx, M. *Trends in Biotechnology* **2014**, *32*, 125–131.
142. Ruf, A.; d'Hendecourt, L.L.S.; Schmitt-Kopplin, P. *Life* **2018**, *8*,
143. Hall, R.D. in *Annual Plant Reviews Volume 43* (John Wiley & Sons, Ltd, 2011), pp. 1–24.
144. Pischetsrieder, M. *Angewandte Chemie International Edition* **2018**, *57*, 11476–11477.
145. Erbersdobler, H.; Bock, G. *Naturwissenschaften* **1967**, *54*, 648.
146. Brüggemann, J.; Erbersdobler, H. *Zeitschrift für Lebensmittel-Untersuchung und Forschung* **1968**, *137*, 137–143.
147. Nakayama, T.; Hayase, F.; Kato, H. *Agricultural and Biological Chemistry* **1980**, *44*, 1201–1202.
148. Ahmed, M.U.; Thorpe, S.R.; Baynes, J.W. *Journal of Biological Chemistry* **1986**, *261*, 4889–4894.
149. Sell, D.R.; Monnier, V.M. *Journal of Biological Chemistry* **1989**, *264*, 21597–21602.
150. Grandhee, S.K.; Monnier, V.M. *Journal of Biological Chemistry* **1991**, *266*, 11649–11653.
151. Shipanova, I.N.; Glomb, M.A.; Nagaraj, R.H. *Archives of Biochemistry and Biophysics* **1997**, *344*, 29–36.
152. Lindenmeier, M.; Faist, V.; Hofmann, T. *Journal of Agricultural and Food Chemistry* **2002**, *50*, 6997–7006.
153. Hellwig, M.; Henle, T. *Zeitschrift für Lebensmittel-Untersuchung und Forschung* **2010**, *230*, 903–914.
154. Rizzi, G.P. *Journal of Agricultural and Food Chemistry* **2004**, *52*, 953–957.
155. Smith, P.R.; Thornalley, P.J. *European Journal of Biochemistry* **1992**, *210*, 729–739.
156. Jakas, A.; Horvat, Š. *Biopolymers* **2003**, *69*, 421–431.
157. Bell, L.N. *Food Chemistry* **1997**, *59*, 143–147.
158. Hao, C.; March, R.E. *Journal of Mass Spectrometry* **2001**, *36*, 509–521.
159. Yaylayan, V.A. *Trends in Food Science & Technology* **1997**, *8*, 13–18.
160. Ajandouz, E.H.; Puigserver, A. *Journal of Agricultural and Food Chemistry* **1999**, *47*, 1786–1793.
161. Hertkorn, N.; Frommberger, M.; Witt, M.; Koch, B.P.; Schmitt-Kopplin, P.; Perdue, E.M. *Analytical Chemistry* **2008**, *80*, 8908–8919.
162. Kind, T.; Fiehn, O. *BMC Bioinformatics* **2007**, *8*, 105.

163. Senior, J.K. *American Journal of Mathematics* **1951**, *73*, 663–689.
164. Marshall, A.G.; Hendrickson, C.L. *Annual Review of Analytical Chemistry* **2008**, *1*, 579–599.
165. Makarov, A.; Denisov, E.; Kholomeev, A.; Balschun, W.; Lange, O.; Strupat, K.; Horning, S. *Analytical Chemistry* **2006**, *78*, 2113–2120.
166. Forcisi, S.; Moritz, F.; Kanawati, B.; Tziotis, D.; Lehmann, R.; Schmitt-Kopplin, P. *Journal of Chromatography A* **2013**, *1292*, 51–65.
167. Nikolaev, E.N.; Kostyukevich, Y.I.; Vladimirov, G.N. *Mass Spectrometry Reviews* **2016**, *35*, 219–258.
168. Marshall, A.G.; Hendrickson, C.L.; Jackson, G.S. *Mass Spectrometry Reviews* **1998**, *17*, 1–35.
169. Hertkorn, N.; Ruecker, C.; Meringer, M.; Gugisch, R.; Frommberger, M.; Perdue, E.M.; Witt, M.; Schmitt-Kopplin, P. *Analytical and Bioanalytical Chemistry* **2007**, *389*, 1311–1327.
170. Rychlik, M.; Kanawati, B.; Schmitt-Kopplin, P. *Trends in Analytical Chemistry* **2017**, *96*, 22–30.
171. da Silva, R.R.; Dorrestein, P.C.; Quinn, R.A. *Proceedings of the National Academy of Sciences of the United States of America* **2015**, *112*, 12549–12550.
172. Evans, A.M.; DeHaven, C.D.; Barrett, T.; Mitchell, M.; Milgram, E. *Analytical Chemistry* **2009**, *81*, 6656–6667.
173. Cuadros-Inostroza, A.; Giavalisco, P.; Hummel, J.; Eckardt, A.; Willmitzer, L.; Peña-Cortés, H. *Analytical Chemistry* **2010**, *82*, 3573–3580.
174. Schmitt-Kopplin, P.; Gabelica, Z.; Gougeon, R.D.; Fekete, A.; Kanawati, B.; Harir, M.; Gebefuegi, I.; Eckel, G.; Hertkorn, N. *Proceedings of the National Academy of Sciences* **2010**, *107*, 2763–2768.
175. Koch, B.P.; Dittmar, T.; Witt, M.; Kattner, G. *Analytical Chemistry* **2007**, *79*, 1758–1763.
176. Marshall, A.G. *Analytical Chemistry* **1979**, *51*, 1710–1714.
177. Kanawati, B.; Bader, T.M.; Wanczek, K.-P.; Li, Y.; Schmitt-Kopplin, P. *Rapid Communications in Mass Spectrometry* **2017**, *31*, 1607–1615.
178. Ruddy, B.M.; Blakney, G.T.; Rodgers, R.P.; Hendrickson, C.L.; Marshall, A.G. *Journal of the American Society for Mass Spectrometry* **2013**, *24*, 1608–1611.
179. Kim, S.; Kramer, R.W.; Hatcher, P.G. *Analytical Chemistry* **2003**, *75*, 5336–5344.
180. Hughey, C.A.; Hendrickson, C.L.; Rodgers, R.P.; Marshall, A.G.; Qian, K. *Analytical Chemistry* **2001**, *73*, 4676–4681.
181. Marshall, J.W.; Schmitt-Kopplin, P.; Schuetz, N.; Moritz, F.; Roullier-Gall, C.; Uhl, J.; Colyer, A.; Jones, L.L.; Rychlik, M.; Taylor, A.J. *Food Chemistry* **2018**, *242*, 316–322.

182. Koch, B.P.; Dittmar, T. *Rapid Communications in Mass Spectrometry* **2006**, *20*, 926–932.
183. Kroll, J.H.; Donahue, N.M.; Jimenez, J.L.; Kessler, S.H.; Canagaratna, M.R.; Wilson, K.R.; Altieri, K.E.; Mazzoleni, L.R.; Wozniak, A.S.; Bluhm, H.; Mysak, E.R.; Smith, J.D.; Kolb, C.E.; Worsnop, D.R. *Nature Chemistry* **2011**, *3*, 133–139.
184. Yassine, M.M.; Harir, M.; Dabek-Zlotorzynska, E.; Schmitt-Kopplin, P. *Rapid Communications in Mass Spectrometry* **2014**, *28*, 2445–2454.
185. Walker, A.; Pfitzner, B.; Neschen, S.; Kahle, M.; Harir, M.; Lucio, M.; Moritz, F.; Tziotis, D.; Witting, M.; Rothballer, M.; Engel, M.; Schmid, M.; Endesfelder, D.; Klingenspor, M.; Rattei, T.; Castell, W. zu; Hrabé de Angelis, M.; Hartmann, A.; Schmitt-Kopplin, P. *The ISME journal* **2014**, *8*, 2380–2396.
186. Idborg, H.; Zamani, L.; Edlund, P.-O.; Schuppe-Koistinen, I.; Jacobsson, S.P. *Journal of Chromatography B* **2005**, *828*, 9–13.
187. Tolstikov, V.V.; Fiehn, O. *Analytical Biochemistry* **2002**, *301*, 298–307.
188. Cubbon, S.; Bradbury, T.; Wilson, J.; Thomas-Oates, J. *Analytical Chemistry* **2007**, *79*, 8911–8918.
189. Hemmler, D.; Heinzmann, S.S.; Wöhr, K.; Schmitt-Kopplin, P.; Witting, M. *Electrophoresis* **2018**, *39*, 1645–1653.
190. Kolb, V.M.; Bajagic, M.; Zhu, W.; Cody, G.D. in *Astrobiology and Planetary Missions*, edited by Hoover, R.B.; Levin, G.V.; Rozanov, A.Y. & Gladstone, G.R. (International Society for Optics and Photonics, 2005), Vol. 5906.
191. Mottram, D.S. in *Flavours and Fragrances: Chemistry, Bioprocessing and Sustainability*, edited by Berger, R.G. (Springer, 2007), pp. 269–283.
192. Ibáñez, C.; Simó, C.; García-Cañas, V.; Acunha, T.; Cifuentes, A. *Analytical and Bioanalytical Chemistry* **2015**, *407*, 6275–6287.
193. Roullier-Gall, C.; Boutegrabet, L.; Gougeon, R.D.; Schmitt-Kopplin, P. *Food Chemistry* **2014**, *152*, 100–107.
194. Liger-Belair, G.; Cilindre, C.; Gougeon, R.D.; Lucio, M.; Gebefugi, I.; Jeandet, P.; Schmitt-Kopplin, P. *Proceedings of the National Academy of Sciences of the United States of America* **2009**, *106*, 16545–16549.
195. Garrett, R.; Vaz, B.G.; Hovell, A.M.C.; Eberlin, M.N.; Rezende, C.M. *Journal of Agricultural and Food Chemistry* **2012**, *60*, 4253–4258.
196. Golon, A.; Kropf, C.; Vockenroth, I.; Kuhnert, N. *Foods* **2014**, *3*, 461–475.
197. Lucio, M.; Fekete, A.; Frommberger, M.; Schmitt-Kopplin, P. in *Handbook of Molecular Microbial Ecology I. Metagenomics and Complementary Approaches*, edited by de Bruijn, F.J. (John Wiley & Sons, Inc, 2011), pp. 683–695.
198. Tziotis, D.; Hertkorn, N.; Schmitt-Kopplin, P. *European Journal of Mass Spectrometry* **2011**, *17*, 415–421.

199. R Development Core Team. *R: A Language and Environment for Statistical Computing*. Available at <http://www.R-project.org> (2008).
200. Kroh, L.W. *Food Chemistry* **1994**, *51*, 373–379.
201. Mossine, V.V.; Linetsky, M.; Glinsky, G.V.; Ortwerth, B.J.; Feather, M.S. *Chemical Research in Toxicology* **1999**, *12*, 230–236.
202. Dalko, P.I.; Moisan, L. *Angewandte Chemie International Edition* **2001**, *40*, 3726–3748.
203. Pfeifer, Y.V.; Haase, P.T.; Kroh, L.W. *Journal of Agricultural and Food Chemistry* **2013**, *61*, 3090–3096.
204. Henning, C.; Glomb, M.A. *Glycoconjugate Journal* **2016**, *33*, 499–512.
205. Degenhardt, T.P.; Brinkmann-Frye, E.; Thorpe, S.R.; Baynes, J.W. in *The Maillard Reaction in Foods and Medicine*, edited by O'Brien, J.; Nursten, H.E.; Crabbe, M.J. & Ames, J.M. (Elsevier Reference Monographs, 1998), pp. 3–10.
206. Mottram, D.S.; Nobrega, I.C.C. *Journal of Agricultural and Food Chemistry* **2002**, *50*, 4080–4086.
207. Vallejo-Cordoba, B.; González-Córdova, A.F. *Electrophoresis* **2007**, *28*, 4063–4071.
208. Davídek, T.; Clety, N.; Devaud, S.; Robert, F.; Blank, I. *Journal of Agricultural and Food Chemistry* **2003**, *51*, 7259–7265.
209. Katayama, H.; Tatemichi, Y.; Nakajima, A. *Food Chemistry* **2017**, *228*, 279–286.
210. Ibanez, C.; Simo, C.; Garcia-Canas, V.; Acunha, T.; Cifuentes, A. *Analytical and Bioanalytical Chemistry* **2015**, *407*, 6275–6287.
211. Hemmler, D.; Roullier-Gall, C.; Marshall, J.W.; Rychlik, M.; Taylor, A.J.; Schmitt-Kopplin, P. *Scientific Reports* **2017**, *7*, 3227.
212. Moritz, F.; Kaling, M.; Schnitzler, J.-P.; Schmitt-Kopplin, P. *Plant, Cell & Environment* **2017**, *40*, 1057–1073.
213. Delphine Laroque; Claude Inisan; Céline Berger; Éric Vouland; Laurent Dufossé; Fabienne Guérard. *Food Chemistry* **2008**, *111*, 1032–1042.
214. Herzsprung, P.; Hertkorn, N.; Tümpling, W. von; Harir, M.; Friese, K.; Schmitt-Kopplin, P. *Analytical and Bioanalytical Chemistry* **2014**, *406*, 7977–7987.
215. Ashoor, S.H.; Zent, J.B. *Journal of Food Science* **1984**, *49*, 1206–1207.
216. Brotzel, F.; Mayr, H. *Organic and Biomolecular Chemistry* **2007**, *5*, 3814–3820.
217. Munch, G.; Schick Tanz, D.; Behme, A.; Gerlach, M.; Riederer, P.; Palm, D.; Schinzel, R. *Nature Biotechnology* **1999**, *17*, 1006–1010.
218. Lericci, C.R.; Barbanti, D.; Manzano, M.; Cherubin, S. *Lebensmittel-Wissenschaft & Technologie* **1990**, *23*, 289–294.
219. Hwang, I.G.; Kim, H.Y.; Woo, K.S.; Lee, J.; Jeong, H.S. *Food Chemistry* **2011**, *126*, 221–227.

220. de Roos, K.B. in *Flavor precursors. ACS symposium series*, edited by Teranishi, R.; Takeoka, G.R. & Güntert, M. (American Chem. Soc, 1992), pp. 203–216.
221. Friedman, M.; Molnar-Perl, I. *Journal of Agricultural and Food Chemistry* **1990**, *38*, 1642–1647.
222. Hofmann, T.; Schieberle, P. *Journal of Agricultural and Food Chemistry* **1995**, *43*, 2187–2194.
223. Van den Ouweland, G.A.M.; Peer, H.G. *Journal of Agricultural and Food Chemistry* **1975**, *23*, 501–505.
224. Martins, S.I.F.S.; van Boekel, M.A.J.S. *Food Chemistry* **2005**, *92*, 437–448.
225. Yaylayan, V.A.; Ismail, A.A.; Mandeville, S. *Carbohydrate Research* **1993**, *248*, 355–360.
226. Hayward, L.D.; Angyal, S.J. *Carbohydrate Research* **1977**, *53*, 13–20.
227. Bunn, H.F.; Higgins, P.J. *Science* **1981**, *213*, 222–224.
228. O'Brien, J.; Morrissey, P.A.; Ames, J.M. *Critical Reviews in Food Science and Nutrition* **1989**, *28*, 211–248.
229. Adams, A.; de Kimpe, N. *Food Chemistry* **2009**, *115*, 1417–1423.
230. Rizzi, G.P. *Food Reviews International* **2013**, *29*, 178–191.
231. Ledl, F.; Severin, T. *Zeitschrift für Lebensmittel-Untersuchung und Forschung* **1978**, *167*, 410–413.
232. Wang, H.-Y.; Qian, H.; Yao, W.-R. *Food Chemistry* **2011**, *128*, 573–584.
233. Davies, M.J.; Truscott, R.J.W. *Journal of Photochemistry and Photobiology B: Biology* **2001**, *63*, 114–125.
234. Bensasson, R.V.; Land, E.J.; Truscott, T.G. *Flash Photolysis and Pulse Radiolysis. Contributions to the Chemistry of Biology and Medicine* (Elsevier Science, 1983).
235. Papeschi, G.; Monici, M.; Pinzauti, S. *Med. Biol. Environ.* **1982**, *10*, 245–250.
236. de La Rochette, A.; Birlouez-Aragon, I.; Silva, E.; Morlière, P. *Biochimica et Biophysica Acta (BBA) - General Subjects* **2003**, *1621*, 235–241.
237. Nagaraj, R.H.; Monnier, V.M. *Biochimica et Biophysica Acta (BBA) - General Subjects* **1992**, *1116*, 34–42.
238. Wondrak, G.T.; Roberts, M.J.; Jacobson, M.K.; Jacobson, E.L. *Journal of Investigative Dermatology* **2002**, *119*, 489–498.
239. Linetsky, M.; Ortwerth, B.J. *Photochemistry and Photobiology* **1996**, *63*, 649–655.
240. Ortwerth, B.J.; Malladi, P.; H, N.R.; Mikhail, L. *Photochemistry and Photobiology* **1997**, *65*, 666–672.
241. Argirova, M.D.; Breipohl, W. *Free Radical Research* **2002**, *36*, 1251–1259.
242. Wondrak, G.T.; Jacobson, E.L.; Jacobson, M.K. *Photochemical & Photobiological Sciences* **2002**, *1*, 355–363.

-
243. Hellwig, M.; Gensberger-Reigl, S.; Henle, T.; Pischetsrieder, M. *Seminars in Cancer Biology* **2018**, *49*, 1-8.
244. Encinas, M.V.; Rufs, A.M.; Lissi, E.A. *Journal of the Chemical Society, Perkin Transactions 2* **1985**, 457-460.
245. Lebedeva, N.V.; Chen, T.K.; Forbes, M.D.E. *Applied Magnetic Resonance* **2010**, *38*, 155-166.
246. Steenken, S.; Jaenicke-Zauner, W.; Schulte-Frohlinde, D. *Photochemistry and Photobiology* **1975**, *21*, 21-26.
247. Bohart, G.S.; Carson, J.F. *Nature* **1955**, *175*, 470-471.
248. Kessel, L.; Kalinin, S.; Soroka, V.; Larsen, M.; Johansson, L.B.-Å. *Acta Ophthalmologica Scandinavica* **2005**, *83*, 221-227.
249. Aiona, P.K.; Luek, J.L.; Timko, S.A.; Powers, L.C.; Gonsior, M.; Nizkorodov, S.A. *ACS Earth and Space Chemistry* **2018**, *2*, 235-245.
250. Timko, S.A.; Gonsior, M.; Cooper, W.J. *Water Research* **2015**, *85*, 266-274.
251. Murphy, K.R.; Stedmon, C.A.; Graeber, D.; Bro, R. *Analytical Methods* **2013**, *5*, 6557-6566.
252. Hemmler, D.; Roullier-Gall, C.; Marshall, J.W.; Rychlik, M.; Taylor, A.J.; Schmitt-Kopplin, P. *Scientific Reports* **2018**, *8*, 16879.
253. Smith, C.A.; Want, E.J.; O'Maille, G.; Abagyan, R.; Siuzdak, G. *Analytical Chemistry* **2006**, *78*, 779-787.
254. Tautenhahn, R.; Böttcher, C.; Neumann, S. *BMC Bioinformatics* **2008**, *9*, 504.
255. Prince, J.T.; Marcotte, E.M. *Analytical Chemistry* **2006**, *78*, 6140-6152.
256. Baisier, W.M.; Labuza, T.P. *Journal of Agricultural and Food Chemistry* **1992**, *40*, 707-713.
257. Morales, F.J.; van Boekel, M.A.J.S. *International Dairy Journal* **1998**, *8*, 907-915.
258. Matiacevich, S.B.; Santagapita, P.R.; Buera, M.P. *Critical Reviews in Food Science and Nutrition* **2005**, *45*, 483-495.
259. Graham, L.; Nagaraj, R.H.; Sayre, L.M.; Monnier, V.M. in *The Maillard Reaction in Foods and Medicine*, edited by O'Brien, J.; Nursten, H.E.; Crabbe, M.J. & Ames, J.M. (Elsevier Reference Monographs, 1998), p. 410.
260. Graham, L. *Biochimica et Biophysica Acta (BBA) - Protein Structure and Molecular Enzymology* **1996**, *1297*, 9-16.
261. Davies, M.J. *Biochimica et Biophysica Acta (BBA) - Proteins and Proteomics* **2005**, *1703*, 93-109.
262. Pattison, D.I.; Rahmanto, A.S.; Davies, M.J. *Photochemical & Photobiological Sciences* **2012**, *11*, 38-53.
263. Agon, V.V.; Bubb, W.A.; Wright, A.; Hawkins, C.L.; Davies, M.J. *Free Radical Biology and Medicine* **2006**, *40*, 698-710.

264. Chang, S.H.; Teshima, G.M.; Milby, T.; Gillece-Castro, B.; Canova-Davis, E. *Analytical Biochemistry* **1997**, *244*, 221–227.
265. Tomita, M.; Irie, M.; Ukita, T. *Biochemistry* **1969**, *8*, 5149–5160.
266. Sjöberg, B.; Foley, S.; Staicu, A.; Pascu, A.; Pascu, M.; Enescu, M. *Journal of Photochemistry and Photobiology B: Biology* **2016**, *159*, 106–110.
267. Wilkinson, F.; Helman, W.P.; Ross, A.B. *Journal of Physical and Chemical Reference Data* **1995**, *24*, 663–677.
268. Kai, S.; Suzuki, S. *Heterocycles* **1996**, *43*, 1185–1188.
269. Michaeli, A.; Feitelson, J. *Photochemistry and Photobiology* **1994**, *59*, 284–289.
270. Miskoski, S.; Garcia, N.A. *Photochemistry and Photobiology* **1993**, *57*, 447–452.
271. Gomyo, T.; Yang, Y.; Fujimaki, M. *Agricultural and Biological Chemistry* **1968**, *32*, 1061–1069.
272. Liu, F.; Lu, W.; Fang, Y.; Liu, J. *Physical Chemistry Chemical Physics* **2014**, *16*, 22179–22191.
273. Hwang, S.H.; Wang, Z.; Suh, H.-W.; Lim, S.S. *Food & Function* **2018**, *9*, 1790–1799.
274. Yilmaz, Y.; Toledo, R. *Food Chemistry* **2005**, *93*, 273–278.
275. Hayase, F.; Koyama, T.; Konishi, Y. *Journal of Agricultural and Food Chemistry* **1997**, *45*, 1137–1143.
276. Morales, F.J.; Babbel, M.-B. *Journal of Agricultural and Food Chemistry* **2002**, *50*, 2788–2792.
277. Lederer, M.O.; Klaiber, R.G. *Bioorganic & Medicinal Chemistry* **1999**, *7*, 2499–2507.
278. Karstens, T.; Rossbach, V. *Die Makromolekulare Chemie* **1989**, *190*, 3033–3053.
279. Moritz, F.; Janicka, M.; Zygler, A.; Forcisi, S.; Kot-Wasik, A.; Kot, J.; Gebefügi, I.; Namiesnik, J.; Schmitt-Kopplin, P. *Journal of Breath Research* **2015**, *9*, 27105.
280. Parker, J.K. in *Flavour Development, Analysis and Perception in Food and Beverages*, edited by Parker, J.K.; Elmore, J.S. & Methven, L. (Woodhead Publishing, 2015), pp. 151–185.
281. Schieberle, P. *Annals of the New York Academy of Sciences* **2005**, *1043*, 236–248.
282. Davidek, T.; Illmann, S.; Rytz, A.; Blank, I. *Food & Function* **2013**, *4*, 1105–1110.
283. Glomb, M.A.; Tschirnich, R. *Journal of Agricultural and Food Chemistry* **2001**, *49*, 5543–5550.
284. Blaženović, I.; Kind, T.; Ji, J.; Fiehn, O. *Metabolites* **2018**, *8*, 31.
285. Atanassov, I.; Hvarleva, T.; Rusanov, K.; Tsvetkov, I.; Atanassov, A. *Biotechnology & Biotechnological Equipment* **2009**, *23*, 1449–1452.
286. Arbulu, M.; Sampederro, M.C.; Gómez-Caballero, A.; Goicolea, M.A.; Barrio, R.J. *Analytica chimica acta* **2015**, *858*, 32–41.

-
287. Gougeon, R.D.; Lucio, M.; Frommberger, M.; Peyron, D.; Chassagne, D.; Alexandre, H.; Feuillat, F.; Voilley, A.; Cayot, P.; Gebefuegi, I.; Hertkorn, N.; Schmitt-Kopplin, P. *Proceedings of the National Academy of Sciences of the United States of America* **2009**, *106*, 9174–9179.
288. Dixon, R.A.; Strack, D. *Phytochemistry* **2003**, *62*, 815–816.
289. Dettmer, K.; Aronov, P.A.; Hammock, B.D. *Mass Spectrometry Reviews* **2007**, *26*, 51–78.
290. Theodoridis, G.; Gika, H.G.; Wilson, I.D. *Trends in Analytical Chemistry* **2008**, *27*, 251–260.
291. Greco, G.; Grosse, S.; Letzel, T. *Journal of Separation Science* **2013**, *36*, 1379–1388.
292. Falasca, S.; Petruzzello, F.; Kretz, R.; Rainer, G.; Zhang, X. *Journal of Chromatography A* **2012**, *1241*, 46–51.
293. Chalcraft, K.R.; McCarry, B.E. *Journal of Separation Science* **2013**, *36*, 3478–3485.
294. Louw, S.; Pereira, A.S.; Lynen, F.; Hanna-Brown, M.; Sandra, P. *Journal of Chromatography A* **2008**, *1208*, 90–94.
295. Haggarty, J.; Oppermann, M.; Dalby, M.; Burchmore, R.; Cook, K.; Weidt, S.; Burgess, K. *Metabolomics* **2015**, *11*, 1465–1470.
296. Granafei, S.; Azzone, P.; Spinelli, V.A.; Losito, I.; Palmisano, F.; Cataldi, T.R.I. *Journal of Chromatography A* **2016**, *1477*, 47–55.
297. Pyke, J.S.; Callahan, D.L.; Kanojia, K.; Bowne, J.; Sahani, S.; Tull, D.; Bacic, A.; McConville, M.J.; Roessner, U. *Metabolomics* **2015**, *11*, 1552–1562.
298. Haggarty, J.; Burgess, K.E.V. *Current Opinion in Biotechnology* **2017**, *43*, 77–85.
299. Alvarez-Segura, T.; Torres-Lapasió, J.R.; Ortiz-Bolsico, C.; García-Alvarez-Coque, M.C. *Analytica chimica acta* **2016**, *923*, 1–23.
300. Wang, Y.; Lehmann, R.; Lu, X.; Zhao, X.; Xu, G. *Journal of Chromatography A* **2008**, *1204*, 28–34.
301. Roullier-Gall, C.; Witting, M.; Tziotis, D.; Ruf, A.; Gougeon, R.D.; Schmitt-Kopplin, P. *Tetrahedron* **2015**, *71*, 2983–2990.
302. Thurman, E.M.; Ferrer, I. *Journal of Chromatography A* **2012**, *1259*, 158–166.
303. Rauha, J.-P.; Vuorela, H.; Kostianen, R. *Journal of Mass Spectrometry* **2001**, *36*, 1269–1280.
304. Pérez-Magariño, S.; Revilla, I.; González-SanJosé, M.L.; Beltrán, S. *Journal of Chromatography A* **1999**, *847*, 75–81.

List of Tables

Table 1.1 First observation and characterization of selected compounds identified as markers for the Maillard reaction and advanced glycation.	21
Table 4.1 Fluorescence local maxima obtained by EEM-PARAFAC analysis.	69
Table A.1 Chromatographic conditions of the tandem HILIC-RP coupling.....	94
Table A.2 Number of features (retention time– <i>m/z</i> -pairs) detected in a beef meat extract and brewed coffee by ESI(+)-MS.	102
Table B.1 List of assigned molecular formulae classified as Maillard reaction products and ribose.....	108
Table B.2 List of detected contaminants.....	113
Table C.1 Ribose-glycine derived Maillard reaction products, which appear in the "general" Maillard reaction products formation and degradation pathways shown in Figure 3.5; (n.d.) not detected or S/N < 8.	121
Table C.2 Ribose-isoleucine derived Maillard reaction products, which appear in the "general" Maillard reaction products formation and degradation pathways shown in Figure 3.5; (n.d.) not detected or S/N < 8.	124
Table C.3 Ribose-lysine derived Maillard reaction products, which appear in the "general" Maillard reaction products formation and degradation pathways shown in Figure 3.5; (n.d.) not detected or S/N < 8.	127
Table C.4 Ribose-cysteine derived Maillard reaction products, which appear in the "general" Maillard reaction products formation and degradation pathways shown in Figure 3.5; (n.d.) not detected or S/N < 8.	130
Table D.1 Measured pH values during irradiation of Maillard model systems in the custom-built photolysis system used for online EEM measurements.	133
Table D.2 Measured pH values (mean from n = 2 irradiation experiments) before and after irradiation of Maillard model systems in the Suntest CPS system.....	133
Table D.3 Calibration standards used for quantification of urea and asparagine in ribose-histidine model systems. Standards were prepared in 2% acetonitrile solution. Concentration values are given in nmol mL ⁻¹	138

List of Figures

Figure 1.1 Scheme of possible routes of reactive intermediates produced in the initial, inter-mediate, and final phase of the Maillard reaction, respectively. Some reactive intermediates formed throughout the Maillard reaction might act as secondary precursors leading to a restart of the reaction cascade. Stable reaction products, including short-chain carboxylic acids, heterocyclic compounds and melanoidins, are mainly formed in the intermediate and final phase.....	10
Figure 1.2 UV/Vis-spectrum of a typical melanoidin (solid curve) interpreted as the sum of many individual chromophores (dashed curves).....	11
Figure 1.3 Analytical workflow to study Maillard reaction products by non-targeted mass spectrometry.....	22
Figure 1.4 Holistic description of the Maillard reaction using the concept of “chemical pools”.	23
Figure 1.5 Definition of chemical space and its coverage by comprehensive databases. (a) The number of elemental compositions and the number of underlying chemical structures per composition build the chemical space, which must be covered by analytical methods in non-targeted approaches. (b) Chemical subspaces, which are relevant for simple sugar-amino acid model systems and their coverage by HMDB v4.0 and FooDB v1.0 databases, respectively. Widths of the boxes represent the relative number of elemental compositions and heights represent the average number of isomers per composition, respectively. Therefore, the area illustrates the coverage of the chemical subspaces. (c) Number of all compounds and compounds listed as possible MRPs or AGEs in the HMDB v4.0 and FooDB v1.0 database, respectively.	25
Figure 1.6 Theoretical peak capacities of common separation techniques and spectroscopic / spectrometric detectors. The maximum overall peak capacity in hyphenated setups results from the product of the two peak capacities from the separation and detection techniques.	26
Figure 1.7 Van Krevelen diagram illustrating the position of different compound classes relevant to the Maillard reaction. H/C versus O/C atomic ratios of around 7 500 CHNOS compounds taken from HMDB v4.0. Common positions of compound classes formed during the MR are highlighted: carbohydrates and derivatives (dark blue), amino acids and peptides (red), furans (light blue), and azoles and azines (green).....	27
Figure 1.8 Outline of the thesis.....	30
Figure 2.1 Progression of reaction products in a ribose-glycine Maillard model system after thermal treatment at 100 °C for two, four, six, and ten hours. (a) Raw FT-ICR mass spectra with fixed peak intensity scale.	

- (b) Classification of the detected signals into Maillard reaction products (square) and carbohydrate degradation products (circle). Glycine degradation products were not detected. 36
- Figure 2.2 | Compositional characteristics of MRPs and ribose. (a–d) Van Krevelen diagrams (H/C vs. O/C) were used to visualize the reaction progression. Features on imaginary lines with a slope of 2 indicate dehydration series, those on vertical and horizontal lines represent redox reaction series.^[179] Selected known marker compounds illustrate the position in the diagrams depending on structural characteristics: ribose 1, Amadori product (ARP, 2), 1-deoxypentosone 3, *N*-(carboxymethyl)glycine 4, *N*-(2-furanylmethylene)glycine 5, and furfural 6. (e) The bar chart illustrates the absolute number of assigned molecular formulae for each reaction time classified into compositional spaces (CHO, CHN₁O, and CHN₂O). 37
- Figure 2.3 | Time-resolved coherences between MRPs. (a) Mass difference network of MRPs, carbohydrate decomposition products and the ribose precursor. 98% of assigned ion signals (357/366) could be connected in the network by allowing only a set of seven simple transformations from the Hodge scheme: 2.01565 (2H), 12.00000 (Strecker degradation, +H₂O/–CH₂O), 18.01057 (H₂O, in bold), 43.98983 (CO₂), 57.02146 (glycine condensation), 75.03203 (glycine addition), 150.05283 (pentose addition). The transformations (edges) in the graph are undirected, reverse reactions are also possible. (b) The selection shows the coherences between observed molecular formulae as expected for the initial and intermediate phase by the reaction scheme (dashed box in c). (c) Fundamental Maillard reaction scheme adapted from Hodge.^[16] 39
- Figure 2.4 | Visualization of dehydration series by Kendrick mass defect (KMD) analysis.^[179] Conversion of the IUPAC mass to a Kendrick mass scale (IUPAC × 18/18.01057) projects dehydration series onto horizontal lines. Only series including at least three intermediates ($n \geq 3$) are shown. Most series can be formed from the ARP by condensation with carbohydrate type (C_c(H₂O)_n) fragments (grey), redox reactions (green) or a combination of both. Formation of nitrogen-free compounds (blue) and MRPs containing two nitrogen atoms (orange) must involve further release or addition/condensation of glycine. 40
- Figure 3.1 | Formation of MRPs and UV absorbing products. (a) Number of MRPs produced in four different ribose-amino acid model systems heated for two, four, six, and ten hours (100 °C). (b) Absorbance at 294 nm of ribose-amino acid models heated for ten hours (100 °C). Error bars indicate the standard deviation of the mean absorbance value ($n = 3$). 47
- Figure 3.2 | Compositional characterization of MRPs. (a–d) Van Krevelen diagrams (H/C vs. O/C atomic ratios) of four ribose-amino acid model systems heated for ten hours at 100 °C. Scaling of points is according to their relative peak intensity in the mass spectra. Color gradient according to the degree in unsaturation (number of double bond equivalents per carbon atom (DBE/C)). 49

- Figure 3.3 | Changes in unsaturation over time and characteristics of compositional spaces. (a) Progression of H/C and O/C atomic ratios over time for ribose-glycine (dark grey), ribose-isoleucine (grey), ribose-lysine (white) and ribose-cysteine (red) MRPs. Points represent intensity weighted mean values of the H/C and O/C ratios, respectively. Linear regression lines visualize the direction of MRPs moving with increasing reaction time. (b) Absolute number of MRPs depicted for different chemical spaces.....51
- Figure 3.4 | Number of carbon atoms in MRPs. Relative peak intensities classified by the number of carbon atoms of thermally synthesized (10 h, 100 °C) (a) ribose-glycine, (b) ribose-isoleucine, (c) ribose-lysine, and (d) ribose-cysteine MRPs.53
- Figure 3.5 | General Maillard reaction product formation and degradation pathways. Maillard reaction products with identical element core compositions detected (S/N ratio ≥ 8) in at least three of the four investigated Maillard model systems revealed identical reaction behavior following a well-defined series of dehydration and redox reactions. The scheme could be sub-divided into four pathways of similar assembly: (a) ARP formation and degradation, (b) diketosamine degradation, (c-d) C2- and C3-cleavage. Molecular formulae shown have the same core composition but differ in the amino acid residues (-R). Embedded bar charts illustrate the relative peak intensity contributions after ten hours.....54
- Figure 4.1 | Photolytic degradation of MRPs in three model systems (ribose-lysine, -arginine, and -histidine) heated for ten hours at 100 °C. Excitation-emission-matrices retrieved from diluted model systems (1:800 v/v in H₂O) (a-c) before irradiation and (d-f) after solar irradiation for 8 h. (g-i) Changes in fluorescence intensity after an irradiation time of 8 h. All fluorescence intensity values are expressed in quinine sulfate units (ppm).....67
- Figure 4.2 | Four component EEM-PARAFAC models obtained from EEM measurements. (a) Ribose-lysine, (b) ribose-arginine, and (c) ribose-histidine model systems. All model systems were irradiated for 20 h. EEM spectra were recorded every 20 min.....69
- Figure 4.3 | Changes in the absorption spectra upon irradiation. Differential absorbance spectra of (a) ribose-lysine, (b) ribose-arginine, and (c) ribose-histidine model systems irradiated for eight hours. UV/Vis spectra were recorded every 20 minutes simultaneously with EEMs presented above. Embedded black curves represent UV/Vis absorption spectra of unirradiated model systems (10 h, 100 °C), respectively.....71
- Figure 4.4 | Effect of solar irradiation on elemental compositions of ribose-histidine MRPs. Model systems were irradiated for eight hours and compared to unirradiated control samples. Irradiation experiments were performed in duplicate. Each sample then was analyzed by FT-ICR-MS in triplicate injections (N = 2 × 3). Peak intensities of all features found in irradiated samples were compared to the same features in the

- unirradiated control samples by Student's t-Test ($n = 3$): Features, which showed a significant decrease in peak intensities in both independent irradiation experiments are colored in blue. Features, which showed a significant increase or were newly formed upon irradiation are highlighted in red, respectively. (a) Volcano plot. (b) Number of molecular formulae showing significant changes in peak intensities. (c) Van Krevelen diagram of all significantly affected molecular formulae. Pie charts illustrate the reduced occurrence of nitrogen-free (CHO) MRPs in photochemical reactions. Black pie chart represents elemental compositions, which did not show a significant change in peak intensities upon irradiation.73
- Figure 4.5 | Van Krevelen diagram of all molecular formulae reproducibly found in two independent replicate experiments (each analyzed in triplicate) after heating a ribose-histidine model system for ten hours at 100 °C. Color indicates the number of nitrogen atoms in the formulae. Scaling is relative to the average peak intensity recorded by FT-ICR-MS.74
- Figure 4.6 | LC-MS/MS analysis of known AGEs and MRPs that can be formed in the ribose-lysine and arginine Maillard reaction, respectively. Log₂ fold changes represent the changes in peak intensities between irradiated (8 h) and unirradiated control samples. Two independent irradiation experiments (experiment A: dark grey, experiment B: grey) were carried out. Each experiment was analyzed in triplicate injections by LC-MS/MS.76
- Figure 4.7 | Overview of compositional descriptors retrieved for the ribose-histidine model system after molecular formulae computation from FT-ICR-MS data. Bar charts are grouped into features, which showed a significant decrease (blue; log₂FC < -1 and $p < 0.01$, Student's t-Test ($n = 3$)) and significant increase (red; log₂FC > 1 and $p < 0.01$, Student's t-Test ($n = 3$)) in peak intensities in both independent irradiation experiments, respectively. Features that did not show a significant change in peak intensities after an irradiation time of eight hours are colored in black. Represented descriptors are (a) number of carbon atoms per formula, (b) measured m/z -values, (c) number of oxygen atoms per formula, (d) number of nitrogen atoms per formula, (e) average number of double bond equivalents per carbon atom, and (f) average carbon oxidation state.78
- Figure 4.8 | Pairwise comparison of mass difference incidences. Incidence rates were computed from all recorded mass differences in the mass spectra of thermally synthesized MRPs (left panel) and photochemically synthesized products (right panel). The top ten of the most frequently occurring mass differences were assigned to their element compositional equivalents representing possible net chemical transformations. Incidences represent the relative probability by which a monoisotopic signal in the mass spectrum can be linked to another monoisotopic signal with a given mass difference md_i79
- Figure A.1 | Configuration of the tandem HILIC-RP system. (a) Pre-fractionation of the sample in a first loading (trapping) step (0–5 min)

into hydrophobic and hydrophilic compounds. Addition of high organic mobile phase via pump 2 and a T-piece ensures retention of hydrophilic compounds on the HILIC column. (b) Independent gradient elution of hydrophilic components retained on the HILIC column (5–25 min). (c) Independent gradient elution of hydrophobic components trapped on the RP column (25–45 min).....	96
Figure A.2 (a) Analysis of 34 food relevant reference standards including amino acids, mono- and disaccharides, dicarboxylic acids, and phenols. (b) Influence of the acetonitrile content in the eluent composition during the loading step (0–5 min) on the distribution of red wine components onto the HILIC or RP stationary phase. Bar charts illustrate the number of detected features ($S/N > 3$) in the three sections of the chromatogram, respectively. Error bars indicate the standard deviation of the mean ($n = 3$).....	97
Figure A.3 Non-target analysis of a red wine sample by tandem HILIC-RP chromatography. (a-b) Retention time versus m/z -value plots of processed results obtained in electrospray negative (ESI(-)) and positive (ESI(+)) mode, respectively. Each dot represents an analytical signal (feature) colored according to the observed peak intensity. (c) Comparison of detected features in ESI(+) and ESI(-) mode. (d) Relative deviation of the retention times of all detected features from the mean for nine replicate measurements detected during HILIC (left) and RP separation (right); ESI(+) = red; ESI(-) = blue.	100
Figure A.4 Selectivity of the two analytical columns used in the tandem LC system and selectivity of ionization modes for food relevant compound classes. (a) Pie charts illustrating the preferred selectivity of the HILIC and RP column. (b) Sub-classification of major compound classes.	101
Figure A.5 Non-target analysis of a (a) beef meat extract and (b) coffee extract by tandem HILIC-RP chromatography, respectively. Retention time versus m/z -value plots of processed results obtained in electrospray positive (ESI(+)) mode. Each dot represents an analytical signal (feature) colored according to the observed peak intensity.....	103
Figure A.6 Selectivity of the two analytical columns used in the tandem LC system for food relevant compound classes. Compound classes were obtained from searching possible metabolites in FooDB database (http://foodb.ca , release: 06/29/2017) based on the experimental mass (± 10 ppm). Pie charts illustrating the preferred selectivity of the HILIC and RP column for a measured meat and coffee extract.	103
Figure B.1 Peak alignment based on experimental m/z -values with maximum of 1 ppm alignment window. Violin plots illustrate the quality of the alignment. Violins are horizontally divided into 25%, 50%, and 75% quantiles.	105
Figure B.2 Error plot retrieved after molecular formula assignment. More than 90% of all molecular formulae were found within an error range of +/- 200 ppb, more than 75% within +/- 100 ppb.....	106

Figure B.3 Classification of a ribose-glycine model system (10 h) into reaction pools according to the approach of Yaylayan. ^[159]	107
Figure B.4 Van Krevelen diagrams (H/C vs. O/C) for nitrogen-free MRPs detected after six (top) and ten hours (bottom). Color code illustrates the average carbon oxidation state (OS _C). Bubble size is scaled to relative peak intensity. C ₃ H ₆ O ₄ (probably glyceric acid) was only detected in the Maillard model systems after six hours. However, it could also be produced when ribose was heated alone for ten hours.	114
Figure B.5 Van Krevelen diagrams (H/C vs. O/C) for nitrogen-containing MRPs detected at four different reaction times (two, four, six, and ten hours). Color code illustrates the average carbon oxidation state (OS _C). Bubble size is scaled to relative peak intensity.....	115
Figure C.1 Direct-infusion FT-ICR-MS spectra. (a) Raw spectra of four different ribose-amino acid model systems heated for ten hours (100 °C). Red diamonds indicate the position of the Amadori rearrangement products in the mass spectra. (b) Isotopic fine structure validation of the ribose-cysteine Amadori product ion (C ₈ H ₁₄ NO ₆ S ⁻) by means of the exact masses and relative abundances of nine isotope signals. (c) Mass accuracy and peak intensity of 1 493 monoisotopic peaks assigned to their molecular formulae.....	117
Figure C.2 Classification of detected reaction products as Maillard reaction products (MRPs), carbohydrate and amino acid degradation products.....	118
Figure C.3 Van Krevelen diagrams of MRPs found in (a-c) three different pentose-glycine and (d-f) three hexose-glycine Maillard reaction model systems heated for 24 h at 100 °C.....	119
Figure C.4 Relative peak intensities explained by MRPs classified by the number of nitrogen atoms in the molecular formulae of model systems heated for ten hours (100 °C).....	120
Figure D.1 Principal component analysis of ribose-histidine FT-ICR-MS raw data. Samples were irradiated for four and eight hours in a suntester system. Additionally, control samples, which were kept under the same conditions, however, protected from light exposure, as well as freshly prepared model systems were analyzed. All experiments were carried out in two independent experiments. Each sample was injected in triplicate measurements (total number of samples per treatment = 6). Samples and replicate injections were measured in randomized order.	134
Figure D.2 Effect of solar irradiation on elemental compositions of ribose-lysine MRPs. Model systems were irradiated for eight hours and compared to unirradiated control samples. Irradiation experiments were performed in duplicate. Each sample then was analyzed by FT-ICR-MS in triplicate injections (N = 2 × 3). Peak intensities of all features found in irradiated samples were compared to the same features in the unirradiated control samples by Student's t-Test (n = 3): Features, which showed a significant decrease in peak intensities in both independent irradiation experiments are colored in blue. Features, which showed a	

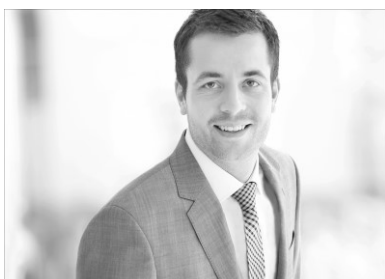
- significant increase or were newly formed upon irradiation are highlighted in red, respectively. (a) Volcano plot. (b) Number of molecular formulae showing significant changes in peak intensities. (c) Van Krevelen diagram of all significantly affected molecular formulae. Pie charts illustrate the reduced occurrence of nitrogen-free (CHO) MRPs in photochemical reactions. Black pie chart represents elemental compositions, which did not show a significant change in peak intensities upon irradiation.....135
- Figure D.3 | Effect of solar irradiation on elemental compositions of ribose-arginine MRPs. Model systems were irradiated for eight hours and compared to unirradiated control samples. Irradiation experiments were performed in duplicate. Each sample then was analyzed by FT-ICR-MS in triplicate injections ($N = 2 \times 3$). Peak intensities of all features found in irradiated samples were compared to the same features in the unirradiated control samples by Student's *t*-Test ($n = 3$): Features, which showed a significant decrease in peak intensities in both independent irradiation experiments are colored in blue. Features, which showed a significant increase or were newly formed upon irradiation are highlighted in red, respectively. (a) Volcano plot. (b) Number of molecular formulae showing significant changes in peak intensities. (c) Van Krevelen diagram of all significantly affected molecular formulae. Pie charts illustrate the reduced occurrence of nitrogen-free (CHO) MRPs in photochemical reactions. Black pie chart represents elemental compositions, which did not show a significant change in peak intensities upon irradiation.....136
- Figure D.4 | Quantification of (a) urea and (b) asparagine in ribose-histidine model systems. After lyophilization, the model systems were reconstituted in 2% acetonitrile solution to achieve a dilution factor of 1:10 (*v/v*) with respect to the original model system. Calibration curves were computed from analyzed standard solutions as shown below.137
- Figure D.5 | Screening of fragment spectra containing imidazole specific fragments at $m/z = 81.045$. Fragment spectra were acquired by data-dependent LC-MS/MS. Histograms illustrate the \log_2 fold change (irradiated samples vs. control samples) calculated from the peak intensities of the precursor ions, respectively, which represent the effect of irradiation on ribose-histidine samples after eight hours. Gray histogram represents all chromatographic features with available MS/MS spectra ($N = 580$). Blue histogram shows only features, which contained an imidazole characteristic fragment ($m/z = 81.045$) in their MS/MS spectra ($N = 355$).....138
- Figure D.6 | Non-targeted analysis of unirradiated model systems by tandem HILIC-RP chromatography. Retention time versus m/z -value plots of (a) a ribose-lysine, (b) a ribose-arginine, (c) and a ribose-histidine model system, heated for ten hours at 100 °C. Each dot in (a-c) represents an analytical signal (feature) colored according to the observed peak intensity. (d) Venn diagram illustrates the amino acid specific chemical diversity in produced MRPs. Between the three model systems,

chromatographic features were considered as the same chemical compound when m/z -values and retention times were equal (m/z -alignment: ± 10 ppm and $\Delta RT \leq 30$ s).....	139
Figure D.7 Compositional descriptors retrieved for 125 antioxidants containing no more than C, H, N, and O elements. Antioxidants were taken from FoodB (Release June 29, 2017).	140
Figure D.8 LC-MS/MS analysis of AGE markers in unirradiated ribose-lysine model systems (blue) and ribose-lysine model systems irradiated for eight hours (red). Structures were confirmed by MS/MS spectra. Detected markers were: (a) carboxymethyllysine (CML), (b) carboxyethyllysine (CEL), (c) GOLD, (d) MOLD, and (e) formyllysine.	141
Figure D.9 LC-MS/MS analysis of AGE markers in unirradiated ribose-arginine model systems (blue) and ribose-arginine model systems irradiated for eight hours (red). Structures were confirmed by MS/MS spectra. Detected markers were: (a) one hydroimidazolone isomer MG-H* (assignment of the three possible isomers MG H1 – MG H3 based on MS/MS data not possible), and (b) argpyrimidine.....	142
Figure D.10 Overview of compositional descriptors retrieved for the ribose-lysine model system after molecular formulae computation from FT-ICR-MS data. Bar charts are grouped into features, which showed a significant decrease (blue; $\log_2FC < -1$ and $p < 0.01$, Student's t-Test ($n = 3$)) and significant increase (red; $\log_2FC > 1$ and $p < 0.01$, Student's t-Test ($n = 3$)) in peak intensities in both independent irradiation experiments, respectively. Features that did not show a significant change in peak intensities after an irradiation time of eight hours are colored in dark gray. Represented descriptors are (a) number of carbon atoms per formula, (b) measured m/z -values, (c) number of oxygen, and (d) number of nitrogen atoms per formula, as well as (e) average number of double bond equivalents per carbon atom and (f) average carbon oxidation state.....	143
Figure D.11 Overview of compositional descriptors retrieved for the ribose-arginine model system after molecular formulae computation from FT-ICR-MS data. Bar charts are grouped into features, which showed a significant decrease (blue; $\log_2FC < -1$ and $p < 0.01$, Student's t-Test ($n = 3$)) and significant increase (red; $\log_2FC > 1$ and $p < 0.01$, Student's t-Test ($n = 3$)) in peak intensities in both independent irradiation experiments, respectively. Features that did not show a significant change in peak intensities after an irradiation time of eight hours are colored in dark gray. Represented descriptors are (a) number of carbon atoms per formula, (b) measured m/z -values, (c) number of oxygen, and (d) number of nitrogen atoms per formula, as well as (e) average number of double bond equivalents per carbon atom and (f) average carbon oxidation state.....	144

List of Schemes

Scheme 1.1 Generalized scheme showing the initial stage of the Maillard reaction for aldose sugars with different carbon chain lengths (n). The two reaction precursors undergo a spontaneous condensation reaction (the intermediate formed by addition of the amino compound to the carbonyl moiety is not shown). The formed Schiff base then rearranges into the Amadori product. In a similar way, ketoses form 2-amino-2-deoxyaldoses (Heyns product) after rearrangement.	3
Scheme 1.2 Formation of dicarbonyls by decomposition of the ARP in the intermediate phase, adapted from Nursten (2005). ^[14] (a) Low pH values favor the formation of 3-deoxyosones and ultimately furfurals via the 1,2-enolization pathway. (b) At high pH values 2,3-enolization rates are thought to be increased leading to 1-deoxy-dicarbonyls.	4
Scheme 1.3 Retro-aldolization of β -hydroxycarbonyls, adapted from Smuda and Glomb (2013). ^[21]	6
Scheme 1.4 Two possible α -dicarbonyl cleavage reactions. (a) Hydrolytic α -dicarbonyl cleavage adapted from Ginz <i>et al.</i> (2000), ^[33] and (b) oxidative α -dicarbonyl cleavage as reported by Davidek and co-workers (2006). ^[31]	7
Scheme 1.5 Two possible β -dicarbonyl cleavage reactions. Hydroxide and amines may act as nucleophilic agents in a hydrolytic β -dicarbonyl cleavage and amine-induced β -dicarbonyl cleavage reaction, adapted from Davidek <i>et al.</i> (2006) ^[19] and Smuda <i>et al.</i> (2010), ^[36] respectively.	8
Scheme 1.6 Strecker degradation of α -amino acids by the action of 1,2-dicarbonyls, adapted from Rizzi (2008) ^[39] and Yaylayan (2003). ^[40]	8
Scheme C.1 Strecker degradation in the Maillard reaction. Enaminols and amino ketones formed in the Strecker degradation of amino acids by dicarbonyls could be a class of compounds with low H/C and O/C ratios as observed in the lysine and isoleucine Maillard reaction.	120

Curriculum Vitae



Daniel Hemmler

daniel.hemmler[at]tum.de

PROFESSIONAL EXPERIENCE

05/2015 – now	Research Associate at the Chair of Analytical Food Chemistry, Technical University of Munich and at the Helmholtz Zentrum München GmbH, Research Unit Analytical BioGeoChemistry.
09/2014 - 03/2015	Master Thesis at the German Cancer Research Center (DKFZ), Heidelberg.
03/2013 - 08/2013	Bachelor Thesis at the Beiersdorf AG, Hamburg.
09/2011 - 02/2012	Practical Study Semester at the Metrohm AG International Headquarters, Herisau, Switzerland.
07/2004 - 04/2009	LC-MS/MS Analyst at the Pharmakin GmbH (ratiopharm group), Ulm.
09/2001 - 06/2004	Apprenticeship Laboratory Chemist at the Merckle GmbH (ratiopharm group), Ulm and Karl-Arnold-Berufsschule, Biberach/Riß.

ACADEMIC EDUCATION

05/2015 – 03/2019	PhD Candidate at the Chair of Analytical Food Chemistry, Technical University of Munich and at the Helmholtz Zentrum München GmbH, Research Unit Analytical BioGeoChemistry.
-------------------	---

09/2013 - 03/2015	<p>Master of Science (M. Sc.) in Analytical und Bioanalytical Chemistry at the Aalen University.</p> <p>Master-Thesis: „Acetylome Analysis of Non-Small Lung Carcinoma Cell Response to High and Low LET Irradiation“, German Cancer Research Center (DKFZ), Heidelberg.</p>
09/2009 - 08/2013	<p>Bachelor of Science (B. Sc.) in Chemistry at the Aalen University.</p> <p>Bachelor-Thesis: “Quantification of ϵ-Poly-L-Lysin and Other Synthetic Polymers in Cosmetic Products by MALDI-TOF Mass Spectrometry”, Beiersdorf AG, Hamburg.</p>
<p>Voluntary commitment, memberships and additional activities during academic education:</p>	
05/2015 - 03/2019	<p>Member of the Helmholtz Graduate School Environmental Health and TUM Graduate School of the Technical University Munich.</p>
03/2014	<p>Participation at the “4. Frühjahrsschule Industrielle Analytik“, organized by the Analytical Chemistry division of the „Gesellschaft Deutscher Chemiker“ (GDCh) and the „Industrieforum Analytik“.</p>
02/2014 - 08/2014	<p>Scientific assistant at the Faculty of Chemistry, Aalen University.</p>
07/2011 - 08/2011	<p>Vacation work pesticide analysis at PTRL Europe, Ulm.</p>
11/2011 - 01/2014	<p>Member of the appointment committee for a professorship in organic chemistry, Aalen University.</p>
07/2011 - 08/2011	<p>Vacation work Bioanalytics at the Nuvisan GmbH, Neu-Ulm.</p>
09/2010 - 02/2013	<p>Elected member of the faculty board at the Faculty of Chemistry, Aalen University.</p>
09/2010 - 02/2013	<p>President of the student representatives „Fachschaft Chemie“, Aalen University.</p>
03/2010 - 07/2011	<p>Tutor in undergraduate courses, Aalen University.</p>

SCHOLARSHIPS AND AWARDS

2018	Best Poster Award , 13th European Fourier Transform Mass Spectrometry Workshop, 2018, Freising, Germany.
2009 - 2015	Scholarship Vocational Training Foundation for the Highly Talented , Federal Ministry of Education and Research (BMBF).
2015	Year's best graduate in Analytical and Bioanalytical Chemistry (Master of Science) , awarded by the Aalen University.
2014	Best graduate in Analytical Chemistry , awarded by the Gesellschaft Deutscher Chemiker (GDCh). Year's best graduate in Chemistry (Bachelor of Science) , awarded by the Aalen University.

Eidesstattliche Erklärung

Ich erkläre an Eides statt, dass ich die bei der promotionsführenden Einrichtung Wissenschaftszentrum Weihenstephan für Ernährung, Landnutzung und Umwelt der Technischen Universität München zur Promotionsprüfung vorgelegte Arbeit mit dem Titel:

Molecular-level analysis of non-volatile Maillard reaction products and their chemical interplay in model reactions

In Chemie am Lehrstuhl für Analytische Lebensmittelchemie unter der Anleitung und Betreuung durch apl.-Prof. Dr. Philippe Schmitt-Kopplin ohne sonstige Hilfe erstellt und bei der Abfassung nur die gemäß § 6 Abs. 6 und 7 Satz 2 angegebenen Hilfsmittel benutzt habe.

- (x) Ich habe keine Organisation eingeschaltet, die gegen Entgelt Betreuerinnen und Betreuer für die Anfertigung von Dissertationen sucht, oder die mir obliegenden Pflichten hinsichtlich der Prüfungsleistungen für mich ganz oder teilweise erledigt.
- (x) Ich habe die Dissertation in dieser oder ähnlicher Form in keinem anderen Prüfungsverfahren als Prüfungsleistung vorgelegt.
- (x) Ich habe den angestrebten Doktorgrad noch nicht erworben und bin nicht in einem früheren Promotionsverfahren für den angestrebten Doktorgrad endgültig gescheitert.

Die öffentlich zugängliche Promotionsordnung der TUM ist mir bekannt, insbesondere habe ich die Bedeutung von § 28 (Nichtigkeit der Promotion) und § 29 (Entzug des Doktorgrades) zur Kenntnis genommen. Ich bin mir der Konsequenzen einer falschen Eidesstattlichen Erklärung bewusst.

Mit der Aufnahme meiner personenbezogenen Daten in die Alumni-Datei bei der TUM bin ich einverstanden.

München, den 01. April 2019